A national laboratory of the U.S. Department of Energy
Office of Energy Efficiency & Renewable Energy

National Renewable Energy Laboratory

*Innovation for Our Energy Future*

# Design and Test of DC Voltage Link Conversion System and Brushless Doubly-Fed Induction Generator for Variable-Speed Wind Energy Applications

## August 1999 — May 2003

T.A. Lipo, D. Panda, and D. Zarko
*University of Wisconsin*
*Madison, Wisconsin*

***Subcontract Report***
**NREL/SR-500-34583**
**November 2005**

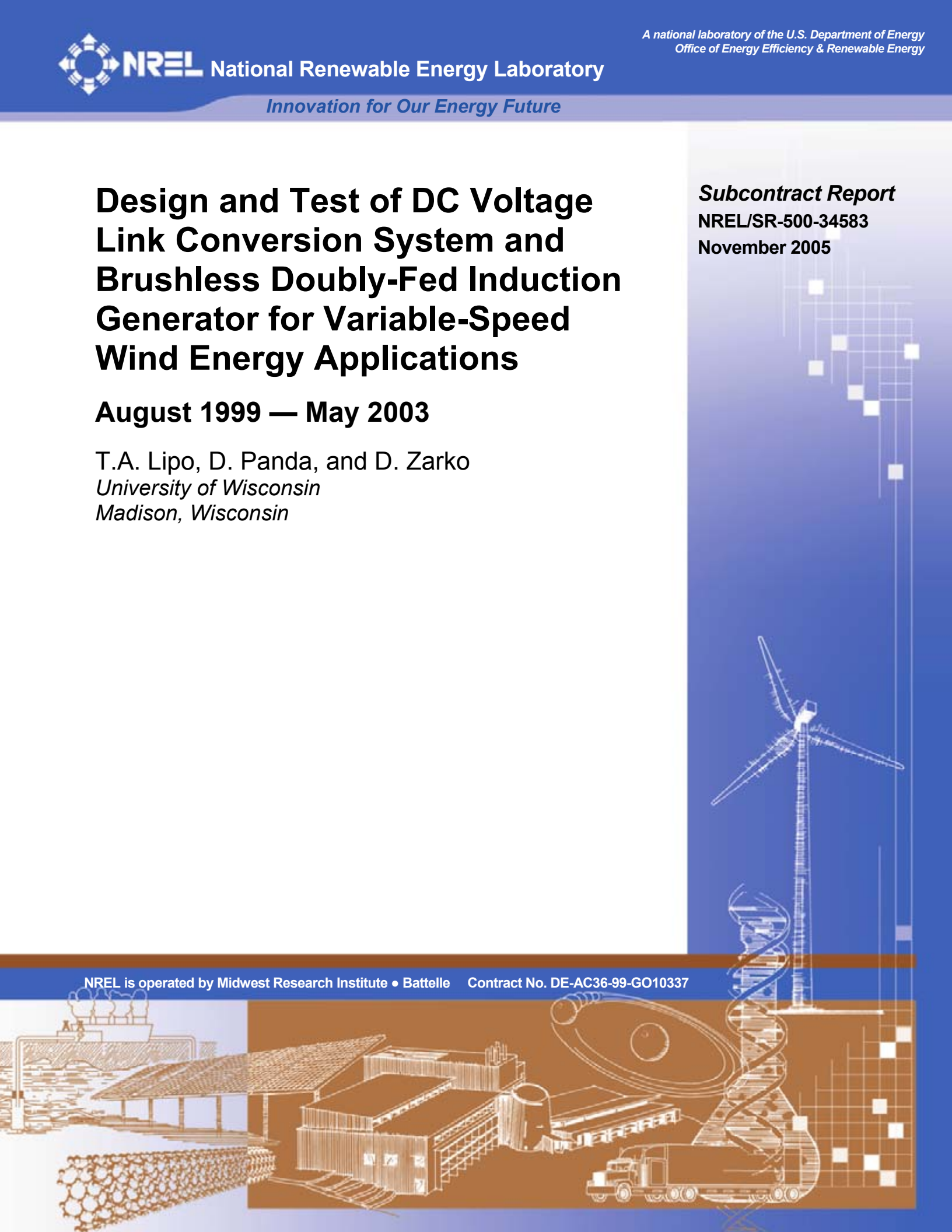

NREL is operated by Midwest Research Institute • Battelle Contract No. DE-AC36-99-GO10337

# Design and Test of DC Voltage Link Conversion System and Brushless Doubly-Fed Induction Generator for Variable-Speed Wind Energy Applications

## August 1999 — May 2003

T.A. Lipo, D. Panda, and D. Zarko
*University of Wisconsin*
*Madison, Wisconsin*

NREL Technical Monitor: Alan Laxson

Prepared under Subcontract No. XCX-9-29204-02

***Subcontract Report***
**NREL/SR-500-34583**
**November 2005**

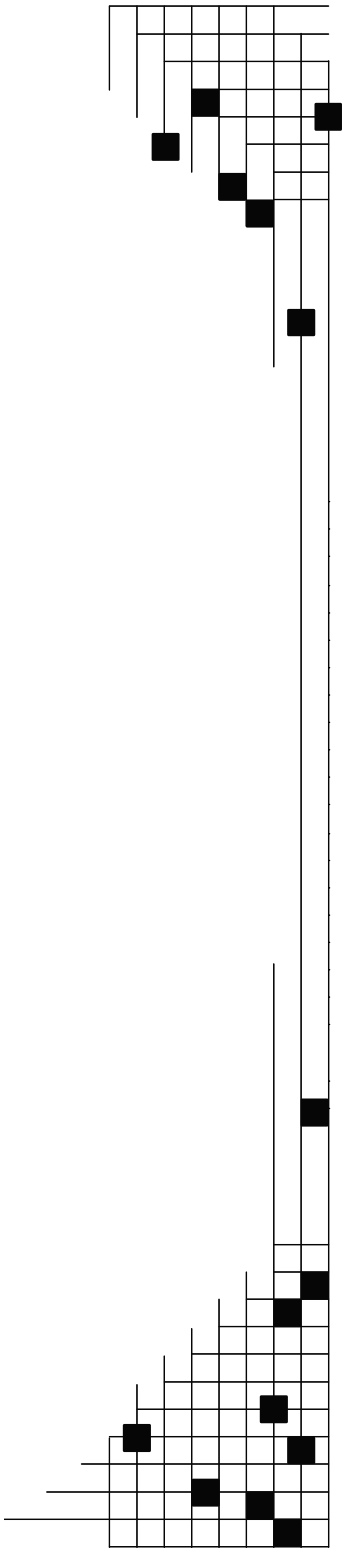

**National Renewable Energy Laboratory**
**1617 Cole Boulevard, Golden, Colorado 80401-3393**
**303-275-3000 • www.nrel.gov**

Operated for the U.S. Department of Energy
Office of Energy Efficiency and Renewable Energy
by Midwest Research Institute • Battelle

Contract No. DE-AC36-99-GO10337

**NOTICE**

This report was prepared as an account of work sponsored by an agency of the United States government. Neither the United States government nor any agency thereof, nor any of their employees, makes any warranty, express or implied, or assumes any legal liability or responsibility for the accuracy, completeness, or usefulness of any information, apparatus, product, or process disclosed, or represents that its use would not infringe privately owned rights. Reference herein to any specific commercial product, process, or service by trade name, trademark, manufacturer, or otherwise does not necessarily constitute or imply its endorsement, recommendation, or favoring by the United States government or any agency thereof. The views and opinions of authors expressed herein do not necessarily state or reflect those of the United States government or any agency thereof.

Available electronically at http://www.osti.gov/bridge

Available for a processing fee to U.S. Department of Energy
and its contractors, in paper, from:

U.S. Department of Energy
Office of Scientific and Technical Information
P.O. Box 62
Oak Ridge, TN 37831-0062
phone: 865.576.8401
fax: 865.576.5728
email: mailto:reports@adonis.osti.gov

Available for sale to the public, in paper, from:

U.S. Department of Commerce
National Technical Information Service
5285 Port Royal Road
Springfield, VA 22161
phone: 800.553.6847
fax: 703.605.6900
email: orders@ntis.fedworld.gov
online ordering: http://www.ntis.gov/ordering.htm

**This publication received minimal editorial review at NREL**

Printed on paper containing at least 50% wastepaper, including 20% postconsumer waste

# Table of Contents

**1. Introduction ..... 1**

1.1 Motivation ..... 1
1.2 Variable-Speed Constant Frequency (VSCF) Wind Generator ..... 1
1.3 Prospect of Wound Rotor Induction Machine for Variable – Speed Constant Frequency (VSCF) Wind Generator ..... 2
1.3.1 Operating Principle of Wound Rotor Induction Machine ..... 2
1.4 Power Converters for VSCF Operation ..... 5
1.4.1 State-of-the-Art Power Converter Wound Rotor Induction Machine Drive ..... 6
1.5 System with Low-Cost Alternative Power Converters ..... 6
1.6 System with Wide Range of Operating Speed ..... 7
1.7 System without Carbon Brushes and Slip Rings ..... 7
1.8 Scope and Organization of this Report ..... 8

**2. Power Converter Topology 1 ..... 11**

2.1 Overview: Diode Bridge with a Boost Chopper, IGBT Inverter, and Two Reversing Contractors ..... 11
2.2 Introduction ..... 11
2.3 Generating Operation ..... 13
2.3.1 Sub-synchronous Operation ..... 13
2.3.2 Super-synchronous Operation ..... 17
2.4 Contractor Operation ..... 21
2.4.1 Reduction of Currents through the Contractor during Make and Break ..... 23
2.5 Control Algorithm during Transition between Sub-and Super-Synchronous Modes ..... 25
2.6 Unity Power Factor Interface to the Grid ..... 28
2.7 Starting Performance ..... 28
2.8 Conclusions: ..... 32

**3. Power Converter Topology 2 ..... 33**

3.1 Overview: Naturally Commutated Thyristor Bridge with Bi-directional Chopper And IGBT Front End Converter ..... 33
3.2 Introduction ..... 33
3.3 Operating Principle ..... 34
3.4 A Doubly Fed Machine Control ..... 35
3.4.1 Machine-Side Converter (MSC) Rectifier Operational Mode ..... 36
3.4.2 Forced Boosting Near Synchronous Speed ..... 37
3.4.3 MSC Inverter Operational Mode ..... 37
3.4.4 Mode Transitional Operation ..... 38
3.4.5 DC Link Control ..... 39
3.4.6 Commutation of Thyristors ..... 40
3.5 Front End Controller ..... 40
3.6 Simulation ..... 41
3.7 Results and Discussion ..... 42
3.8 Conclusions ..... 43

**4. Converter Topology 3 ..... 55**

4.1 Overview: Hybrid PWM Converter with Thyristors and IGTBS ..... 55
4.2 Introduction ..... 55
4.3 Circuit Description ..... 55
4.4 Operating Principle ..... 57
4.5 Special Control Effort and Switching Logic Generation ..... 60
4.6 Control Scheme ..... 61
4.7 Simulation Results and Discussion ..... 61
4.8 Conclusions ..... 62

**5. Converter Topology 4 ..... 73**

5.1 Overview: Reduced-switch-count, Double-converter-fed Wound-rotor Induction Machine Drive ..... 73
5.2 Introduction ..... 73
5.3 Operating Principle ..... 74
5.4 Super-Synchronous Generating Mode ..... 76
5.5 Proposed Power Converter Configuration and Control Strategy ..... 77
5.6 Comparison of the Proposed Converter System with the Conventional Converter System When Used As Machine Side Converters ..... 79
5.7 Comparison of Copper Loss of the Proposed and Conventional Rotor-side Configurations ..... 79
5.8 Starting Method ..... 80
5.8.1 Starting Method I (Extra Switch Starting) ..... 80
5.8.2 Starting Method II (Contractor Starting) ..... 81
5.9 Control Scheme ..... 82
5.10 Simulation Results and Discussions ..... 83
5.11 Conclusion ..... 84

**6. Rotating Transformer Design ..... 93**

6.1 Overview: Analysis and Control Issues ..... 93
6.2 Introduction ..... 93
6.3 Design of Rotary Transformer ..... 94
6.4 Core Assembly ..... 95
6.5 Rotary Transformer Model ..... 97
6.6 Comparison of Two-phase and Three–phase Rotary Transformer ..... 100
6.7 Design Parameters of the Rotary Transformer ..... 103
6.8 Simulation Results ..... 109
6.9 Doubly-fed Induction Machine ..... 112
6.10 Conclusion ..... 114

**7. Control Algorithm Based on Stator Power for the Rotor-side Control of a DFIM System ..... 115**

7.1 Overview ..... 115
7.2 Introduction ..... 115
7.3 Performance of the System with Diode Bridge Combined with a Chopper Inverter ..... 116
7.4 Control of the DFIM through Direct Stator Power on the Rotor-side ..... 119
7.4.1 Concept of Control using Direct Stator Power ..... 120
7.4.2 Effect of Active vectors on Active power ..... 123
7.4.3 Effect of Active Vectors on Reactive Power ..... 124
7.4.4 Effect of Zero Vectors on Active Power ..... 124
7.4.5 Effect of Zero Vectors on Reactive Power ..... 125
7.5 Control Algorithm ..... 125
7.5.1 Measurement of Stator Active and Reactive Power ..... 125
7.5.2 Sector Identification of Rotor Flux ..... 126
7.6 Modified Stator Power Control Algorithm ..... 126
7.7 Simulation Results with and without Rotary Transformer ..... 139
7.8 Conclusion ..... 140

**8. Development of Power Converter and DSP Control Platform And Experimental Test Results ..... 157**

8.1 Overview ..... 157
8.2 Introduction ..... 157
8.3 Design of Power Module ..... 158
8.3.1 Power Rating of Semiconductor Devices ..... 158
8.3.2 DC-Link Design ..... 160
8.3.3 Thermal Design ..... 161
8.3.4 Sensors ..... 163
8.3.5 Other Components ..... 164
8.4 DSP Based Controller Design ..... 164
8.4.1 Mother Board ..... 164
8.4.2 Daughter Board ..... 165

8.5 Status of the Test Set-Up ..... 165
8.6 Status of the Wound-Rotor Induction Machine and Rotary Transformer ..... 166
8.7 Conclusions ..... 166

**9. Conclusions ..... 185**

9.1 Scope of Future Work ..... 188

**Nomenclature ..... 189**

**References ..... 195**

# Chapter 1: Introduction

## 1.1 Motivation

Electric power generated from renewable sources of energy is generally referred to as "Green Power." These renewable sources include solar, wind, wave, hydro, geothermal, biomass, and hydrogen. Among these, wind energy is considered as one of the most economic and viable solutions. Today, there are more than one million "windmills" in operation around the world used for traditional applications. However, there has been a renewed interest in wind energy in recent years because it is a potential source for electricity generation with minimal environmental impact and with no cost for fossil fuel. With the advancement of aerodynamic designs, wind turbines that can capture hundreds of kilowatts or even megawatts of power, are readily available. When such wind energy conversion systems (WECS) are integrated to the grid, they produce a substantial amount of power, which can supplement the base power generated by thermal, nuclear, or hydro power plants.

WECS are broadly classified as grid-connected or isolated systems. While use of isolated WECS is restricted to small-scale power generation in remote areas, grid-connected systems are more popular and much higher power capacities are commercially available. Depending on operating speed, the WECS can be divided into two groups – fixed-speed operation systems and variable-speed operation systems. If there is flexibility in varying the shaft speed, the power capture due to fluctuating wind velocities can be substantially improved. The requirement of variable-speed constant-frequency (VSCF) operation has led to several developments in the generator control of WECS.

The common electric generators used for isolated WECS are the Direct Current (DC) generator, the field-wound or permanent magnet synchronous alternator, or the capacitor-excited induction generator. Of these, the induction generator is most attractive because of its ruggedness, low cost, and low maintenance requirement. The squirrel-cage rotor induction motor is also the most frequently used generator for grid-connected WECS. When directly connected to the grid, the induction generator runs at near-synchronous speed, drawing the magnetizing current from the mains, resulting in nearly constant-speed, constant-frequency (CSCF) operation. However, this machine can be used for VSCF operation, as well, through the use of a power converter.

## 1.2 The Variable-Speed Constant-Frequency (VSCF) Wind Generator

Variable-speed wind turbine control using cage rotor machines has been reported by Miller *et al* [1]. The generator is operated in constant voltage to frequency ratio (V/f) mode by a voltage source inverter. The frequency command is decided by the present rotor speed and the target power. The turbine speed is measured and the target power is determined based on a cubic function of speed. The required frequency is then computed depending on the machine parameters. We estimated the annual energy production of the system by using a Rayleigh annual wind distribution. It is reported that for a turbine with a 5-m radius, the annual energy production was 49.6 megawatt-hours (MWh), compared to 37.2 MWh for a corresponding fixed-speed system.

Vector-controlled squirrel-cage induction generators for VSCF wind power systems are also commercially available. Instantaneous control over the machine torque can be exercised leading to smoother variations in generator power and speed. The utility side converter is simultaneously controlled for unity power factor operation under all wind conditions.

## 1.3 Prospect of Wound-Rotor Induction Machine for VSCF Wind Generator

In spite of the disadvantages associated with the slip-rings, the wound-rotor induction machine has long been a wind electric generator choice. By using a suitable integrated approach in the design of a WECS, use of a slip-ring induction generator has been found to be economically competitive. Control of grid-connected and isolated variable-speed wind turbines with a doubly fed induction generator has been implemented and reported.

### *1.3.1 Operating Principle of Wound-Rotor Induction Machine*

A wound-rotor induction machine can be operated as a doubly-fed induction machine (DFIM) when a power converter is present in its rotor circuit. This converter directs the power flow into and out of the rotor windings. Because the DFIM can operate as either a motor or a generator at sub-synchronous and super-synchronous speeds, there exist four operational modes in which the DFIM operates. All the four modes are explained in Figure 1.1. When the machine runs above synchronous speed, this operation is termed *super-synchronous* operation. Similarly, operation below synchronous speed is called *sub-synchronous* operation. In both sub- and super-synchronous operation, the machine can be operated either as a motor or a generator. In the motoring mode of operation, the torque produced by the machine is positive. On the other hand, during generating operation, the machine needs mechanical torque as input; thus, the torque is negative during generating operation. The principle of a DFIM control in these modes can be understood more clearly by the power-flow diagram given in Figure 1.2. In this figure, Ps is the stator power, Pr is the rotor power, and Pm is the mechanical power. When the DFIM is operating as a motor in the sub-synchronous speed range (Figure 1.2[i]), power is taken out of the rotor. This operational mode is commonly known as slip-power recovery. If the speed increases so that the machine is operating at super-synchronous speeds (Figure 1.2[ii]), the rotor power then changes direction.

When the DFIM is operating as a generator in the sub-synchronous speed range (Figure 1.2[iii]), power is delivered to the rotor. If the speed increases so that the machine is operating at super-synchronous speeds (Fig. 1.2[iv]) the rotor power again changes direction.

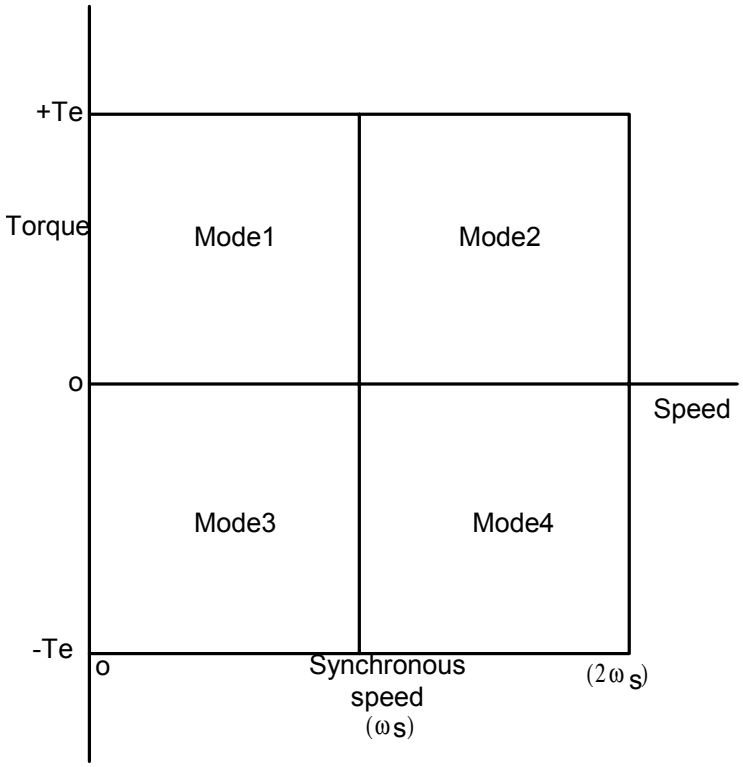


**Figure 1.1. Operating modes of a DFIM: Mode 1 (sub-synchronous motoring mode), Mode 2 (super-synchronous motoring mode), Mode 3 (sub-synchronous generating mode), and Mode 4 (super-synchronous generating mode)**

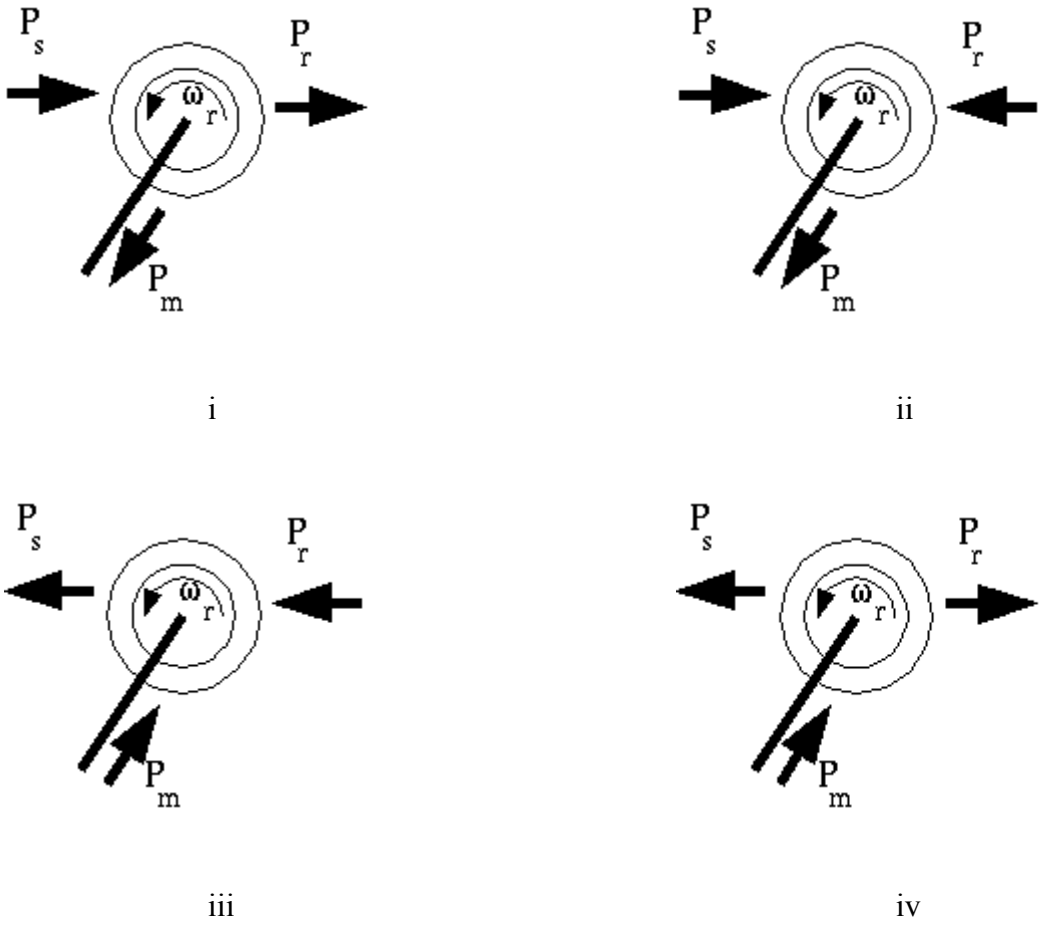


**Figure 1.2. Power-flow diagram of a DFIM for (i) sub-synchronous motoring mode, (ii) super-synchronous motoring mode, (iii) sub-synchronous generating mode, and (iv) super-synchronous generating mode**

Because the machine will be predominantly working as a generator for a wind-energy application, operation in mode 3 and mode 4 is more important than mode 1 and mode 2. However, for an ideal WECS system, all four operating modes are desirable. Motoring modes are useful when the generator needs to speed up quickly in order to achieve the best operating speed and efficiency. However, because of the high inertia of the wind generator power train, the acceleration of the machine may be achieved by the wind torque itself. Hence, motoring operations may be sacrificed if the cost of the system can be reduced substantially.

It should be noted that for sub- and super-synchronous generating modes, the power flows through the rotor are of opposite directions. Hence, the power converter connected with such system should have bi-directional power flow capability.

## 1.4 Power Converters for VSCF Operation

As discussed earlier, wind generation systems generally operate with best efficiency at variable speeds as the wind gusts dictate. Hence, it is necessary to interpose a frequency converter between the variable-frequency generator and a fixed-frequency utility. When a squirrel-cage induction machine is used, a power electronic converter equal to the kilovolt-amperes (KVA) rating of the machine must be used because all power transmitted to the utility passes through the converter. In the case of a wound-rotor machine, the power to the utility passes through both the stator and the rotor. Hence, the machine can be controlled either from the stator or the rotor or from both sides. State-of-the-art technology for wind power employs a DFIM with only rotor-side control, where the stator is directly connected to the grid. In such a control method, the power converter should be rated for the power produced by the rotor windings alone, typically one-third to one-quarter of the total KVA rating of the machine. This approach leads to significant reduction in cost. However, such systems typically use two full-bridge, three-leg insulated gate bipolar transistor (IGBT) -based power converters, which are relatively more costly than a thyristor of equivalent power rating or a diode-bridge-based power converter.

Because the cost of electricity generation utilizing wind is relatively higher than conventional thermal, hydro, or nuclear power plants in most locations, it is important to give serious efforts to reduce the cost of the former and, thus, make it more competitive. The power converter and the generator system together constitute almost 25% of the total cost of the system. Hence, by reducing the cost of the power converter, the system cost can be brought down considerably. In this project, the major focus is to find alternative power converters, which will bring down the cost of the system and which will provide simultaneously satisfactory performance of the system. In the literature, various power converter topologies have been reported for AC/DC, DC/AC, and AC/AC systems. However, the selection of the final power converter for wind energy application should be based on the following criteria.

- Cost-effectiveness
- Suited for wide speed range
- Capable of handling bi-directional power flow
- Suited for unity power factor interface to the gird
- Require low maintenance
- Capable of tracking the peak power operating point with variable wind speed
- Reliability

Cost is an important factor in view of the fact that the existing wind turbines are expensive, and the payback period for such expensive installation is high. The cost of the power converter mainly depends primarily on the cost of the semiconductor devices and passive elements, such as the capacitor, inductor, etc. Thus, by employing relatively cheaper semiconductor devices, the cost can be decreased.

Cost reduction of power electronics can be done in two ways. First, semiconductor device manufacturers constantly introduce new technologies that produce the devices at much cheaper price. Second, if by using the existing power devices, an alternative low-cost topology is found through which VSCF operation can be supported and other performance criteria of the system maintained, cost reduction is also possible. In this project the second approach is followed.

### *1.4.1 State-of-the-Art Power Converter for Wound-Rotor Induction Machine Drive*

The state-of-the-art technology uses two back-to-back IGBT based power converters with a DC link capacitor for VSCF wind power generation. This topology, (Figure 1.3) is the most popular one and currently being used extensively in wind turbine installations. Probably, the ease of control, known technology, and the availability of IGBTs up to the medium power range and versatile usage of the topology are the driving force behind the popular choice of this topology. With the help of this topology, field-oriented control of the machine is possible for the entire range of operating speed. In addition, the line-side inverter can be controlled for bi-directional power flow with the grid at almost unity power factor. The disadvantage of this topology is that it requires two IGBT-based fully controlled power converters. The IGBTs are relatively expensive and, thus, the existing system cost is high.

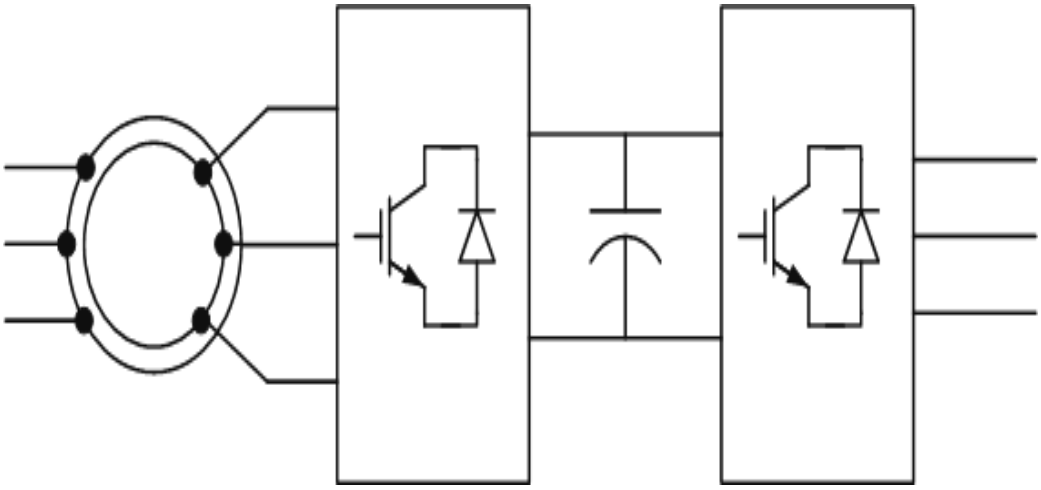

**Figure 1.3. State-of-the-art, back-to-back, IGBT-based power-converter topology for the rotor-side control of a DFIM for wind generator application**

## 1.5 System with Low-Cost Alternative Power Converters

With suitable converter topologies, it is possible to replace some of the IGBTs by diodes or thyristors without sacrificing the performance of the system; therefore, the cost of the power converter can be reduced. In this research, the major motivation is to determine such low-cost alternatives. A total of four alternative low-cost power converters are proposed for the control of a DFIM. Detailed circuit schematics, operating principles, and comparative analyses of all the four converters are illustrated in this report. The merits and demerits of each of the proposed power converter are discussed, and the feasibility of each of them for wind generator application is examined. Of the first three circuits, the authors propose two, and another existing power converter is explored for the first time for a wind energy application. In addition, an improved control algorithm is proposed for the fourth existing converter in order to obtain better performance.

## 1.6 System with Wide Range of Operating Speed

Another important aspect for wind turbines is to make them operate with optimum efficiency over all available wind speeds. In reality, the wind speed varies widely at different times and day of the year. Hence, a system with limited speed range capacity may not be adequate to fully exploit the potential of the wind. Even though limited slip operation brings down the cost of the converter, it reduces the utilization of available wind energy appreciably. Alternative solutions need to be explored in order to achieve a wide operating range without increasing the cost appreciably. By increasing the rotor-side power converter, the operating speed range may be extended to some extent. However, in systems where the stator is directly connected to the grid and control is exerted only from the rotor side, field weakening no longer becomes possible. Hence, the machine cannot be made to operate beyond twice the rated speed. Thus, topologically the rotor side control configuration suffers from a maximum speed limitation.

By employing power converters both in the stator and the rotor side, field weakening can be achieved and, therefore, a wide range of operation for speed (beyond twice the rated speed) is possible. In addition, with this arrangement, the excitation current can be shared amicably between the stator and rotor of the machine. By doing so, the winding design (copper volume) and losses in the machine can be optimized, and the machine size may be reduced. However, such methods incur extra cost to the system and may not be viable for wind energy application. In this project, because the major focus is to reduce the cost of the system, half-controlled converters are employed instead on both the stator and rotor sides. Thus, the cost of the machine-side power converter *can be reduced to almost half*. A new control algorithm is also proposed through which the performance of the machine with half-controlled converters can be improved in its operating range. The operating principle, control algorithm, and performance of the system with the proposed configuration will be presented.

## 1.7 System without Carbon Brushes and Slip Rings

As mentioned earlier, slip rings and carbon brushes are the major disadvantages associated with the wound-rotor induction machine. Normally, wind turbines are installed at remote places and maintenance cost for such remote installations are always high. Carbon brushes need regular maintenance; and this potentially increases the cost of the wind generation. In order to avoid the carbon brush and slip ring an alternative solution consisting of a rotary transformer is explored in this project. A 2-phase, 3-wire rotary transformer was designed and accommodated on the same shaft as the machine so that power can be transferred from the rotor winding of the machine to the power converter through the rotary transformer without using any slip ring or carbon brushes. A detailed analysis of the design and control aspect of the rotary transformer is presented later in this report.

## 1.8 Scope and Organization of this Report

In Chapters 2 through 5, four alternative power converter topologies are proposed, and their operating principles are explained. The merits and demerits of each power converter are illustrated through simulation results. A state-of-the-art simulation package, SABER, is used for simulating the system, which consists of a power converter, the DFIM, and an ideal turbine. A detailed simulation for each power converter is presented.

In Chapter 2, we illustrate a new converter topology consisting of a diode bridge, a boost chopper, a regular IGBT inverter, and two reversing contactors. Various operating modes of a DFIM in association with this new topology are explained, and a suitable control algorithm is presented. Finally, the controller is verified using a SABER simulation.

Chapter 3 deals with a second new converter topology. This new topology consists of a regular IGBT inverter, a thyristor bridge, and a DC/DC chopper interface. The operation of the new proposed topology is verified with SABER, and detailed simulation results are presented for various control modes.

In Chapter 4, another power converter is investigated for the rotor-side control of a DFIM. The power converter itself has already been reported in the literature. However, the possible use of this converter for wind energy application is investigated here for the first time. The control issues related to this power converter are analyzed, and a new control algorithm is proposed for improving the performance of the power converter. The operating modes, working principle, and control scheme for this converter are presented in this chapter. Finally, SABER simulation results are presented.

In Chapter 5, we propose a new control algorithm based on both stator and rotor-side control of a DFIM. Two three-phase half-controlled power converters are employed for both stator and rotor-side control of the machine. The proposed controller is capable of operating over a wide range of speed and, thus, the utilization of wind energy can be improved. At the same time by using half-controlled configuration the cost of the system is also kept low. With this control scheme the machine and power-converter efficiency are expected to improve. Most important, the machine is always made to operate at super-synchronous operating mode, irrespective of the shaft speed of the machine. The advantage of such a control algorithm is that no circulating power flows around the stator and rotor sides of the machine, which otherwise is a typical case for any conventional rotor-side control. After explaining the proposed control scheme, the performance of the system is verified with a SABER simulation, and the simulation results are presented.

Chapter 6 deals with the rotating transformer to be used with a DFIM. The operating principle, design guidelines, and the final design values of a rotating transformer are presented. A comparison is made between two-phase and three-phase rotary transformers and the advantages and disadvantages of each of them are illustrated. A detailed analysis and the effect of rotating transformer on the overall control and performance of the system are also explained.

Chapter 7 discusses a direct stator power-based control approach for the rotor-side control of a DFIM. First, the basic control principle is explained for a balanced system, then the same is extended for an unbalanced system. The impact of this control algorithm on the two-phase rotating transformer is illustrated. A detailed analysis of the nature of unbalance introduced into the system by the two-phase rotary transformer is provided, and a direct-stator power-based control algorithm is applied to cope with such unbalancing. Several other conventional control algorithms, such as field orientation control with or without rotor-winding current measurements, are also investigated, and the simulation results are presented.

The development of power hardware and the digital signal processor (DSP) -based digital controller are discussed in Chapter 8. A typical experimental result for a V/F control implementation of a 7.5-kW induction motor with the designed power converter is shown as a validation and test of the experimental set up. Photographs of different hardware components as well as photographs of the complete hardware system are given in this chapter. Unfortunately, the test machine has yet to arrive, so the results with the actual system are not available in this report. However, another supplementary report will be submitted after the testing of the system is completed. Finally, conclusions are stated in Chapter 9, and suggestions for future work are proposed.

# Chapter 2: Power Converter Topology 1

## 2.1 Overview: Diode Bridge with a Boost Chopper, IGBT Inverter, and Two Reversing Contactors

In this chapter, we propose novel power converter topology consisting of a diode bridge, a boost chopper, a conventional IGBT inverter, and two reversing contactors. When connected through the rotor of the machine, the proposed configuration supports the generating operation in both sub- and super-synchronous speed ranges of operation. This system can be considered as one possible low-cost solution for wind energy application. Its cost is reduced considerably because one full-bridge IGBT-based inverter is simply replaced by a diode bridge and boost chopper. With this new configuration, the system is interfaced with the grid at near-unity power factor, provides bidirectional power flow through the grid and also supports smooth starting of the system from a standstill. Hence, it can be used as an alternative low-cost power converter for wind energy application. The system is verified with SABER simulations.

## 2.2 Introduction

The simple diode bridge is well known as the most economic solution among all the rectifier topologies that are available. However, it suffers from the disadvantage of drawing higher ripple current from the utility. The diode rectifier also does not have a voltage-boosting capability, which limits its usefulness. A diode bridge used in combination with a boost chopper, however, removes some of these disadvantages. First of all, it inherits excellent boosting capability from the chopper, and the chopper can control the ripple current of the system up to a certain extent. Thus, the overall power factor of the system can be improved by adding the chopper. The cost of such a single-switch rectifier-chopper combination is much less than a six-switch active-boost rectifier, and the benefit of cost-effectiveness is largely retained. The diode-bridge with boost chopper combination can also be used for the rotor-side control of a wound-rotor induction machine when the rotor generates slip power (sub-synchronous motoring and super-synchronous generating modes). However, this topology does not support the rotor-side control when the rotor requires slip power (i.e., during sub-synchronous generating and super-synchronous motoring) because the diode bridge does not have regenerative operation.

On the other hand, a conventional IGBT converter can be used for the utility side converter, as well as the rotor-side control of a wound-rotor induction machine as the need arises. Thus, by employing a diode bridge-boost chopper and a regular IGBT inverter in different combinations, it may be possible to control the rotor-power flow of a wound-rotor induction machine to the grid.

We propose such a power converter topology for the rotor-side control of a DFIM. The proposed circuit (Figure 2.1) consists of a diode bridge with boost chopper, an IGBT-based inverter, and two reversing contactors. It can be seen that this circuit has fewer semiconductor devices compared to the conventional back-to-back IGBT configuration. Because the cost of a diode bridge is much less than an equivalent IGBT or thyristor bridge, the proposed circuit is expected to be less expensive. The operation of this topology is different for the sub- and super-synchronous speed regime. In sub-synchronous operation, the diode bridge is connected to the utility, and the rotor of the machine is

connected to the IGBT-based inverter. During super-synchronous operation, the IGBT inverter is connected to the line and the diode bridge to the machine rotor.

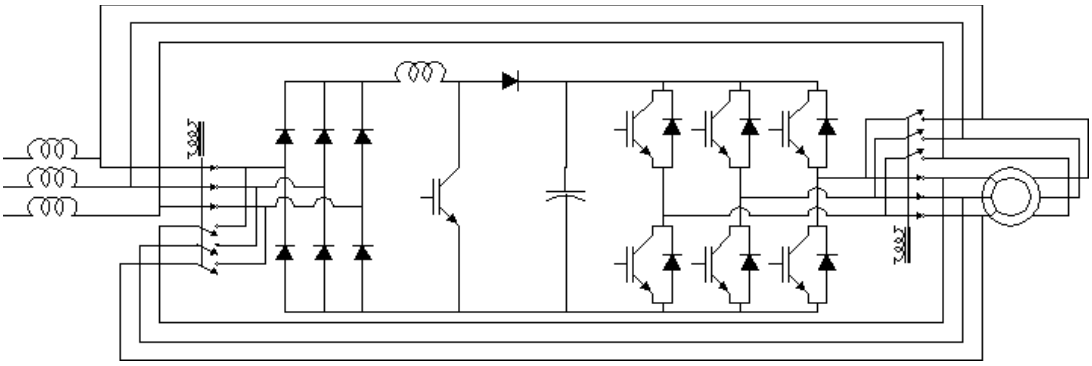

**Figure 2.1. Proposed power converter with diode bridge, boost chopper, IGBT converter, and two reversible contactors**

When operating sub-synchronously, the boost chopper may also be used for improving the power factor of the system. In the super-synchronous mode of operation, the circuit is flipped so that the rotor of the machine is connected to the diode bridge, and the IGBT-based converter becomes connected to the utility. The rotor voltage, being a function of speed, provides the boost operation required to maintain the DC bus voltage above the peak line voltage. During this mode of operation, the boost chopper is not enabled. The changeover of circuits between the machine side and the utility takes place when the rotor passes through the synchronous speed. The changeover is made using two reversing contactors (Figure 2.1). Whereas a contactor with high interrupting current capacity appears initially to be expensive, it is important to note that the switch need only be rated for a small fraction of rated current. By reducing the interrupting current through the contactors by suitable control strategy, this topology becomes, in reality, a cost-effective solution.

Although the circuit of Figure 2.1 appears to be relatively simple and cost-effective, a number of issues must be resolved for successful operation of the system:

- A separate controller for the machine side as well as the front end has to be designed for the sub-synchronous and super-synchronous regions to achieve smooth operation over a wide range of speeds.
- Smooth transition of speed and reliable changeover of power electronics circuitry at synchronous speed must be ensured
- Special care has to be taken during sub-synchronous motoring and super-synchronous generating operation so that the DC bus voltage does not exceed the designed limit.
- Separate power factor correction methods must be adopted for sub-synchronous and super-synchronous modes of operation.

Once all the above issues are resolved, this proposed circuit might be considered as one cost-effective solution for wind turbine application. We verified the feasibility of this circuit by means of a SABER simulation. Based on the simulations, we found that this proposed topology provides a promising solution for wind generation. An in-depth discussion of this topology in connection with system simulation, control system design, line-side filter design, starting performance, and power factor correction will be presented in the remainder of this chapter.

## 2.3 Generating Operation

The following two sections describe the configuration of the wind turbine during sub-synchronous and super-synchronous operation, as well as some of the issues that must be addressed.

### *2.3.1 Sub-Synchronous Operation*

For the above topology, during sub-synchronous operation, the IGBT inverter is connected to the machine side, and the diode bridge is connected to the line side (Figure 2.2). The torque and speed of the machine are controlled through field orientation. The boost chopper controls the level of the DC bus voltage. During starting of the wind turbine, a controlled acceleration in the motoring mode would be desirable. During sub-synchronous motoring mode, power flows from the rotor terminals back to the AC grid. Because the diode bridge is connected to the front end, the power cannot be fed back to the grid from the DC bus thus producing, perhaps, an over-voltage. However, by employing a suitable field-oriented control algorithm during the sub-synchronous motoring mode (accelerating mode), only the reactive power need be supplied from the rotor side, and no active power is drawn from the rotor during this period. This mode of operation can be accomplished by forcibly making the q-axis current reference (isq) zero. Thus, during this operation, the maximum acceleration of the rotor depends solely on the input wind torque. With such an arrangement, an over-voltage of the DC bus is avoided.

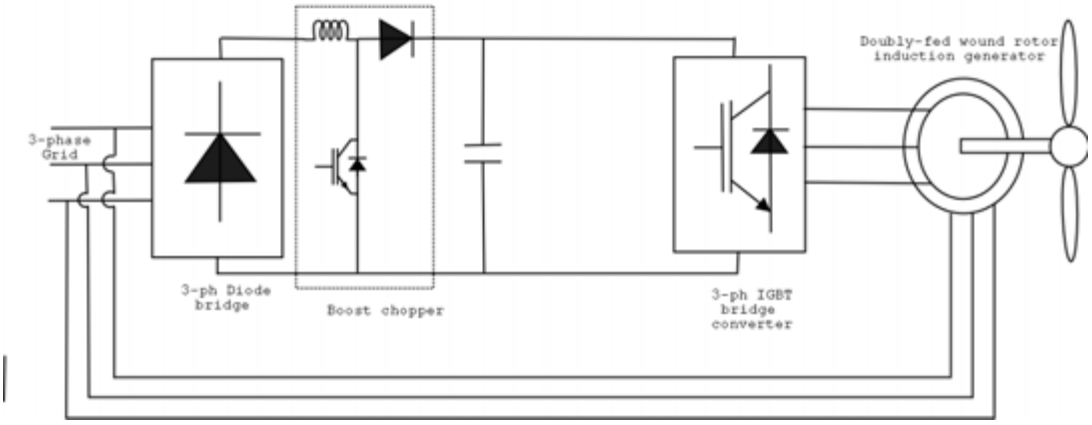


**Figure 2.2. Proposed power converter configurations during sub-synchronous operation**

During sub-synchronous generation, the rotor demands both active and reactive power from the DC bus through the IGBT inverter. With the proposed topology satisfactory sub-synchronous operation is possible without danger of overshooting the DC bus voltage. During steady-state generating operation, the machine operates with conventional field-oriented control, where the demanded active and reactive currents are supplied to the rotor through the IGBT inverter, and the DC bus voltage is controlled through the boost chopper at the front end. A detailed control-block diagram of the proposed converter for sub-synchronous operation is given in Figure 2.3. Figure 2.4 shows the steady-state SABER simulation results for the wind-generator system, and Figure 2.5 shows the transient SABER simulation results.

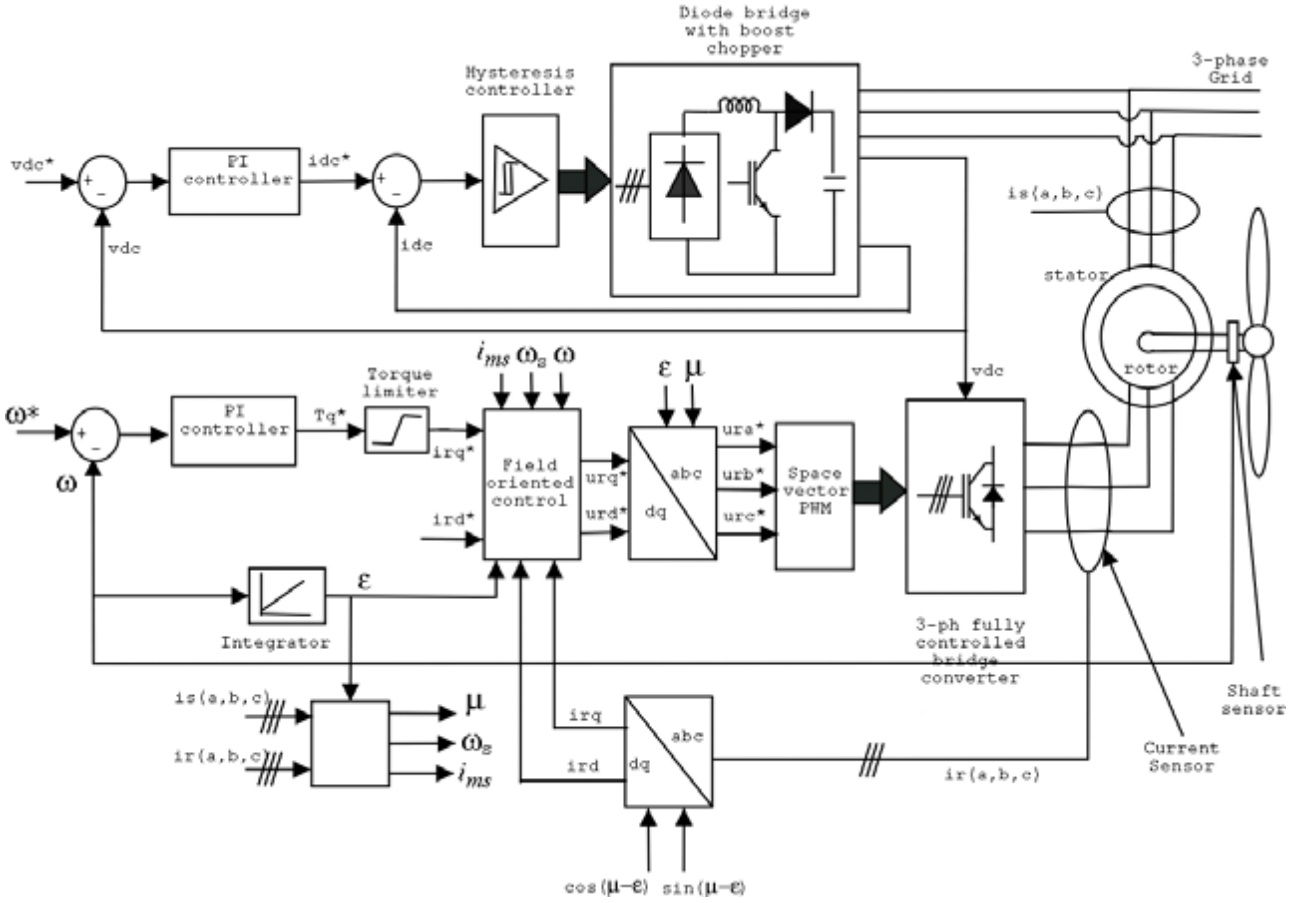


**Figure 2.3. Proposed control algorithm during sub-synchronous operation**

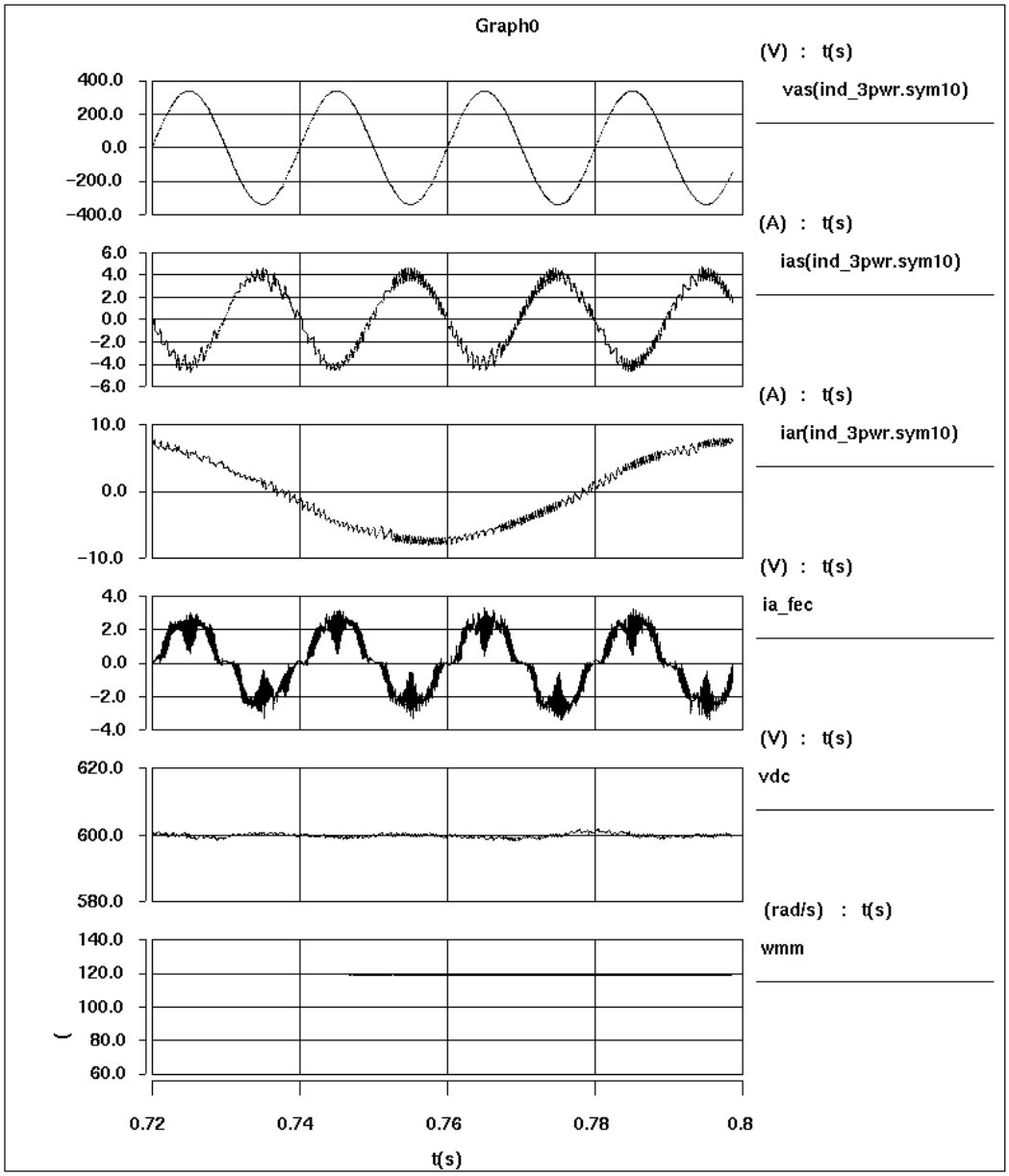


**Figure 2.4. Sub-synchronous steady-state results with the proposed power converter: vas = stator-phase voltage, ias = stator-phase current, iar = rotor-phase current, ia_fec = front-end converter phase current, vdc = DC bus voltage, wmm = mechanical speed of the machine**

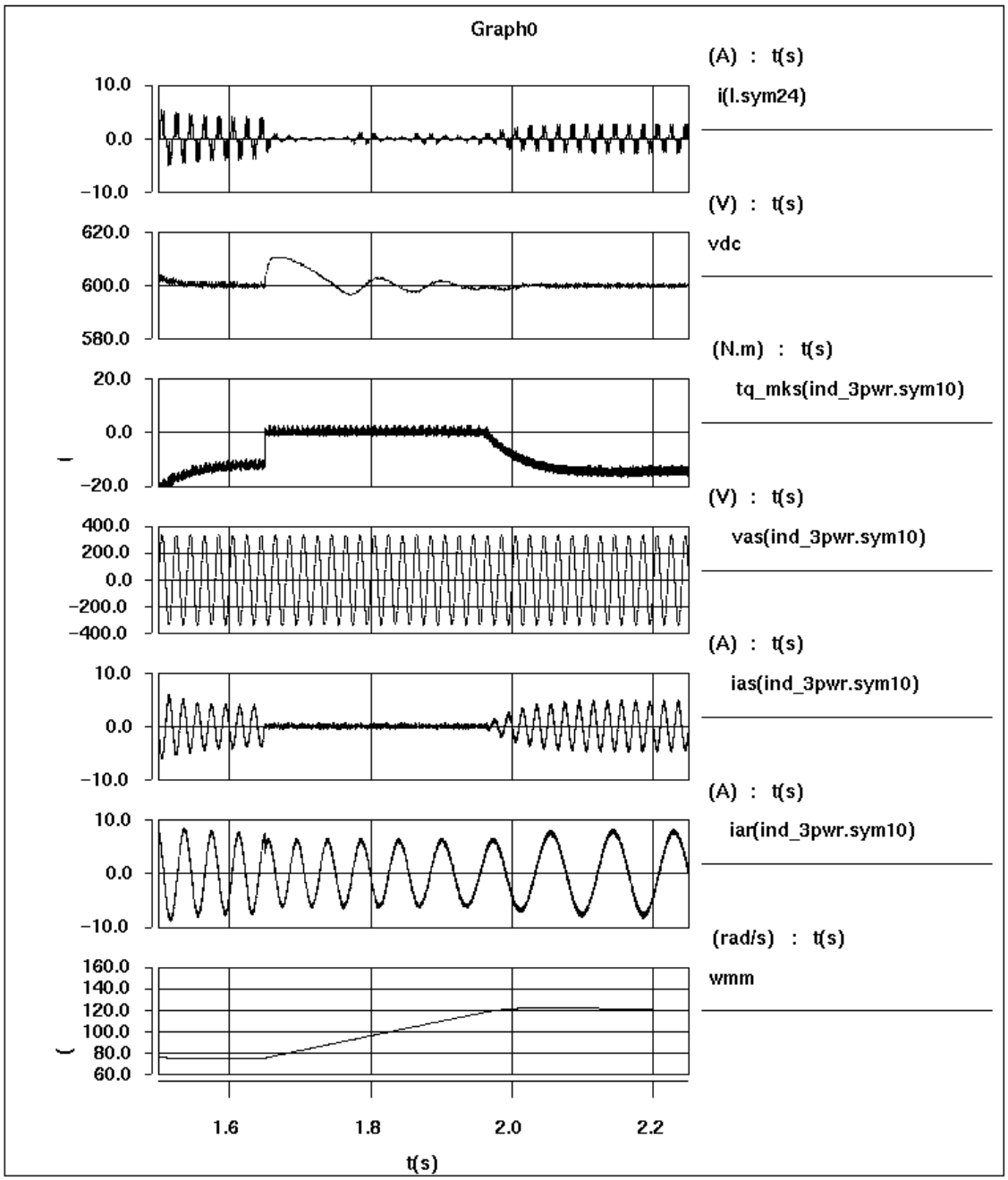


**Figure 2.5. Sub-synchronous transient results with the proposed power converter: i(l.sym24) = phase current through front-end rectifier, vdc = DC bus voltage, tq_mks = torque developed by the machine, vas = stator-phase voltage, ias = stator-phase current, iar = rotor-phase current, wmm = mechanical speed of the machine**

### *2.3.2 Super-Synchronous Operation*

During the super-synchronous mode, the torque of the machine is controlled by the boost chopper. During acceleration in this super-synchronous motoring mode, the machine normally demands power input from the DC bus to the rotor winding. Because, the diode bridge is connected to the rotor during this mode, the DC bus is unable to supply any power to the rotor. Hence, during super-synchronous motoring mode, the boost chopper is turned off (duty ratio is zero) and the rotor must solely accelerate from mechanical torque (wind torque). On the other hand, during super-synchronous generating mode, the power is fed back from the rotor to the DC bus, and during this mode, the boost chopper comes into operation. The duty cycle of the boost switch increases proportionately with the increase in demand of decelerating torque (negative torque).

The IGBT inverter is used as the front-end converter (FEC), which permits the feeding of power to the grid at unity power factor. This FEC can also compensate for the reactive and harmonic components of the stator current by utilizing an active filtering principle. Hence, the front-end converter serves two purposes in this mode. Finally, a unity power factor interface of the system to the grid is ensured by this control method. A detailed control scheme for the super-synchronous mode operation is given in Figure 2.7. The SABER simulation results during steady-state and transient operation for super-synchronous speed regime are given in Figures 2.8 and 2.9.

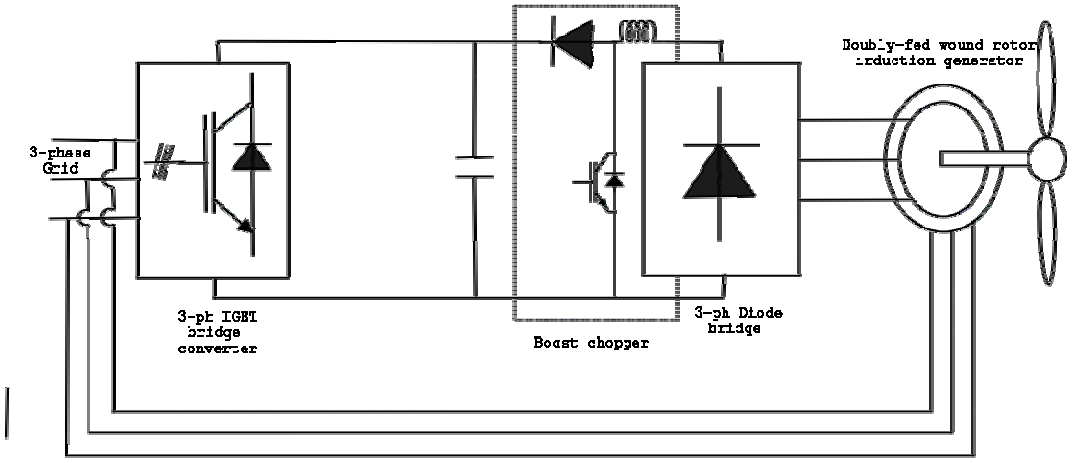


**Figure 2.6. Proposed power converter configuration during super-synchronous mode operation**

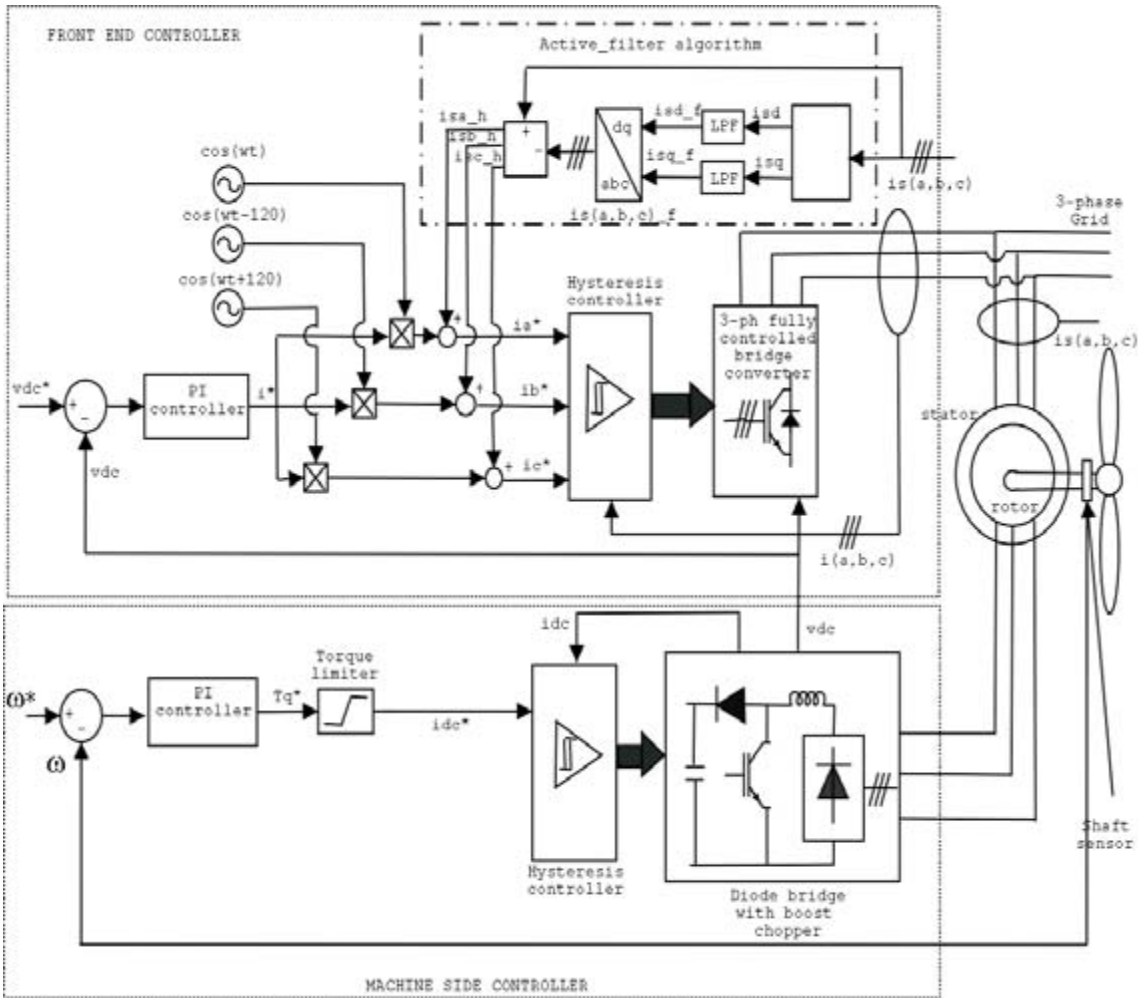


**Figure 2.7. Proposed control-block diagram during super-synchronous mode operation**

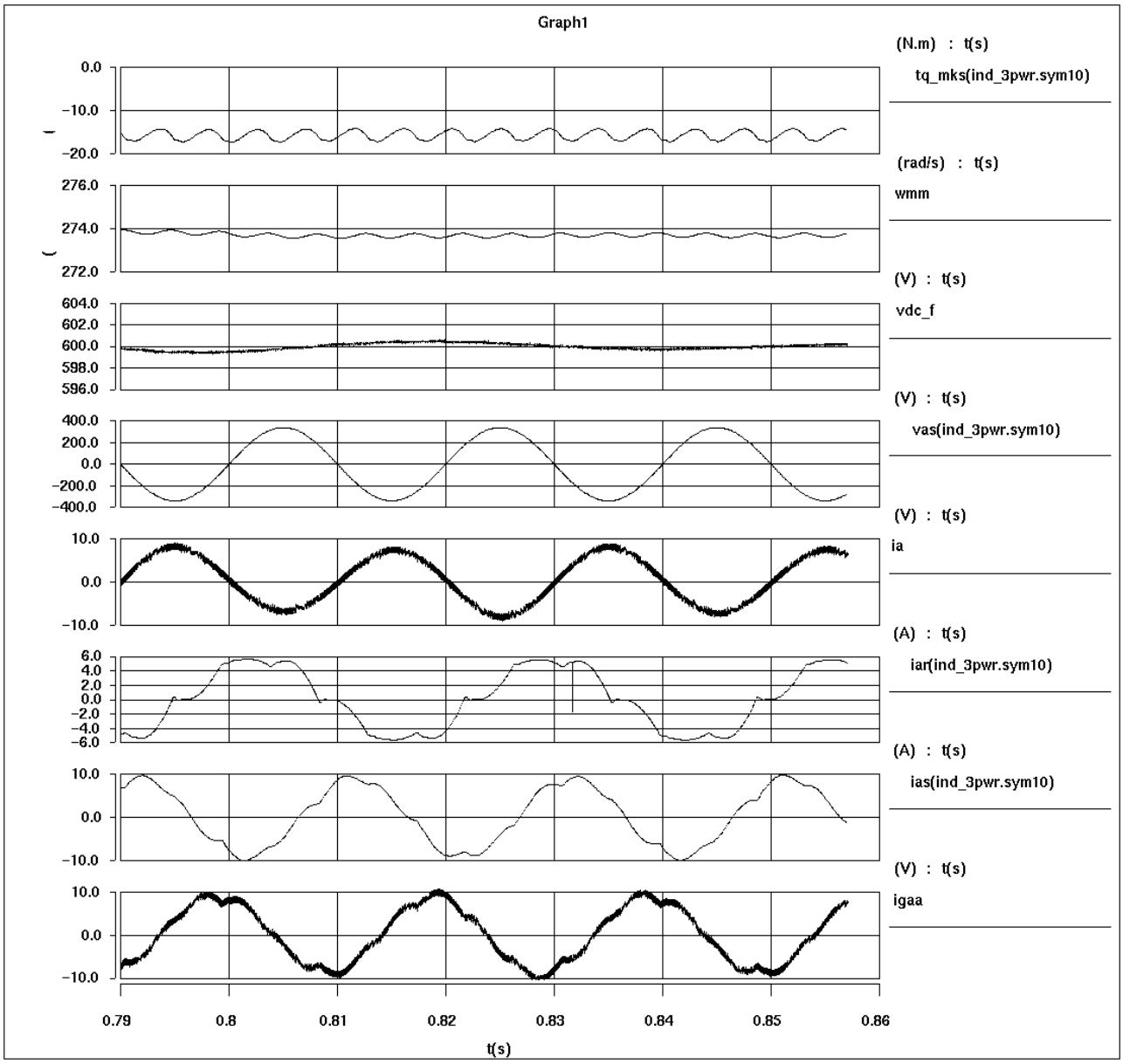


**Figure 2.8. Super-synchronous steady-state results with the proposed power converter: tq_mks = torque developed by the machine, wmm = mechanical speed of the machine, vdc_f = DC bus voltage, vas = stator phase-A voltage, ia = total phase-A grid current, iar = rotor phase-A current, ias = stator phase-A current, igaa = front-end converter phase-A current**

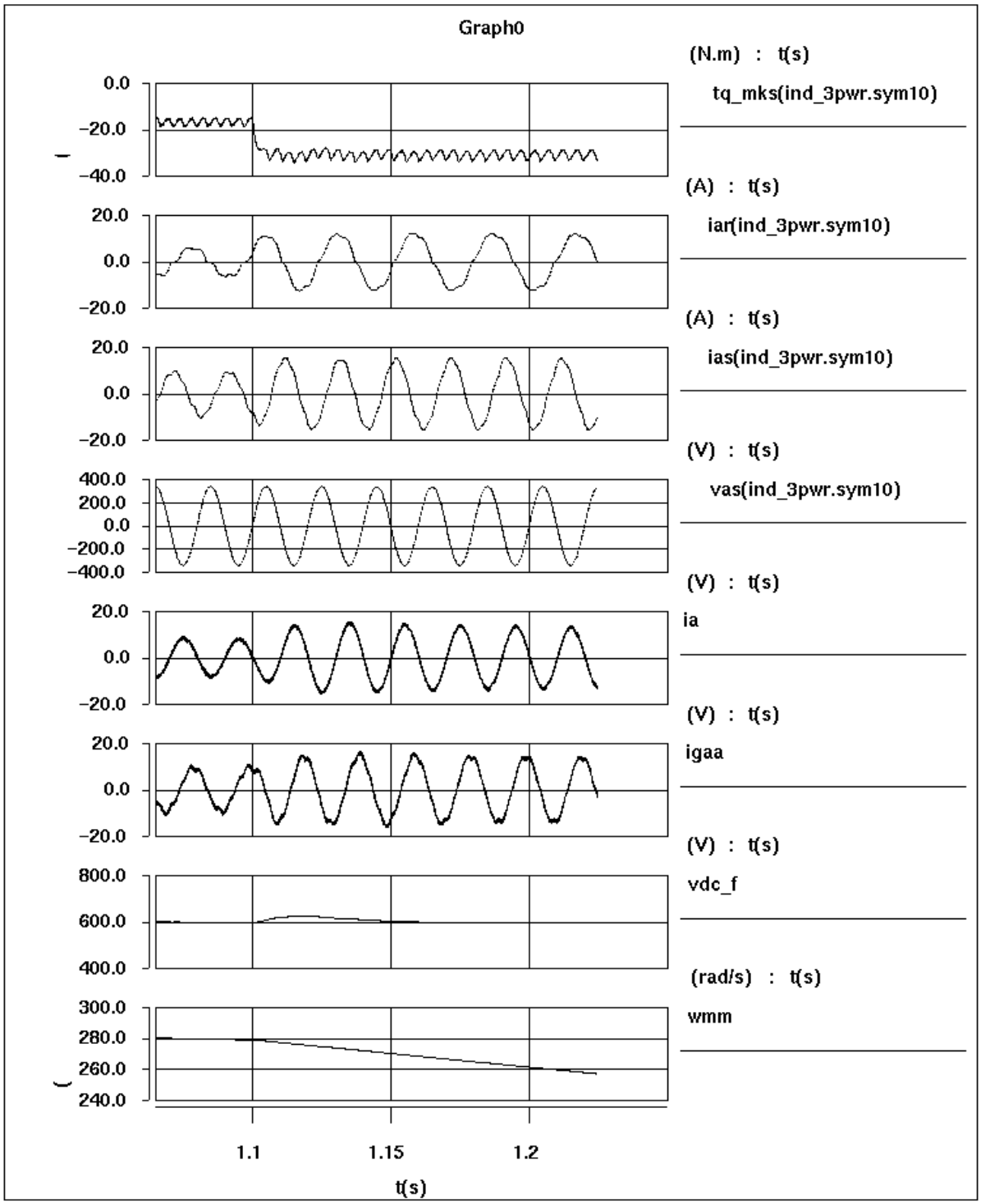


**Figure 2.9. Super-synchronous transient results with the proposed power converter: tq_mks = torque developed by the machine, iar = rotor phase-A current, ias = stator phase-A current, vas = stator phase-A voltage, ia = total phase-A grid current, igaa = front-end converter phase-A current, wmm = mechanical speed of the machine, vdc_f = DC bus voltage**

## 2.4 Contractor Operation

The most difficult mode of the proposed topology is the smooth changeover of the power electronic circuitry from sub- to super-synchronous operation. Two reversible three-phase contactors have been proposed for this purpose. Each contactor has three normally open (no) and three normally closed (nc) contacts. The input side of each no-nc pair is shorted and connected to the power electronic circuit (rectifier or inverter). On the other hand the output side of the no-nc pair is either connected to the grid or to the rotor of the machine, depending on the sub- or super-synchronous regime of operation. The contactor connected to the rectifier is called rectifier-side contactor, and the one connected to the inverter is called the inverter-side contactor.

Once the machine is running in a particular speed zone, operation and control of the machine is well defined. We have verified through simulation that the operation is smooth and satisfactory. The major complexity arises when the machine passes through the synchronous speed because the converter, as well as the controller configuration, changes from sub- to super synchronous regime.

If proper care is not taken, a number of problems may arise during this changeover. The following is a listing of issues that need to be addressed during such changeover.

- **Loss of control:** Contactors cannot make or break instantaneously. Unlike semiconductor devices, the breaking and making time for contactors are high (it may be few milliseconds, 10 ms for our case). In such a case, unless special care is taken, there may be momentary loss of control, and the transition from sub-synchronous to super-synchronous or vice-versa may not be smooth.

- **Asynchronous operation of contactors:** The instant of operation for the two contactors may not be the same. In such a case, operation of both the contactors may not synchronize. The fallout from such a mismatch may be severe. Depending on the contactor connections, this kind of timing mismatch may either cause a short circuit between the stator and the rotor circuit of the machine through the grid or both side converters may become shorted through the wiring of the contactor. A contactor connection with the potential of a rotor/stator short is shown in Figure 2.10. The consequence of both the stator and rotor becoming shorted through the grid may be severe. In order to avoid such problem, the inputs of the contactors are connected to the power electronic circuit, and the outputs are connected to the grid or the rotor. In such an arrangement, if one contactor operates earlier than the other, then the two power electronic circuits will be shorted either through the rotor or the grid. Because the current through each of the converters can be controlled, the second possibility does not cause any problem to the system. Details of how details of the contactors are connected to ensure safe operation are given in Figure 2.11.

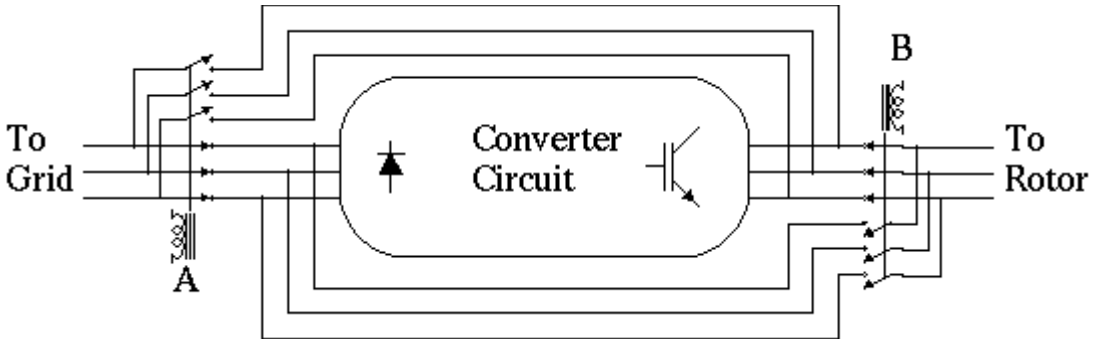


**Figure 2.10. Faulty means of connecting the contactors to the proposed circuit**

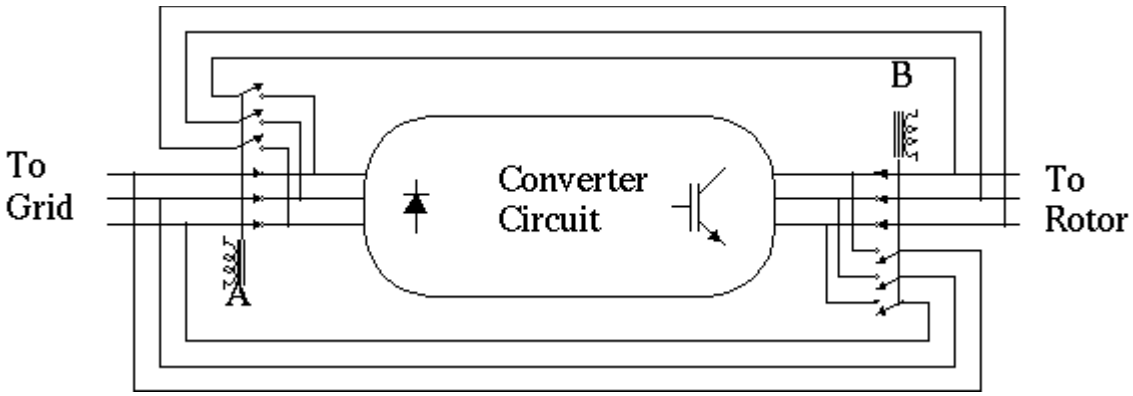


**Figure 2.11. Correct means of connecting the contactors with the proposed circuit**

- **Reduction of interrupting current:** The cost of the contactor clearly depends on the interrupting current it needs to handle. Resistive-grade contactors are cheaper than the equivalent current-carrying inductive-load contactors because the continuous current rating and breaking capacity are the same for resistive-load contactors. On the other hand, with equivalent continuous current rating, inductive-load contactors need to have higher breaking current capacity. With the reduction of interrupting current, the cost decreases sharply. Because the objective of the present investigation is to reduce the cost of the converter, it is important to reduce the current through the contactors at the time of making and breaking the circuit. This reduces cost and extends the life of contactors.

- **Smooth transition between sub- and super-synchronous modes:** For a smooth transition from one speed regime to the other, an overlap of the sub-synchronous and super-synchronous controller may be required.

### *2.4.1 Reduction of Currents through the Contactor during Make and Break*

The reduction of current through the contactor during the changeover may be achieved differently for the two cases given below.

*Case 1: The Machine is Accelerating from Sub-synchronous to Super-synchronous Regime*

When the machine acts as a motor and accelerates from sub-synchronous to the super-synchronous regime with a conventional field-oriented controller, active power is normally extracted from the rotor to the DC bus during the sub-synchronous mode. On the other hand, active power is fed to the rotor from the DC bus during the super-synchronous regime. As explained earlier, during sub-synchronous motoring modes, the proposed controller cannot extract or feed active power from or to the rotor circuit. The machine, therefore, accelerates solely as a result of the wind torque. Thus, both the contactors handle only the reactive power, and the breaking and making current for both the contactors during this mode will be inherently small. In order to make the contactor currents actually be zero, the reactive component of current through the rotor circuit during this transition can be reduced to zero by means of control. For a short time, the reactive current will only be drawn by the stator from the grid. Through such a controller, the interrupting current can be brought down to zero. The power factor of the system during such a transition will be relatively poor, but it can be achieved. The simulation results during a transition are given in Figure 2.12.

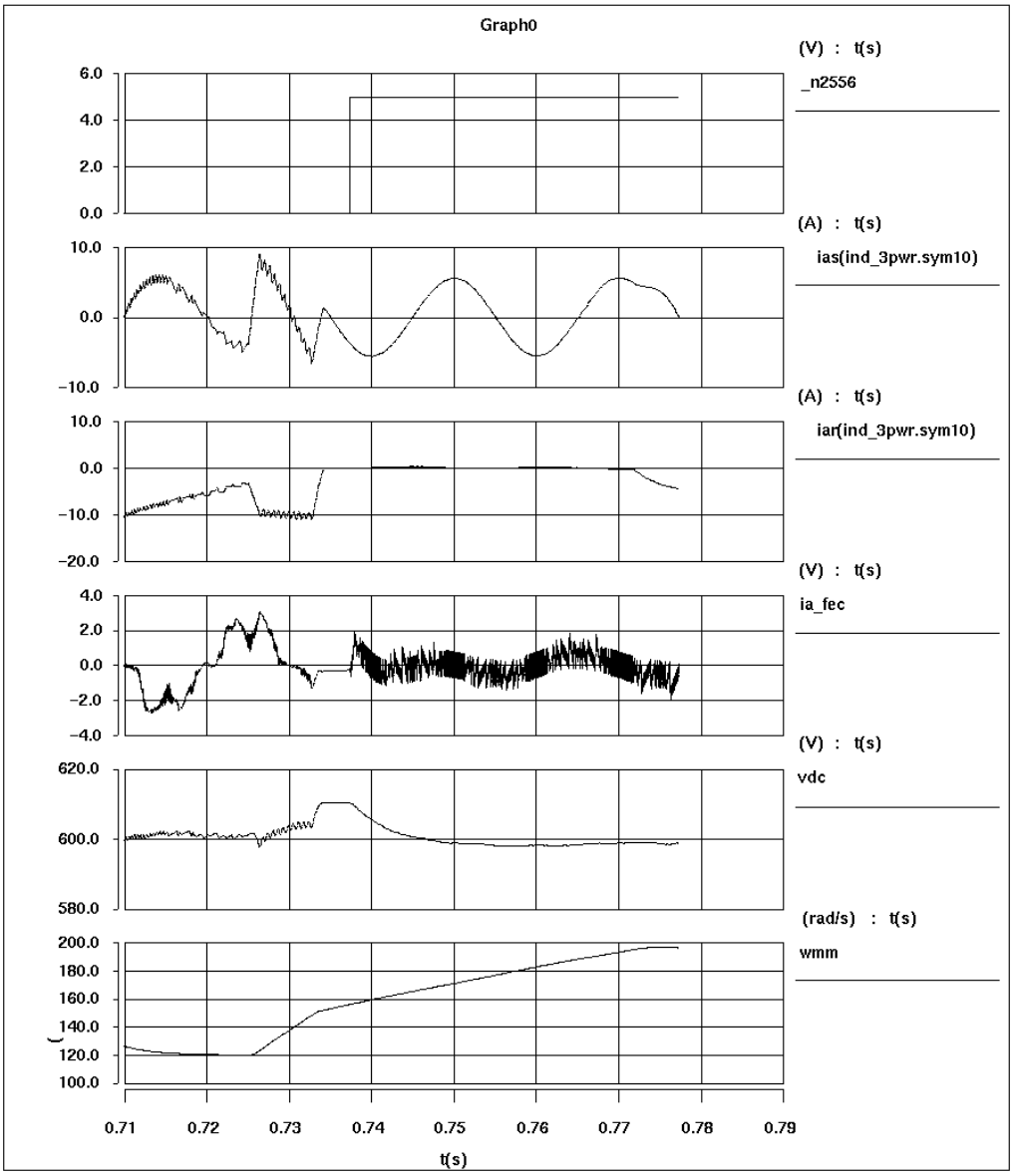


**Fig. 2.12. Simulation results during acceleration from sub-synchronous to super-synchronous regime: _n2556 = contactor changeover logic (low = sub-synchronous mode, high = super-synchronous mode), ias = stator phase-A current, iar = rotor phase-A current, ia_fec = frond-end converter phase-A current, vdc = DC bus voltage, wmm = mechanical speed of the machine**

*Case 2: The Machine is Decelerating from Super-synchronous to Sub-synchronous Regime*

When the machine decelerates from super- to sub-synchronous regime and acts as a generator, the rotor circuit feeds active power to the DC bus during the super-synchronous regime. On the other hand, power is fed to the rotor from the DC bus during sub-synchronous generating mode. In the super-synchronous mode, the rotor is connected to the DC bus through the diode bridge, and the front-end is connected to the IGBT inverter. As the machine approaches synchronous speed, the power flow through the rotor circuit is again reduced. For this condition, the rotor voltage is small compared to the DC bus voltage, and the total power flow from the rotor to DC bus is less.

We know that as the machine decelerates through synchronous speed, the rotor current and therefore the DC bus current will pass through a minimum. In such a case, the IGBT inverter can again be disconnected from the grid with low interrupting current.

Ideally, before breaking the circuit, the current through the inverter side can be brought down to zero by forcibly disabling all the gate drives of the IGBT inverter. When current decreases to zero, the inverter can be disconnected from the grid and connected to the rotor of the machine. Thus, the cost of the inverter side contactor can be further reduced. During this mode of operation, the inverter-side contactor operates first. The rectifier and the inverter are connected to the rotor winding and DC bus for a short interval. At this time, if the gate drive to the boost chopper is disabled, the current through the diode bridge will reduce automatically because most of the rotor current will now flow through the IGBT inverter. The rectifier-side contactor can be disconnected from the rotor side of the machine and connected to the line side. During this process, for a short interval, the line side is totally disconnected from the system. Because the converter is connected to the rotor and DC bus and because the machine is operating at super-synchronous generating mode, energy is dumped to the DC bus capacitor by the rotor. There is a possibility of DC bus voltage increasing, thus endangering the voltage margin of the IGBT inverter. We found through exhaustive simulation that, in reality, the DC bus voltage does not rise substantially because the active power dumped by the rotor at near-synchronous speed is small, and the machine remains in such an operating zone for a small duration. The increase in DC bus voltage is not significant. The system simulated for such a condition is given in Figure 2.13.

The question also arises whether the current through the rectifier side contactor will be reduced during such a changeover. Because, the inverter and the rectifier are connected in parallel and operate simultaneously, the anti-parallel diodes of IGBT module of the inverter and the diodes in the rectifier will act as two parallel circuits. When the corresponding phase IGBTs are in the OFF condition, the diodes of both the inverter and the rectifier will carry the rotor-phase current equally. Hence, the current through the rectifier reduces to half of the original current, and the interrupting current of the rectifier-side contactor will be half of the rotor current. This mode of operation was verified through simulation (Figure 2.14).

## 2.5 Control Algorithm During Transition Between Sub- and Super-Synchronous Modes

When the machine is decelerating from super-synchronous generating mode to sub-synchronous generating mode, a negative torque must be produced by the machine to counter the wind torque. Therefore, the rotor-side controller must be continuously active during this process. In addition, the changeover from one control strategy to the other has to be made in a controlled fashion, so that the current through each contactor before breaking comes closer to zero. In order to facilitate the above objectives, an overlapping of control strategies during transition from super- to sub-synchronous regime has been adopted. When the machine decelerates from super- to sub-synchronous speed, the control of the FEC is disabled first, even if the actual speed is greater than synchronous speed (>1 pu), but less than 1.1 pu speed. When the current through the converter reduces nearly to zero, the front-end converter (IGBT inverter, in this case) is disconnected from the line and connected to the rotor of the machine, and the inverter is used for controlling the rotor of the machine. Thus, during this condition, the controller meant for sub-synchronous machine-side control is being used even

when the machine is still operating above synchronous speed. At this time, the rectifier and the chopper are also physically connected to the rotor even though the main control is being exerted through the inverter. Most of the rotor current now flows through the inverter. The current passes through the rectifier and the contactor connected to its end. When the machine nears synchronous speed, the rectifier is disconnected from the rotor of the machine and is connected to the line. Thus, a smooth changeover between two control zones is made without overshooting the current and voltage in the overall system.

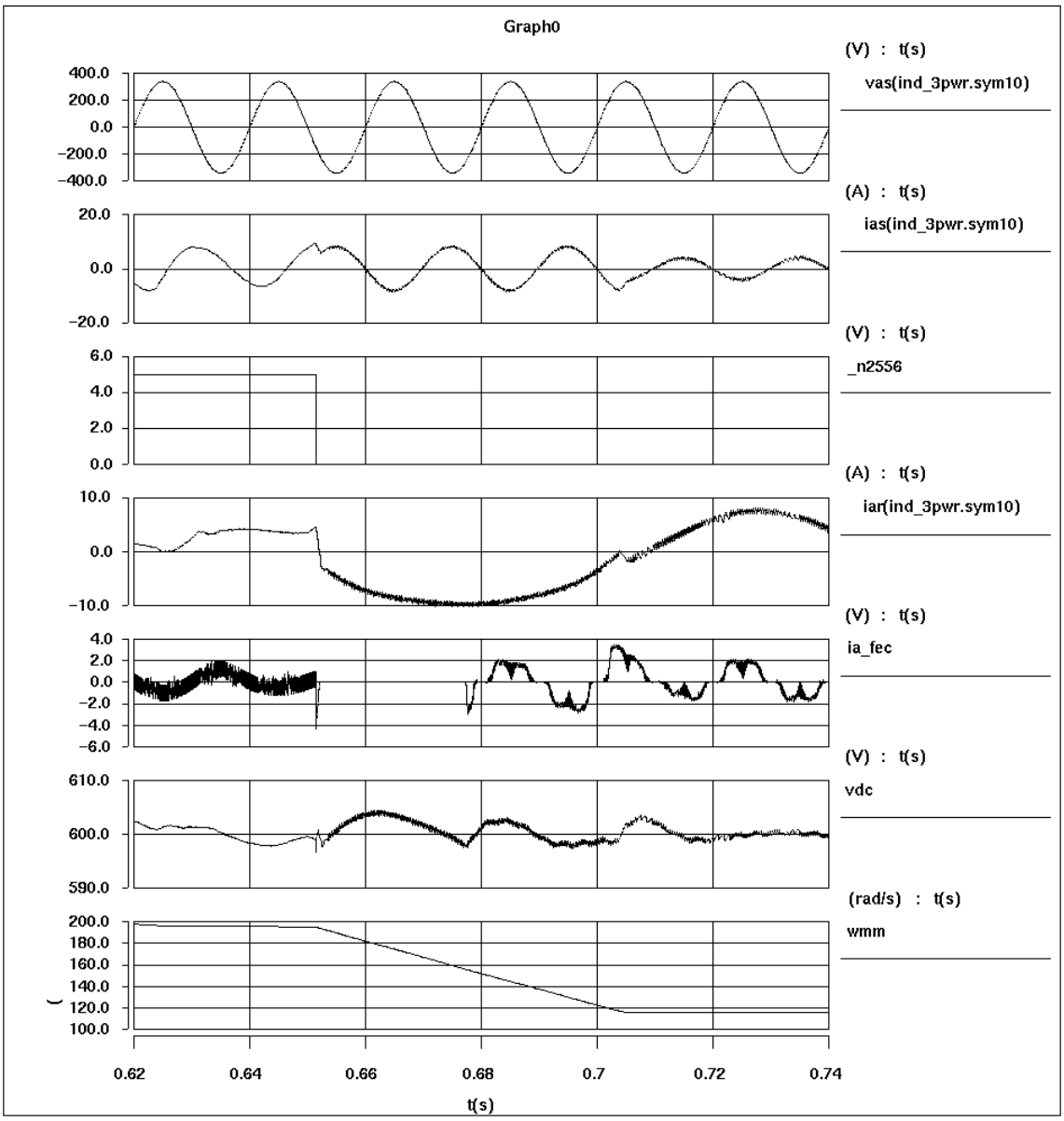


**Figure 2.13. Simulation results during deceleration from super-synchronous to sub-synchronous regime: vas = stator-phase voltage, ias = stator-phase current, _n2556 = contactor changeover logic (low = sub-synchronous mode, high = super-synchronous mode), ia_fec = front end converter phase-A current, vdc = DC bus voltage, wmm = mechanical speed of the machine**

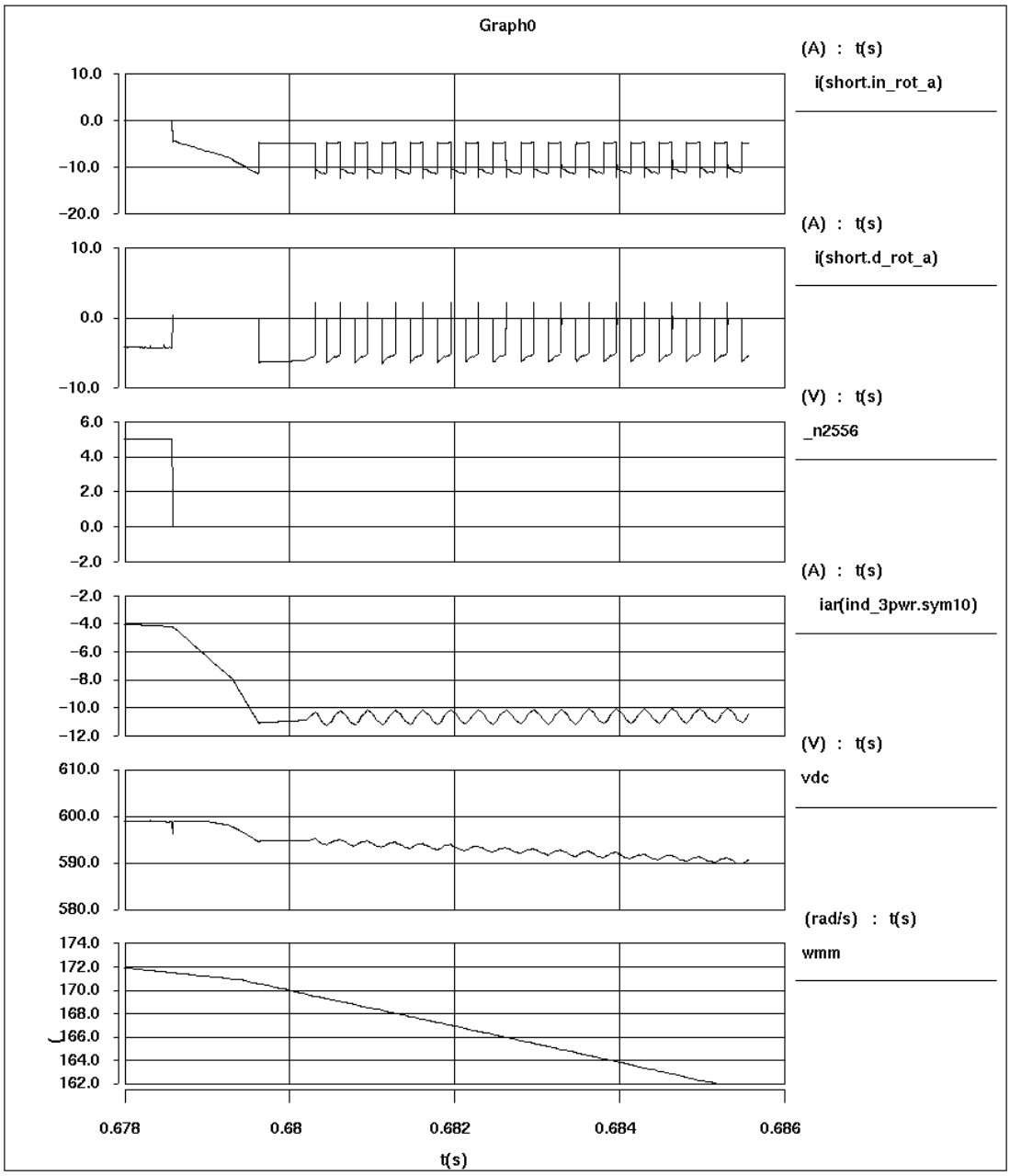


**Figure 2.14. Current sharing between two converters during transition from super- to sub-synchronous regime: i (short.in_rot_a) = current through the IGBT inverter, i(short.d_rot_a) = current through the diode rectifier, _n2556 = contactor changeover logic (low = sub-synchronous mode, high = super-synchronous mode), iar = rotor-phase current, vdc = DC bus voltage, wmm = mechanical rotor speed**

Similarly, when the machine is accelerating from the sub-synchronous to the super-synchronous regions, the controller is disabled if the reference speed is more than 1 pu. This happens even if the actual speed is below the synchronous speed of 1 pu, but above 0.95 pu. The machine speeds up because of wind-produced torque alone. During such a process, current through both the front-end and machine-side converters decreases to zero, and a smooth changeover of near-synchronous speed is executed (figure 2.12 through figure 2.13). In steady state or during a transient when both the reference and actual speed of the machine are in the same speed regime, no overlap or change-of-control strategy is necessary.

## 2.6 Unity Power Factor Interface to the Grid

Using the above-proposed topology, the front-end IGBT-based converter acts as an active filter during super-synchronous mode. The active filter operation provides a system unity power factor interface with the grid. The active filter part is explained in the control-block diagram for the super-synchronous control mode of operation (Figure 2.5). In the front end, line-side inductors are used for boost mode of operation of the inverter; therefore, unity power factor operation is achieved. The simulation results of the current in the FEC during super-synchronous mode are shown in figures 2.8 and 2.9. The traces demonstrate that the total grid currents are of near-unity power factor.

During sub-synchronous mode of operation, the system injects some low-order harmonics because of the diode bridge and boost chopper. By introducing a line-side passive filter, such harmonics can be reduced. Because the rotor side handles only slip power, at sub-synchronous mode the harmonic currents injected by the diode bridge will be less compared to the total power generated by the system. Typically, the rotor will handle 30% of the rated power. With a regular diode bridge and boost chopper and with adequate line-side inductances, the rotor-side total harmonic distortion (THD) can be typically 15-20%. For the 30-kW system considered for our research and with 30% slip, the rotor-side converter handles roughly 9 kW power. Therefore, the harmonic power will be about 1.8 kW to 2.25 kW (20-25% of 9 kW). Because the stator power supplied to the grid is rated at unity power factor, the total power generated by the machine is 21 kW (30 kW-9 kW). Thus, the total harmonic content of the generated power will be a maximum of 8.57% to 11%. Even without any extra filtering arrangement except the line inductance, the harmonic content of the generated power could be reduced substantially. It appears that harmonics can be completely eliminated at the line side during sub-synchronous operating regime. This refinement can be considered as future work.

## 2.7 Starting Performance

Starting performance of the system with our proposed circuit has also been studied through simulation. Initially, the power electronic circuit is connected to the system with its normal sub-synchronous configuration — the rotor side is connected to the IGBT inverter and the line side is connected to the diode bridge along with the boost chopper. During starting, all the gate drives of the power converter are forcibly lowered, and, the DC bus is charged through the line-side rectifier. Because the DC bus voltage is much higher than the rotor voltage, the diodes of the IGBT inverter are all reverse biased initially. Therefore, the rotor circuit behaves as if it is open circuited, and no active or reactive power flows through the rotor. Thus, during starting, the machine accelerates as a result of wind torque alone. As soon as the machine reaches a certain threshold speed, the gate drives of the converter are enabled, and the whole system starts operating in speed/torque-controlled mode.

The simulation results during starting are given in figures 2.15 and 2.16. From the simulation results, it can be seen that initially the rotor current is zero (until 1 second after the start), and until then, the stator is drawing purely reactive current from the grid. It can also be seen that until 1 second, the phase difference between the stator voltage vas and stator current ias is almost 90 degrees. As soon as the rotor converter is enabled, the rotor starts supplying reactive power and the stator current comes down to zero. Because the machine is still accelerating, the operation is in the sub-synchronous motoring mode. As discussed earlier, in sub-synchronous motoring mode, the inverter only supplies the reactive component of current to the rotor from the DC bus, whereas no active component of current is supplied to the machine during that operation. The machine develops zero torque at this time. The machine speeds up only through the wind-produced torque. Once the machine reaches the set speed, it starts operating as a generator. (In this particular case, the reference speed was set at 0.75 pu speed or 118 radians per second). After the machine reaches its set speed, the inverter begins supplying both active and reactive current to the rotor and the stator current is opposite in phase with the stator voltage. Thus, the stator is feeding power to the grid at unity power factor. With the proposed converter topology, successful on-the-fly starting of the system has been illustrated.

During starting, the machine can be controlled as a motor and can be accelerated in a controlled manner by connecting it with the converter in the super-synchronous configuration (Figure 2.6). In such a case, the diode bridge and boost chopper will be connected to the rotor winding, and the front end will be connected to the grid through the IGBT inverter. Hence, the machine can be made to work as a motor during sub-synchronous operation with such a converter configuration. The slip power can be controlled and taken back to the grid via the DC bus. Once the machine achieves sufficient speed, the converter configuration can be changed by the contactor operation as is desired for the different operating speed ranges. As a result, controlled starting can be realized with the proposed power converter.

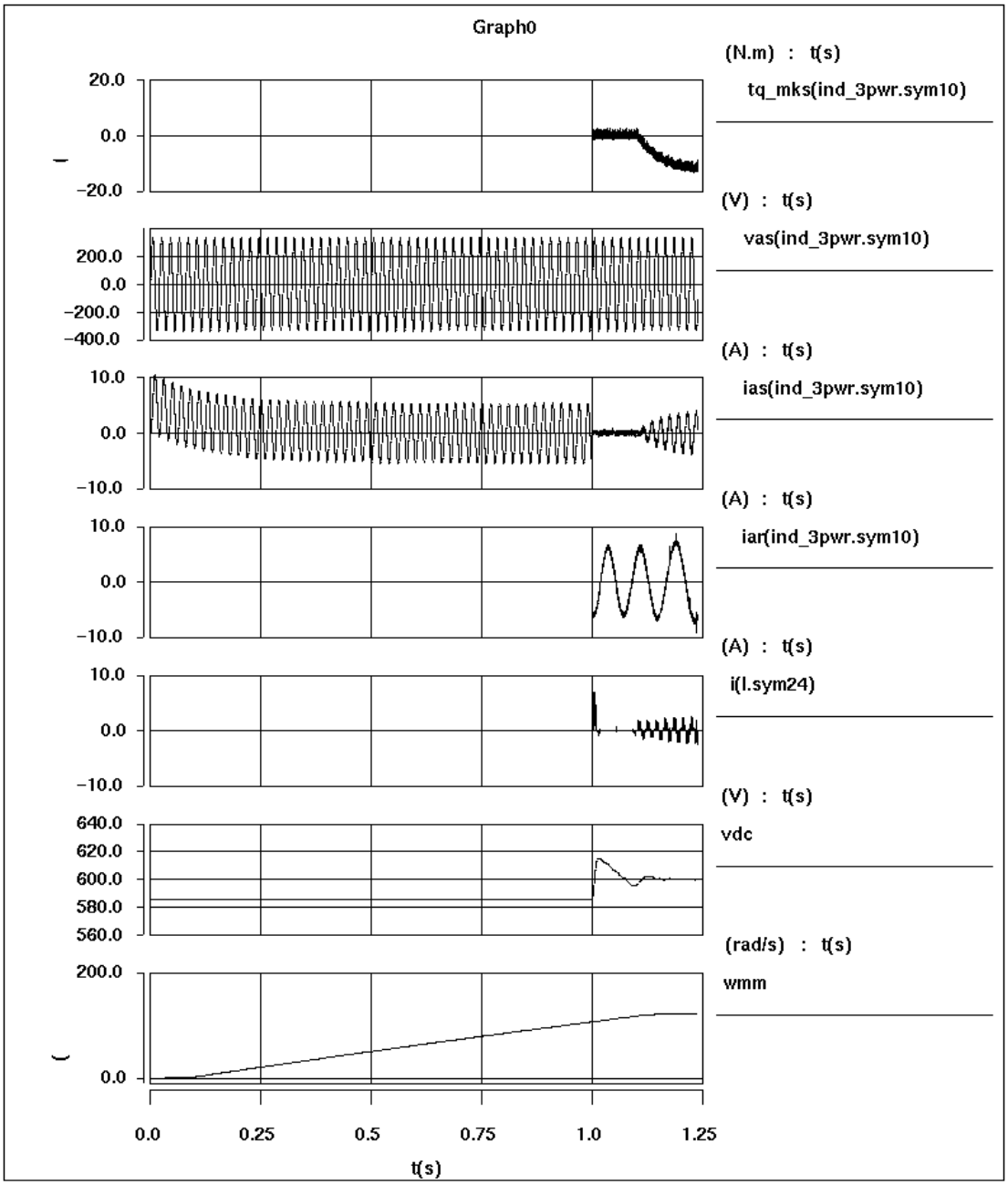


**Figure 2.15. Simulation results during starting from standstill: tq_mks = torque developed by the machine, vas = stator-phase voltage, ias = stator-phase current, iar = rotor-phase current, i = phase current through the front-end rectifier, vdc = DC bus voltage, wmm = mechanical speed of the machine**

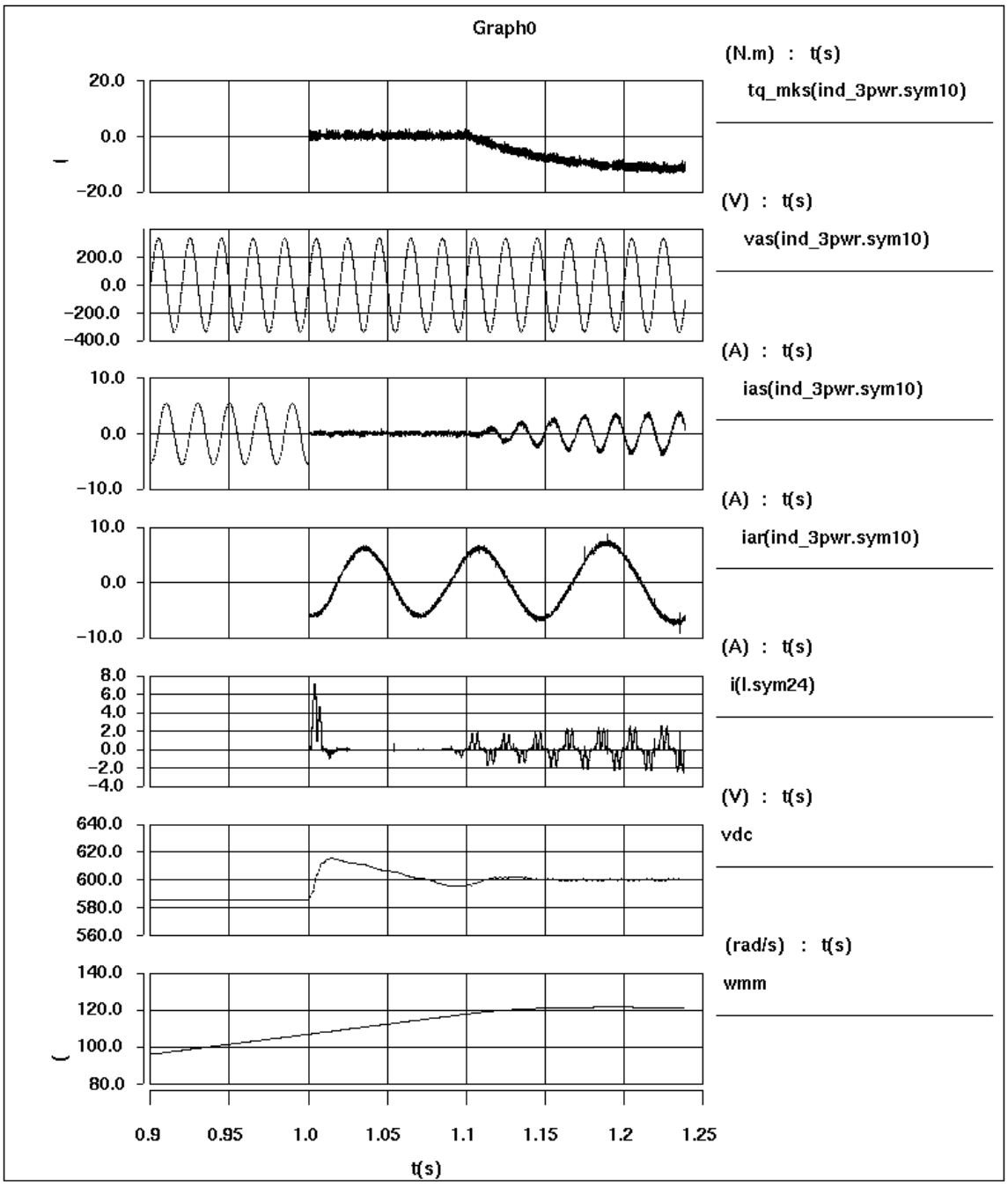


**Figure 2.16. Simulation Results during starting from standstill: tq_mks = torque developed by the machine, vas = stator-phase voltage, ias = stator-phase current, iar = rotor-phase current, i = phase current through the front-end rectifier, vdc = DC bus voltage, wmm = mechanical speed of the machine**

## 2.8 Conclusions

In this chapter, we prepare a novel power converter topology consisting of a diode bridge, a boost chopper, an IGBT converter, and two reversible contactors. This topology is valid for wind energy application, and the potential of the converter in connection to a DFIM control is explored. We found that with the power converter, the wind generator can be controlled in both sub- and super-synchronous regime. The operation of the generator in both the speed regimes is illustrated through SABER simulation results.

Separate control algorithms for both speed regimes are proposed and explained. We demonstrate smooth starting operation with the proposed converter. In super-synchronous operation, the machine torque is controlled by controlling the DC bus current employing a diode bridge and boost chopper. The front-end power converter interfaces the rotor circuit with the grid and also acts as an active filter for the additional harmonics injected by the stator of the machine to the grid. On the other hand, for sub-synchronous operation, the machine is controlled by the IGBT converter and a truncated field-oriented control is employed for that purpose. The front-end diode bridge and boost chopper supplies the rotor slip power through the DC bus and, thus, regulates the DC bus voltage.

A near-unity power factor interface of the system with the grid was achieved. Specifically, in the super-synchronous machine, the power factor is very satisfactory. In sub-synchronous speed operation, the THD of the system is about 8-10%, which is not poor, but certainly there is some room for improvement. This, too, can be considered as a future issue for research.

The cost of the system is reduced appreciably by removing one IGBT inverter and replacing it with a diode bridge and a boost chopper. Suitable control algorithms were found so that the interrupting current through the reversing contactors is brought down close to zero, which certainly reduces the cost of the contactors and, in turn, reduces the system cost further.

A suitable starting method for the wind generator from standstill condition was demonstrated. In conclusion, it can be stated that the proposed power converter can be considered as a candidate for an alternative low-cost option for variable-speed wind energy application.

# Chapter 3: Power Converter Topology 2

## 3.1 Overview: Naturally Commutated Thyristor Bridge with Bi-directional Chopper and IGBT Front End Converter

In this section, we introduce a second topology composed of a thyristor bridge, a DC/DC bi-directional chopper interface, and a line-side IGBT converter. We investigated it for driving a doubly fed wound-rotor induction generator and for interfacing the entire system to the grid. The power-converter combination interfaces the entire system to the grid at nearly unity power factor and controls a DFIM in all its four operating modes. It appears that the cost of the proposed converter will also be less than a conventional three-phase IGBT inverter because the rotor-side power converter consists of only two IGBTs and a conventional line-commutated thyristor bridge. For any line-commutated thyristor bridge, the chances of commutation failure may arise if the line-side voltage is very small or close to zero, which is a typical case for a wound induction machine when it is operating near synchronous speed. With a conventional thyristor bridge, commutation failure may be seen when the machine operates at close to synchronous speed. However, with the proposed system, forced commutation is possible and chances of commutation failure are avoided. In addition, a forced boosting phenomenon is achieved with the proposed method. It controls the system reliably, even close to synchronous speed, which otherwise is not possible with a conventional thyristor bridge (or diode bridge) and boost chopper. However, a problem is found when the machine passes through synchronous speed. Thus, with the proposed system, reliable and smooth operation of the generator is possible over the entire speed range except during transition through the synchronous speed. With the proposed configuration, the cost of the system will be reduced without any major sacrifice in the performance. The proposed system has been verified through SABER simulation, and the simulation results are presented.

## 3.2 Introduction

In this section we propose a novel power converter and associated control strategy for the rotor-side control of a DFIM. The proposed power converter consists of a thyristor bridge with a bi-directional chopper, which will replace one of the IGBT inverters of a conventional back-to-back IGBT converter based system. The proposed power converter, shown in Figure 3.1, is expected to have a lower cost than the comparable IGBT bridge inverter, while still allowing for the full four-mode operation of a DFIM.

A conventional IGBT-based converter is used at the front end, through which the rotor of the machine is connected to the line. The front-end converter, (FEC) controls the power flow between the rotor of the machine and the grid and also functions as an active filter for compensating the additional harmonics introduced by the stator. The complete system is made to operate at almost unity power factor. The main objective of the proposed controller is to reduce the converter cost without any major sacrifice in the performance of the system. In this work, the whole system (machine, power converter, and associated control system) was simulated in SABER, and the simulation results for both sub- and super-synchronous speeds are presented.

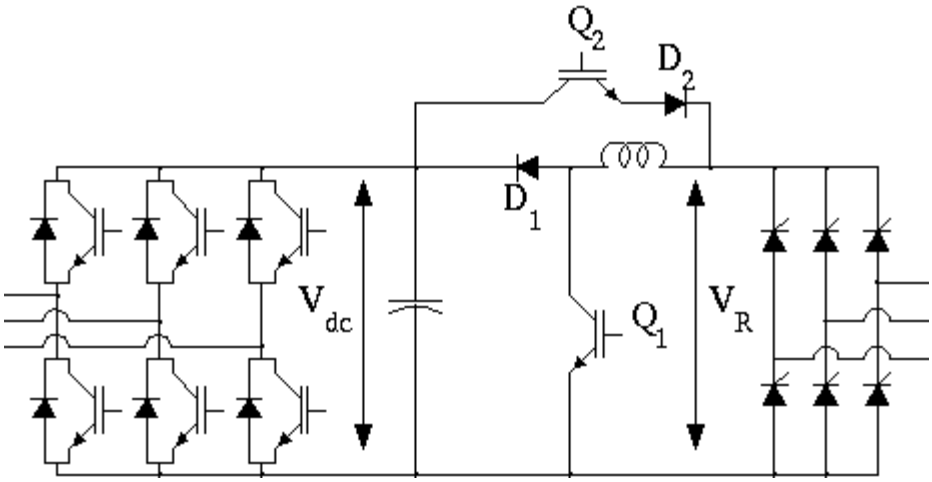


**Figure 3.1. Naturally commutated thyristor bridge with bi-directional chopper and IGBT front-end converter**

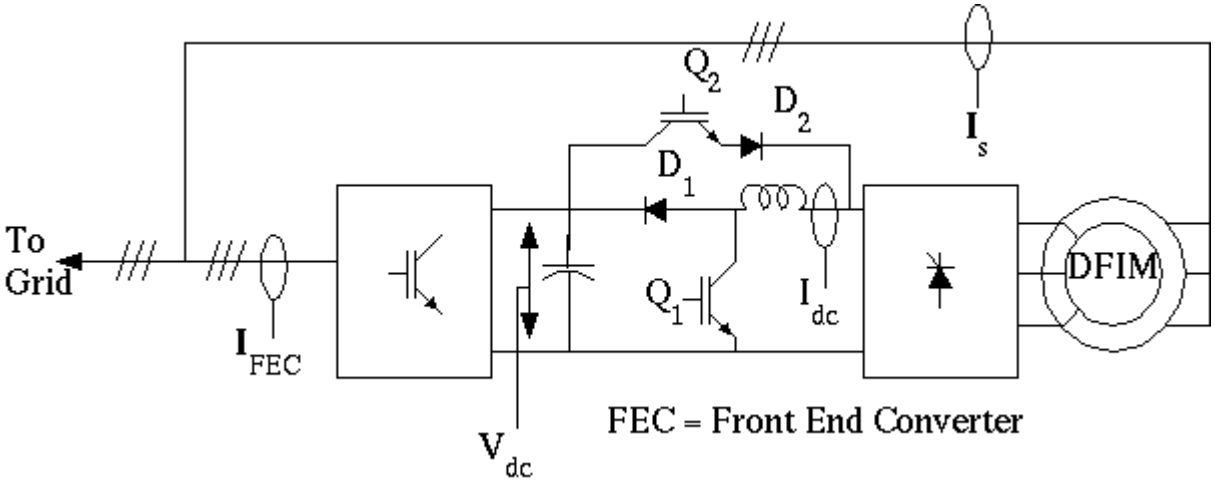


**Figure 3.2. System block diagram along with the proposed power converter**

## 3.3 Operating Principle

The operation of the overall system can be divided into two sections: front-end line-side operation and machine-side operation, as shown in Figure 3.3, which adds the control topology to the system-block diagram. The FEC maintains the DC bus voltage at its rated value by controlling the power flow between the grid and the DC bus, as well as maintaining the interface of the overall system to the grid at nearly unity power factor. The machine-side inverter controls the speed and torque of the machine by controlling the DC link current.

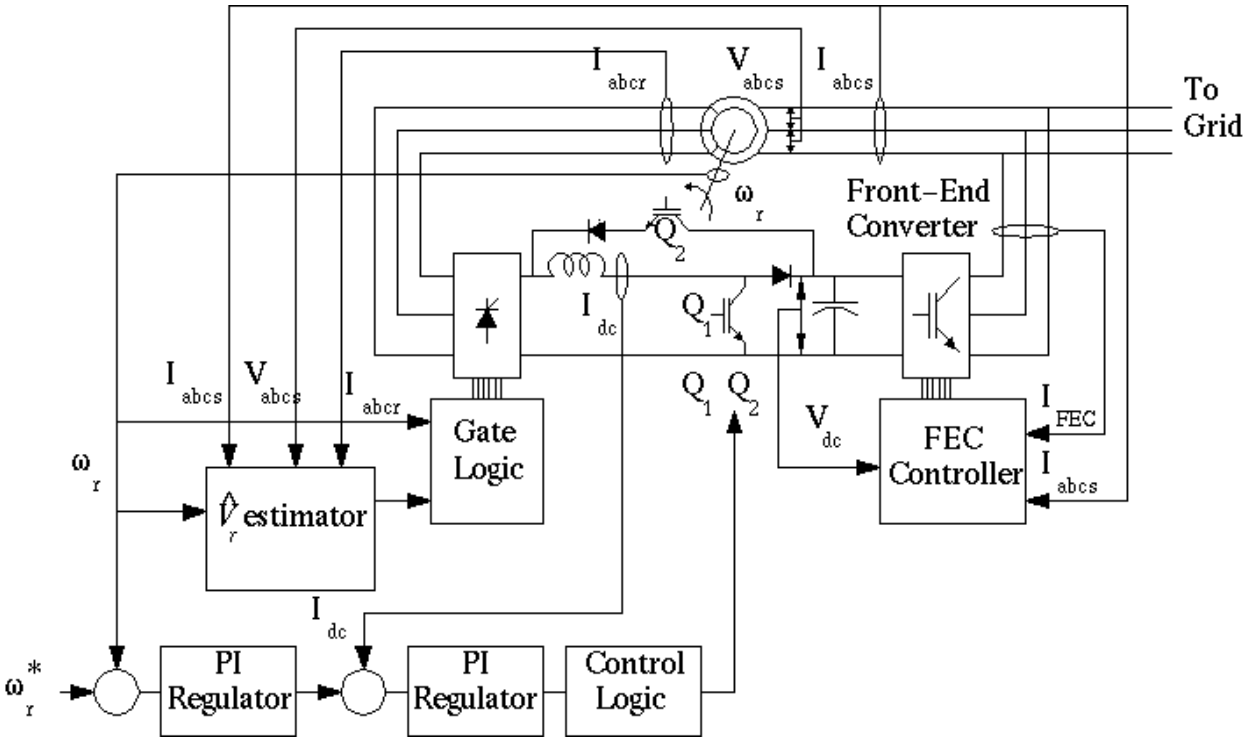


**Fig. 3.3. Complete system block diagram including the controller**

## 3.4 A Doubly Fed Machine Control

A DFIM is formed when a power converter is present in the rotor circuit of a wound-rotor induction machine. The DFIM is controlled by directing the power flow into and out of the rotor windings. Because the DFIM can operate as either a motor or a generator at both sub-synchronous and super-synchronous speeds, there are four operational modes in which the DFIM operates, as explained in Chapter 1. However, for the sake of completeness, we discuss it again here. The principle of a DFIM control in these modes can be understood by the power-flow diagrams given in Figure 3.4. In this figure, Ps is the stator power, Pr is the rotor power, and Pm is the mechanical power. When the DFIM is operating as a motor in the sub-synchronous speed range (Figure 3.4[i]) power is taken out of the rotor. This operational mode is commonly known as slip-power recovery. If the speed increases so that the machine is operating at super-synchronous speeds (Fig. 3.4[ii]), then the rotor power changes direction from the sub-synchronous operation.

When the DFIM is operating as a generator in the sub-synchronous speed range (Fig. 3.4[iii]), power is delivered to the rotor. If the speed increases so that the machine is operating at super-synchronous speeds (Fig. 3.4[iv]), then the rotor power changes direction from the sub-synchronous operation. Depending upon the direction of power flow in the rotor circuit, the machine-side converter (MSC) control is divided into two operational modes: (i) rectifier operational mode and (ii) inverter operational mode.

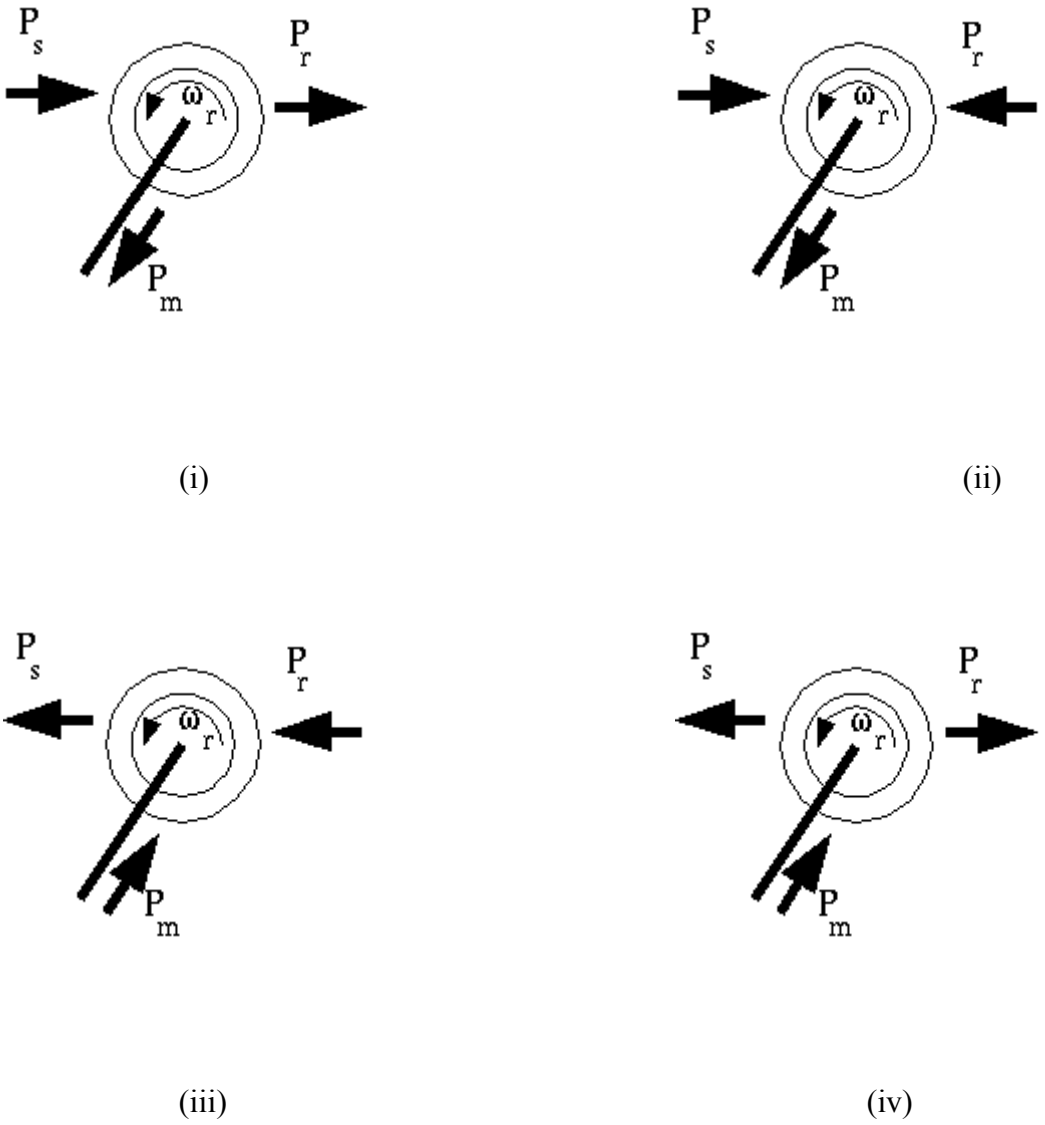


**Figure 3.4. Power-flow diagram of a DFIM machine for: (i) sub-synchronous motoring mode, (ii) super-synchronous motoring mode, (iii) sub-synchronous generating mode, and (iv) super-synchronous generating mode**

### *3.4.1 Machine-Side Converter (MSC) Rectifier Operational Mode*

During sub-synchronous motoring and super-synchronous generation, the MSC will be operating in the rectifier operational mode because power is flowing from the rotor into the converter. Normally, in this mode of operation, the switch Q2 and diode D2 (Figure 3.6) will be turned OFF. The effective circuit during this mode of operation is given in Figure 3.5. The link current is controlled by operating switch Q1. The figure shows that the DC link in this mode resembles a boost chopper, feeding power from Vr to Vdc.

### *3.4.2 Forced Boosting Near Synchronous Speed*

With the proposed topology and a modified control scheme, the boosting operation of the system can be improved, which is termed here as forced boosting. Forced boosting is particularly important when the machine operates near synchronous speed because the rotor winding voltage is will be close to zero.

It is well known that a conventional boost chopper typically operates at maximum 1:10 input/output voltage ratio. For a voltage ratio more than this value, the performance becomes degraded or operation is no longer possible. However, for a rotor-side control of a DFIM, the rotor side controller should ideally operate at any speed, including those at or close to synchronous speed. With a conventional boost chopper, such operation close to synchronous speed may not be possible. In such a situation, the forced boosting method of this chapter may be applicable.

Forced boosting can be achieved by controlling both Q1 and Q2 when the converter is acting as a rectifier. For example, if Q1 and Q2 both are switched ON simultaneously, then the thyristor bridge will be reverse biased. The rotor-phase currents will flow through the AC side-coupling capacitor, and the DC-link inductor will see the entire DC bus voltage across it, as a consequence, the current through it will build up during this time. If both Q1 and Q2 are switched OFF simultaneously, the inductor current will be forced to flow through the rotor windings, thyristor bridge, and the DC bus. Thus, the inductor will help to force the current flowing from the winding to the DC bus, even if the rotor winding voltage alone is insufficient to have the boost operation by conventional operation of Q1 only. The above forced-boosting operation is extremely helpful while the machine is operating near synchronous speed. Thus, the operation close to synchronous speed becomes feasible, and this feature will be illustrated through simulation results later in this chapter.

### *3.4.3 MSC Inverter Operational Mode*

During sub-synchronous generating and super-synchronous motoring operation, the MSC will be operating in the inverter mode because power is flowing from the converter into the rotor. In this mode, the switch Q1 will always be ON and diode D1 will be OFF since it is reverse biased by

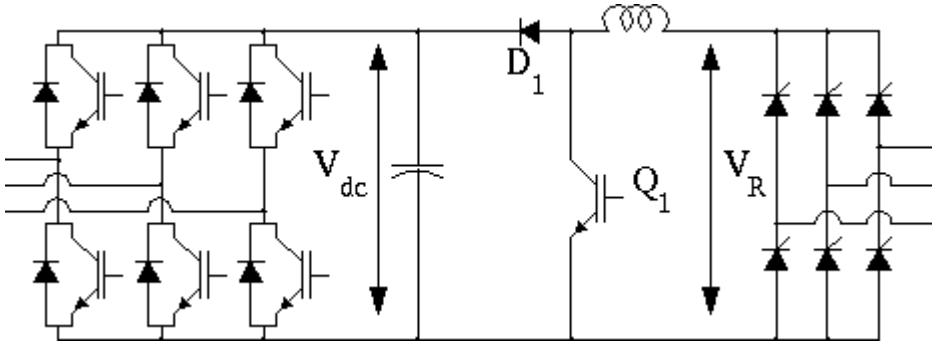


**Figure 3.5. MSC rectifier mode circuit**

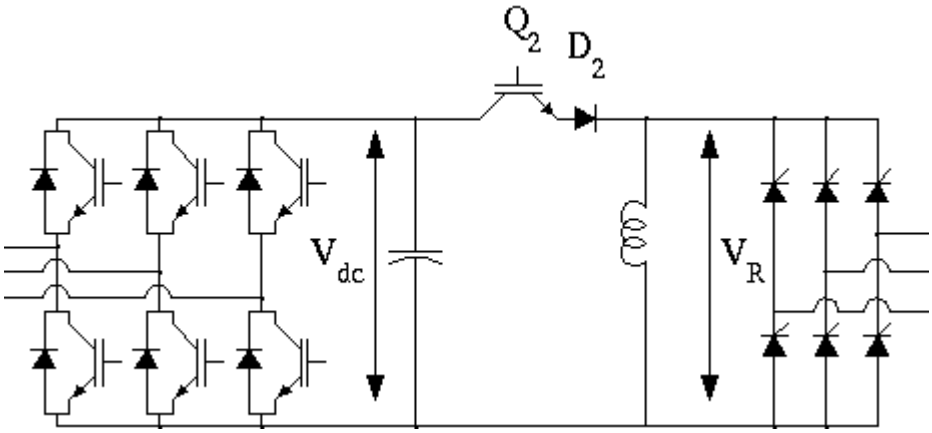


**Fig. 3.6 MSC inverter mode circuit**

the DC bus voltage. Thus, the effective circuit diagram during the inverter mode of operation is given in Figure 3.6. The link current is controlled by modulating switch Q2. When Q2 is ON, the inductor has the DC bus voltage across it that increases the inductor current. When Q2 is OFF, the inductor current flows through the thyristor bridge and the machine. This circuit diagram resembles a buck-boost chopper, feeding power from Vdc to Vr, while Vr is negative. Hence, the composite DC-to-DC interface may be called a *boost/buck-boost* configuration. A similar eight-switch converter topology was suggested by *Braun et al,* [2] in connection with a DC motor regenerating braking control. However, their topology does not support boost operation during the rectifier mode, and it also does not operate with a unipolar DC bus unlike the proposed converter topology. The unipolar DC bus used here is advantageous because it simplifies the FEC.

### *3.4.4 Mode Transitional Operation*

The transition between sub- and super-synchronous operation requires a precisely timed change in direction of the rotor power flow. If the rotor power flow direction does not change at the proper time, then the machine may be unable to transition between sub- and super-synchronous (or vice versa) operation and will remain in the same speed range. This timing issue can be resolved for the sub- to super-synchronous operation by detecting that the system is approaching synchronous operation and then momentarily turning OFF all of the switches and allowing the wind turbine to push the generator into the super-synchronous operation. When the transition from super- to sub-synchronous operation is desired, negative torque is required in order to decelerate the machine through synchronous speed. This negative torque must be high enough to not only overcome the positive torque from the turbine/prime mover, but also to provide the decelerating action. The challenge is that as synchronous speed is approached, the rotor voltage approaches zero, and the ability to control the machine through the boost converter is lost. One solution is to detect that the synchronous speed is being approached and command the turbine pitch control to momentarily reduce the torque and allow the machine to coast down through synchronous speed. While this option works, it is undesirable because it requires control action external to the converter (turbine pitch control), and the system power output must be reduced during the transition.

An alternative approach to this problem is to employ a forced-boosting operation through which sufficient negative torque can be produced by the machine, even near synchronous speed. Ideally, with forced boosting the torque can be maintained positive or negative even at synchronous speed. However, for a smooth transition through synchronous speed, the firing logic of the thyristor bridge needs to be changed as it enters the super- to sub- and sub- to super-synchronous regime. Otherwise, the developed torque caused by the machine will drag the rotor in the opposite direction rather than in the desired direction. This opposite dragging force may occur due to the following reason.

It was explained earlier that for a DFIM control, the direction of power flow through the rotor changes as it passes through the synchronous speed. Hence, to obtain smooth transition, thyristor firing logic direction has to be changed as it passes through the synchronous speed. Finding out the exact timings for changing the firing signal logic is challenging because it is based on the estimated rotor voltage direction and near-synchronous speed. This voltage is very small, so it is difficult to observe the exact direction-changing instant.

### *3.4.5 DC Link Control*

Because the DC link current is approximately proportional to the torque of the machine for both speed ranges, the speed of the machine can be controlled by regulating the DC link current [3]. The block diagram of the DC link controller is shown in Figure 3.7. The outer speed loop generates a torque command, T*. Because the DC link inductor current always flows in the same direction, the current command, Idc* is proportional to T*. This current command drives the current loop, consisting of a PI controller and a PWM comparator to produce the control signals for the switches Q1 and Q2. The activity of the switches Q1 and Q2 can be determined by the rotor power flow. When power is flowing out of the rotor, then the thyristor bridge is operated as a simple rectifier, and switch Q1 is operated to control the link current through the boost converter action. When power is flowing into the rotor, then the thyristor bridge is operated as an inverter and switch Q2 is used to control the link current through buck-boost operation. In order to form the buck-boost topology, switch Q1 must be kept ON.

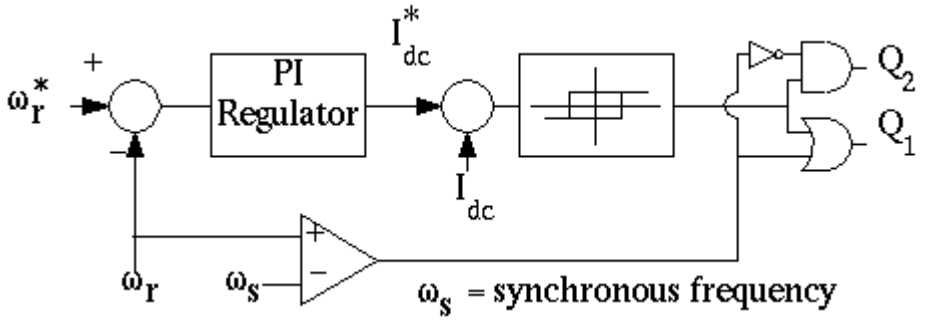


**Figure 3.7. DC link controller block diagram**

### *3.4.6 Commutation of Thyristors*

In addition to controlling the link current during the inverter operation, switch Q2 helps the thyristor bridge to commutate. This feature is required because the DFIM's induced rotor voltage is proportional to the slip. Consequently, as the speed approaches and reaches synchronous speed, the induced rotor voltage approaches and reaches zero volts. This means that at near-synchronous speed, commutation failure would occur for a conventional line-commutated thyristor bridge. In the proposed converter, Q2 provides a forced commutation action by turning it ON and reverse biasing the conducting thyristor with the DC bus voltage. During commutation, the rotor current is able to flow through the rotor-side line-to-line AC capacitors. The operation of Q1 is unimportant for the commutation action; however, if it is kept OFF during this time, then the inductor current will remain relatively constant because it will free-wheel through Q2/D2. The use of Q2 during the commutation process will assure that commutation will occur without failure even near synchronous speed.

The thyristor bridge can be operated either as a rectifier or as an inverter depending on the direction of the rotor-power flow. During rectifier operation, the thyristor gate signals are all asserted so that the bridge behaves like a regular diode rectifier bridge. During inverter operation, the thyristor gate signals are generated so that each upper-half phase leg conducts from 210° to 330° of the phase voltage, while the lower-half phase legs conduct from 30° to 150°. This operation corresponds to the direct opposite of regular rectifier operation. The firing signals are derived by examining the estimated rotor voltages. The estimated rotor voltage is obtained from an observer that measures the rotor and stator current, the stator voltage and the rotor speed.

## 3.5 Front-End Controller

The converter used at the grid interface is termed the front-end converter (FEC). The FEC employs a three-phase IGBT inverter bridge topology and is controlled to enable bi-directional power flow while keeping the DC bus voltage within good regulation. It can be operated at any desired power factor; therefore, it can act as a reactive power source. The converter is operated as a PWM voltage source inverter in the current-controlled mode so that the harmonics in the line-current waveforms are substantially reduced. Because the DFIM's rotor is fed through a DC link chopper and thyristor bridge, the currents in the rotor will no longer be sinusoidal. These non-sinusoidal rotor currents will induce low-order harmonics into the stator. Because the stator is directly connected to the grid, the grid will also see the equivalent lower-order harmonics, which is clearly not desirable.

In addition to the rotor-induced harmonics, the stator may also inject reactive power into the grid. However, both the reactive power and the rotor-induced harmonics are taken care of by the FEC's controller. The complete block diagram of the FEC's controller is given in Figure 3.8. The FEC controller compensates for the power factor and harmonics by extracting the extra reactive component and harmonic components from the measured stator currents and, then, generating a compensating

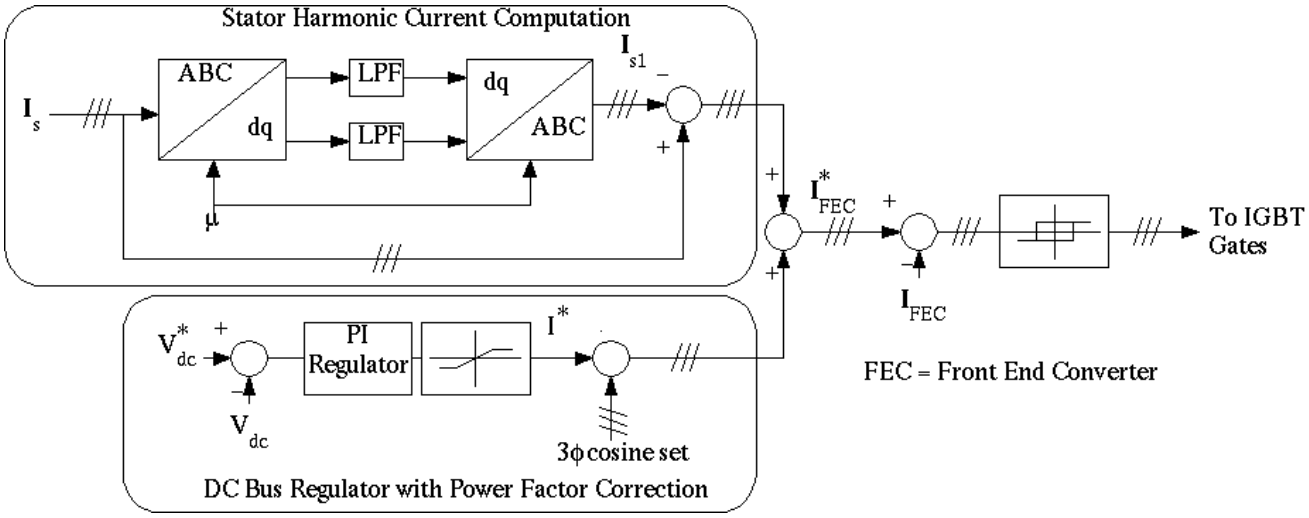


**Fig. 3.8 Front-end controller block diagram**

current command. The fundamental components of each phase current can be extracted by low-pass filtering the currents in the synchronous reference frame and then returning the filtered currents to the stationary frame [4]. The harmonic and reactive components can be found by subtracting the fundamentals from the actual currents of respective phases. Hence, by adding these components to the original current reference of the FEC, the final current references are generated. A hysteresis current regulator is used to control the current loop.

## 3.6 Simulation

The complete system including the DFIM model, FEC, MSC, and associated control system has been simulated in SABER. Detailed models for the semiconductor devices were used in the simulation, including turn-on and turn-off times. The machine parameters are listed in Appendix 5.1 at the end of Chapter 5.

The system was operated as a generator in the sub-synchronous and super-synchronous modes of operation. Steady-state and transient rotor-speed commands were simulated in both the sub- and super-synchronous regions. When the machine approaches synchronous speed while transitioning from the sub- to super-synchronous region, the rotor-side control is momentarily disabled to allow the machine to pass through synchronous speed. Similarly, during the transition from the super- to sub-synchronous region, the external wind-turbine pitch control was utilized to make the prime mover torque zero, while both the stator and rotor are open circuited. After the machine coasted to below synchronous speed, the stator was reconnected to the grid and the rotor-side control was re-enabled.

Finally, the operation of the machine employing a forced-boosting method was simulated, and it was shown that the machine can operate quite well in the vicinity of synchronous speed. Also, employing forced boosting. The controlled transition from super- to sub-synchronous operation may be possible without employing pitch control. The forced-boosting phenomenon is illustrated with the simulation results section 3.7.

## 3.7 Results and Discussion

Sample simulation results for the sub-synchronous and super-synchronous operating modes are presented in figures 3.9 through 3.14. From these results, it is seen that the MSC controls the speed quite smoothly, while the FEC maintains a nearly unity power factor interface with the grid. Results are given for steady-state (Figure 3.9) and during a speed-command transient (figures 3.11 to 3.14).

In Fig. 3.9, the current through the FEC (igaa) is not sinusoidal. This result occurs because igaa has to compensate for the reactive power and harmonics introduced by the stator of the machine. The current (ia) is the system grid current and consists of the summation of igaa and the stator current (ias). Notice that ia is nearly sinusoidal and 180° out of phase with the grid voltage (vas).

Transient results showing transitions within the sub- and super-synchronous regions are given in figures 3.11 to 3.14. From these results, it may be seen that the transient results are smooth and well controlled. Transient results showing the transition from sub-synchronous to super-synchronous operation are shown in Figure 3.15. In this figure, it may be seen that near synchronous speed the rotor control is disabled; the rotor phase and DC bus currents reduce to zero, while the machine accelerates only because of wind torque. This effect can also be observed in the speed trajectory, because synchronous speed, the slope of speed trajectory is different from the rest of the acceleration period trajectory. The signal scr_lgc in this figure shows whether the converter is working as a rectifier (+1) or inverter (-1).

Transient results showing the transition from super-synchronous to sub-synchronous operation are shown in Figure 3.16. In this simulation, pitch control is used for reducing the torque at the shaft of the machine. During deceleration, the stator and rotor are both disconnected from the grid, so that the machine coasts down through synchronous speed. In Figure 3.16, the signal pitch_ctrl_en indicates that pitch control is enabled. During this transition, because no electrical torque is produced, the deceleration time is decided solely by the mechanical time constant of the machine. This appears to be a disadvantage of the proposed converter. However, with a forced-boosting scheme it may be possible to achieve such controlled transition, which is illustrated below with a simulation result.

The simulation result of the complete system with forced boosting operation is given in Figure 3.17. It can be seen from the plots that the speed of the machine is about 163 rad/s, which is close to synchronous speed (157 rad/s). Naturally, the rotor voltage (var) is very small at that time. Even so, it can be seen that the rotor windings are carrying sufficient current and, in effect, the machine is developing sufficient torque to keep the machine well controlled at close to synchronous speed operation. This is achieved because of the forced boosting operation, as explained in Section 3.4.2.

When forced boosting is applied, it appears that it may be possible to operate the machine in controlled transition from super- to sub-synchronous speed operation. A simulation result illustrating such transition is given in Figure 3.18. It shows that transition through the synchronous speed is possible with the forced boosting scheme. However, it can be seen that the transition is not very smooth near synchronous speed. This undesired phenomenon occurs as a result of inaccurate firing logic generation near synchronous speed. As explained earlier in Section 3.4.6, the rotor voltage is very small at this time. Therefore, it is difficult to observe the change in direction of the rotor voltage and, thus, the firing logic generation during transition becomes improper. The rotor speed instead of generating, the machine starts motoring operation. Instead of being reduced, goes up again.

However, within a small time interval, the machine returns to its controlled mode, and the transition between super to sub-synchronous regime takes place. Thus, even though the system works with the forced boosting scheme, it may not be the optimum solution. We suggest that a better method be investigated in the future so as to obtain smooth transition near synchronous speed with the proposed configuration.

## 3.8 Conclusions

We propose new thyristor-based power-converter topology for the control of a DFIM. With the proposed controller, successful and reliable operation of the machine can be illustrated with simulation results. Because most of the components of this converter are thyristors, the cost of the converter is expected to be less than a regular IGBT inverter.

The DC-to-DC chopper interface works as a boost converter during the super-synchronous generating and sub-synchronous motoring modes of operation. On the other hand, it operates as a buck-boost converter during sub-synchronous generating and super-synchronous motoring modes of operation. With the buck-boost converter configuration, successful inverter operation of the thyristor bridge is obtained with a unipolar DC-link capacitor voltage. Thus, with the boost/buck-boost configuration, successful operation of all four modes of the machine is possible and has been illustrated through the steady-state and transient simulation results presented in this paper. The transition between sub- and super-synchronous operation is obtained through mechanical control (pitch control of turbine blade), which is sluggish in nature.

The proposed thyristor bridge, unlike a traditional line-commutated thyristor bridge, has ensured commutation even at synchronous speed. This is an added advantage of the proposed converter when compared to any other forced-commutated thyristor bridge because no extra commutation circuit is required.

A forced-boosting phenomenon using the proposed converter is illustrated in Figure 3.17, and we show that with such phenomenon the machine can be controlled close to synchronous speed, which otherwise is not possible with a conventional boost chopper. Using forced boosting, the transition between sub- and super-synchronous operations may be achieved with the converter operation. However, it is found that the transition with such a method is not very smooth.

The IGBT-based FEC is used for controlling the power flow between the grid and the rotor of the machine, as well as providing an active filter action to compensate for any additional harmonics injected by the stator of the machine. Successful near-unity power factor operation of the complete system with the grid is illustrated in Figure 3.18. The proposed power converter topology may be used for control of a high-power DFIM control in grid-connected wind-energy applications.

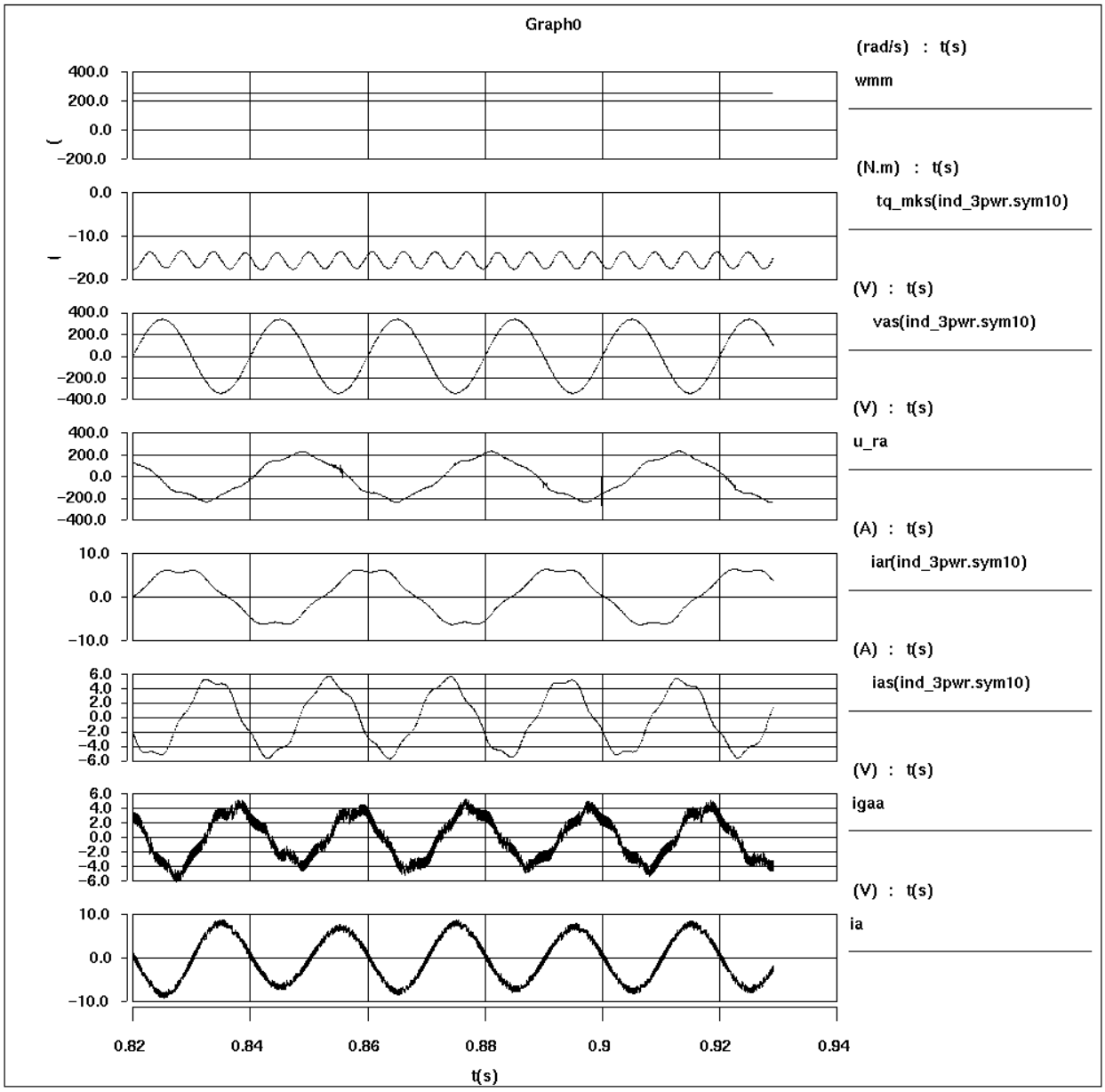


**Figure 3.9. Simulation results of the proposed power converter during super-synchronous steady-state operation: wmm = mechanical speed, tq_mks = torque developed by the machine, vas = stator- or grid-phase voltage, u_ra = rotor-phase voltage, iar = rotor-phase current, ias = stator-phase current, igaa = phase current through the IGBT FEC, ia = total grid current (sum of the current through the FEC and stator of the machine)**

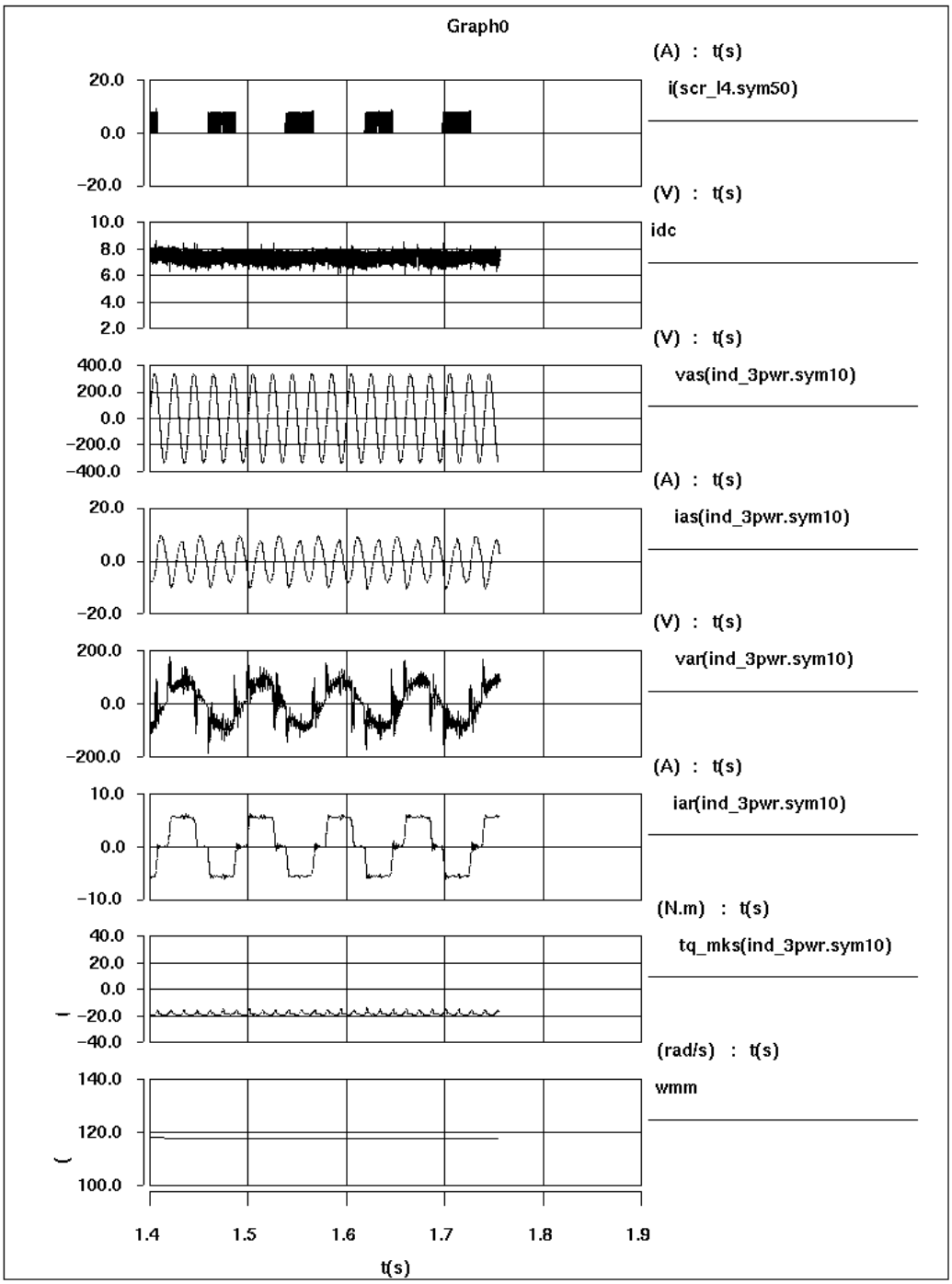


**Figure 3.10. Simulation results of the proposed power converter during sub-synchronous steady-state operation: i = SCR current, idc = DC link current, vas = stator- or grid-phase voltage, ias = stator-phase current, var = rotor-phase voltage, iar = rotor-phase current, tq_mks = torque developed by the machine, wmm = mechanical speed**

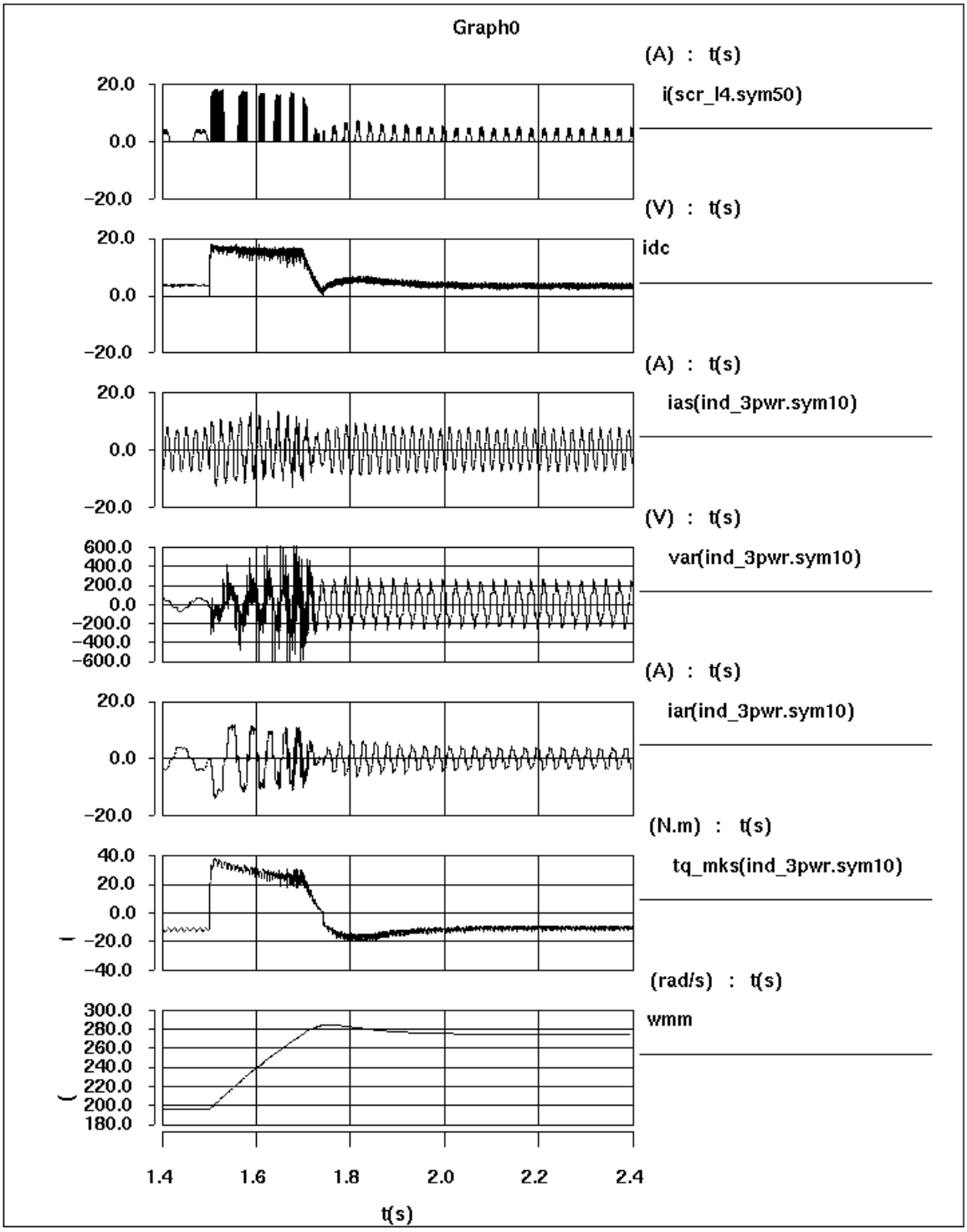


**Figure 3.11. Simulation results of the proposed power converter during a super-synchronous transient operation, from low to high speed: i = SCR current, idc = DC link current, ias = stator- by the machine, wmm = mechanical speed phase current, var = rotor-phase voltage, iar = rotor-phase current, tq_mks = torque developed**

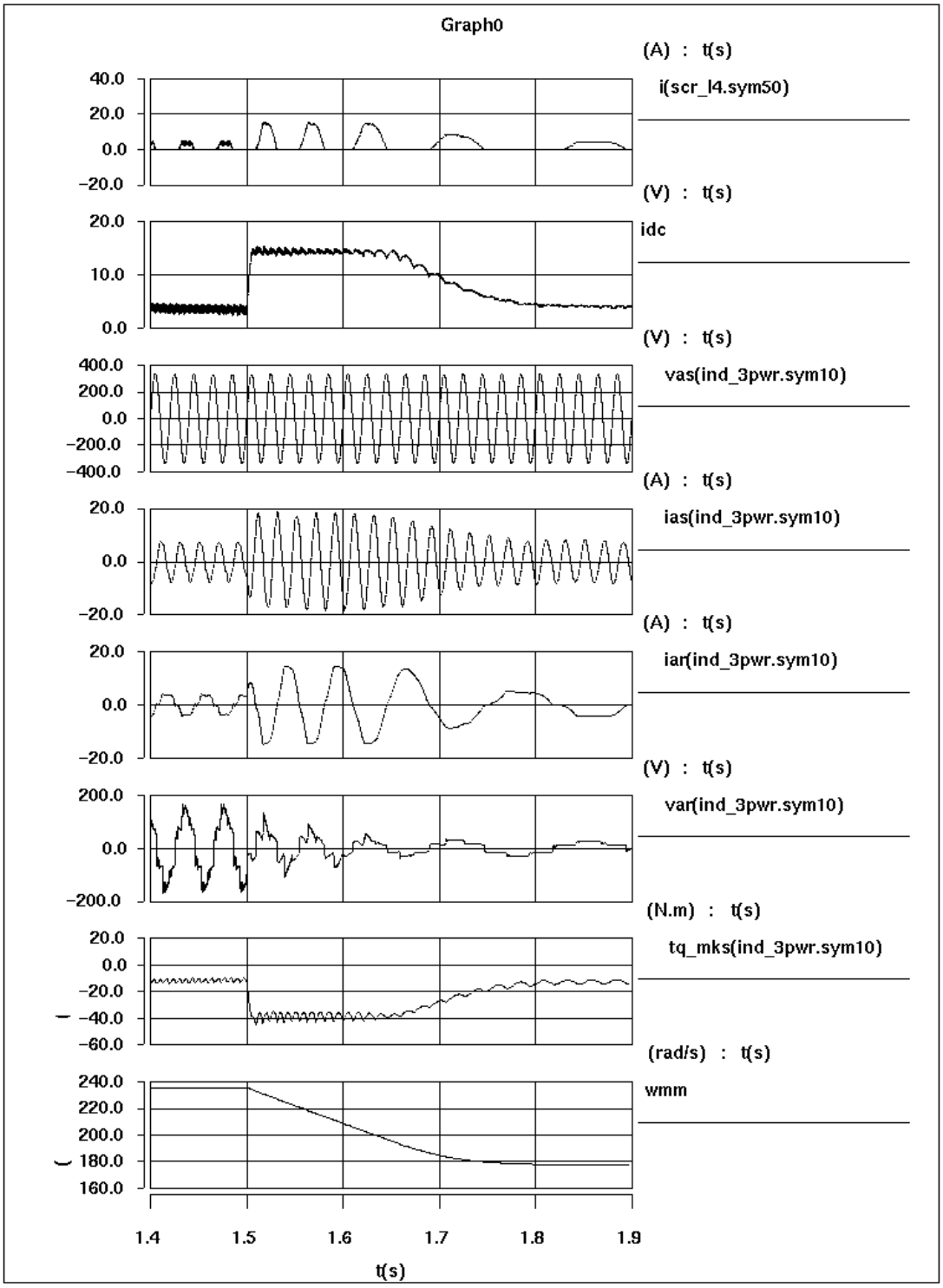


**Figure 3.12. Simulation results of the proposed power converter during a super-synchronous transient operation, from high to low speed: i = SCR current, idc = DC link current, vas = stator- or grid-phase voltage, ias = stator-phase current, iar = rotor-phase current, var = rotor-phase voltage, tq_mks = torque developed by the machine, wmm = mechanical speed**

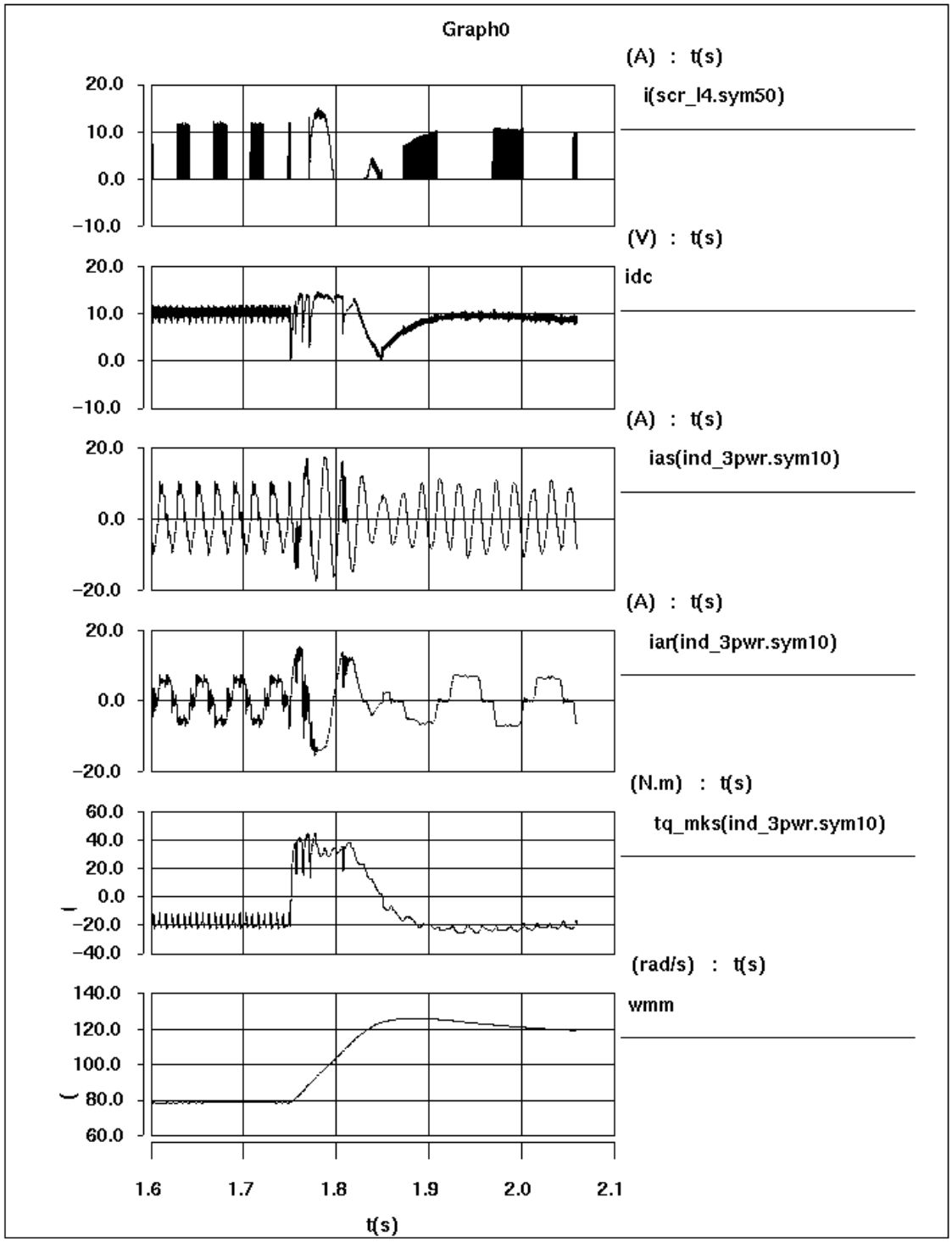


**Figure 3.13. Simulation results of the proposed power converter during a sub-synchronous transient operation from low to high speed: i = SCR current, idc = DC link current, ias = stator-phase current, iar = rotor-phase current, tq_mks = torque developed by the machine, wmm = mechanical speed**

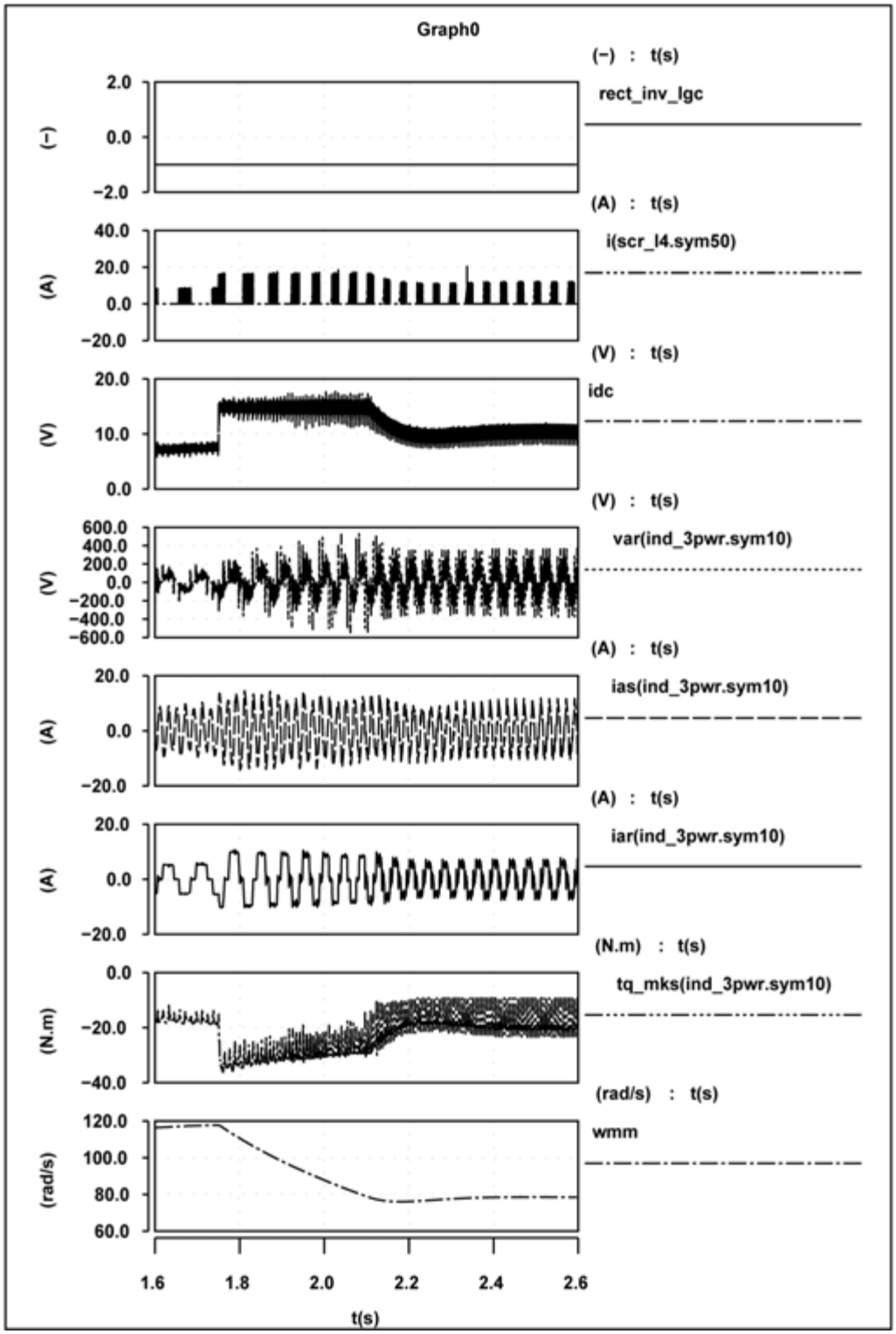


**Figure 3.14. Simulation results of the proposed power converter during a sub-synchronous transient operation from high to low speed: rect_inv_lgc = rectifier mode (+1) / inverter mode (-1), i = SCR current, idc = DC link current, var = rotor-phase voltage, ias = stator-phase current, iar = rotor-phase current, tq_mks = torque developed by the machine, wmm = mechanical speed**

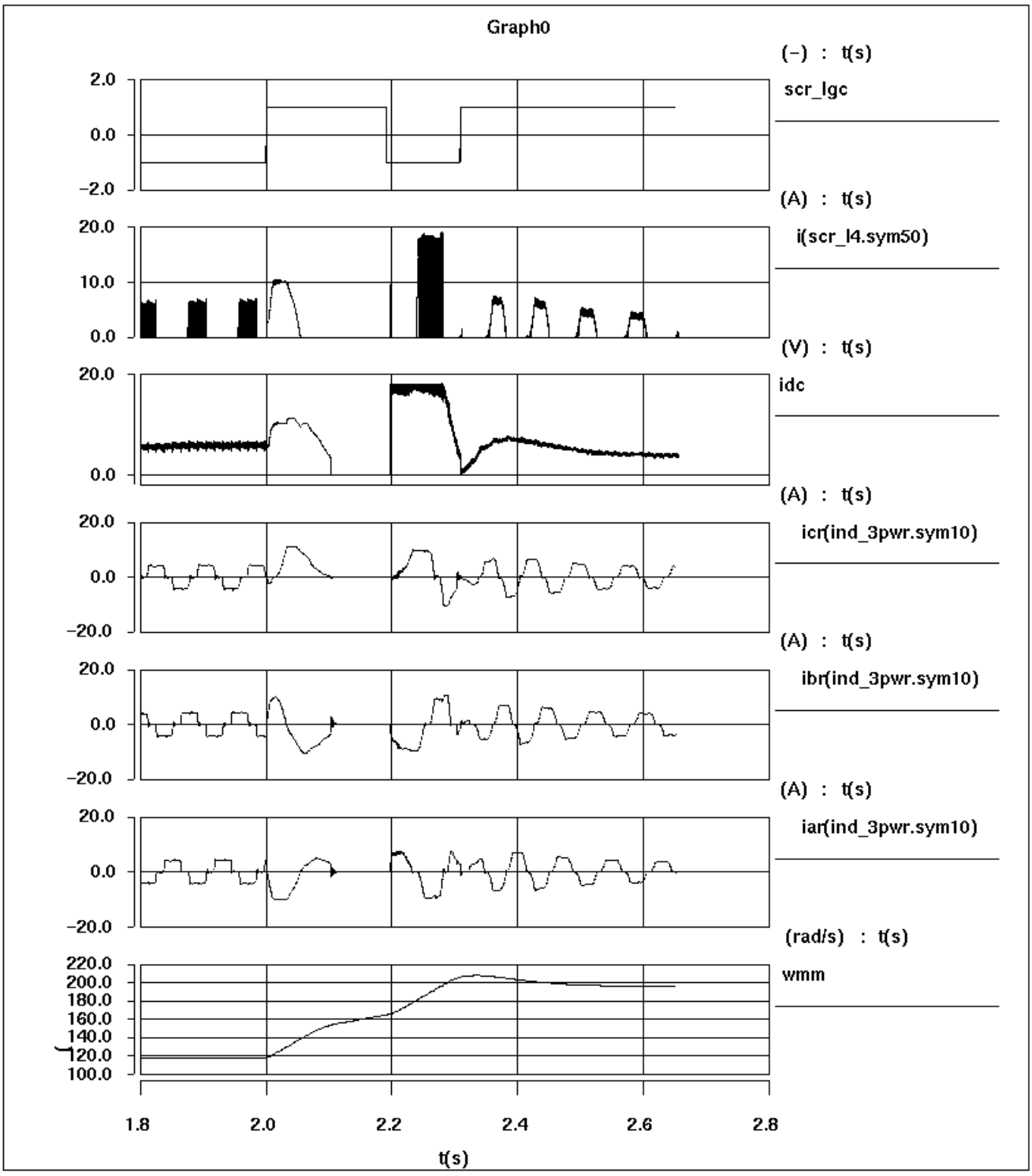


**Figure 3.15. Simulation results of the proposed power converter transitioning from sub- to super-synchronous operation: rect_inv_lgc = rectifier mode (+1) / inverter mode (-1), i = SCR current, idc = dc link current, iar = rotor-phase current, wmm = mechanical speed**

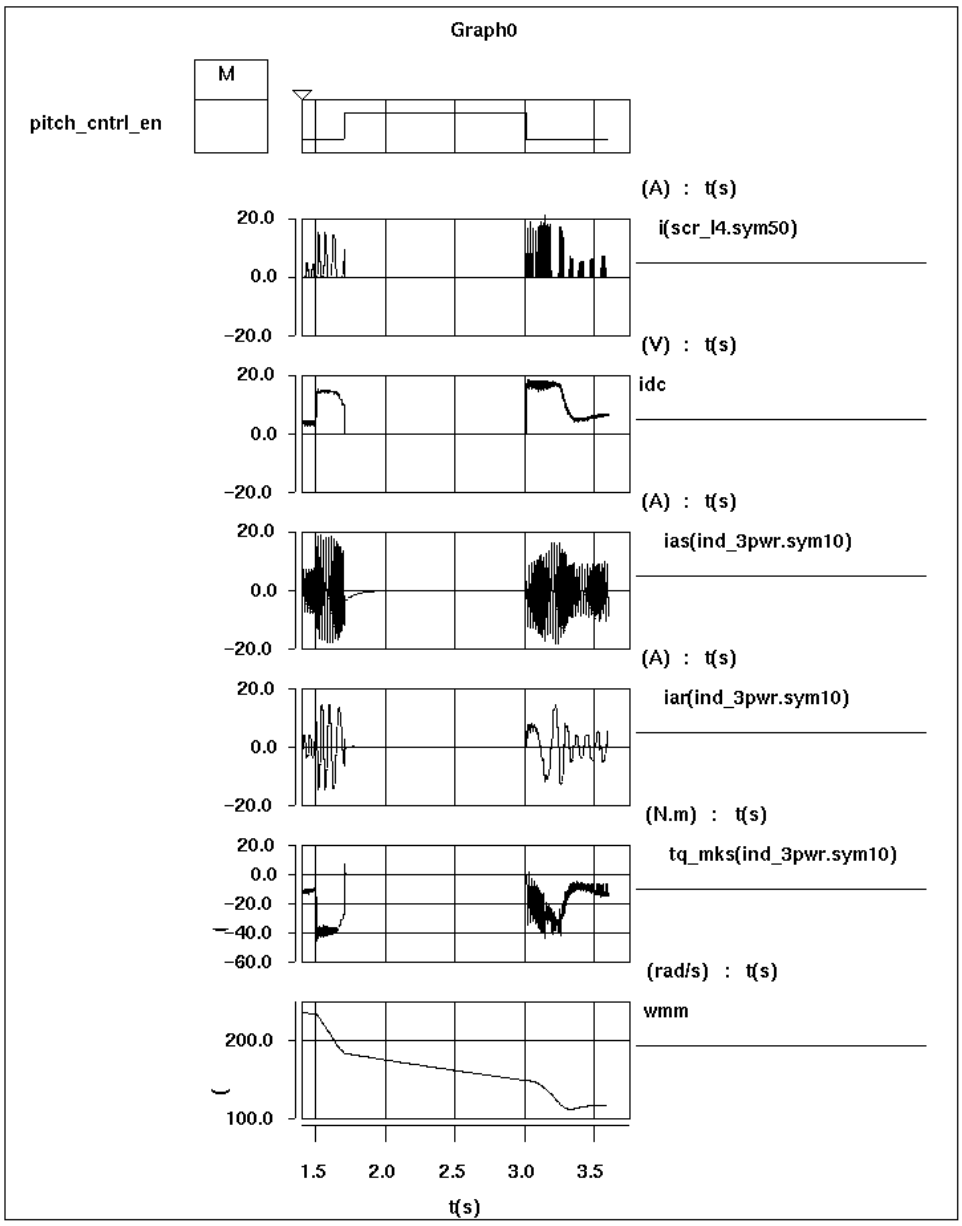


**Figure 3.16. Simulation results of the proposed power converter transitioning from super- to sub-synchronous operation: pitch_cntrl_en = rotor pitch control (+1) / converter control (0), i = SCR current, idc = DC link current, ias = stator-phase current, iar = rotor-phase current, tq_mks = torque developed by the machine, wmm = mechanical speed**

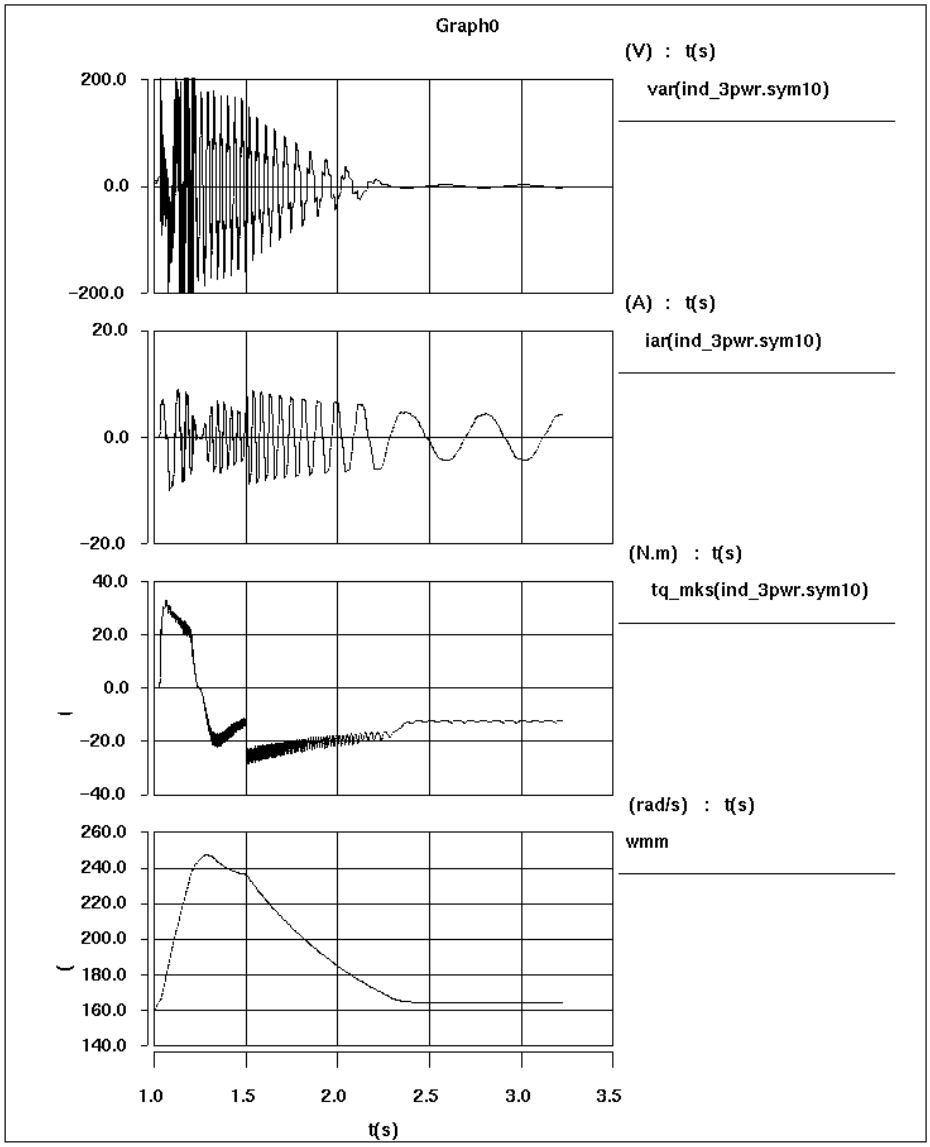


**Figure 3.17. Simulation results of the DFIM operating near synchronous speed with the proposed power converter and with forced-boosting control scheme: var = rotor-phase voltage, iar = rotor-phase current, tq_mks = torque developed by the machine, wmm = mechanical speed**

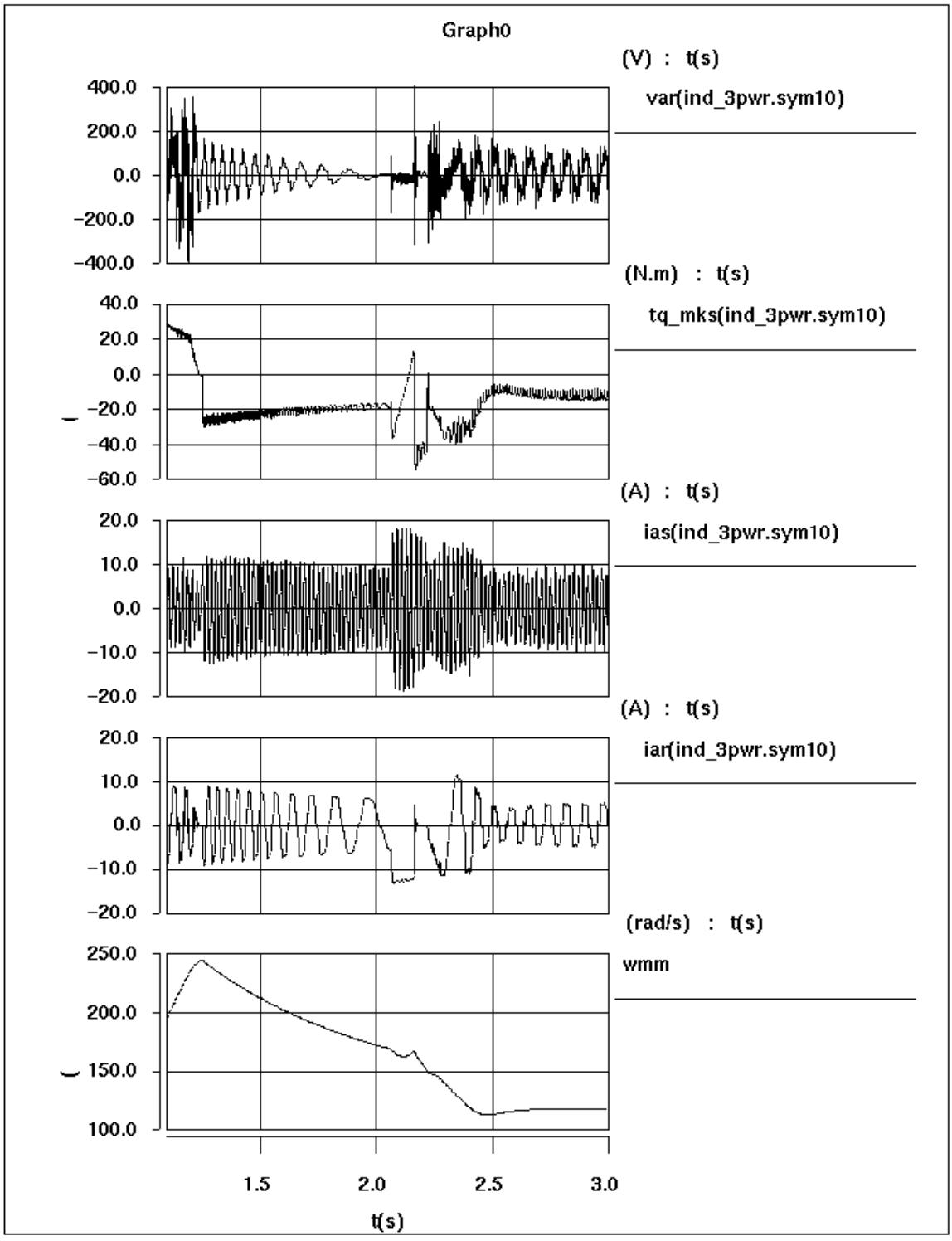


**Figure 3.18. Simulation results of the proposed power converter transitioning from super- to sub-synchronous operation with forced-boosting control scheme: var = rotor-phase voltage, tq_mks = torque developed by the machine, ias = stator-phase current, iar = rotor-phase current, wmm = mechanical speed**

# Chapter 4: Converter Topology 3

## 4.1 Overview: Hybrid PWM Converter with Thyristors and IGBTs

We investigated the use of a hybrid power converter consisting of a thyristor bridge and two IGBTs in a back-to-back converter configuration for the rotor-side control of a DFIM for wind-energy application. The converter topology, its operating principle, and detailed controller design are explained in this chapter. Finally, the topology is simulated in SABER, and the relevant simulation results are presented. We show that the hybrid topology can be thought of as a replacement for the existing IGBT-based topology, and the cost of the converter will be less. The power converter can be operated as a unity power factor boost rectifier in the front end. Also, another similar converter topology can be used for the machine-side control of a DFIM. The major drawback of this power converter is that it requires more components and thus it needs more physical connection points and wirings. This in turn, may increase the manufacturing cost. In addition, the THD of the current waveform employing the hybrid converter is higher compared to a regular IGBT inverter. The power converter needs a relatively complex control scheme.

## 4.2 Introduction

Typical rotor-side control of a DFIM for wind-energy application employs an IGBT bridge with anti-parallel diodes as a power converter, which supports bi-directional power flow. The IGBT-based topology, while realizing excellent power quality and control flexibility, is expensive because of the high cost of the IGBTs and their gate drive circuits, compared to thyristors and their gate circuits. In order to reduce the cost of the wind generator system, the hybrid topology [5] given in Figure 4.1 may be used as an alternative. The use of a reduced number of IGBTs allows substantial cost reduction when compared to the traditional IGBT bridge. Furthermore, the hybrid network reduces the harmonic distortion of the input currents and provides DC voltage boost capability compared to a diode rectifier. We investigated the given circuit topology for a rectifier application in an earlier paper [5]. However, the detailed control algorithm and analysis of this circuit for rectifier, as well inverter, application was not reported in that paper.

In this project, this topology has been investigated as a prospective candidate for wind-energy applications. Instead of using two back-to-back IGBT converters, two back-to-back hybrid converters of this topology can be used for the rotor-side control of a DFIM. All four operating modes of DFIM can be realized using this power converter. In the following section, the circuit description, operating principle, and the control algorithm for the given hybrid converter is explained in detail. Finally, the hybrid converter control algorithm is verified using a SABER simulation and the relevant simulation results are presented.

## 4.3 Circuit Description

The hybrid converter shown in Figure 4.1 consists of two IGBTs (Sw1, Sw2), a three-phase thyristor bridge (six thyristors, T1-T6, and six diodes, D1-D6), and some passive components necessary to support the forced commutation of the thyristors. The two IGBTs in this topology allow forced commutation of the thyristors. Forced commutation simply means that the thyristors can be switched whenever it is desired. In particular, the two clamp circuits, each consisting of a MOSFET, a diode, a

capacitor, and a resistor, control the turn-off of the thyristors. The resistors (Rs1, s2) and the capacitors (Cs1, Cs2) are used as common snubbers for the lower half and the upper half

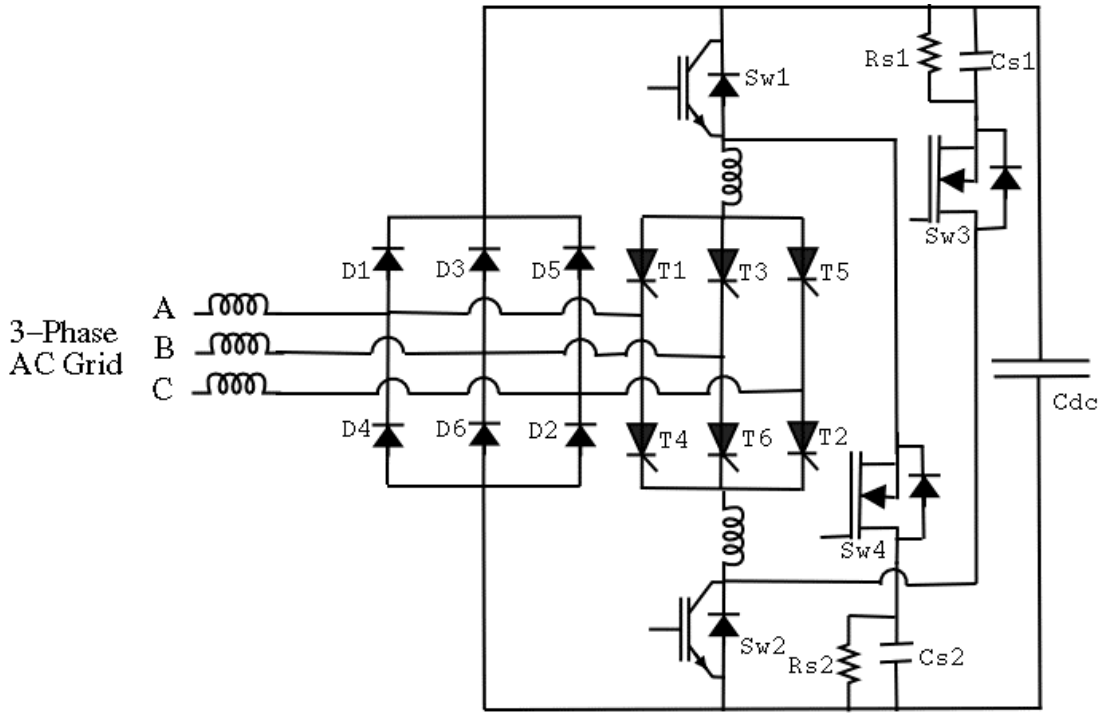


**Figure 4.1. Hybrid bi-directional power converter**

thyristors respectively. The MOSFETs (Sw3, Sw4) are used to support the reverse recovery current of the upper- and lower-half thyristors. The MOSFETs and the corresponding IGBT switches are complementary to each other. They are interlocked with a small dead time so that the DC bus does not become shorted through these devices at any time. The inductors, $L_P$ and $L_n$, shown in Figure 4.1 are necessary to limit the di/dt seen by the thyristors after the series IGBT is turned on. However, the values of these inductors are very small (a few μH). Air core inductors can be used for such purpose.

Because the topology will be used for rotor-side control of a DFIM, it needs to support bi-directional power flow. When power is extracted from the rotor of the machine (during super-synchronous generating and sub-synchronous motoring modes), the converter acts as a rectifier. During this mode of operation, the diode rectifier carries most of the current. The hybrid network is controlled to reduce the harmonic distortion of the input currents and regulate the DC bus voltage. When the rotor is taking energy from the DC bus, the thyristor bridge carries the current to the rotor winding. This mode of operation occurs during super-synchronous motoring and sub-synchronous generating operation.

In AC-to-DC and DC-to-AC modes of power flow, the limiting factor of the hybrid converter with respect to a full IGBT bridge is the switching frequency. This frequency has to be limited due to the slow turn on and turn off of the thyristors. Also, for the given hybrid converter, only one upper-half and one lower-half thyristor can be turned on at a time; the rest of the thyristors will be turned off automatically. When the thyristors are OFF, it reduces the effective switching frequency of a

thyristor compared to their commutating IGBTs (Sw1, Sw2). If the commutating IGBTs are switched at 10kHz, then each lower-half or upper-half thyristors can be switched typically at 10/3 = 3.33 kHz frequency. Because a single IGBT is being used for commutating all three thyristors, the commutating IGBT has to support three times switching frequency of an individual thyristor. Hence, a trade-off must be achieved between the switching frequency and the input line reactors in order to obtain the desired THD of the three-phase current waveforms.

## 4.4 Operating Principle

The proposed hybrid converter can be operated as a bi-directional power converter in the same manner as a conventional IGBT-based converter. For AC-to-DC operation, it can be operated as a boost rectifier, and for DC-to-AC operation it can be controlled as a buck converter. In order to explain the operating principle of the given hybrid converter, the four operating modes of the converter, when it is acting as AC-to-DC boost rectifier, are described in Figure 4.2. For simplicity, the operation is explained with reference to phase A. For symmetric operation, the operation of the other two phases will be the same with simple 120° shifting in phase.

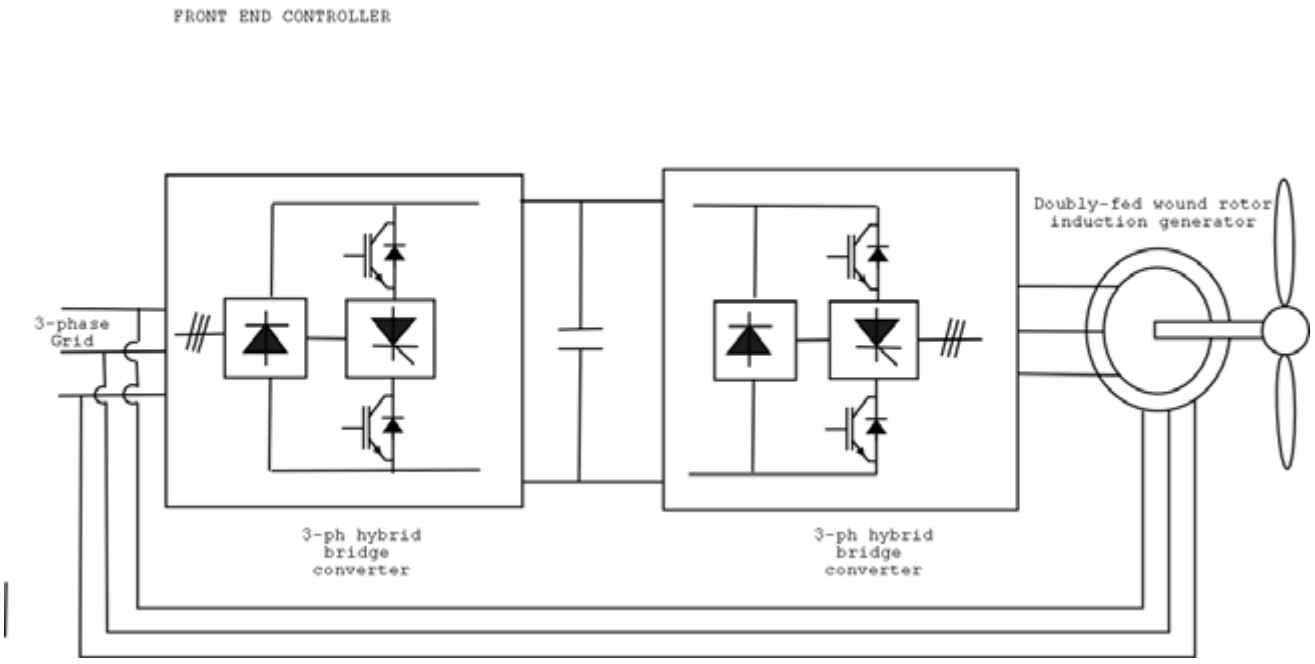


**Figure 4.2. Back-to-back hybrid converters for rotor-side control of a DFIM control for wind-energy application**

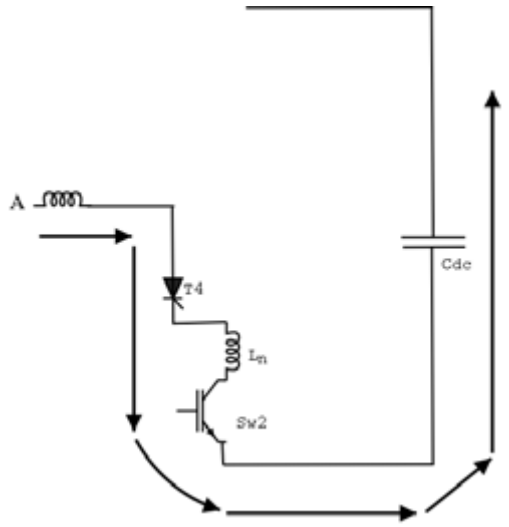


(i) Mode 1

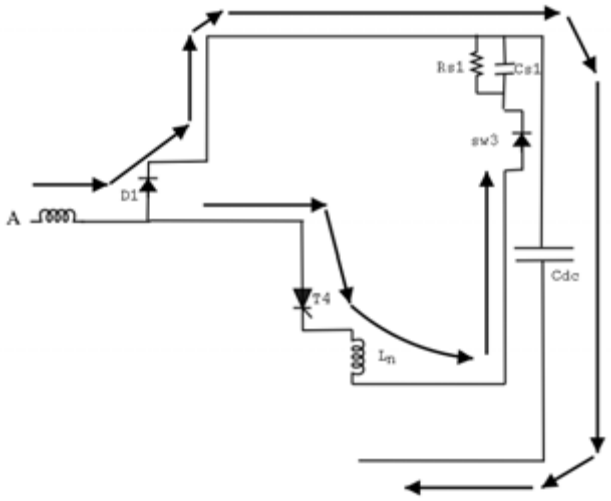


(ii) Mode 2

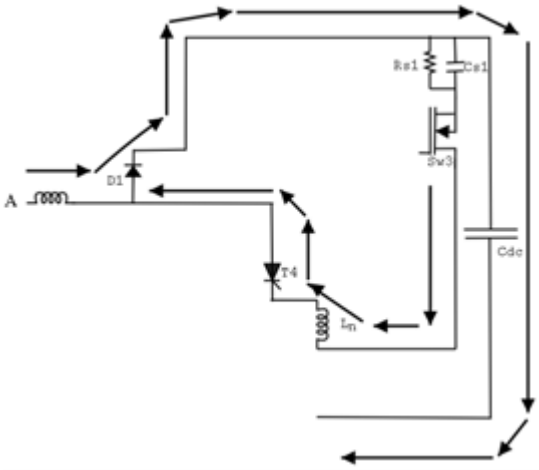


(iii) Mode 3

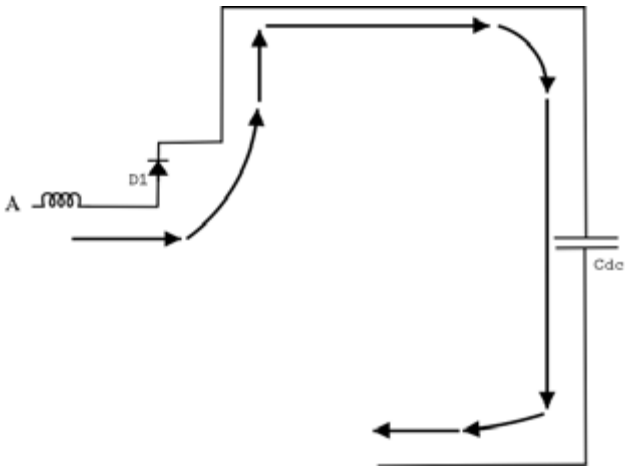


(iv) Mode 4

**Figure 4.3. Four operating modes of the hybrid converter with respect to phase A: (i) mode 1, (ii) mode 2, (iii) mode 3, and (iv) mode 4**

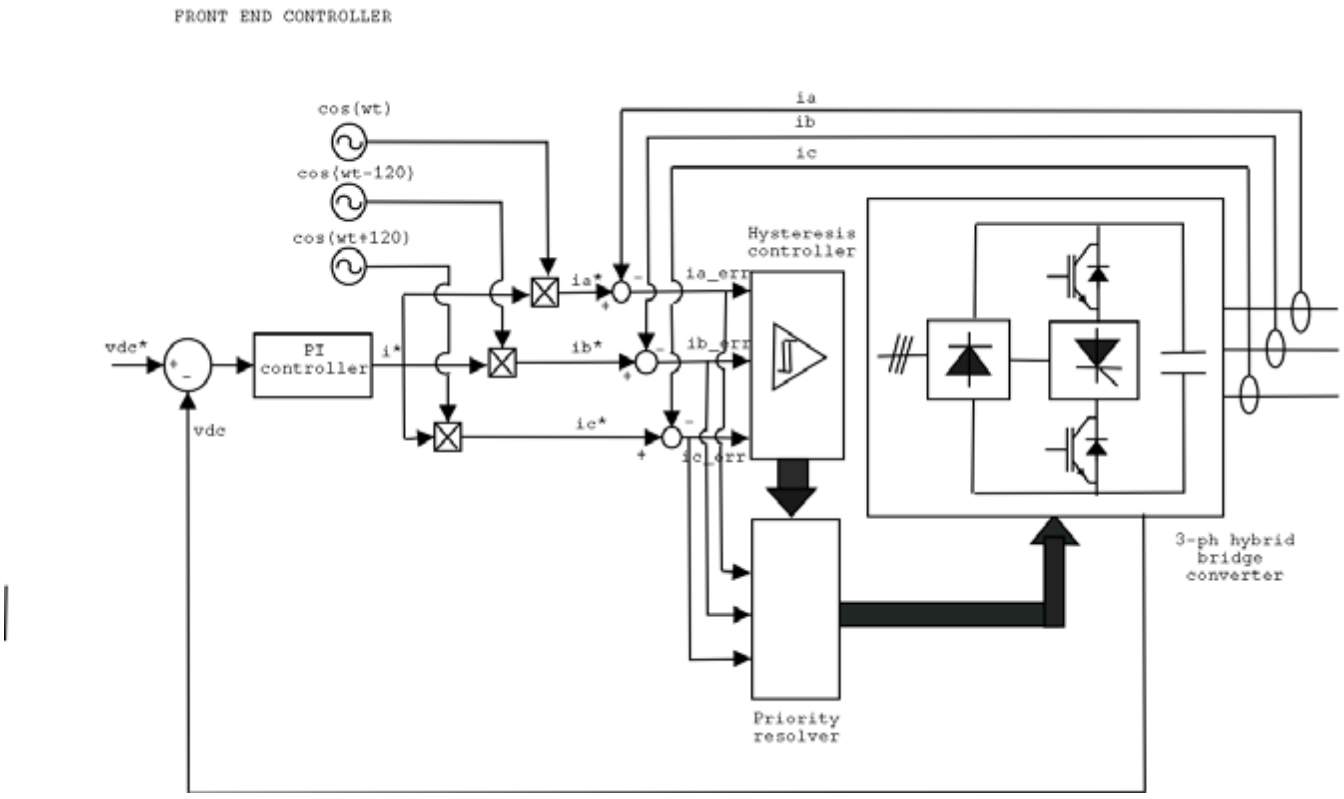


**Figure 4.4. Control-block diagram of the hybrid converter when it is acting as a FEC**

In mode 1 operation, the lower-half thyristor (T4) of phase A and lower IGBT (Sw2) are turned on. Current flows from the AC side to the negative DC rail and, in effect, the current through the phase reactor increases. In mode 2 operation the lower IGBT (Sw2) is turned off. The current through the lower-leg thyristor (T4) of phase A is gradually reduced, and the phase-A current is gradually shifted to the upper-half diode (D1) of phase A (Figure 4.2b). However, because of the stored charge, the recombination current of the thyristor (T4) still flows through the clamping diode and snubber circuit (Rs1, Cs1) connected between the lower-half thyristors and upper DC bus rail. The operation of mode 2 continues until the current through the thyristor (T4) reverses its direction. When the current is reversed, operation enters mode 3, and at that time the reverse recovery current flows through the diode D1, the upper rail DC bus, the snubber circuit, the MOSFET (Sw3), and the thyristor T4 (Figure 4.2b). When the reverse recovery current becomes zero, the entire phase current becomes shifted to the phase-A upper half diode D1 and thyristor T4 is finally turned off. However, in order to ensure the thyristor is properly turned off, the lower IGBT (Sw3) should not be turned on at least for a time interval equal to the specified turn-off time ($t_q$) given in data sheet for a particular thyristor. This last mode of operation is called mode 4 operation (Figure 4.2d).

Thus, the whole operation mode 4 emulates the regular boost rectifier operation of an IGBT converter. In a regular three-phase boost rectifier, the conduction of an IGBT is the same as mode 1 in this case. The rest of the modes together emulate the diode conduction period of a regular IGBT boost rectifier. The only difference between them is that the switching process of the hybrid converter is more complex and distributed over four operating modes.

## 4.5 Special Control Effort and Switching Logic Generation

Unlike an IGBT bridge, all the phase currents of the given hybrid power converter cannot be controlled independently all the time. For example, when the phase-A lower thyristor (T4) is turned on, none of the phase-B or phase-C lower-half thyristors (T6 or T2) can be switched on simultaneously. Thus, if the current regulator of two phases demand switching two of the upper-half thyristors or two of the lower-half thyristors at the same time, this condition may not be possible with this converter. In the case of two lower-half phase thyristors getting positive gate signal at the same time, the one with more positive phase voltage will only be turned on. The other phase thyristor will be reverse biased and will have to wait for its turn in the next switching cycle. Therefore, the phase current corresponding to the waiting thyristors will deviate from its reference value further from the previous error. The error between the reference current and the actual current of this hybrid converter will be much higher compared to a regular IGBT-based converter phase current, where the lower- or upper-half switches can be turned on at the same time for two or three phases, if it is required.

In the hybrid converter, one of the phase voltages will be higher than the rest of the two phases in every 60° phase belt. Hence, within that phase belt, the thyristor with higher phase voltage will be the most privileged one, with a traditional control algorithm. If two thyristors receive a gate signal at the same time, the privileged one will be turned ON and the others will be forced to turn OFF irrespective of the demands of their respective current regulators. Each phase current will have much smoother current waveform within a 60° phase belt than during the rest of the period. However, the resultant waveform may not be the best current wave shape. Rather, the preferred waveform will be the one that will result in uniform harmonics throughout its 360° phase span. In order to achieve the above result, a new control algorithm is proposed. A priority resolver block is introduced in the new control algorithm, which decides the best case for a phase thyristor to be turned ON. If only one thyristor receives a positive gate signal at a time, then there will be no change in the control algorithm. But in the case of multiple phases getting positive gate signals for their upper or lower-half thyristors, then the priority resolver decides the most eligible phase to be turned ON, based on the following criterion.

The priority resolver checks the absolute error in all the concerned phase currents with respect to their references, and the phase with maximum error is chosen as the best fit for next switching. If the privileged phase becomes the best fit, then there will be no change in switching logic. However, for any other phases being chosen as the best fit for switching, then the gate signal for the privileged phases will be forcibly made low and only the device with the best fit will be allowed to have positive gate signal. The same logic is applied for the upper- and lower-half phase thyristors. Using such a priority resolver, it may be possible to have uniform current waveform for all three phases through out the 360° region.

From the above discussion it is quite apparent that the zero switching vector cannot be achieved using the hybrid converter at any point of time that obviously limits the power quality of the system. Similarly, when a particular phase thyristor is being switched off, another phase cannot be turned on unless the turn-off process is completed. If the incoming phase is switched on before the outgoing phase is switched off completely, the outgoing phase thyristor may remain ON undesirably, and simultaneously the incoming phase may not be turned ON at all. This complex and shared

commutation process limits the switching frequency of individual phases to a much lower value compared to the switching frequency of the commutating IGBTs (sw1, sw4). Hence, the size of the AC-side reactors may have to be increased for better power quality or to have lower THD in the current waveforms.

## 4.6 Control Scheme

The fundamental control algorithm for this hybrid converter is similar to that of a conventional IGBT-based boost converter. For a rectifier application, the DC bus voltage is actively controlled by an outer loop. The output of this controller generates the current references for all three phase in synchrony with their phase voltages. The current references are compared with the actual currents, and the error is passed through a hysteresis controller. The output of the hysteresis controller generates the "raw" switching logic for the thyristor bridge of the hybrid converter. However, these raw switching logic signals are passed through a priority resolver block, after which the final switching logic for the thyristors, as well the upper and lower commutating IGBTs, are generated. For any lower-leg thyristors receiving positive gate signal, this indicates that the lower IGBT will also be turned ON. Similarly, for any upper-leg thyristors getting positive signals, this indicates that the upper IGBT is turned ON. Similarly, when lower-leg thyristors are in the process of being switched OFF, all the gate signals for the lower-leg thyristors and the lower-leg IGBT will be disabled and, at that time, the gate signal for the commutating MOSFET will be applied. Similar logic is followed for controlling the upper-leg thyristors and IGBT. The block diagram of the above control scheme is given in Figure 4.4.

## 4.7 Simulation Results and Discussion

The outlined control scheme in the previous section and the power converter given in Figure 4.1 has been verified through SABER simulation, and the simulation results are presented in this section. Currents are shown for all three phases. Also the currents through different important components are presented. The results are given for full load and 20% operating load conditions. The three phase currents for full-load conditions are given in Figure 4.5. It may be seen that all the phase current waveforms are sinusoidal, and they do not contain appreciable harmonics. However, the THD may be slightly higher than a regular IGBT inverter. Such higher THD becomes more prominent for reduced-load operation. The results for three-phase currents at 20% load are given in Figure 4.7. The current through the upper- and lower-half individual thyristors and the IGBTs are also included in figures 4.6 and 4.8. It can be seen that each individual thyristor switches ON and OFF for one half cycle, and for the other half cycle remains OFF permanently. The current waveforms through phase-1 upper- (scr.sym31) and lower-leg thyristor (scr.sym34) along with lower-leg IGBT (bjt_l4.bjt_l4_2) are given in figures 4.6 and 4.8; These depict when the hybrid converter is operating at full load and 20% load condition, respectively. It can be seen that the lower-leg IGBT carries all the three-phase currents and conducts for both half cycle as desired by all the lower-leg thyristors. Thus, the RMS current through the IGBT and its switching frequency will be higher compared to individual thyristor which will increase the switching loss of the IGBT and, thus, may require an over-rated IGBT for this hybrid converter, which may be considered as one of the drawback for this power converter.

From the plots in Figure 4.6, it can also be observed that current through each thyristor has some negative component that can be accounted for by the reverse recovery through a thyristor. Figure 4.1 shows the two MOSFETs that provide the reverse recovery current path for the thyristors. A typical reverse recovery current through the lower-leg phase A thyristor (scr.sym31) and the MOSFET (sw1_l4_l4_1) and its antiparallel diode (d.sym56) are shown in Figure 4.9. During the turning-off of the lower-leg phase-A thyristor, the current through the thyristor first passes through the anti-parallel diode of the MOSFET. When the current reverses its direction through the commutating thyristor, the diode stops conducting, and the MOSFET comes into conduction. Thus, a complete commutation cycle of a particular phase is demonstrated with this simulation result.

The performance of this hybrid converter largely varies with the turn-off time of the thyristors. The simulation results shown in figures 4.5 through 4.9 are conducted for a thyristor with 50-µs turn-off time. However, the same system is simulated using thyristor with 100-µs turn-off time, and the simulation results are given in figures 4.10a and 4.10b. The harmonic content of phase currents for such simulation conditions is much higher than the results shown in previous plots. This higher THD is a direct consequence of choosing a thyristor with higher turn-off time. Similarly, a thyristor with 25 µs turn-off time was simulated and simulation results of the phase currents and their FFT are given in figures 4.11a and 4.11b, respectively. It can be seen that the current waveforms and their THD have improved markedly by choosing a faster thyristor. However, the flip side is that a thyristor that turns off faster is more expensive.

## 4.8 Conclusions

In this chapter, a hybrid converter configuration has been explored for rectifier and inverter application. The major objective of this chapter was to explore the potential of this hybrid converter as a replacement for the IGBT-based full-bridge power converter with similar performance. It is shown through analysis and simulation that the performance of the hybrid converter is largely dependent on the control scheme. Finally, an improved control scheme is proposed in this chapter for controlling this hybrid converter. The controller was verified with SABER simulation, and the results were presented. Also, it is shown that the performance of the hybrid converter can be improved largely by using a faster turn-off thyristor. However, the cost of the system goes up with a faster turn-off thyristor. Thus, a trade-off between the thyristor turn-off time and THD content of the phase currents has to be reached. The detail simulation results and the component currents are given, and the reverse recovery operation of the thyristor is illustrated through simulation results. It was shown that the RMS currents through the IGBTs are relatively higher than the RMS phase current, which may be considered as a drawback for this topology. Also, the components and connections are quite numerous, which may introduce higher manufacturing cost and wiring complexity. In summary, it can be concluded that the hybrid converter is a potential low-cost solution for a controlled rectifier and inverter application. It can be used for wind-energy application as both machine-side and FEC for a DFIM drive.

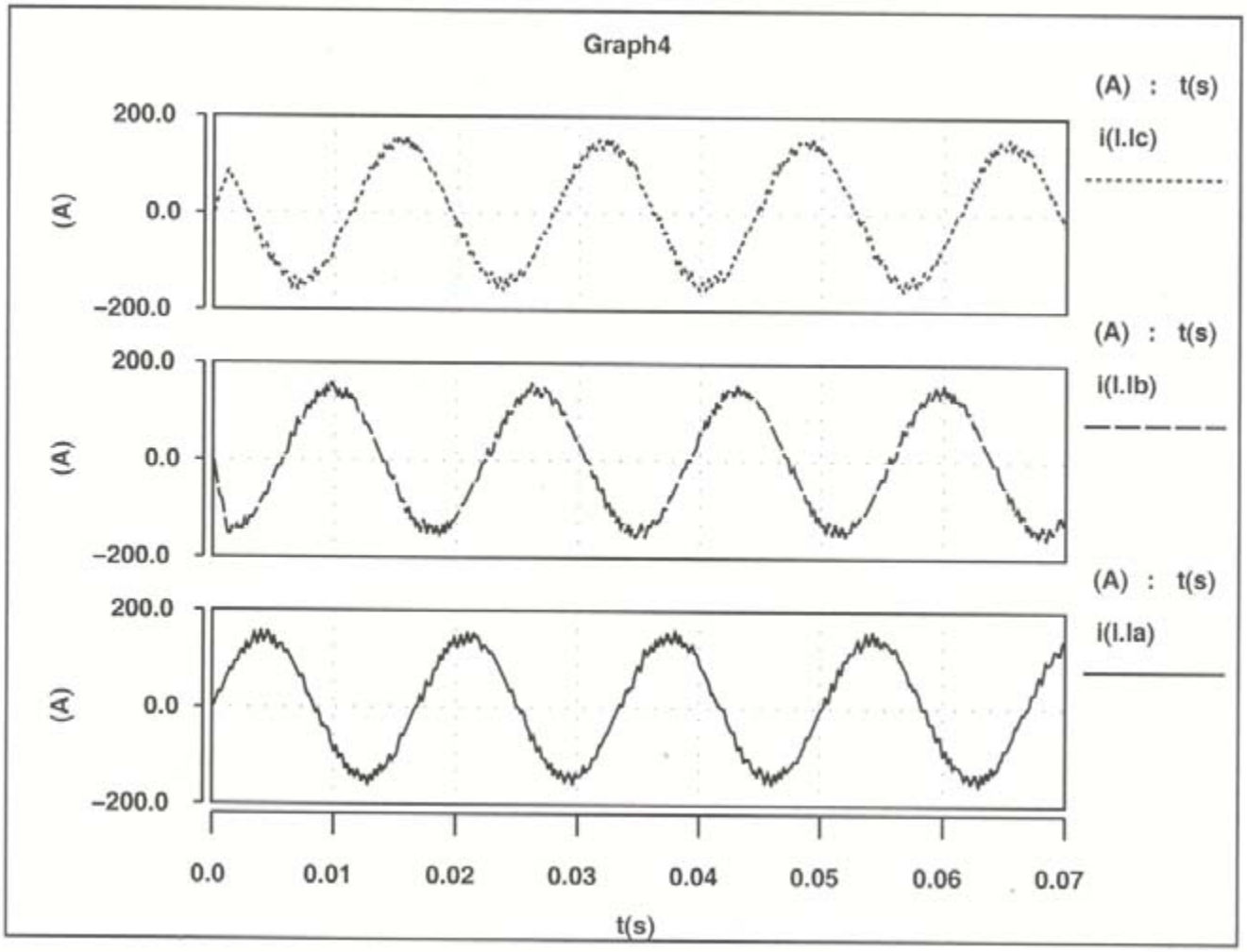


**Figure 4.5. Simulation results showing three-phase currents of the hybrid converter when it is operating at full load and acting as a unity power factor FEC**

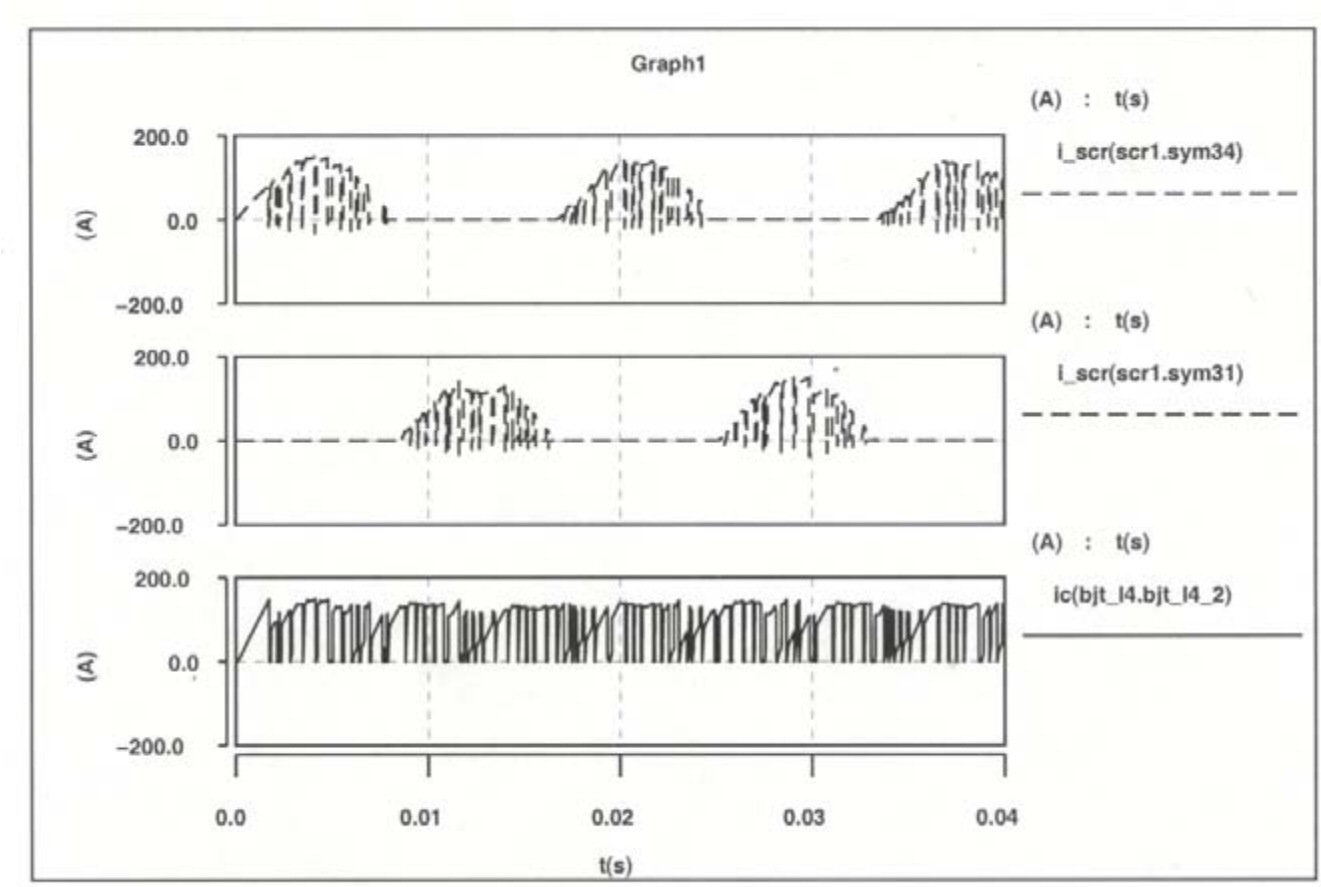


**Figure 4.6. Simulation results for the hybrid converter when operating at full load: i_scr(scr1.sym34) = current through lower-half thyristor (T4) of phase A, i_scr(scr1.sym31) = current through lower-half thyristor (T1) of phase A , ic(bjt_l4.bjt_l4_2) = current through lower-half IGBT (Sw2)**

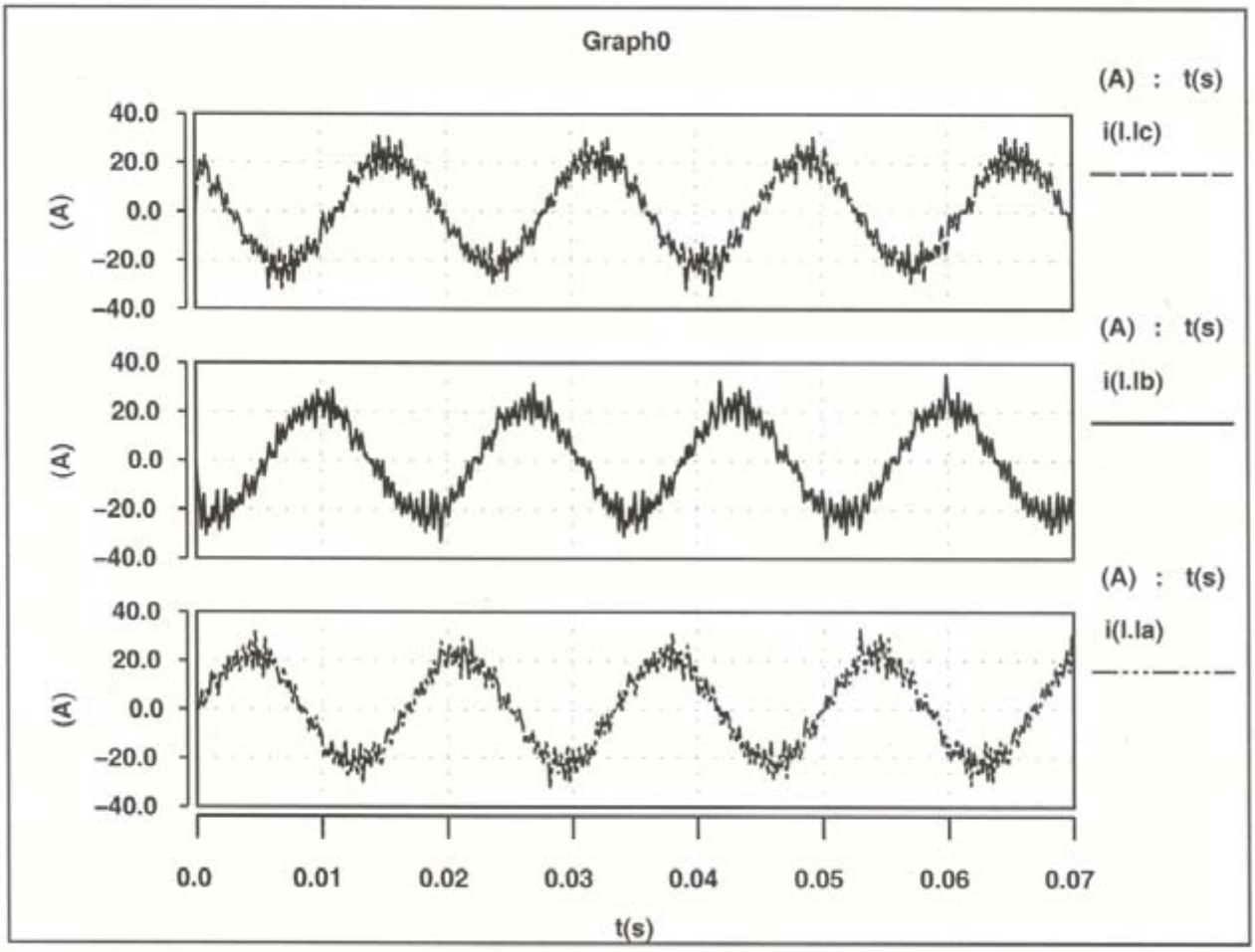


**Figure 4.7. Simulation results of three-phase currents of the hybrid converter when it is operating at 20% load condition**

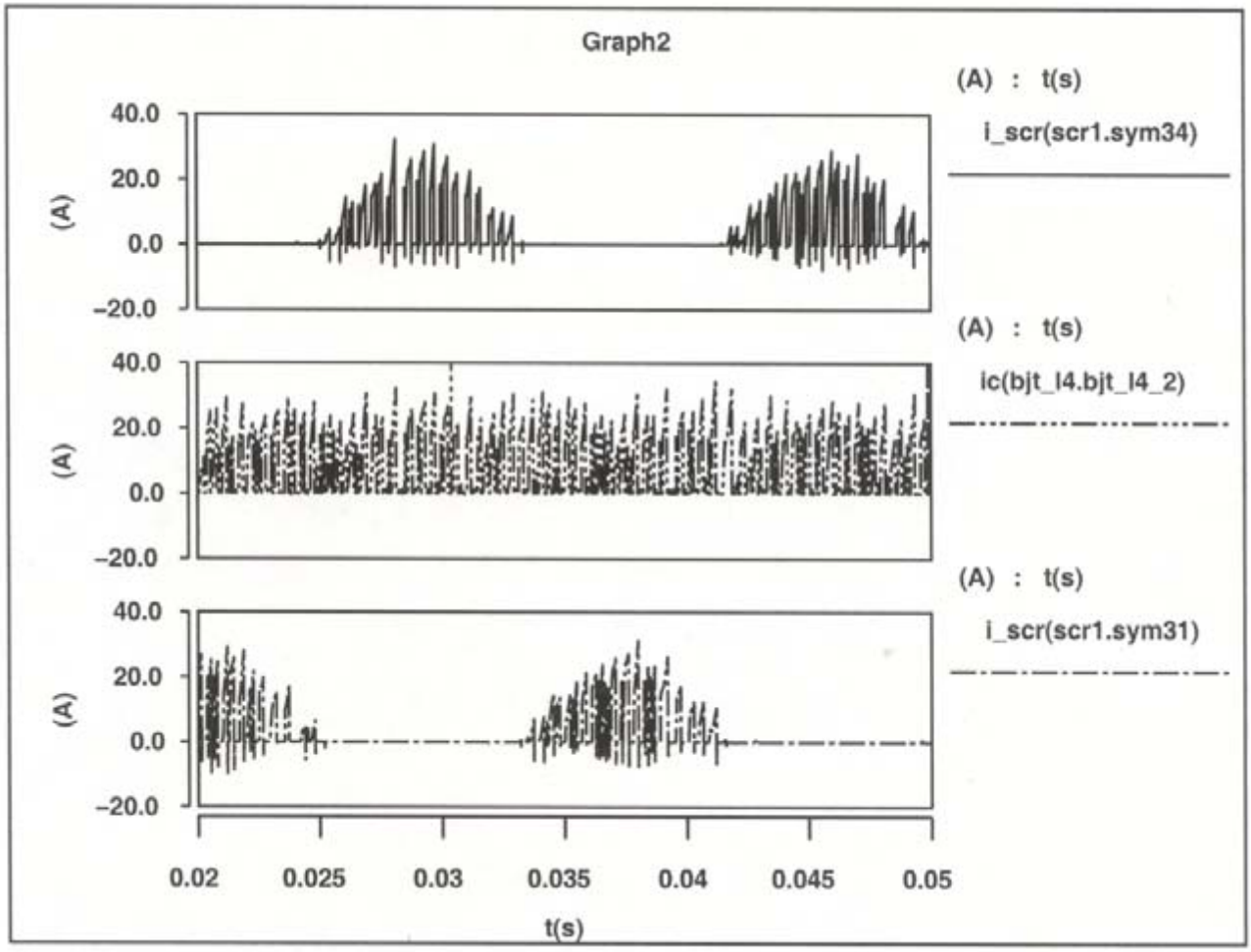


**Figure 4.8. Simulation results for the hybrid converter when operating at 20% load: i_scr(scr1.sym34) = current through lower-half thyristor (T4) of phase A, ic(bjt_l4.bjt_l4_2) = current through lower-half IGBT (Sw2), i_scr(scr1.sym31) = current through upper-half thyristor (T1) of phase A**

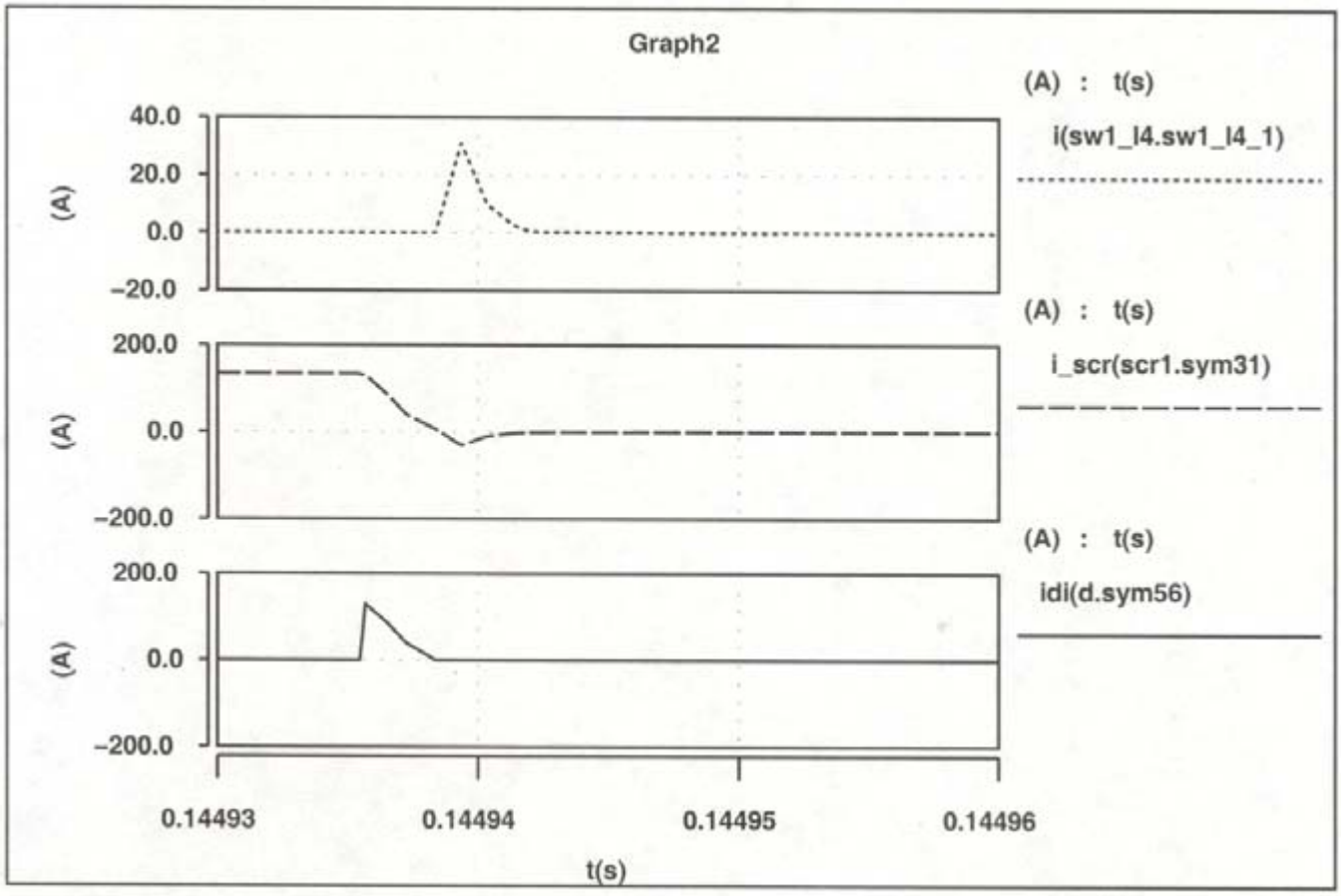


**Figure 4.9. Simulation results for the hybrid converter when operating at full load: i(sw1_l4.sw1_l4_1) = current through the lower MOSFET (Sw4), i_scr(scr1.sym31) = current through upper half thyristor (T1) of phase A, idi(d.sym56) = current through the anti-parallel diode of the lower-half MOSFET (Sw4)**

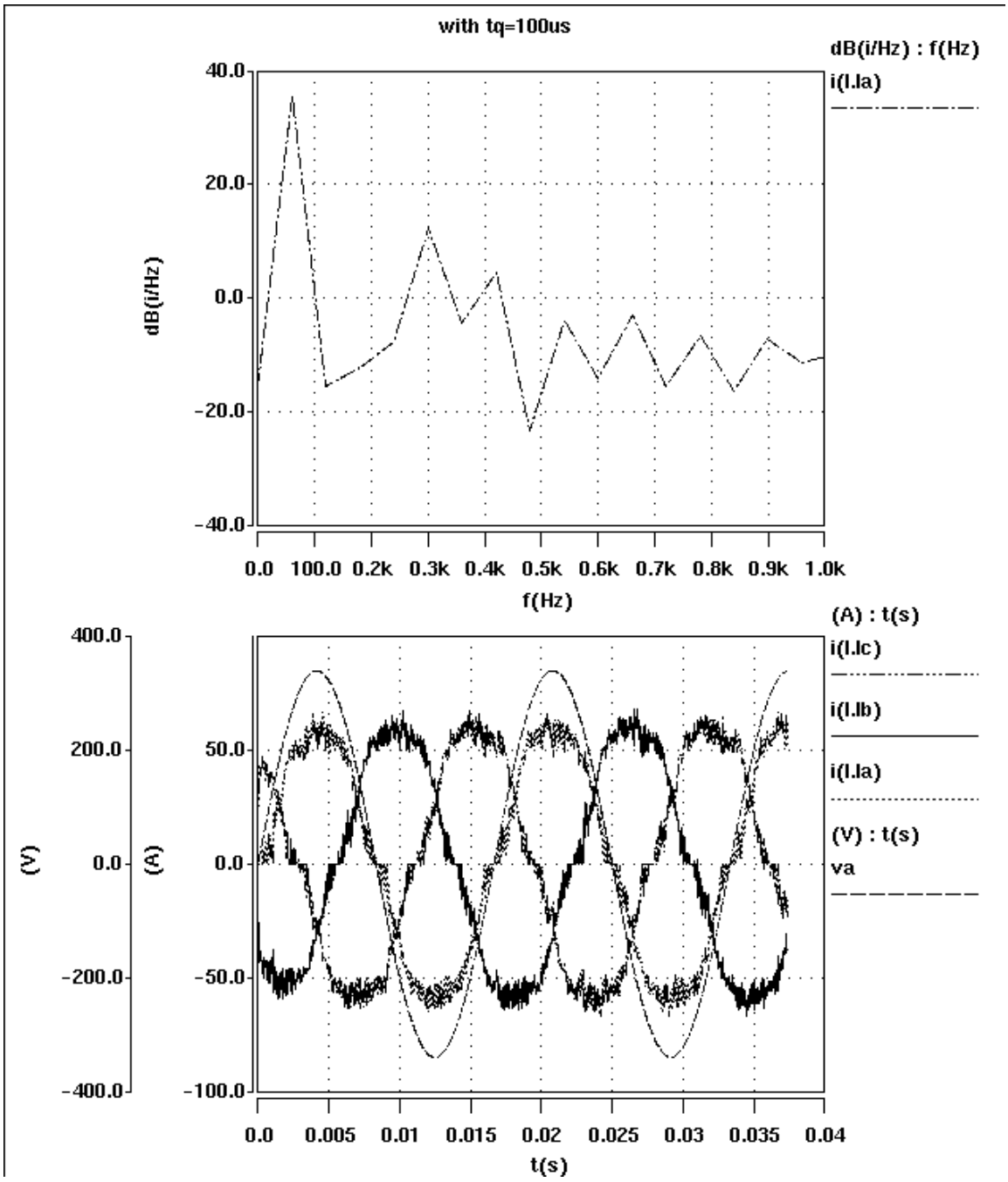


**Figure 4.10a. Simulation results for the hybrid converter when it is acting as a unity power factor FEC: Three-phase current waveforms and phase A voltage along with the FFT when a thyristor of 100 μs turn-off time is used**

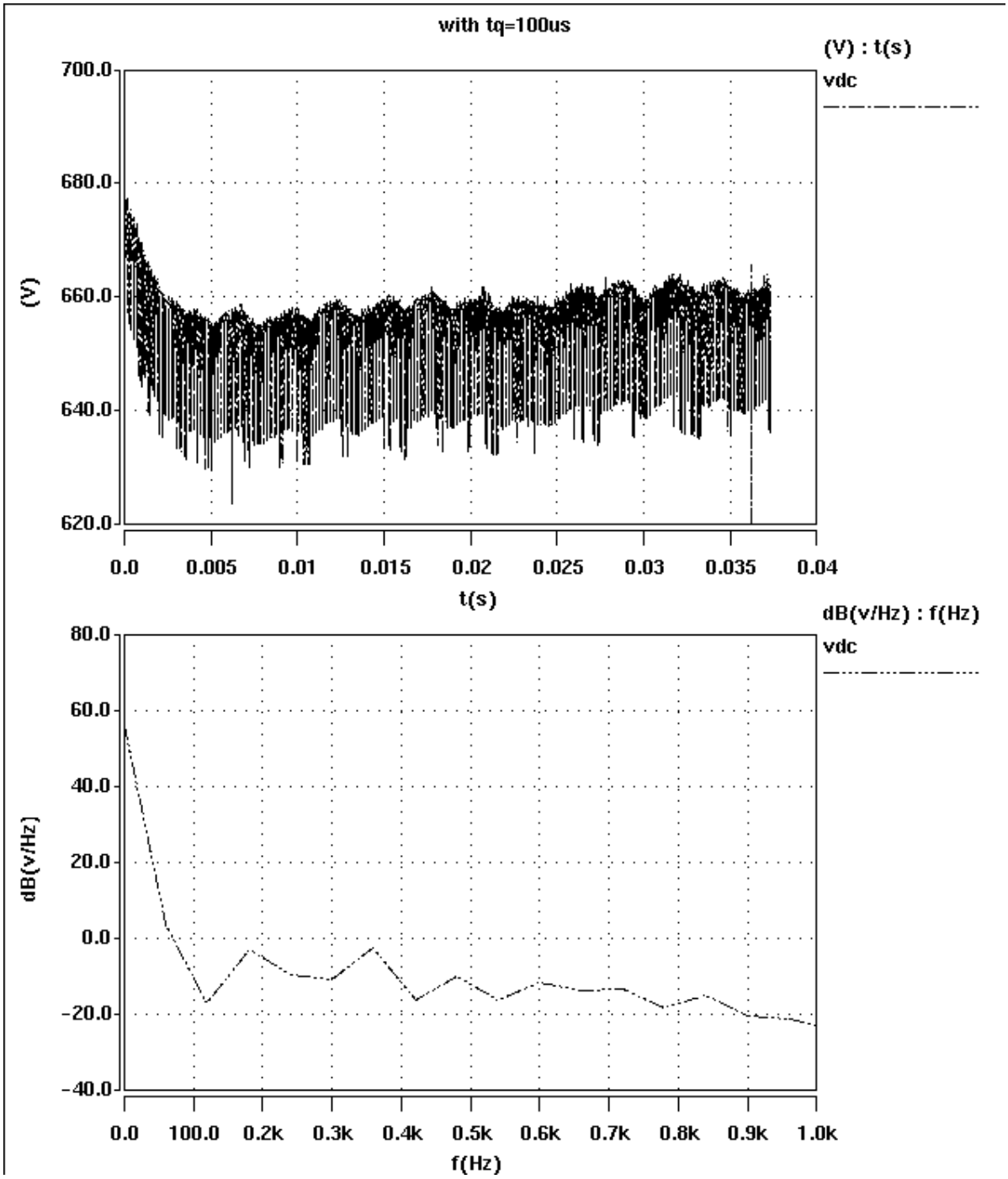


**Figure 4.10b. Simulation results for the hybrid converter when it is acting as a unity power factor FEC: DC bus voltage along with its FFT when a thyristor of 100 μs turn-off time is used**

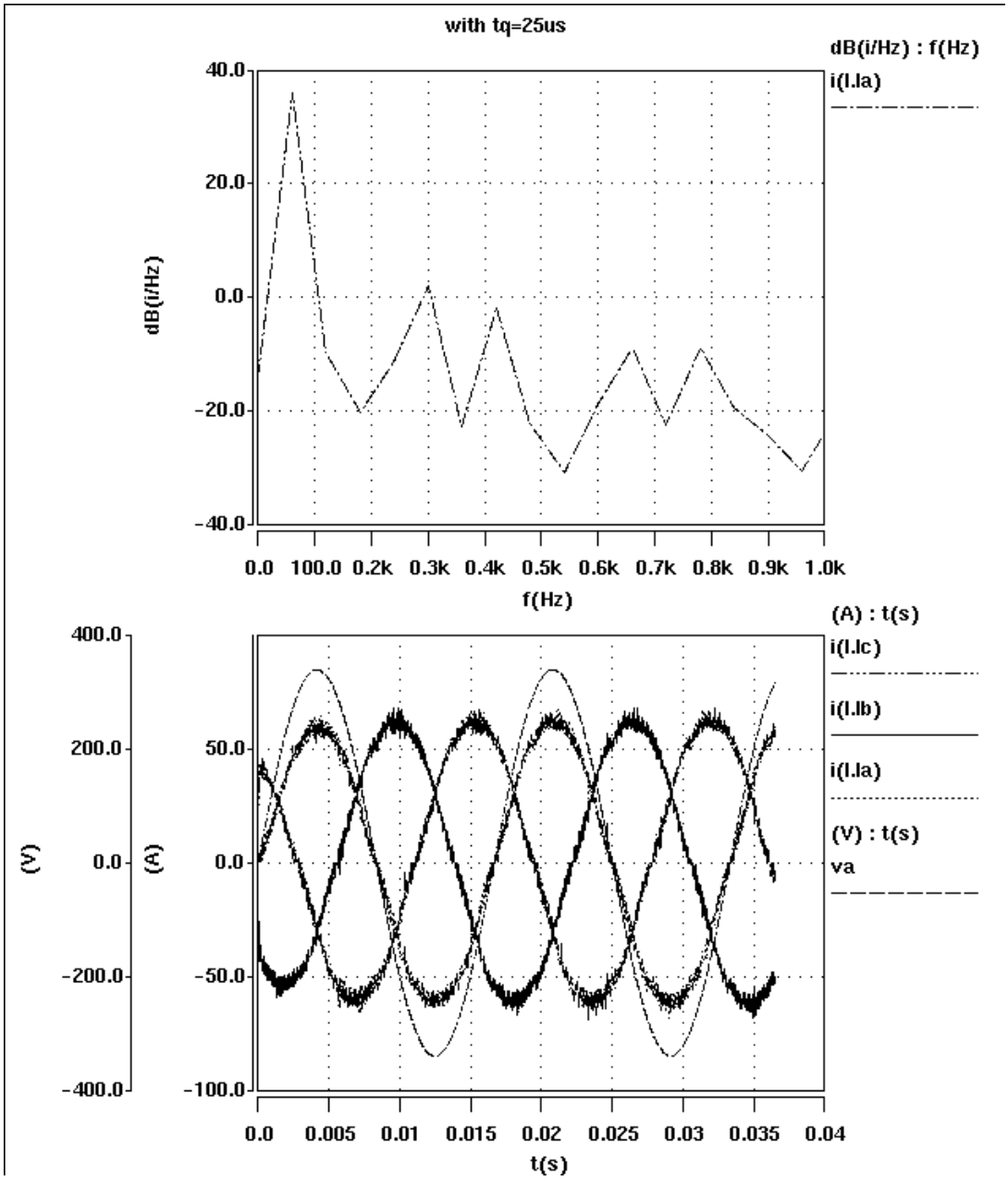


**Figure 4.11a. Simulation results for the hybrid converter when it is acting as a unity power factor FEC: three-phase current waveforms and phase voltage along with the phase current FFT when a thyristor of 25 μs turn-off time is used**

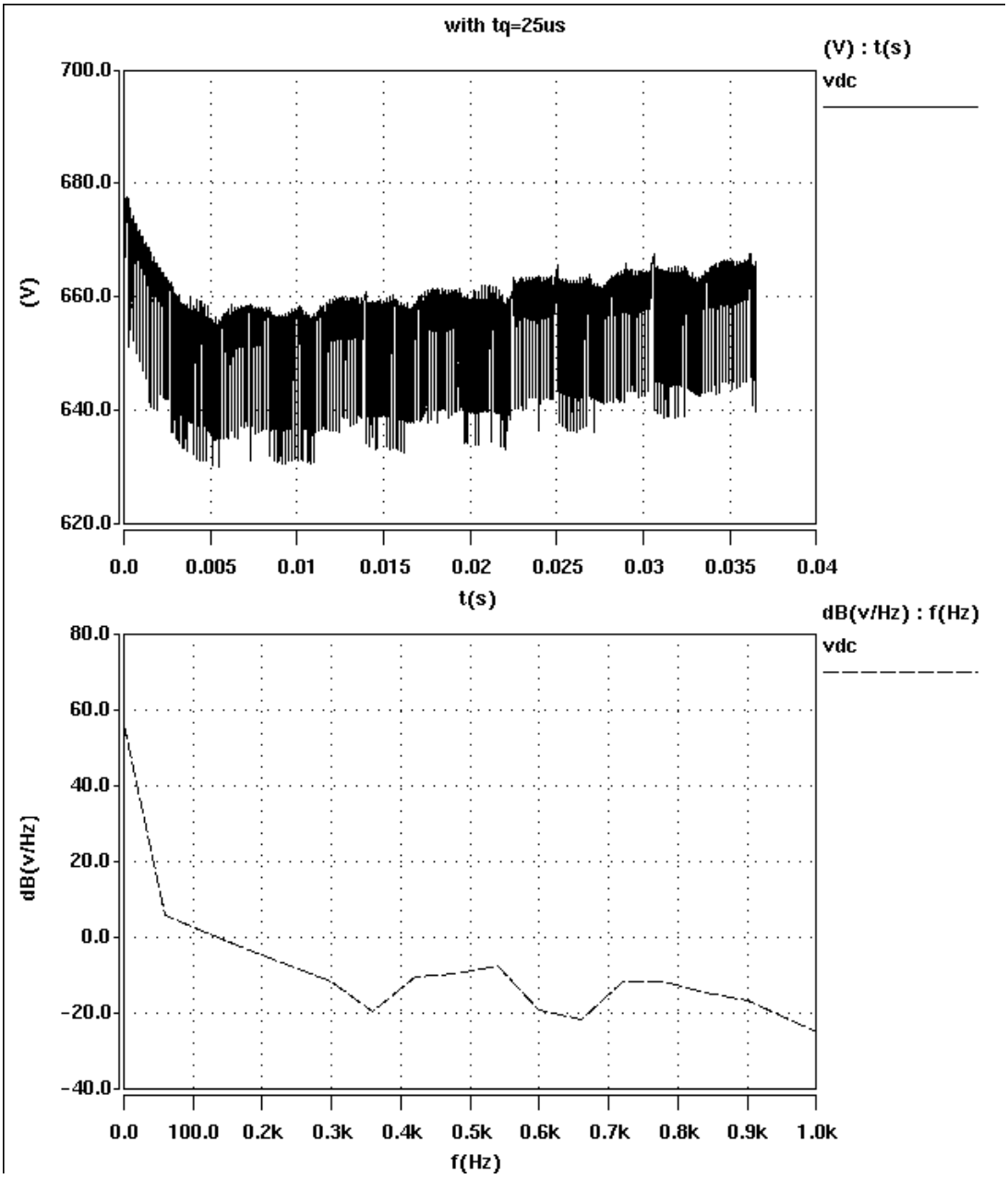


**Figure 4.11b. Simulation results for the hybrid converter when it is acting as a unity power factor FEC: DC bus voltage along with its FFT when a thyristor of 25 μs turn-off time is used**

# Chapter 5: Converter Topology 4

## 5.1 Overview: Reduced-Switch-Count, Double-Converter-Fed, Wound-Rotor Induction Machine Drive

In this chapter we propose reduced-switch-count double-sided, converter-fed, wound rotor induction machine control for wind energy application. The outputs of the two converters are combined electromechanically in the machine and are capable of simultaneously sharing the power from stator and rotor equally. We also propose a new configuration using two half-controlled converters for both the stator and rotor circuit to reduce cost. The proposed controller reduces the required KVA rating of both machine side converters, improves the inefficiency, and facilitates operation over a wide range of speed. The combined KVA rating of the machine-side converters are even less than that of the machine-side converter for a conventional rotor-side-control configuration. Also, the proposed configuration is suitable for use with a rotary transformer because neither the stator nor the rotor winding will encounter zero frequency over the entire range of operating speed. The proposed configuration is simulated in SABER for a 30-kW wound-rotor machine; the simulation results are presented.

## 5.2 Introduction

Systems that generate electricity from wind generally operate with best efficiency if they can vary their speed in proportion to the varying wind speed.. Hence, it is necessary to interpose a frequency converter between the variable-frequency generator and a fixed-frequency utility. When a squirrel-cage induction machine is used, an electronic power converter equal to the KVA rating of the machine must be used because all the power transmitted to the utility passes through the converter. For high power (more than a few hundred kilowatts), placing two or more inverters in parallel is typically an option. In the case of a wound-rotor machine, the power to the utility passes through both the stator and the rotor. Hence, two independent converters can be employed: One for the stator side and one for the rotor side, so the problem of paralleling can be eliminated.

The state-of-the-art technology for wind power employs a DFIM with only rotor-side control, wherein the stator is directly connected to the grid. In such a control method, the power converter should be rated for the power produced by the rotor windings alone, typically one-third to one-fourth of the total KVA rating of the machine [6,7,8,9]. This leads to significant reduction in cost. However, such systems operate only over a limited range of speed. In reality, the wind speed varies widely at different times and days of the year. Hence, a system with limited speed range capacity may not be adequate to exploit the potential of the wind fully.

By increasing the rotor-side power converter rating, the operating speed range may be extended to some extent. However, in systems where the stator is directly connected to the grid and control is exerted only from the rotor side, field weakening is typically no longer possible. Thus, topologically, the rotor-side control configuration suffers from a maximum speed limitation.

By employing power converters, both in the stator- and the rotor-side field, weakening is achievable and, therefore, a wide range of speed operation (beyond twice the rated speed) is possible. In addition,

with this arrangement, the excitation current can be shared equally between the stator and the rotor of the machine. By doing so, the winding design (copper volume) and losses in the machine can be optimized, and the machine size may be reduced.

A control algorithm employing full-bridge converters for both the stator and the rotor was reported in [10] for high-power motoring application. However, such a method adds extra cost to the system and may not be viable for wind energy applications. In this paper, the major focus is to reduce the cost of the system, while retaining all the advantages of a double-sided converter. Instead of a full-bridge converter, in this project, half-controlled converters were employed in both the stator and the rotor side. Thus, the cost of the machine-side power converter was reduced to almost half compared to the rotor-side control method. We also propose a new control algorithm whereby the performance of the machine can be improved at all operating ranges with half-controlled converters. The operating principle, control algorithm, and performance of the system with the proposed configuration are presented in this paper.

## 5.3 Operating Principle

The operating principle of a DFIM is well documented in the literature [6,7,8,9]. In a DFIM, the power flows through both the stator- and the rotor-side of the machine, and control can be realized either from the stator side or the rotor side, or from both the sides. Normally, four operating modes are observed in this machine, as discussed previously. The machine can be controlled as a generator or as a motor in both the sub- and super-synchronous operating mode. Depending upon the operating modes, the power flow varies in the stator and the rotor winding of the machine. Detailed power-flow diagrams for different operating modes are given in Figure 5.1.

In conventional rotor-side control, with two back-to-back IGBT-based power converters, all four operating modes can be realized. However, during such operation, in sub-synchronous generating (i) and sub-synchronous motoring (ii) modes the power flow direction through the stator and the rotor side are of opposite direction. A condition occurs wherein circulating power flows around the stator and the rotor, reducing efficiency at speeds below synchronicity. To avoid these circulating currents, operation of the machine can be restricted to the super-synchronous mode. However, in a conventional rotor-side control scheme, the super-synchronous speed mode is achieved only when the rotor is running above the rated synchronous speed. Thus, it suffers from a physical speed limitation, and the operation of the wind turbine gets restricted to a limited speed zone. In addition, the machine cannot be operated beyond twice the rated speed because field weakening is not possible when the stator is directly connected to the grid.

The method we propose in this section explores a new control scheme whereby the machine can be theoretically operated at any speed (speed is limited only by mechanical restriction). At the same time, it will always operate in super-synchronous mode. Thus, the proposed control scheme promises a wide range of speed and power flows out of both the stator and the rotor windings without any penalty from circulating power flow for the entire speed range. Because this report is focused on wind energy applications, the machine is intended to always operate as a generator. Therefore, all our discussion of analysis and control of the machine will be restricted to super-synchronous generating mode (mode [iii] in Figure 5.1).

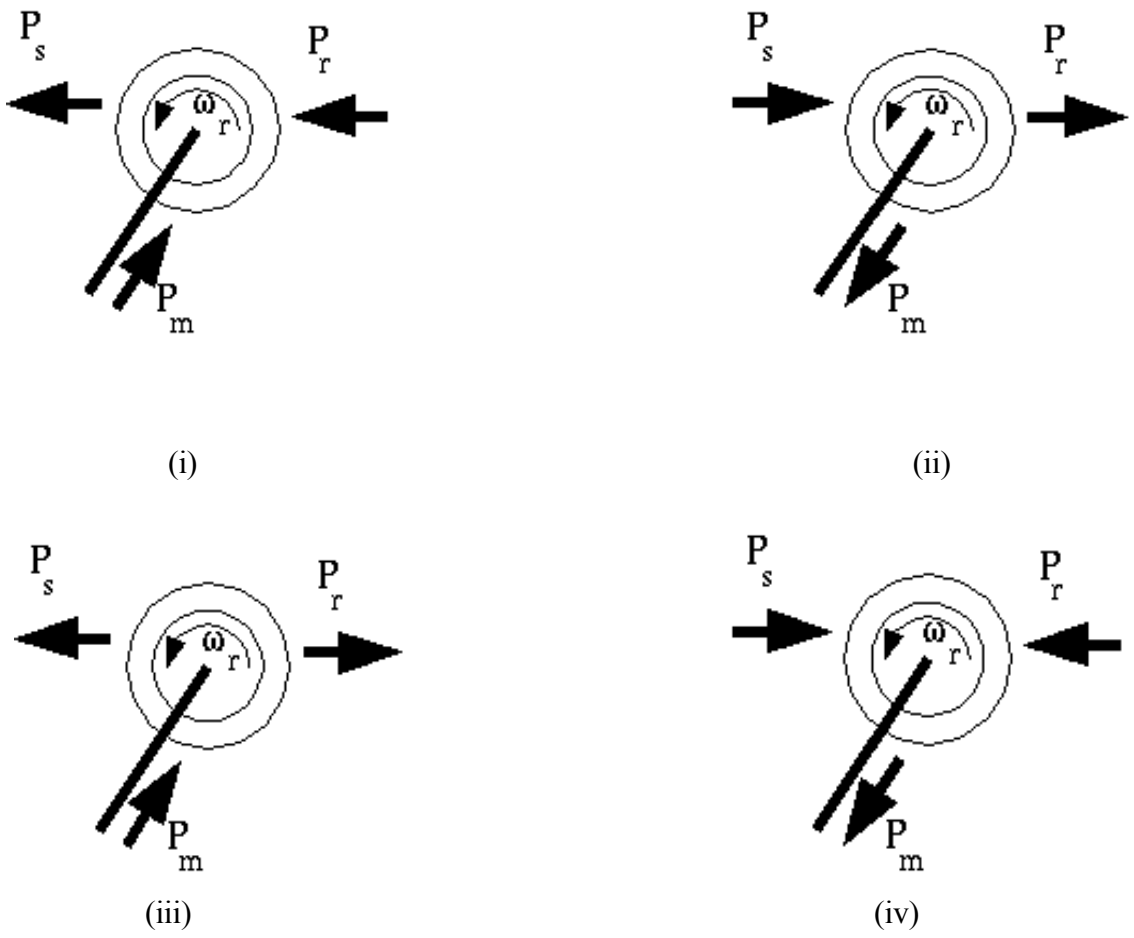


**Figure 5.1. Power-flow diagram of a DFIM for: (i) sub-synchronous generating mode, (ii) sub-synchronous motoring mode, (iii) super-synchronous generating mode and (iv) super-synchronous motoring mode**

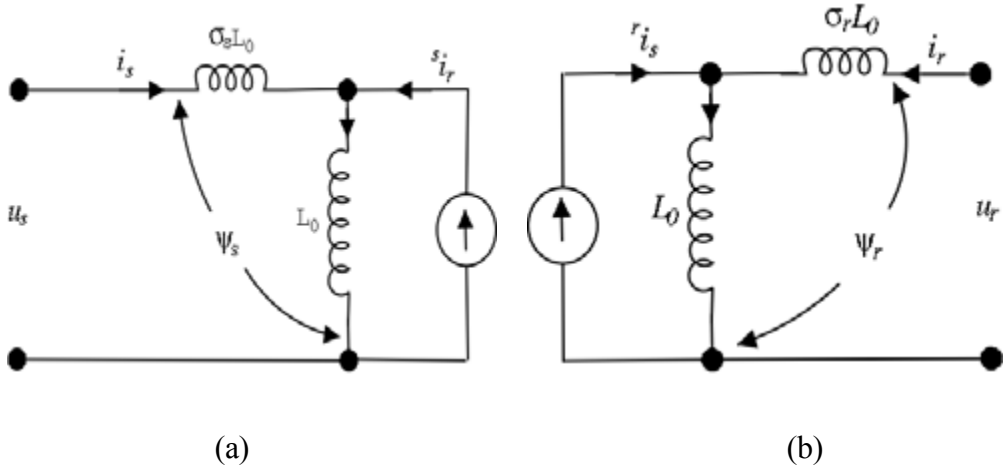


**Figure 5.2. Equivalent circuit diagrams of a DFIM: (a) for rotor-side control and (b) for stator-side control**

## 5.4 Super-Synchronous Generating Mode

Simplified equivalent circuits of a DFIM controlled from the rotor side and the stator side are given in Figure 5.2. In Figure 5.2a, it is assumed that the rotor currents can be injected at any desired phase, frequency, or magnitude. Therefore, the rotor circuit can be represented by a controllable current source. The equivalent circuit is drawn in the stator reference frame. Hence, the rotor current is represented as $i_r^s$. Similarly, when the control is exerted from the stator side, the equivalent circuit can be drawn as in Figure 5.2b. In the latter, the stator circuit is represented as a controllable current source. The steady-state phasor diagram for the super-synchronous generating mode in stator reference frame is given in Figure 5.3. In this diagram, counterclockwise direction of rotation is assumed as the positive direction. Neglecting the stator resistance, it may be assumed that the stator flux $\psi_s$ has two components: the stator leakage component and the magnetizing component (Figure 5.2a). The stator current alone causes the former, whereas both the stator and rotor currents cause the latter. An equivalent current $i_{ms}$ can be defined in the stator reference frame, which is responsible for the stator flux. This is termed the stator flux magnetizing current. The direction of $\psi_s$ (which is in phase with $i_{ms}$) is defined as the d-axis, and the direction of the stator voltage, which

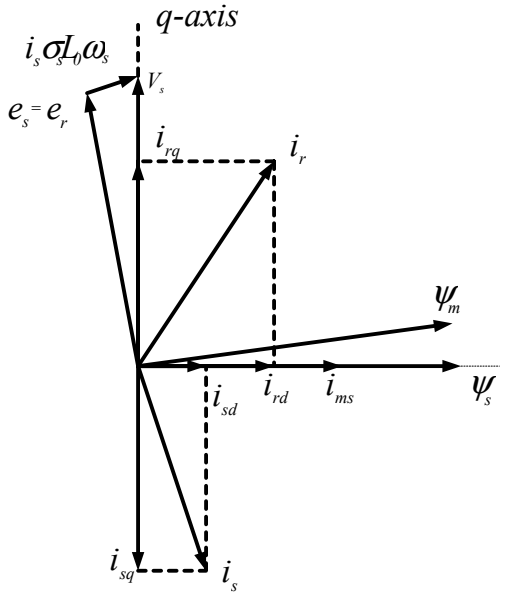


**Figure 5.3. Steady-state phasor diagram (stator reference frame) of a DFIM for the super-synchronous generating mode**

is in quadrature with $\psi_s$, is termed the q-axis. It is possible to resolve $i_s$ and $i_r^s$ along and perpendicular to $i_{ms}$. The components of the currents along the d-axis are represented with subscript 'd,' and those along the q-axis with subscript 'q.' The mathematical relations between the currents in this stator flux reference and the expression for the torque are given below.

$$i_{sq} = -(n_r / n_s) \times i_{rq} \qquad \text{(Equation 5.1)}$$

$$i_{ms} = (n_r / n_s) i_{rd} + i_{sd} \qquad \text{(Equation 5.2)}$$

$$T_q = \frac{3}{2}\frac{P}{2} i_{ms} i_{rq} \frac{L_0}{1+\sigma_s} \qquad \text{(Equation 5.3)}$$

From the above equations, it may be seen that the magnetizing current of the machine $i_{ms}$ is a summation of the d-axis components of the stator and the rotor currents. Also, the q-axis components of both sides are simply related by their turn ratio and are of opposite direction. The same relationship can be explained with the phasor diagram (Figure 5.3). The torque of the machine is a product of magnetizing component and q-component of the rotor current. Hence, torque can be controlled either by controlling flux component, the torque component, or by controlling both simultaneously.

## 5.5 Proposed Power Converter Configuration and Control Strategy

The proposed wind generator system Figure 5.4 has both the stator and the rotor side connected to the grid through two power stages in each side. By employing two half-controlled converters in the machine end, both the stator and rotor powers are controlled. In contrast, the front end of both sides are connected to the utility with a single full-bridge converter. Thus, the total power of the machine can be shared arbitrarily between the stator and the rotor of the machine. Because the machine is being controlled from both sides, the frequency and voltage of both sides of the machine can be varied at will. Hence, by choosing the frequencies of the stator- and the rotor-side that are of opposite sign and setting their individual absolute frequencies at less than the shaft frequency, the machine can always be made to

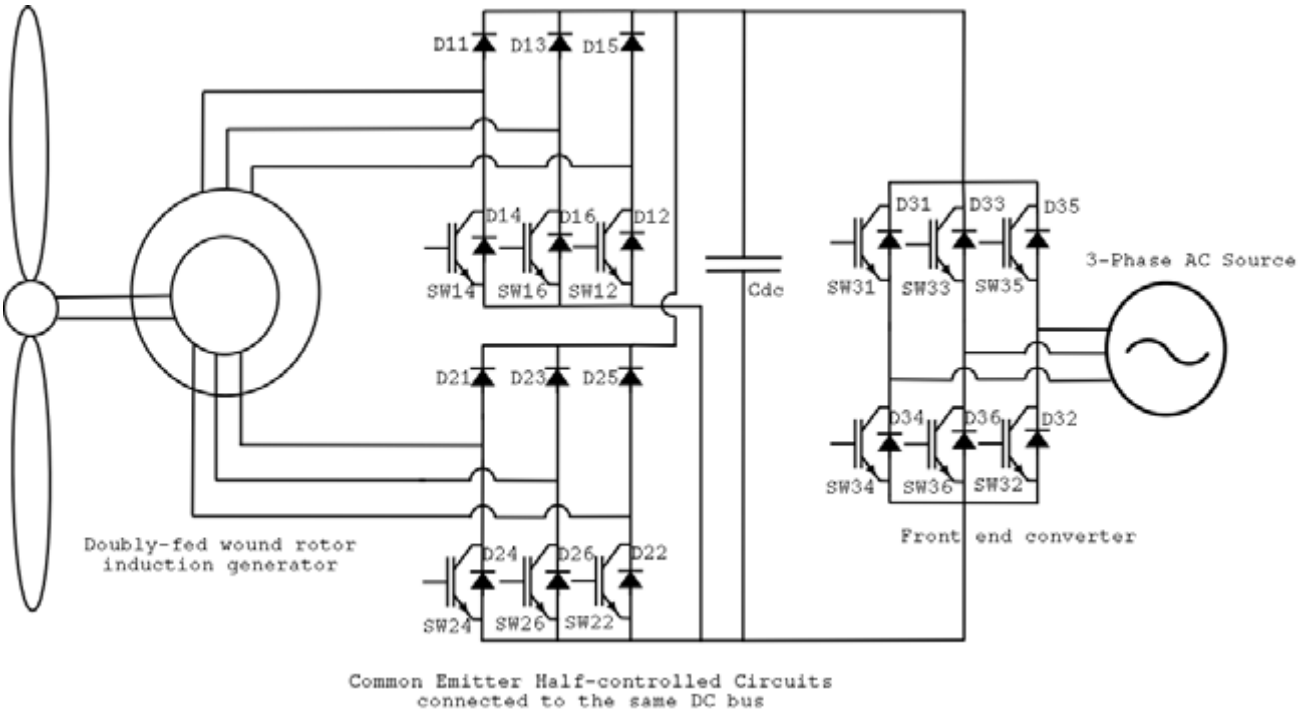


**Figure 5.4. Proposed configuration for double converter-fed wound-rotor induction machine with a common FEC (lower)**

operate at super-synchronous generating mode. For example, at any given frequency of the shaft ($f_{shaft}$), by choosing the stator frequency of the machine anything less than $f_{shaft}$, ($f_s$) and by maintaining the rotor frequency as $f_r = f_s - f_{shaft}$, the machine may be made to operate in super-synchronous generating mode. In this operating mode, as stated earlier, the power is extracted from both the stator and the rotor winding of the machine [8]. If the stator and the rotor frequencies are varied in the manner explained above, power will be generated throughout the speed range from both the stator and the rotor. The converters connected to the machine windings will always function as rectifiers. The control of a doubly fed induction generator can be realized by using two half-controlled rectifiers. Because the system is connected at the front end with a fully controlled bridge converter, unity power factor interfacing of the system is also ensured. However, a fully controlled bridge power converter at the front end handles all the power coming out of the machine, which appears to be a disadvantage of this topology.

An earlier paper investigated the potential of the half-control circuits [11]. It was shown that the half-controlled boost rectifier circuits along with conventional control algorithms generate low-order, even harmonics in both the AC-side current waveforms and DC bus voltage, which is not acceptable for many applications. The distortion in the current and voltage waveforms can be reduced considerably if the half-controlled converters are made to operate with current commands within a certain band of lagging power factor (typically 15 to 30 degree lagging current). The lagging power factor angles are a function of line-side inductance and the load current. However, when the generator is required to produce unity or leading power factor currents, the THD of the current waveforms become distorted.

In our proposed doubly fed wound rotor induction generator system, the excitation current, as well as the active component of the currents, will pass through the half-controlled converters and the corresponding machine windings. Therefore, the machine will encounter leading current waveforms. The stator-side terminal voltage $V_s$ will lag behind the stator-induced voltage $e_s$ (Figure 5.3) so that the machine will operate as a generator. If $i_{sd}$ is made zero, then the stator current will be 180° out of phase with the stator terminal voltage. Hence, it can be inferred that the stator current will be lagging with respect to stator-induced voltage $e_s$, and the lagging angle is dependent on the leakage inductance and the stator current. If load current is varied, then the stator current angle will also vary proportionately with respect to the stator-induced voltage. Similarly, if excitation is partially provided through the stator winding (i.e., for any positive value of) $i_{sd}$, the phase angle between $e_s$ and $i_s$ will be reduced, and the power factor will be approaching unity power factor. Thus, beyond a certain value of $i_{sd}$, the current will start leading the induced voltage.

Similar operation may be explained for the rotor side (Figure 5.2b), and a phasor diagram similar to Figure 5.3 except based in the rotor reference frame. To operate the stator and the rotor side at reduced leading power factor or in the lagging power-factor operating mode, the excitation current through the individual stator and rotor side should be much lower than the torque component of the current. The best means to achieve this result is to distribute the flux equally between the stator and the rotor windings. In such case, each individual half-controlled converter will handle only 50% of the excitation current. On the other hand, both converters will carry the rated active component of the current. Thus, each converter will carry 1 per unit (pu) active component of current and 0.5 pu reactive component current. With such an arrangement, power factor in each converter can be controlled to a certain extent.

For smaller or zero load, the flux may be reduced proportional to the torque demand. Thus, by controlling the field current as a function of load, the phase currents through both the stator and the rotor windings can be achieved with less distortion.

## 5.6 Comparison of the Proposed Converter System with the Conventional Converter System When Used as Machine Side Converters

By controlling the machine with half-controlled converters installed in both the stator and the rotor sides, the total KVA rating of the combined machine-side converter can be reduced compared to the converter employed for rotor-side only control of the machine. In the later case, the converter has to supply the full excitation current, as well as the active torque component of the current through the rotor winding. If one assumes that both the rated magnetizing current and the torque component of currents are same (i.e., 1 pu each) and are orthogonal to each other, the total current rating of the rotor-side converter, as well as the current rating of the rotor winding, goes up to 1.414 pu ($\sqrt{(1^2+1^2)}=1.414$). Hence, both the rotor-side converter and the rotor windings need to be over designed by 41.4% to accommodate the magnetizing current. However, by splitting up the excitation current equally (0.5 pu) between the stator and the rotor windings, the KVA rating of the power converter on each side will be reduced to only 1.118 pu ($\sqrt{(1^2+0.5^2)}=1.118$) of the rated power. Because each half-controlled circuit use only three switches instead of six switches compared its fully controlled counterpart, the KVA rating of the active switches combining both the stator- and the rotor-side machine-end power converter reduces to only 1.118 pu of the rated power of the machine. With the proposed power converter configuration, the KVA rating of the combined machine-side power converter is reduced by 30%. Using similar arguments, it may be shown that with the proposed configuration, the efficiency of the combined machine-side power converter will be higher than the conventional rotor-side control scheme.

## 5.7 Comparison of Copper Loss of the Proposed and Conventional Rotor-side Configurations

In a similar analysis, it can be shown that by reducing the burden on rotor winding, the total copper loss of the machine is expected to improve. Because at rated load both windings will carry 1.118 pu current and assuming that the resistances of both the stator and rotor windings are $R$ and the rated active power component of the current of the machine is $I_{base}$ - the effective copper loss of the proposed system will be: $2\times1.118^2\times I_{base}^2\times R=2.5\times I_{base}^2\times R$ . In contrast, for conventional rotor-side control, the rotor and the stator windings will carry unequal currents: 1.414 pu current for rotor side and 1.0 pu for stator side. The total copper loss of the machine for a conventional method will be $3I_{base}^2R$ ($(1^2+1.4141^2)\times I_{base}^2\times R=3\times I_{base}^2\times R$).

Therefore, it can be concluded that in the proposed control method, the total copper loss of the machine will improve by 16.67% ($\frac{(3-2.5)}{3}\times100=16.67\%$). However, since half controlled circuits drive the machine from both the stator and the rotor, the current waveforms are expected to have some amount of unwanted even harmonics. The latter will introduce some extra loss in the windings, as well as in the power converters. Hence, the gain achieved as a result of to the splitting of excitation currents may be offset to some extent by the losses caused by unwanted harmonics in the winding currents. A detailed

analysis and loss comparison between the conventional scheme and the proposed method will be taken up as future work. Again, in the conventional scheme, when the losses in the rotor windings are larger, the cooling of the machine will become difficult compared to the proposed method. It is important to note that by running the system always in super-synchronous generating mode and by employing two separate sets of power converter in both the stator and the rotor side, the flow of circulating currents between the stator- and the rotor-side converters is avoided.

From the above discussion, it may be concluded at this point that by employing double-side half-controlled converters, the KVA rating of the machine-side power converter can be improved, and a wide operating range may be achieved; the possibility of temperature rise in the rotor may be reduced. The possibility of circulating currents is avoided and unity power factor interfacing through the FEC can be ensured. In addition, the half-controlled power converters are much simpler, the shoot-through failure is eliminated, isolated gate drive is not required, and the combined switch counts are limited to six. Therefore, control and PWM generation for both machine-side converters can be achieved by a single DSP. Again, for a given shaft speed, a combination of the stator and the rotor frequency can be chosen at will, which is clearly an advantage for operation with rotary transformer and for the position estimation algorithm of the machine.

## 5.8 Starting Method

The power flow in the half-controlled circuits is unidirectional (Figure 5.4). In this case, the power cannot flow from the DC bus to the machine. Because, both the stator and the rotor windings are connected to the DC bus with similar half-controlled configurations, during starting excitation cannot be provided to the machine from either side. Hence, alternative arrangements are required. Two such alternative configurations are presented in Figure 5.5 and Figure 5.6.

### *5.8.1 Starting Method I (Extra Switch Starting)*

A modified circuit topology of Figure 5.4 is proposed in Figure 5.5, where an extra IGBT (Sw_st) switch in series with a diode (D_st) is added between the phase A of the stator winding and the DC bus.

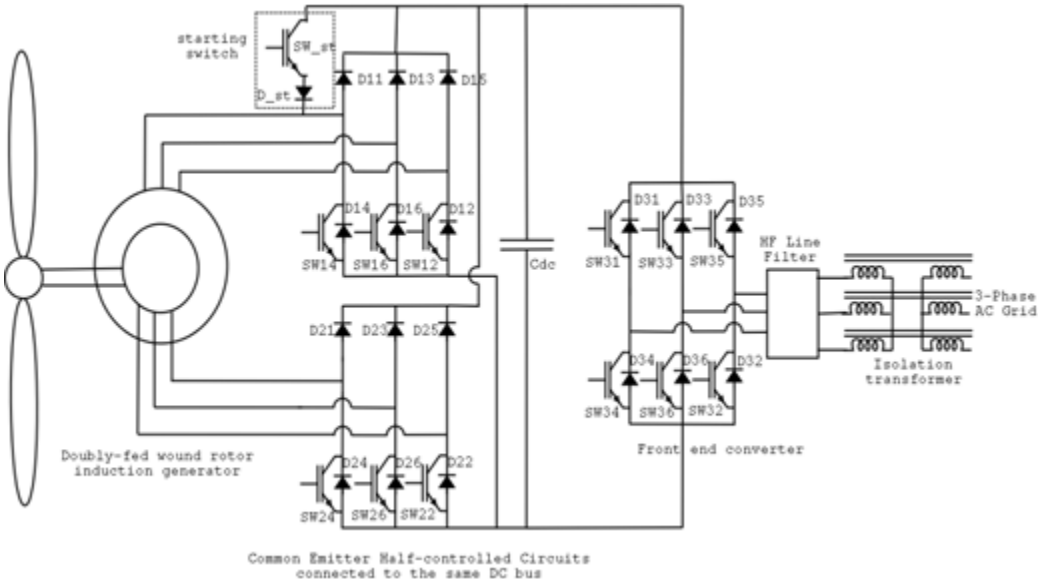


**Figure 5.5. Modified converter configuration with starting excitation capability for a DFIM; with an extra semiconductor starting switch**

This extra switch is used for providing starting excitation to the machine. With this extra switch, DC excitation can be provided to the stator though phase A and either one of phase B or phase C. In this example, phase B is chosen for that purpose. Thus, controlling Sw_st and Sw16 simultaneously, a DC current flows from the DC bus through phase A and phase B, while phase C remains open circuited. This DC excitation will generate a DC flux in the stator magnetic circuit.

The rotor is assumed to be rotating freely by wind torque; therefore the rotating phases in the rotor will pass through this DC flux, and voltages will be induced in the rotor windings. At this time, power can be extracted from the rotor winding to the DC bus by actively controlling the rotor-side half-controlled converter. After a few cycles of such operation, when sufficient current builds up through the rotor winding, Sw-st will be switched off. A regular half-controlled converter for the stator side will be activated, and the control will be shifted from starting mode to normal running mode. This algorithm is verified through SABER simulation; the simulation result for the same case is presented in the subsequent sections of this paper. The simulation verified that the extra starting switch need not be of the same rated current as the machine. A current rating of 15-20% of the rated current for the starting

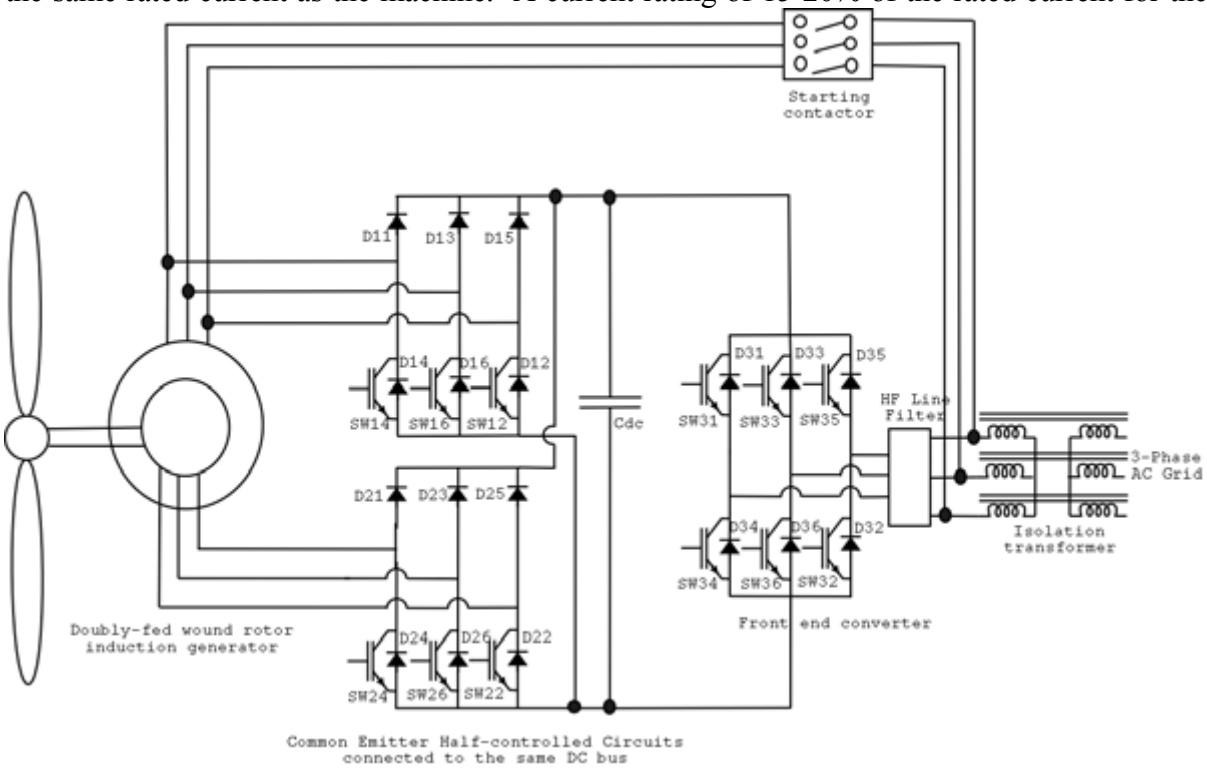


**Figure 5.6. Modified converter configuration with starting excitation capability for a DFIM with a contactor starting configuration**

switch will be enough to achieve successful starting of the machine. Thus, it may be inferred that adding an extra switch for starting purposes does not add much extra cost to the system. However, after adding the starting switch, the impossibility of shoot-through in phase A of the stator-side half-controlled converter will be lost.

### *5.8.2 Starting Method II (Contactor Starting)*

In another alternative starting method, the special starting switch Sw_st and D_st are not required. Instead a three-phase contactor (Figure 5.6) can be employed between the stator winding and the grid.

Initially, the stator of the machine will be connected to the grid through the contactor, and the complete excitation current will be provided to the machine from the stator side. When sufficient voltage builds up in the rotor windings, the contactor will be switched OFF and the stator winding will be controlled by the half-controlled converter connected to the stator side of the machine. The control will be shifted to its regular running mode. In such a starting method, an extra contactor will be required. This method is also verified through SABER simulations. The advantage of the contactor starting method is that the shoot-through safe topology of the half-controlled circuit is retained.

## 5.9 Control Scheme

A detailed control-block diagram of the proposed configuration is given in Figure 5.7. The proposed control algorithm employs a conventional PI controller for its outer speed loop. The speed-loop controller generates torque reference as its output. To facilitate the controller, the relation between the stator and rotor q-axis component of current, the expression of torque, and expression of magnetizing currents given in equations (5.1) to (5.3) can be referenced. From these equations, it is clear that the quadrature axis rotor current $i_{rq}$ generates the machine torque. The stator q-axis current $i_{sq}$ is automatically developed as the reflection of $i_{rq}$ (Figure 5.3). Thus, in the control-block diagram, it is shown that the torque reference ($T_q^*$) is directly proportional to $i_{rq}^*$. The stator component q-axis current reference is generated in Figure 5.4. The magnetizing current $i_{ms}$ can be supplied from both of the half-controlled converters by arbitrary current sharing, as given by Equation 5.3. However, in the proposed method, both converters always share the magnetizing current equally. In the block diagram, it is shown that the total magnetizing current is multiplied with a gain of 0.5 to generate the individual magnetizing reference currents ($i_{sd}^*, i_{rd}^*$) for the two half-controlled converters. Interestingly, the total magnetizing flux current reference $i_{ms}^*$ is not constant for the proposed method. Thus, the iron losses using this type of controller will be reduced by the square of the magnetizing current, in addition to the reduced copper loss mentioned previously. This current is a function of the required torque $T_q^*$ of the machine (Figure 5.2). Equation 5.3 shows that the torque is a function of $i_{ms}$ and $i_{rq}$, so that the magnetizing current is varied as a function of load. This scheme also causes reduction in the total harmonic distortion (THD) in the stator and the rotor winding currents for all load conditions.

Because half-controlled circuits drive the machine and because the excitation current capability is a function of load, current is varied with load in this proposed method of excitation. Once the d-axis and q-axis current references for both the stator and the rotor windings are found, a dq to abc transformation is applied so that the three-phase reference currents for stator and rotor currents are generated. A hysteresis controller is employed in each side for controlling the stator and rotor currents. The speed of the machine is sensed through a shaft sensor and by integrating it, the position of the rotor $\varepsilon$ is found. In the proposed control scheme, the stator and rotor windings are intended to share the power equally. To achieve this result, the stator and rotor frequencies are always maintained at half of the shaft frequency, and their phase sequence is opposite to each other. The stator frequency sequence is maintained in the same direction as the shaft, and the rotor frequency is of opposite sign. By passing the speed signal through a gain block of 0.5 and then integrating, the position of the stator flux $\mu$ is obtained. These $\varepsilon$ and $\mu$ values are required for dq to abc transformation (Figure 5.7).

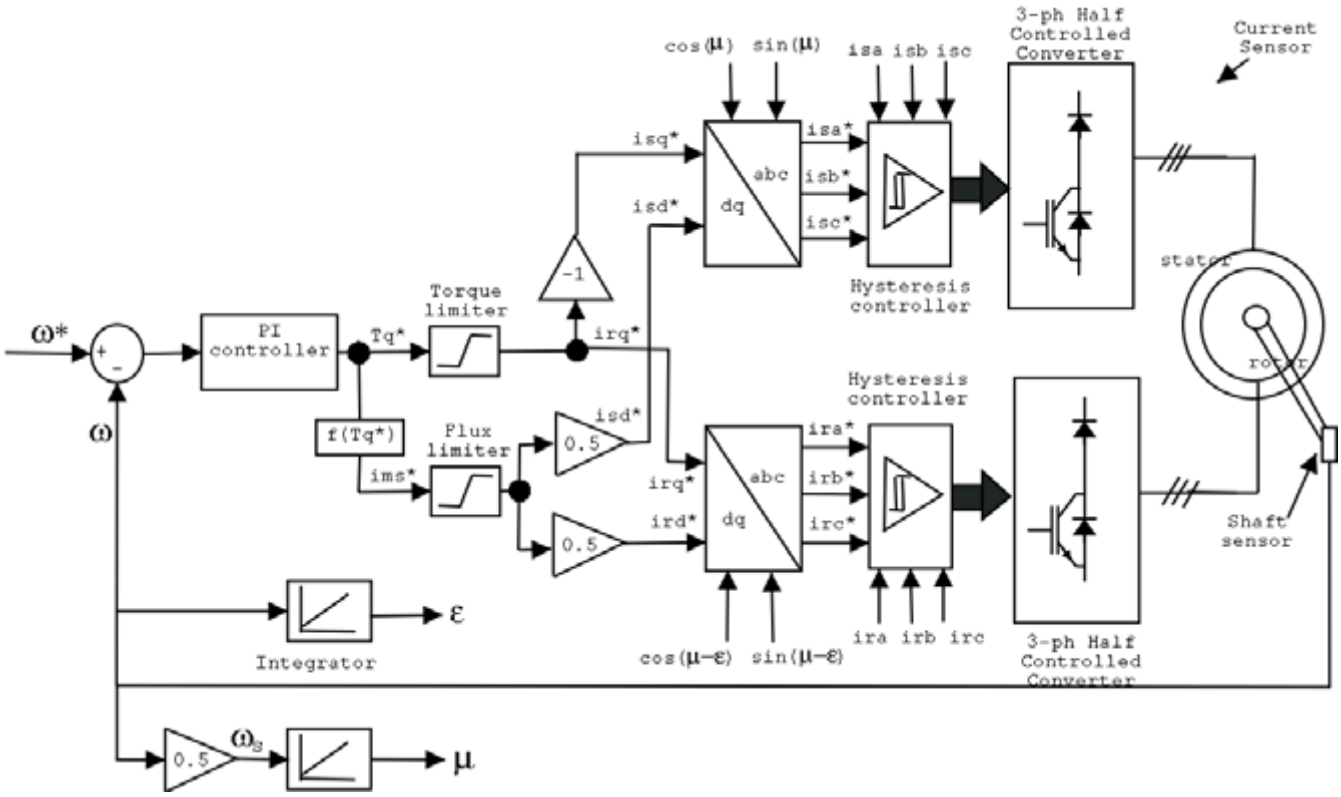


**Figure 5.7. Block diagram of the proposed double-sided control algorithm**

## 5.10 Simulation Results and Discussion

The proposed control scheme with the half-controlled power converters was studied for future implementation on a 30-kW DFIM using SABER. The simulation results with full excitation current and 25% rated load are shown in Figure 5.8. The results at 25% load with field excitation as the function of load are shown in Figure 5.9. The current waveforms are markedly improved in the case of variable field excitation. In contrast, the waveforms with rated excitation and at lower load are highly distorted, and the effect of the distortion is visible in the torque waveform. Hence, the proposal to vary the field excitation as function of load is validated. Steady-state simulation results at two typical operating speeds (30 Hz and 90 Hz of shaft speed), and the FFT of the current waveforms are given in figures 5.10 and 5.11. Both the stator and rotor current waveforms are of the same frequency, and their magnitude differs slightly because of non-unity turn ratio between them. Also, the current waveforms are quite smooth, and the corresponding FFT shows that the currents contain typical even-order harmonics, but their magnitude is not appreciably high.

The simulation results of starting performance with both contactor-start method and the switch-start method are given in figures 5.12 and 5.13, respectively. In the contactor-start method (Figure 5.12), it may be seen that initially the stator was drawing the excitation current from the grid, and the rotor voltages were induced as a result of the stator excitation. When the rotor currents build up sufficiently, the contactor is switched OFF and the stator-side half-controlled converter takes over the control. Similarly, for the switch-start method (Fig. 5.13), the DC excitation is initially provided through phase A and phase B. Because of this excitation, rotor voltage builds up, and when the rotor starts generating,

the DC excitation is taken off and the half-controlled converter is switched ON with its regular control scheme. Thus, it is demonstrated that the machine can successfully start with both the method without incurring much extra cost to the system.

## 5.11 Conclusion

A new double-side control algorithm for a DFIM employing two half-controlled three-phase converters is explored in this chapter. With the proposed control algorithm, the machine is capable of operating for a wider range of speed and the total power of the machine is shared between the stator and the rotor-side converter equally. The system is capable of operating at high power range without the difficulties of paralleling the converters. In addition, by using the half-controlled configuration, system cost is also reduced. Splitting the excitation current equally between the stator and rotor windings and making excitation current a function of the load current markedly improves the phase currents through the stator and the rotor, as well as the voltage across the DC bus. In the proposed configuration, the absolute values of the stator and the rotor frequencies are always the same, and their sum is equal to the rotor-shaft frequency. Thus, iron losses are minimized, and the sharing of load between the stator and the rotor is always equal in our proposed algorithm, which obviously also reduces the losses in the winding and helps improve the machine efficiency.

The splitting of excitation current equally between the stator and the rotor windings further reduces the KVA rating of the machine-side converters. Such an arrangement is expected to reduce the overall machine and converter loss. In the proposed configuration, the power converters are shoot-through safe, and no dead-time delay is necessary, which is a distinct advantage for a system with high switching

**Table 5.1. Machine Parameters**

| *Parameter* | *Measurement* |
|---|---|
| Power | 30 kW |
| Voltage (*Vs*) | 480 V |
| Frequency (*fs*) | 60 Hz |
| Poles (*P*) | 6 |
| Inertia (*J*) | 5 kg/m$^2$ |
| Frictional coefficient (*B*) | 0.0519247 |
| Magnetizing inductance (Lm) | 24.1 mHz |
| Stator leakage inductance ($\sigma_s L_0$) | 1.326 mHz |
| Rotor leakage inductance ($\sigma_r L_0$) | 1.2467 mHz |
| Stator resistance (*Rs*) | 0.107 ohm |
| Rotor resistance (*Rr*) | 0.062 ohm |
| Turns ratio ($n_s / n_r$) | 1.21 |

frequency. Also, by using a similar common-emitter half-controlled configuration in both the stator and rotor side, the converters do not need an isolated power supply for their gate drives. Because both the stator- and the rotor-side frequency can be controlled at will, the zero frequency condition can be avoided so that the proposed algorithm is suitable for sensorless operation and supports the operation of rotary transformer over the entire range of operating speed. Simulation results have been shown to verify the proposed control method. The primary disadvantage of the proposed method is that the motoring mode of operation is sacrificed. However, for wind energy applications, that is not a serious problem because wind itself can be used for accelerating the machine.

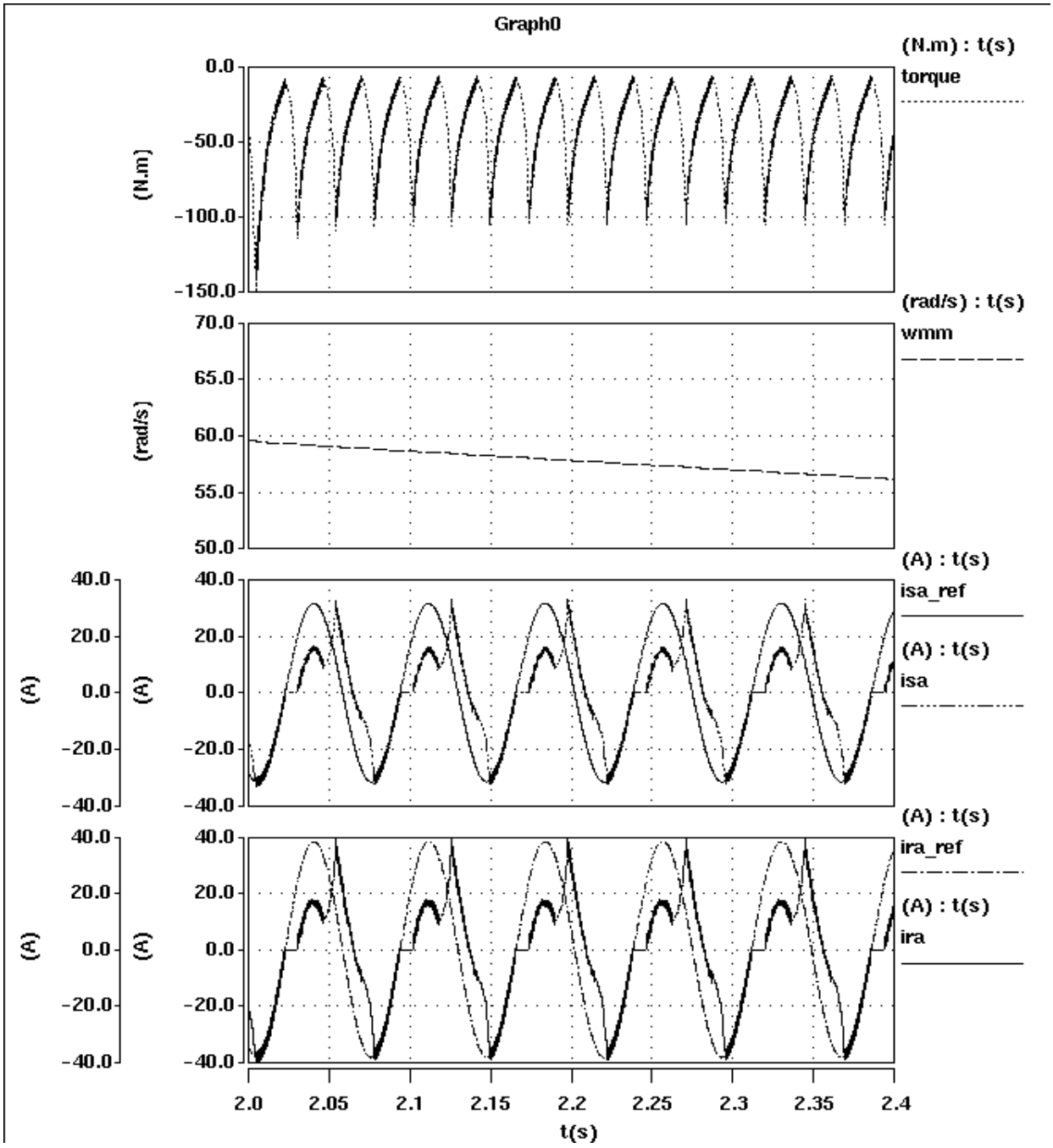


**Figure 5.8. Simulation results at 25% load with full-field excitation**

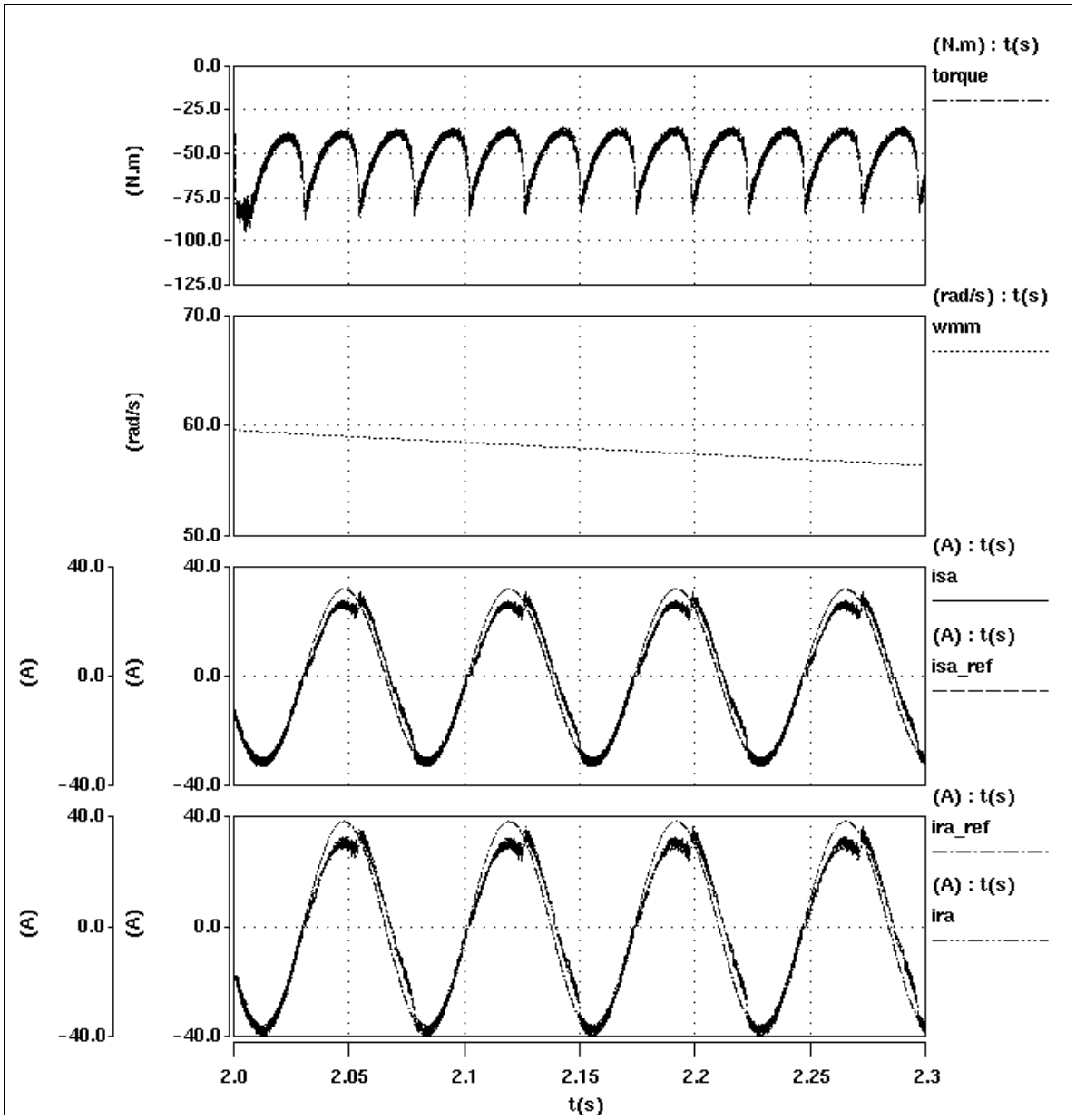


**Figure 5.9. Simulation results at 25% load with field excitation as a function of load**

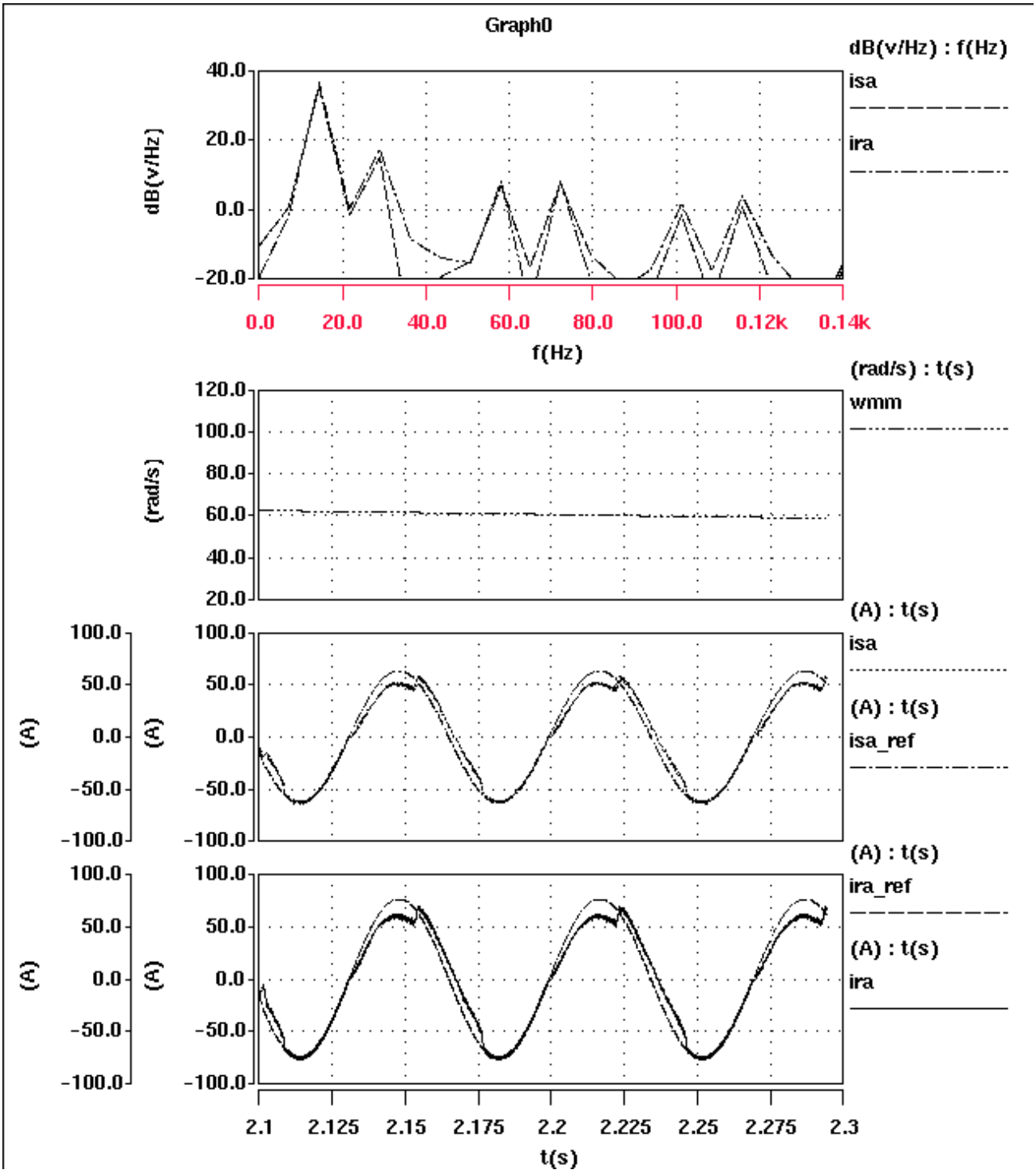


**Figure 5.10. Typical simulation results of a 30kW DFIM; with rotor shaft frequency at 30Hz**

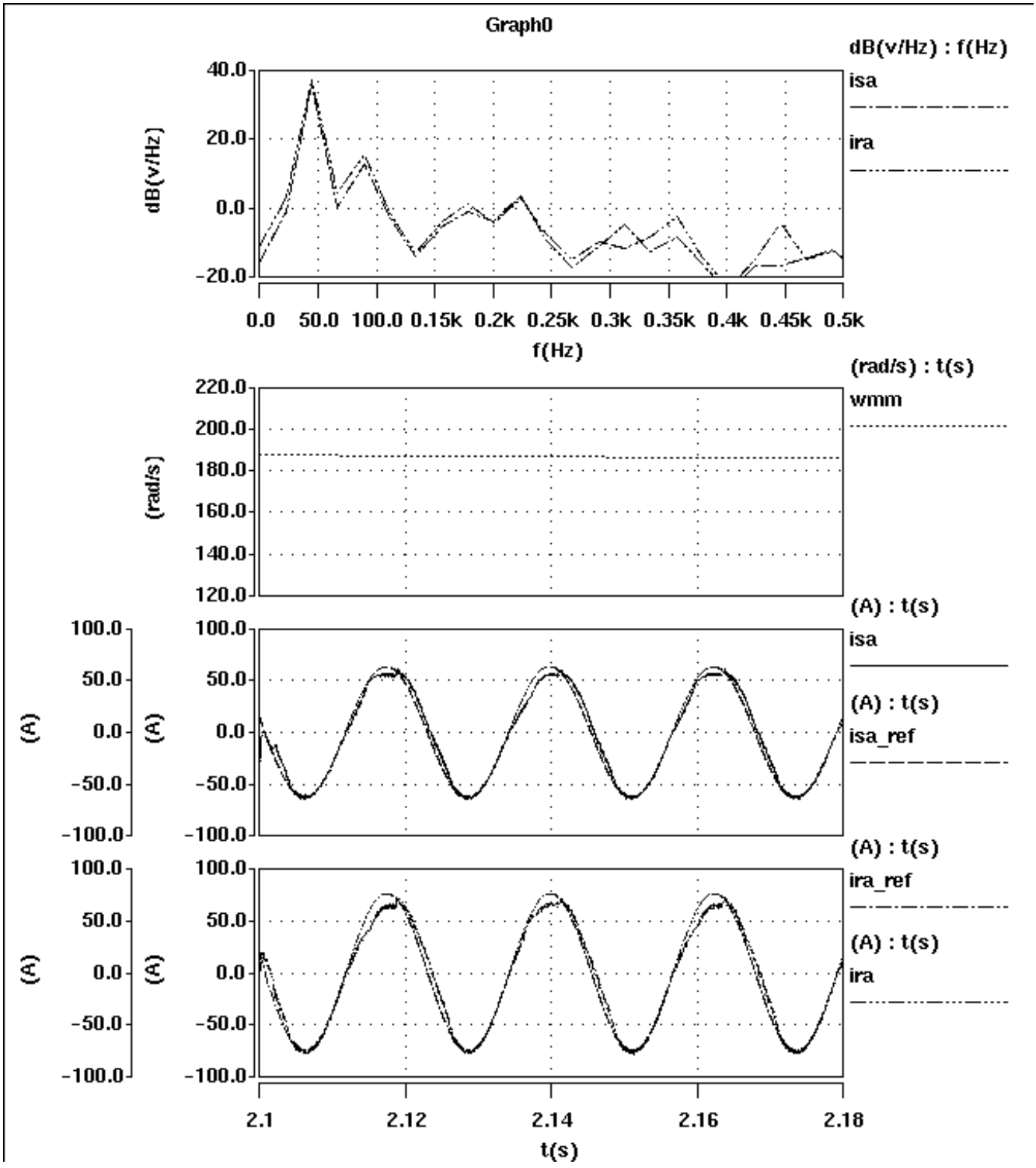


**Figure 5.11. Typical simulation results of a 30-kW DFIM; with rotor shaft frequency at 90 Hz**

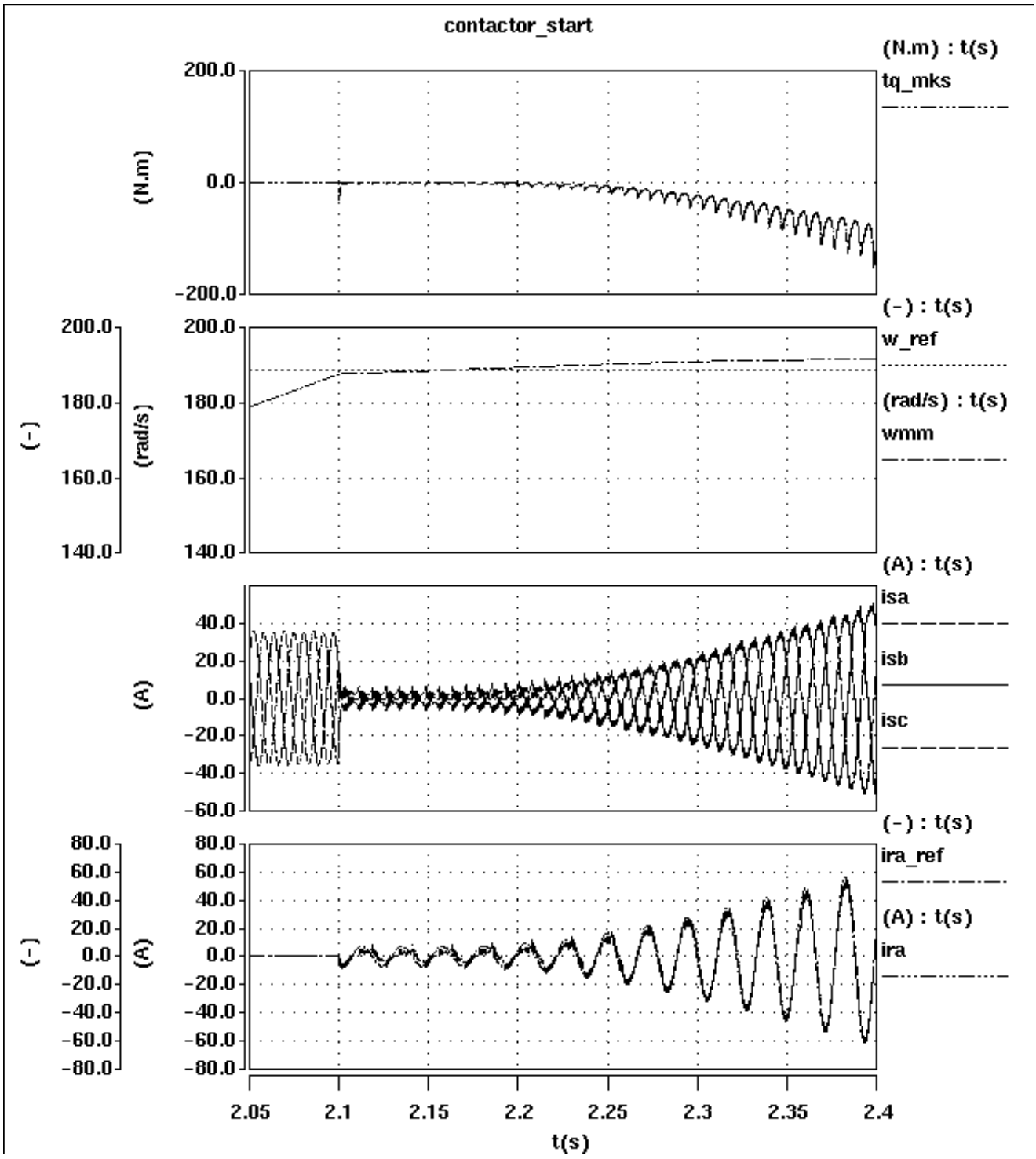


**Figure 5.12. Simulation results during starting of a 30-kW DFIM; with contactor start method**

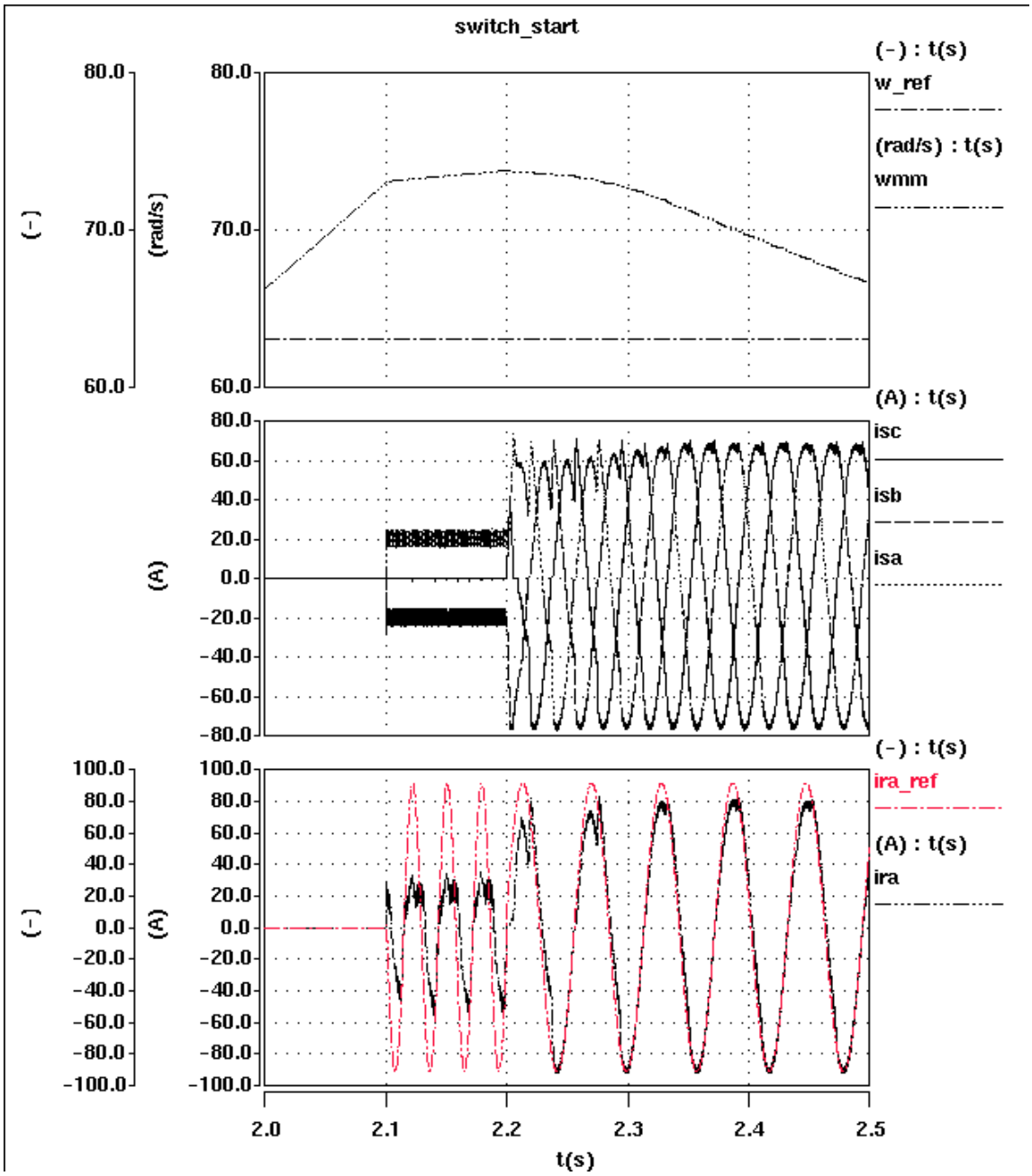


**Figure 5.13. Simulation results during starting of a 30-kW DFIM; with extra switching start method**

# Chapter 6: Rotating Transformer Design

## 6.1 Overview: Analysis and Control Issues

In this chapter, we propose a new rotary transformer concept that replaces the slip ring and carbon brushes of a DFIM. The operating principle, design and mounting of a rotary transformer are explained. We compare the two-phase with the three-phase rotary transformer, and we show that the former is superior to the latter in terms of power density of the transformer. Finally, we present a design of a two-phase rotary transformer. The performance of the designed transformer is verified with a MATLAB/SIMULINK model, and the simulation results are presented. The schematic of a 30-kW wound rotor induction machine with detailed design dimension is also included in this chapter.

## 6.2 Introduction

Traditionally, a wound-rotor induction machine is used with slip ring and carbon brush in its rotor circuit. Because of this feature, it is called a slip-ring induction motor. However, the use of the slip ring and carbon brush is a potential because the maintenance schedule for replacing the carbon brushes introduces extra running cost. In addition, carbon brushes and slip rings sometimes introduce faults that could interrupt the power generation and cause an unscheduled breakdown. Thus, to increase the reliability of the power supply, it is advantageous to avoid these carbon brush and slip rings. In particular, for wind turbines that are installed remotely, it is advisable to have a rugged system with minimal maintenance requirement. For such a system, we propose a new solution with rotary transformer.

In a rotary transformer, the primary winding rotates along with the shaft and rotor of the machine. The rotor windings are physically connected to this winding. Thus, the rotor current of the machine completes its current path through the primary of the transformer winding. On the other hand, the secondary winding of the rotary transformer is stationary; thus, it can be directly connected to a power converter or any other suitable external load without the need of a slip ring and carbon brush. The principle of a rotary transformer is almost the same as that of a conventional transformer except that in the former, an air gap exists between the stationary and the rotating windings. This air-gap will introduce an additional leakage inductance in the rotating transformer, which will increase its size compared to a no-rotating transformer. However, by introducing this rotary transformer into a wound-rotor induction machine, the carbon brush and slip ring can be eliminated, and the system can be made much more rugged.

In this chapter, we explain the operating principle and design of a rotary transformer. A comparative study between the two-phase and three-phase rotary transformer is made. We also show that the design of a two-phase rotary transformer can reduce the volume of the system. A detailed design of a two-phase rotary transformer is then outlined. With the designed values, we created a model of the rotary transformer and simulated it in MATLAB. We include a detailed dimension of a 30-kW wound rotor-induction machine supplied by the WEG manufacturing company in Brazil.

## 6.3 Design of Rotary Transformer

Typically, a rotary transformer (Figure 6.1) mounted on the shaft of a wound rotor induction

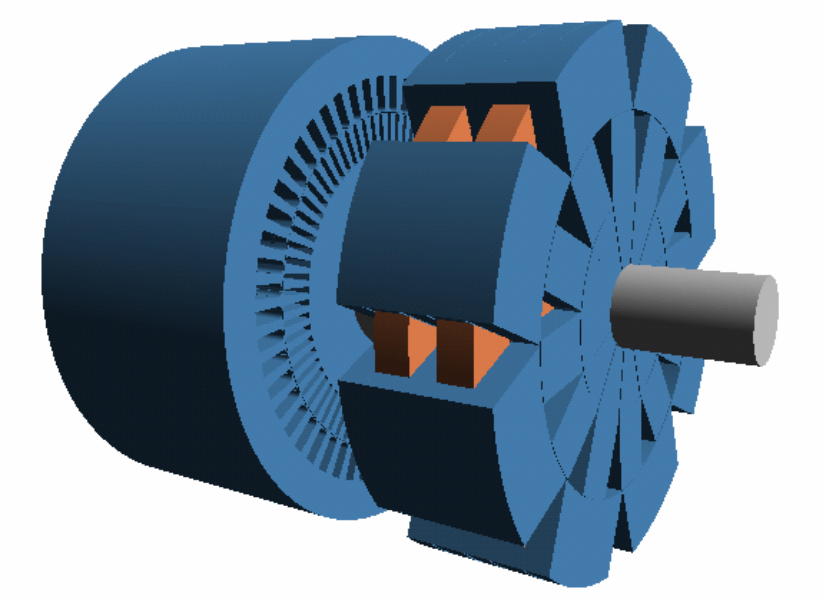

**Figure 6.1. Rotary transformer and induction generator**

machine is designed so that its secondary is stationary and its primary rotates with the rotor. Both primary and secondary are wound circumferentially around the shaft centerline so no speed voltages are introduced. Instead of using three primary windings, each connected to the corresponding phase of the wound rotor, and having the three secondary windings connected to the converter, only two windings on each side were used. A three-phase to two-phase transformation was employed. This technique causes the magnetomotive forces (MMF) of the two windings to be shifted by 60° and have the same amplitude. The angle of 60° is desirable because the MMF in the vertical middle section of the transformer core is proportional to the difference of the MMF of the two windings. If it is assumed that these MMFs are sinusoidal with the same amplitude, then their difference would have the same amplitude. Therefore, the width of the middle section of the core can be the same as the width of the outer ones. The operation of the rotary transformer has been evaluated using the MATLAB/Simulink model based on solution of the nonlinear magnetic circuit.

## 6.4 Core Assembly

The core assembly is a very important issue because the core has to be made of thin laminations that are punched and assembled following the flux path in the transformer. Rotary transformers are commonly used for transferring low-power high-frequency signals, in which case compact ferrite cores are used. The laminated core in the case of the low-frequency higher-power rotary transformer is not compact, so its configuration and assembly is a specific problem. The simplest way is to punch the laminations in the form shown in Figure 6.2, where the transformer is sliced axially. The laminations are then assembled radially. The disadvantage of this approach is the diameter difference between the outer and the inner laminations when assembled while their thickness is constant. This means that the inner diameter determines the maximum number of laminations that can be used. Therefore, laminations have to be assembled in packages with an opened gap between them (Figure 6.3). This greatly simplifies the construction of the core, which decreases the cost of the transformer. Pulling the wires through the gaps can now easily solve the problem of winding connections within the motor and the converter. However, this configuration increases the leakage reactance of the transformer and reduces the amount of iron in the core, which results in increased size of the transformer. Also, magnetizing reactance decreases, which results in higher values of the magnetizing current.

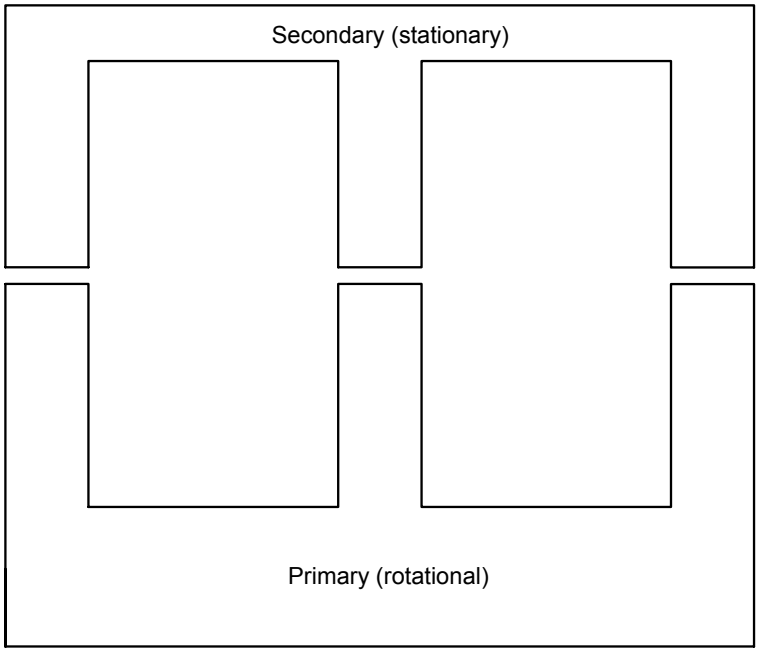


**Figure 6.2. Shape of the core laminations**

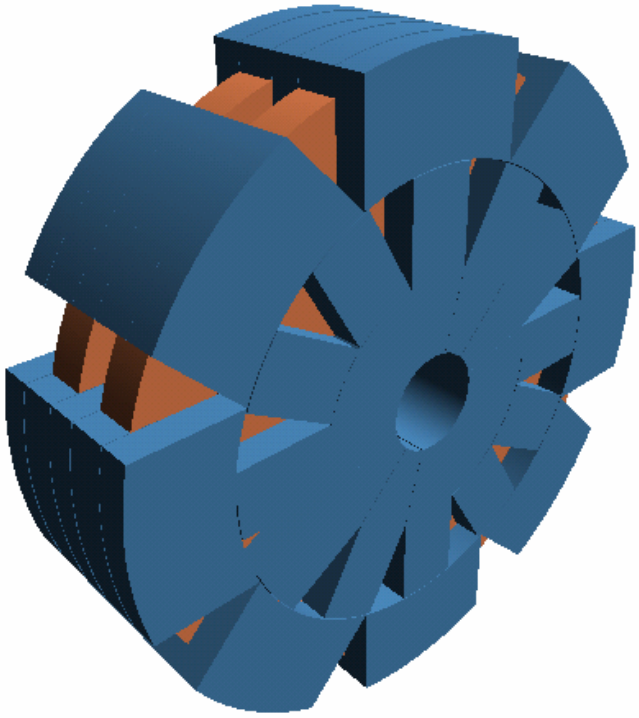

**Figure 6.3. Rotary transformer with core and winding assembly**

## 6.5 Rotary Transformer Model

The rotary transformer model is based on a solution of the equivalent magnetic circuit shown in Figure 6.4. The stated variables used in the model are flux linkages of the four windings of the transformer. For the circuit in Figure 6.4, the following set of equations can be written as follows:

$$v_1 = i_1 R_1 + N_1 \frac{d\phi_1}{dt},\ \phi_1 = \phi_{l1} + \phi_{m1} \tag{6.1}$$

$$v_2 = i_2 R_2 + N_2 \frac{d\phi_2}{dt},\ \phi_2 = \phi_{l2} + \phi_{m1} \tag{6.2}$$

$$v_3 = i_3 R_1 + N_1 \frac{d\phi_3}{dt},\ \phi_3 = \phi_{l3} + \phi_{m2} \tag{6.3}$$

$$v_4 = i_4 R_2 + N_2 \frac{d\phi_4}{dt},\ \phi_4 = \phi_{l4} + \phi_{m2} \tag{6.4}$$

where $v_1$, $v_2$, $v_3$, $v_4$ are instantaneous voltages of the windings, $i_1$, $i_2$, $i_3$, $i_4$ are instantaneous currents, $R_1$, $R_2$ are resistances, and $N_1$, $N_2$ are numbers of turns of the primary and secondary windings. Flux linkages are denoted by $\phi$ and leakage fluxes by $\phi_l$. The flux linkages $\phi_{m1}$ and $\phi_{m2}$ represent main fluxes referred to the flux paths shown in Figure 6.4. Leakage flux $\phi_l$ can be written as follows:

$$N_1 i_1 = \phi_{l1} R_{l1} \tag{6.5}$$

$$N_2 i_2 = \phi_{l2} R_{l2} \tag{6.6}$$

$$N_1 i_3 = \phi_{l3} R_{l1} \tag{6.7}$$

$$N_2 i_4 = \phi_{l4} R_{l2} \tag{6.8}$$

where $R_{l1}$ and $R_{l2}$ are magnetic reluctances of the leakage paths of the primary and secondary windings. Using equations 6.1 to 6.8, the currents $i_1$, $i_2$, $i_3$ and $i_4$ can be expressed in terms of flux linkages:

$$i_1 = \frac{N_1\phi_1 - N_1\phi_{m1}}{N_1^2} R_{l1} \tag{6.9}$$

$$i_2 = \frac{N_2\phi_2 - N_2\phi_{m1}}{N_2^2} R_{l2} \tag{6.10}$$

$$i_3 = \frac{N_1\phi_3 - N_1\phi_{m2}}{N_1^2} R_{l1} \tag{6.11}$$

$$i_4 = \frac{N_2\phi_4 - N_2\phi_{m2}}{N_2^2} R_{l2} \tag{6.12}$$

For the two paths marked in Fig. 6.4 the set of equations in terms of MMFs can be written

$$N_1 i_1 + N_2 i_2 = \phi_{m1} R_{cg1} + (\phi_{m1} - \phi_{m2}) R_{cg3} \tag{6.13}$$

$$N_1 i_3 + N_2 i_4 = \phi_{m2} R_{cg2} + (\phi_{m2} - \phi_{m1}) R_{cg3} \tag{6.14}$$

where $R_{cg1}$, $R_{cg2}$ and $R_{cg3}$ are reluctances of the core and air gap for the three magnetic paths in the transformer. These reluctances are nonlinear functions of the main fluxes $\phi_{m1}$ and $\phi_{m2}$ and have to be calculated using look-up tables. If currents are expressed using (9) to (13), then from (13) and (14) the main fluxes can be expressed as

$$\phi_{m1} = \frac{(\phi_1 R_{l1} + \phi_2 R_{l2})(R_{cg2} + R_{l1} + R_{cg3} + R_{l2}) + (\phi_3 R_{l1} + \phi_4 R_{l2}) R_{cg3}}{(R_{cg1} + R_{l1} + R_{cg3} + R_{l2})(R_{cg2} + R_{l1} + R_{cg3} + R_{l2}) - R_{cg3}^2} \tag{6.15}$$

$$\phi_{m2} = \frac{(\phi_3 R_{l1} + \phi_4 R_{l2})(R_{cg1} + R_{l1} + R_{cg3} + R_{l2}) + (\phi_1 R_{l1} + \phi_2 R_{l2}) R_{cg3}}{(R_{cg1} + R_{l1} + R_{cg3} + R_{l2})(R_{cg2} + R_{l1} + R_{cg3} + R_{l2}) - R_{cg3}^2} \tag{6.16}$$

The MATLAB/Simulink model based on equations 6.1 to 6.16 is shown in Figure 6.7. For the purpose of the design, we assumed that the transformer primary winding is connected to two independent voltage sources with voltages that are phase-shifted by 60° (Figure 6.5). Normally, the transformer primary windings would be connected to each phase of the rotor winding of the DFIM. If one neglects the voltage drops on the machine's rotor impedance, the line-to-line voltages $v_{AB1}$ and $v_{CB1}$ applied to the transformer windings (Figure 6.6) would be phase shifted by 60°.

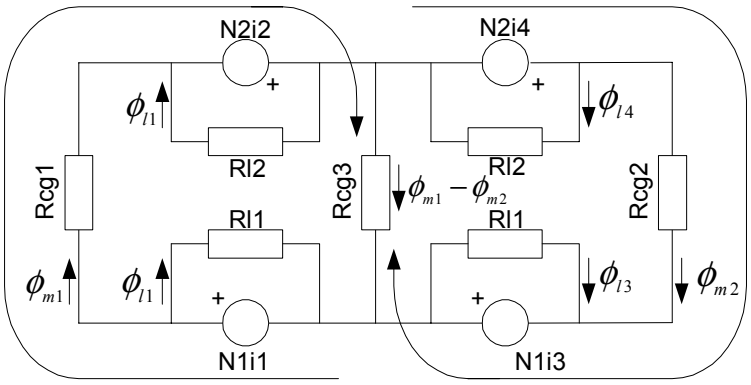


**Figure 6.4. Equivalent magnetic circuit**

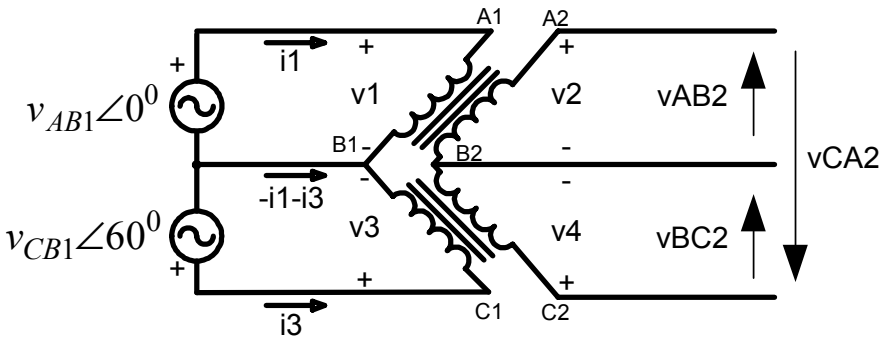


**Figure 6.5. Winding connections**

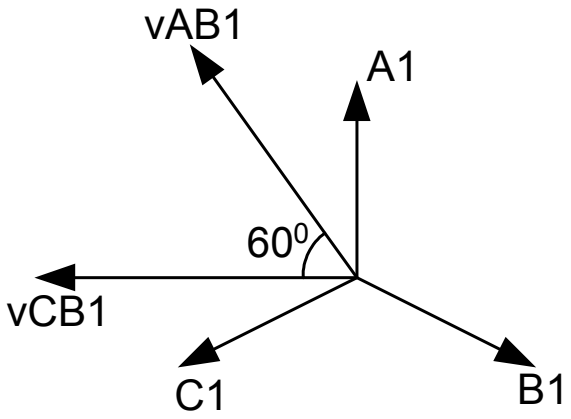


**Figure 6.6. Voltage vectors on the primary side**

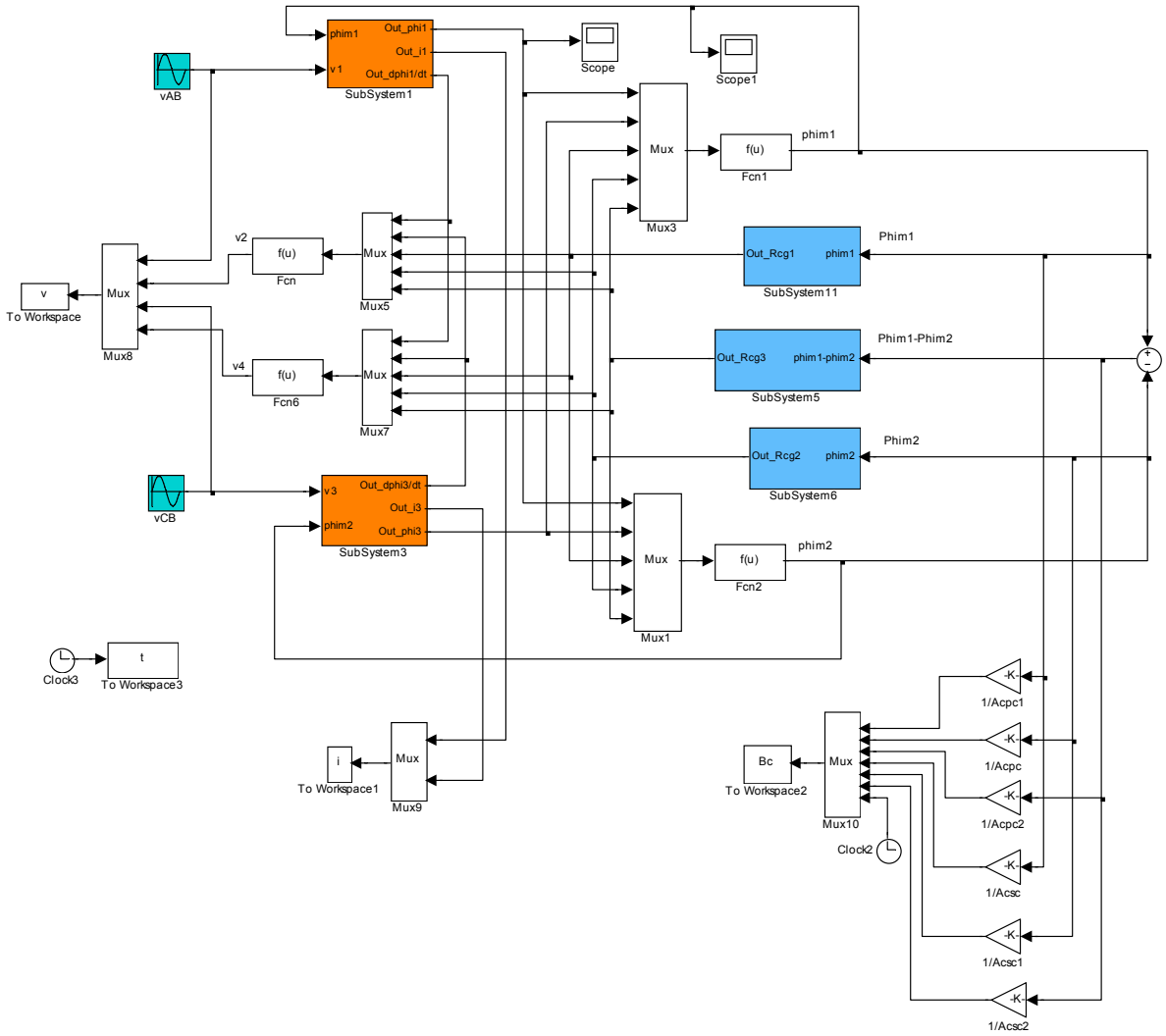


**Figure 6.7. MATLAB/Simulink model of the rotary transformer**

## 6.6 Comparison of Two-phase and Three-phase Rotary Transformer

The purpose of the two-phase transformer is to achieve smaller size and less weight in the transformer, compared to the three-phase version. The mass of the two-phase transformer relative to the mass of its three-phase counterpart can be determined with the help of some simple sizing equations assuming the same current and flux density loading for both transformers.

To determine apparent power, we assumed the following parameters. The current density $\Gamma$ and the core flux $\lambda$ in both transformers was the same. Both transformers were designed for the same apparent power rating $S$. The number identifying 2 was added to the subscript of all physical quantities related to the two-phase transformer, and identifying number 3 was added to all quantities related to the three-phase transformer. Then the following is true for apparent power:

$$\begin{aligned} S_2 &= 2V_{ll}I_2 \\ S_3 &= \sqrt{3}V_{ll}I_3 \\ S_2 &= S_3 = S \end{aligned} \tag{6.17}$$

where $V_{ll}$ is line-to-line primary voltage, and $I_2$ and $I_3$ are phase currents of the two transformers. The ratio of the phase current is as follows:

$$\frac{I_2}{I_3} = \frac{\sqrt{3}}{2} \tag{6.18}$$

The current through the conductor is equal to the product of the current density and the area of the conductor (i.e. $I = \Gamma A_c$ ). With the same current density, the ratio of the conductor areas is then also

$$\frac{A_{c2}}{A_{c3}} = \frac{\sqrt{3}}{2} \tag{6.19}$$

The phase voltage of the winding can generally be expressed as

$$V_f = 4.44N\lambda f \tag{6.20}$$

where $N$ is the number of turns, $\lambda$ is core flux, and $f$ is frequency. Assuming the same core flux, the ratio of the number of turns for both transformers will be equal to the ratio of the corresponding phase voltages, which is as follows:

$$\frac{N_2}{N_3} = \frac{V_{2f}}{V_{3f}} = \frac{V_{ll}}{\frac{V_{ll}}{\sqrt{3}}} = \sqrt{3} \tag{6.21}$$

The ratio of the total copper mass for all phases, assuming the same winding length, is then

$$\frac{m_{Cu2}}{m_{Cu3}} = \frac{2\rho_{Cu}N_2A_{c2}l}{3\rho_{Cu}N_3A_{c3}l} = \frac{2}{3}\frac{\sqrt{3}}{1}\frac{\sqrt{3}}{2} = 1 \tag{6.22}$$

where $\rho_{Cu}$ is copper density, and $l$ is winding length. Hence, the same amount of copper is needed for both transformers.

If one assumes that both transformers have the same outer diameter, which is constrained by the dimensions of the DFIM and if we ignore the fact that copper and iron have different densities then the total mass of both transformers will be roughly proportional to the transformer length. The cross section of laminations for both transformers is shown in figures 6.8 and 6.9. The slot width is marked as $b_s$. The slot width is 50% larger in the case of the two-phase transformer because we have 50% more copper per phase. The width of the core sections through which the flux passes in the radial direction is marked as $b$. One has to bear in mind that in the three-phase transformer, the flux that passes through the section between two adjacent phases is produced by the difference of the MMFs of two windings in which the

currents are phase shifted by 120°. Hence the flux in that section will be $\sqrt{3}$ times higher than the flux in the most outer sections, which is produced only by the MMFs of the individual phases. Therefore, the width of the inner sections will have to be $\sqrt{3}$ times larger than the width of the outer sections (Figure 6.9. The inner sections could be made with the same width as the outer ones if the middle phase is wound in the opposite directions. Then the MMFs of the adjacent slots would theoretically be phase shifted by 60°, as in the case of a two-phase transformers, so that their difference would have the same magnitude as the magnitude of the individual phase MMFs. However, this would cause serious unbalance of the magnetization currents [12].

Using the design parameters of the two-phase transformer given in section 6.5, the relationship between $b_s$ and $b$ is approximately

$$\frac{b_s}{b} \approx 1.3$$

The total length of the two-phase transformer is then

$$l_2 = 3b + 3b_s \approx 3b + 3 \cdot 1.3b = 6.9b \tag{6.23}$$

The total length of the three-phase transformer is as follows:

$$l_2 = \left(2 + 2\sqrt{3}\right)b + 3b_s \approx \left(2 + 2\sqrt{3}\right)b + 3 \cdot 1.3b = 9.36b \tag{6.24}$$

Therefore, the approximate ratio of the masses of the three-phase and two-phase transformers is

$$\frac{m_3}{m_2} \approx \frac{9.36b}{6.9b} = 1.35 \tag{6.25}$$

The mass of the three-phase transformer is approximately 35% higher than the mass of the two-phase transformer, with the same apparent power rating. Hence, the advantage of the two-phase transformer is obvious. However, the problem with the two-phase rotary transformer is the unbalance of currents and voltages that occurs when the transformer is loaded. This happens because of the unbalanced impedances in all three phases on the primary and the secondary side of the transformer.

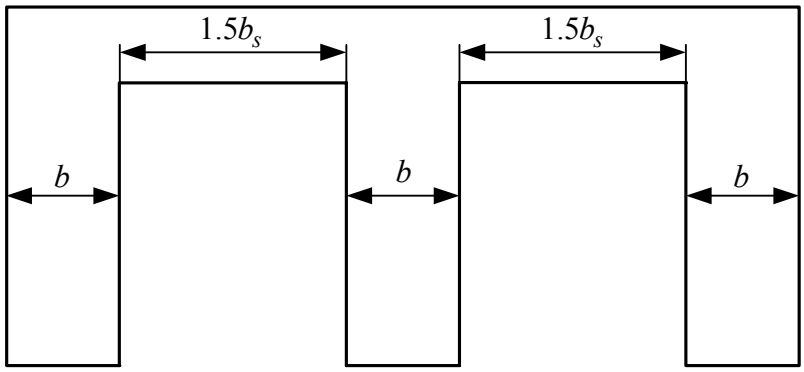


**Figure 6.8. Dimensions of the two-phase transformer laminations**

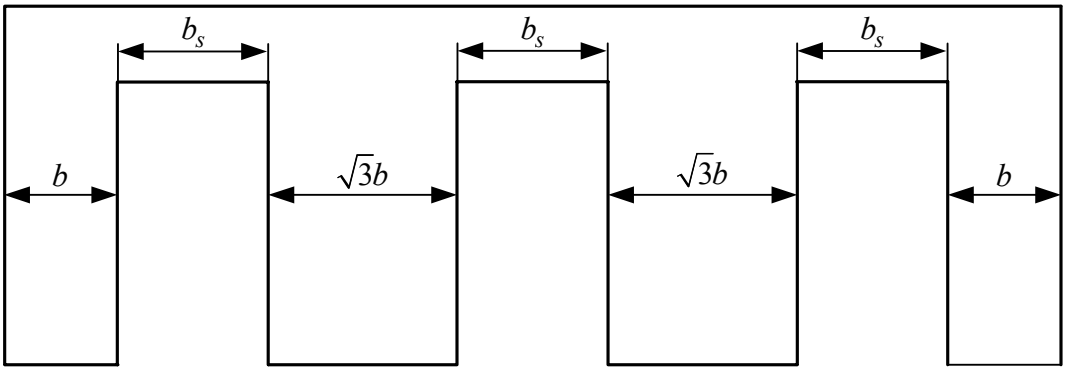


**Figure 6.9. Dimensions of the three-phase transformer laminations**

## 6.7 Design Parameters of the Rotary Transformer

We "manually" change the dimensions of the design of the rotary transformer in a consecutive manner until the satisfying properties were obtained. The geometric constraints dictated by the available space in the induction generator frame were satisfied as well. The rotary transformer we designed in cooperation with the company WEG in Brazil[1], which is the manufacturer of the prototype. The magnetic and insulating materials and the wire sizes were selected according to recommendations from WEG. The prototype was built according to dimensions listed below.

Primary slot: $h_1 = 2.86$ mm (11 layers of resiglass band)

$h_2 = 1$ mm, $h_3 = 50.14$ mm, $b = 33$ mm

$$h = h_1 + h_2 + h_3 + h_2/2 = 54.5 \text{ mm}$$

[1] WEG, address, contact info

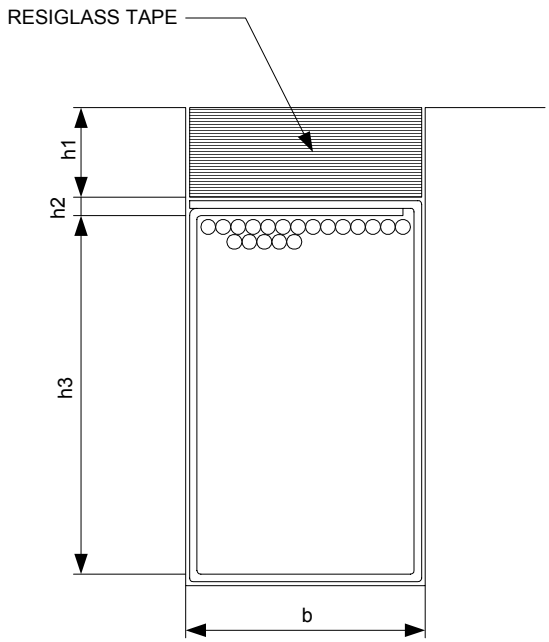


**Figure 6.10. Slot and winding dimensions**

Secondary slot: $h_1 = 1$ mm (4 layers of resiglass band; this is optional and will be decided during manufacturing)

$h_2 = 1$ mm, $h_3 = 61.5$ mm, $b = 33$ mm

$$h = h_1 + h_2 + h_3 + h_2/2 = 64 \text{ mm}$$

Dimension $h_3$ in the case of the primary and secondary slot also includes an additional 0.5 mm for the core assembly tolerance. The same tolerance was assumed when width $b$ was determined. All four windings were wound in the same direction (Figure 6.11).

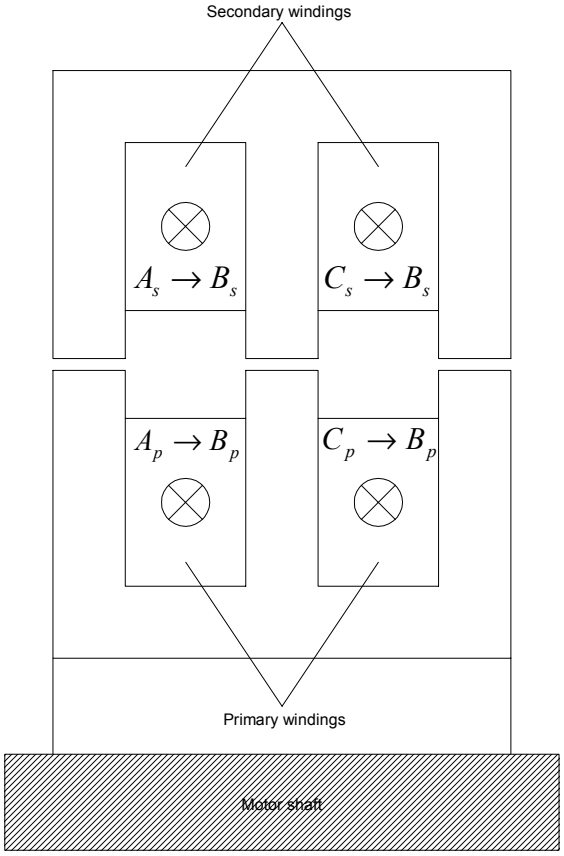


**Figure 6.11. Winding direction**

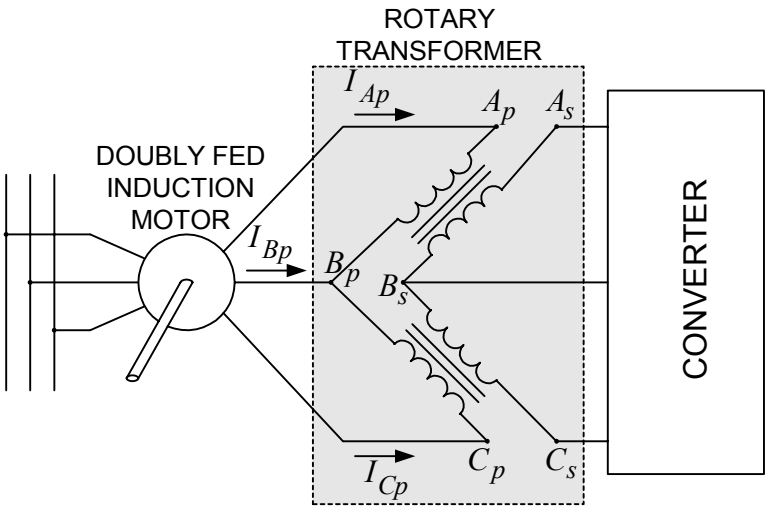


**Figure 6.12. Connection of the rotary transformer to the system**

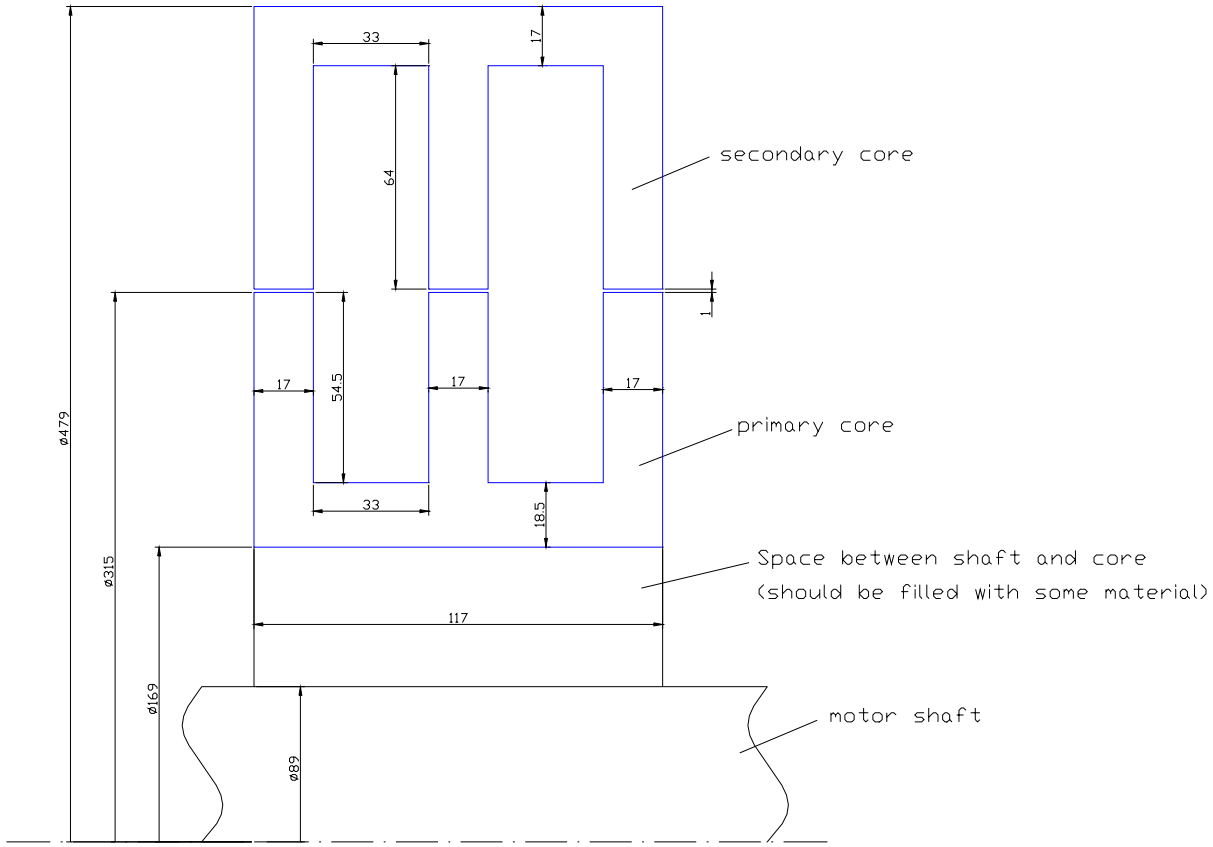


**Figure 6.13. Axial cross-section of the transformer**

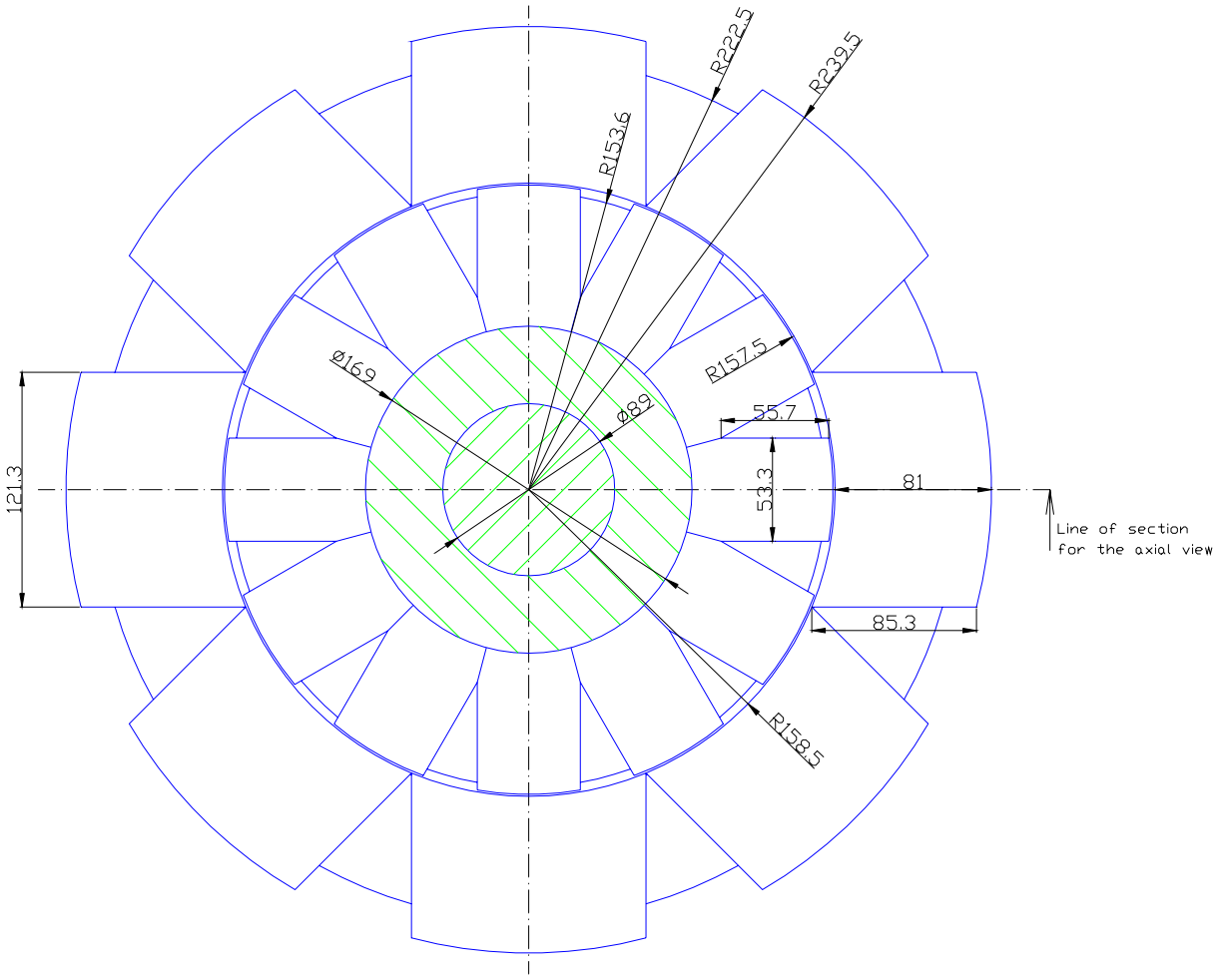


**Figure 6.14. Radial cross-section of the transformer**

**Table 6.1. Transformer Data**

| Parameter | Measurement |
|---|---|
| Rated power | 20 kVA |
| Rated voltage | 347 V/347 V |
| Rated current | 28.8 A/28.8 A |
| Frequency | 60 Hz |
| Magnetizing current (no-load operation) | 10.7 A |
| Number of turns of the primary winding ($N_1$) | 95 |
| Number of turns of the secondary winding ($N_2$) | 99 |
| Current density in the primary winding | 2.72 A/mm$^2$ |
| Current density in the secondary winding | 2.33 A/mm$^2$ |
| Diameter of the primary winding wire | (bare 1.5 mm; insulated 1.645 mm) |
| Number of strands to form the primary conductor | 6 |
| Diameter of the secondary winding wire | (bare 1.5 mm; insulated 1.645 mm) |
| Number of strands to form the secondary conductor | 7 |
| Resistance of the primary winding ($R_1$) | 0.154 Ω |
| Resistance of the secondary winding ($R_2$) | 0.205 Ω |
| Fill factor of the primary winding | 0.736 |
| Fill factor of the secondary winding | 0.726 |
| Magnetizing inductance ($L_m$) | 116 mHz |
| Leakage inductance of the primary winding ($L_{l1}$) | 5 mHz |
| Leakage inductance of the secondary winding ($L_{l2}$) | 8.6 mHz |
| Core mass | 37.6 kg |
| Copper mass | 40.8 kg |
| Transformer mass (iron+copper) | 78.4 kg |
| Core material | E 1008T sheet steel |

## 6.8 Simulation Results

The waveforms of the voltages and currents were simulated using the MATLAB/Simulink model for the no-load operation of the two-phase rotary transformer with design parameters given in section 6.7 (figures 6.15 to 6.18.).

Figure 6.16 shows that the induced voltages will be slightly unbalanced, which can be expected because of the unbalanced impedances in the primary circuit. The flux densities shown in figures 6.18 and 6.19 are rather low, which means that the iron will be practically unsaturated. This was a necessary trade-off because the entire flux that passes through the iron is equal to the flux that passes through the air gap. Hence, if one attempts to design the transformer with a higher flux density in the iron core (1.6-1.8 T), the same flux density will be present in the air gap. The compromise is to have a high value of magnetizing current and a very low power factor. The intent was to design the transformer with a magnetizing current of about 30% of the rated current.

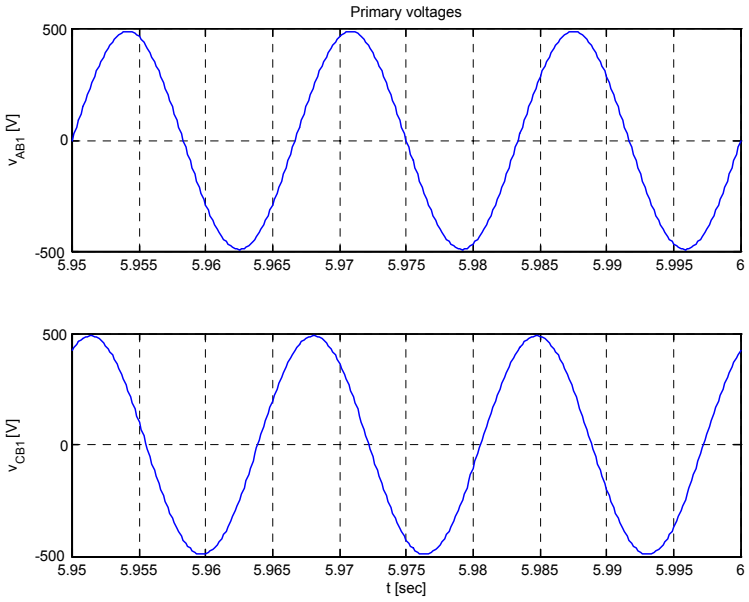


**Figure 6.15. Primary-side voltages**

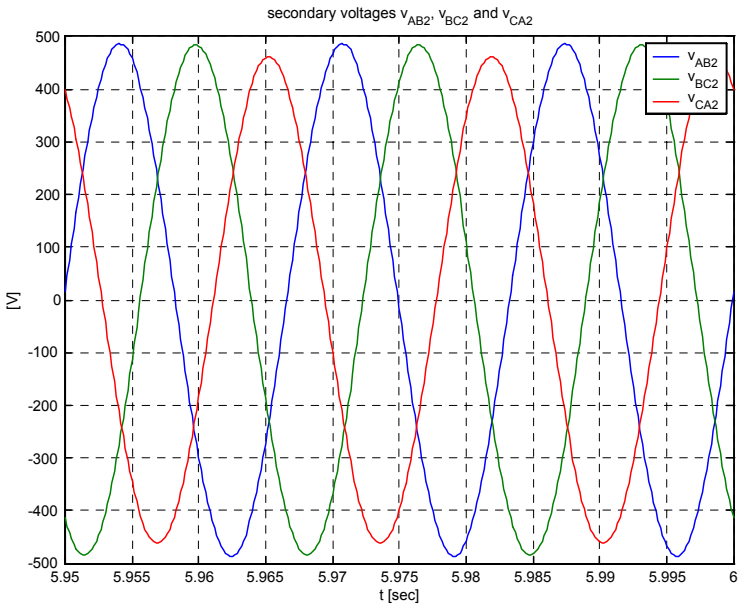


**Figure 6.16. Induced no-load operation secondary voltages**

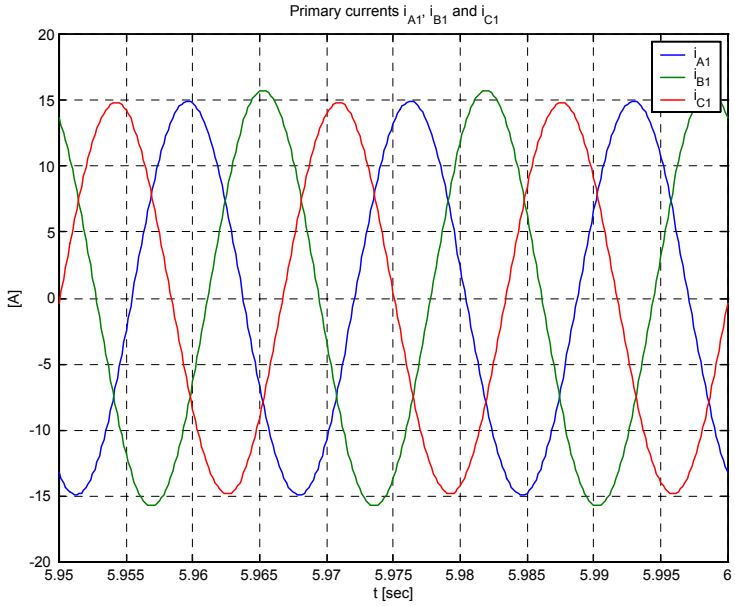


**Figure 6.17. Primary currents in no-load operation**

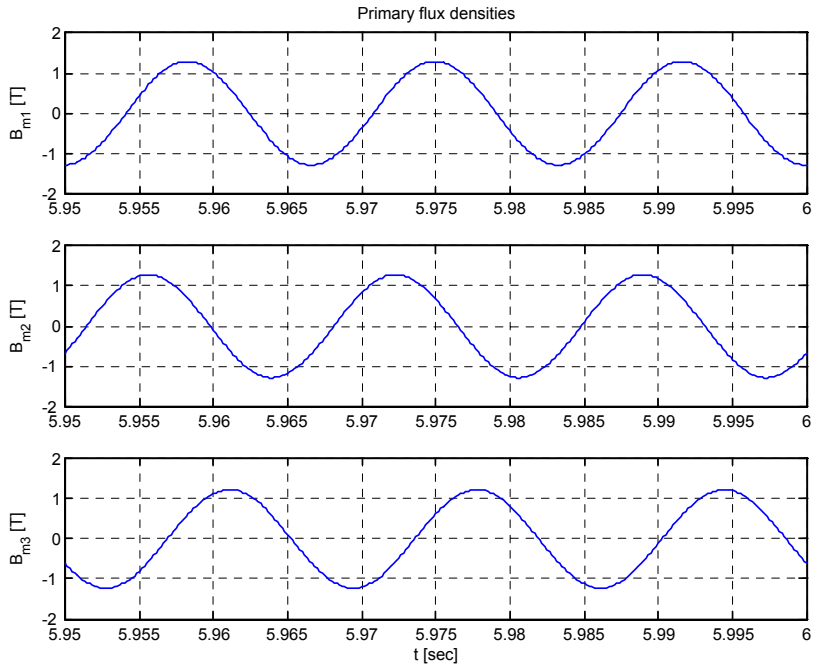


**Figure 6.18. Flux densities in the iron core sections of the primary winding**

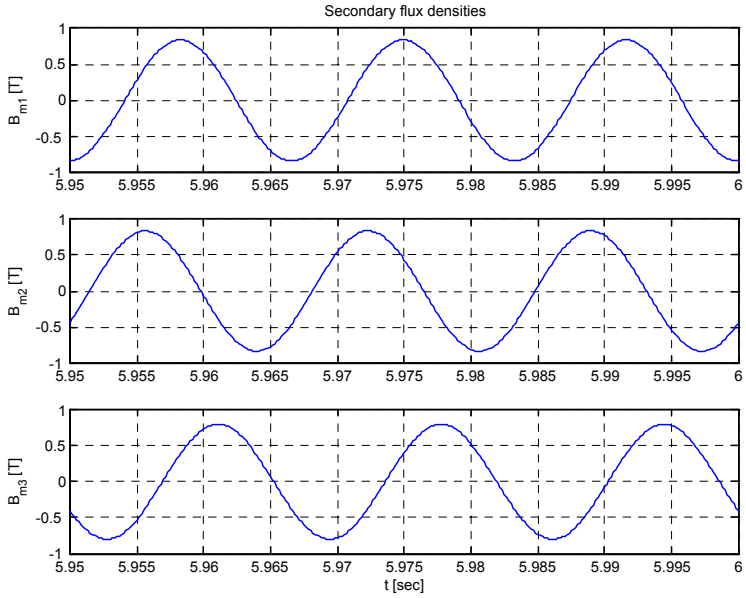


**Figure 6.19. Flux densities in the iron core sections of the secondary**

## 6.9 Doubly-fed Induction Machine

The manufacturing drawing of the DFIM manufactured by WEG of Brazil is shown in Figure 6.20. The rotary transformer will be placed inside the motor frame in the designated space. The amount of available space was one of the constraints for the rotary transformer design. The outer diameter of the rotary transformer had to be the same as the outer diameter of the machine core. This constraint is present for mechanical reasons, because the stationary part of the rotary transformer has to be attached to the frame. The other reason is the issue of cooling. In the DFIM of this power rating (30 kW), heat is taken away through the motor frame. Therefore, it is important to have a good contact between the core and the frame in order to maximize the heat exchange.

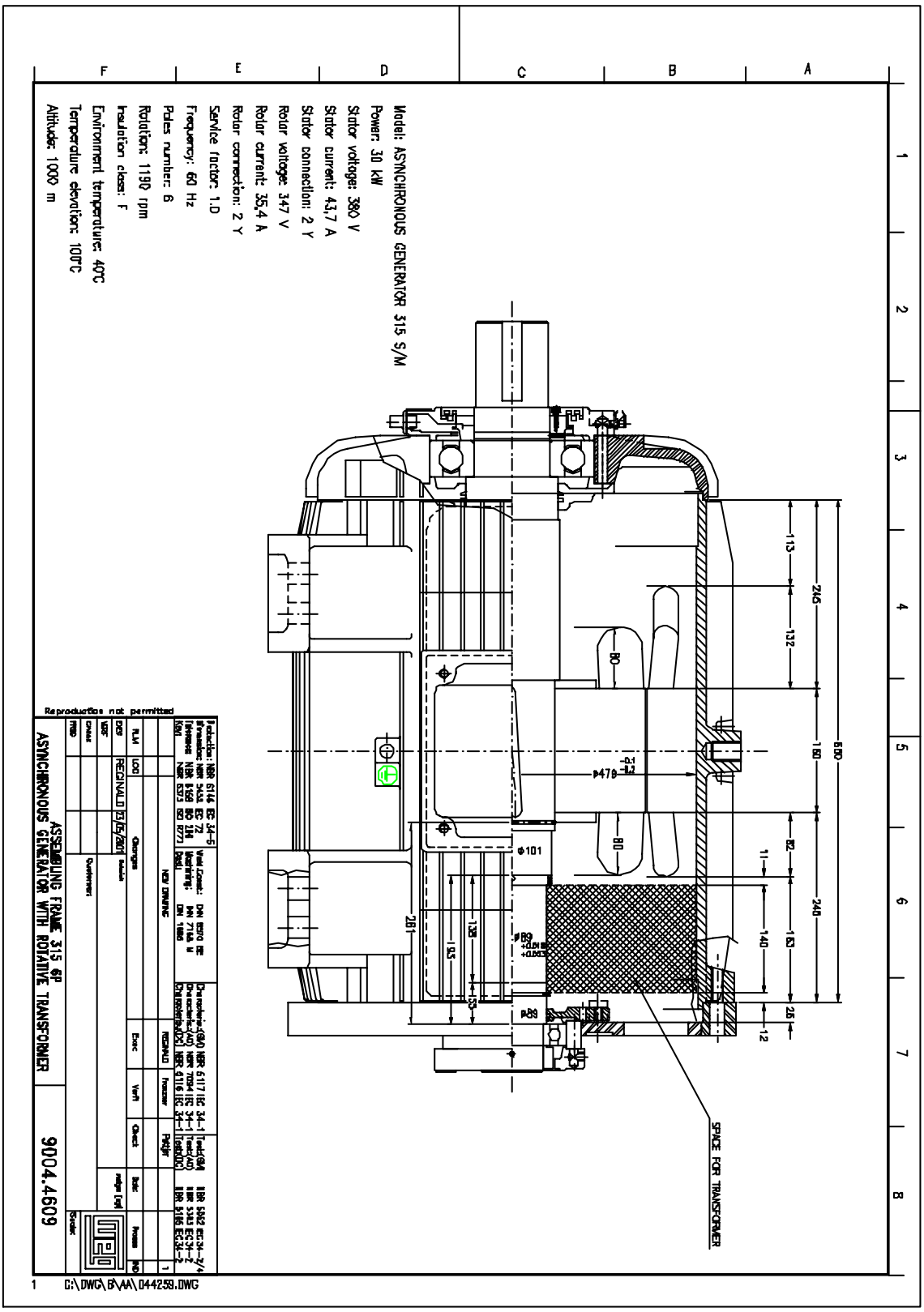


**Figure 6.20. Doubly fed induction machine**

## 6.10 Conclusions

The design and analysis of a rotary transformer has been explained in this chapter, and we present a design for a 20-KVA rotary transformer. The schematic of a rotary transformer along with a wound rotor induction machine is given and the basic operating principle explained. A comparative study between two-phase and three-phase rotary transformer was carried out, and we showed that with two-phase configuration, the volume of the rotary transformer can be reduced by 35%. On the other hand, the two-phase rotary transformer introduces an unbalance into the system.

# Chapter 7: Control Algorithm Based on Stator Power for the Rotor-side Control of a DFIM System

## 7.1 Overview

In this chapter we explore control algorithms for a wound-rotor induction machine drive with or without a rotary transformer. First, we look at performance with a diode bridge and chopper combination for the rotor-side control of a DFIM and unbalanced two-phase rotary transformer. Then a regular IGBT-based inverter replaces the diode bridge and chopper and a field-oriented control algorithm is applied. Simulation results for both a diode bridge chopper and a field-oriented controller are presented. Finally we devise a control algorithm for direct stator power. The advantage of the direct power stator is that it does not need any rotor voltage or current measurement for the controller. First, we verify the controller in a SABER simulation for a wound-rotor induction machine control without rotary transformer. Then, we explore the use of this controller in an unbalanced system. Through short-circuit and open-circuit simulation of the rotary transformer we determine the degree of unbalancing in both extreme cases. A detailed analysis of the unbalancing nature of the rotary transformer is given. The possibilities of control through direct stator power are analyzed for such unbalanced system. A detailed control algorithm for the direct stator power is explained for a balanced and unbalanced system, and relevant SABER simulation results are presented in this chapter. The performance of the system, including rotary transformer, is also verified with diode-bridge chopper control and control through the IGBT inverter with field orientation with or without direct rotor-winding current measurements.

## 7.2 Introduction

In previous chapters, we discussed the DFIM based on the rectifier-chopper-inverter, and the controller was validated for a balanced system. However, after combining this system with the rotary transformer (discussed in Chapter 6), the system inherently becomes unbalanced. We found that this combination could generate excessive torque ripple that might lead to problems with the associated gearbox and mechanical drive train. The major torque ripple arises as a result of the asymmetric nature of the rotary transformer and lack of sufficient control freedom of the diode bridge and chopper combination. Thus, we believe that a fully controlled PWM inverter and suitable control algorithm may provide better control to the proposed system. We devised a control algorithm based on direct stator power in association with the PWM inverter to solve this problem. We illustrated through simulation how the torque ripple can be minimized with such a control algorithm. The detailed control algorithm with the controller based on direct stator power and the SABER simulation results are provided in this section 7.8.

In the new control algorithm, no rotor-side current or voltage measurement is necessary for control purposes. Instead, only stator voltage and stator current measurements are needed for implementing the controller. However, a DC bus current measurement is necessary for the inverter and to protect the motor. The proposed controller can also work without a rotor position sensor. The FEC control requires the usual DC bus voltage and grid-side phase current measurement.

We described that the operation of the rotary transformer close to synchronous speed functions without any problem down to as low as 6% slip. However, at slips less than 6%, the saturation problem in the transformer surfaces. This is illustrated with simulation results in the latter part of this chapter. By introducing a fully controlled inverter in the rotor side, the system can be operated at both sub- and super-synchronous operating range. However, passing through synchronous speed remains a problem to be solved. At present, the same result can be obtained only by wind torque or by pitch control, as explained earlier in chapters 2 and 4.

In this chapter, we explain the results with the diode bridge-chopper-inverter combination. A control algorithm for direct stator power is then discussed. We simulated a system consisting of a rotary transformer, a DFIM and a fully controlled PWM inverter in association with a control method based on direct stator power.

## 7.3 Performance of the System with Diode Bridge Combined with a Chopper-inverter

The performance of the complete system with our previously proposed diode bridge-chopper-inverter combination was verified. We found that the torque ripple of the system was excessively high, predominantly because the rotor of the machine was connected to the power converter through a two-phase, three-wire, unbalanced rotary transformer (figures 7.1a and 7.1b). The basic objective behind choosing a two-phase rotary transformer, instead of its three-phase balanced counterpart, was to reduce its volume. However, by introducing a two-phase three-wire transformer into the system, the system was made unbalanced. Because the machine and rotary transformer were being controlled by a diode bridge and chopper combination, the control flexibility of the system was also very much limited. In addition, while the rotary transformer was combined with the machine, the actual rotor current of the machine was no longer measurable since the rotor winding along with the primary winding of the rotary transformer was rotating as one unit. Hence, the current through the secondary side of the transformer (stationary part) was only available for measurement. With such a limitation and complexity, neither the controller based on the diode bridge-chopper combination nor the conventional field-oriented controller gave satisfactory system performance.

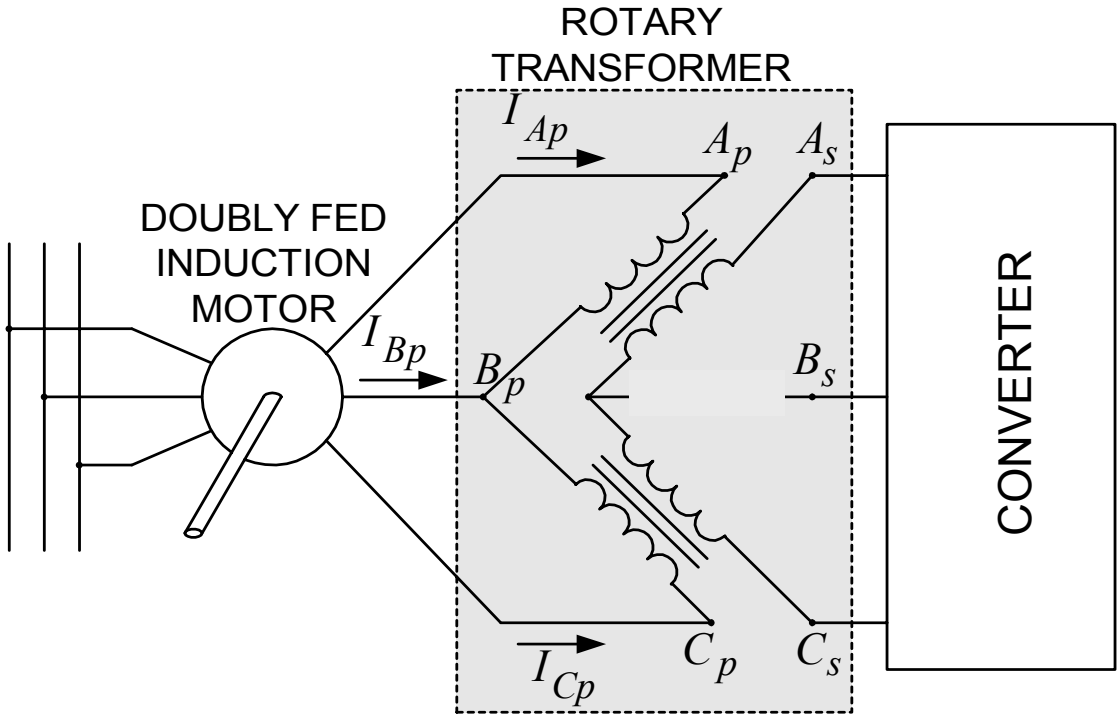


**Figure 7.1a. Schematic of DFIM with rotary transformer and power converter**

Through simulation, we found that in the system with the diode bridge and chopper combination, both the rotor and stator current are unbalanced, resulting in excessive torque ripple in the system (Figure 7.2). For a typical operating point, it may be seen that the torque ripple of the system is as high as ±30%. The percentage of ripple is higher at full load. In addition, both the stator and rotor currents are unbalanced in nature.

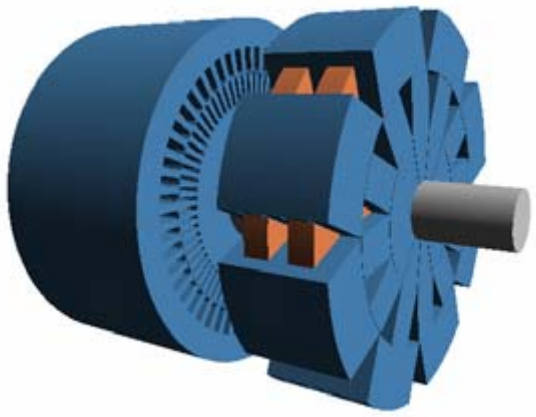

**Figure 7.1b. DFIM with a two-phase rotary transformer**

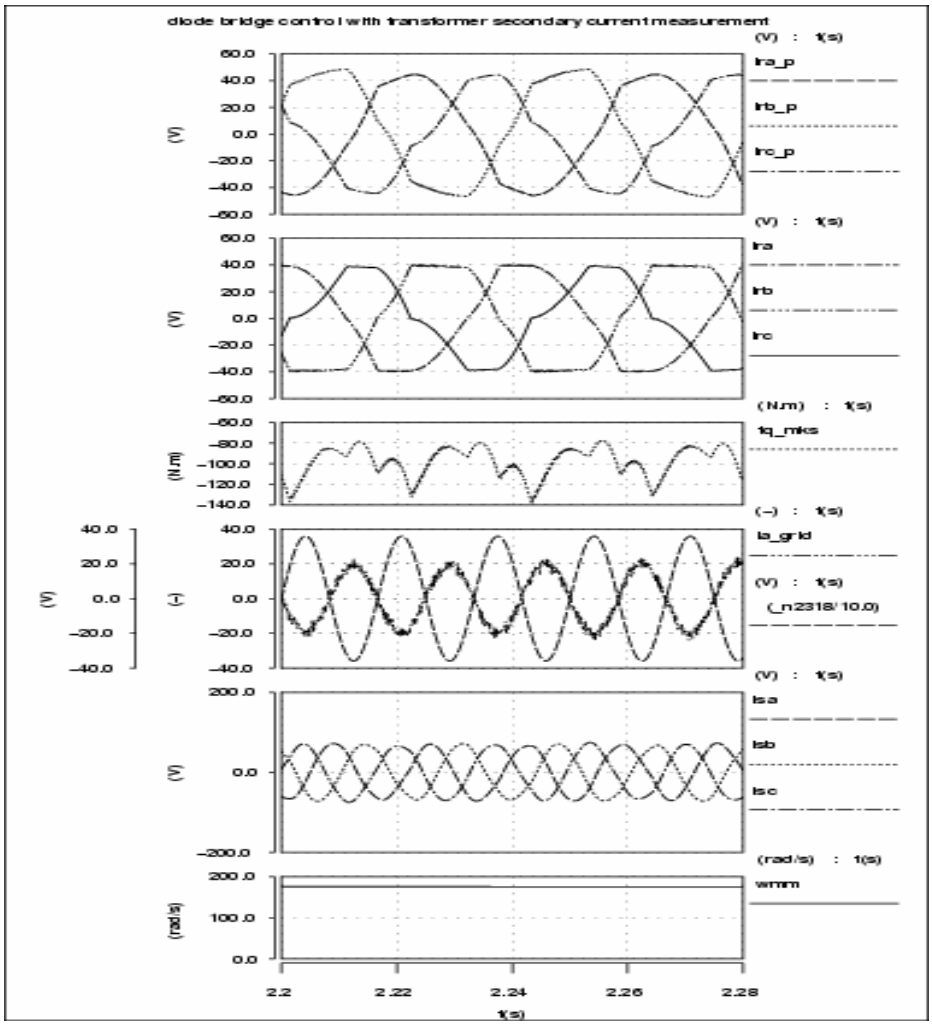


**Figure 7.2. Simulation results for the system when controlled by the diode-bridge and chopper combination, illustrating high torque ripple**

The unbalanced currents in the stator require active filtering using a FEC, which increases the rating of the FEC to some extent. After observing all these shortcomings, we decided to use a PWM inverter in the machine side, too; with its greater control flexibility it eliminates the complexities introduced by the unbalanced rotary transformer. A suitable rotor-side control algorithm based on stator power measurement is devised for such purpose. The detail control algorithm is discussed in the following section.

## 7.4 Control of the DFIM Through Direct Stator Power on the Rotor-side

In the field-oriented control technique, the transient response of the active and reactive power are dependent on the degree of decoupling between the direct and the quadrature axes. This, in turn, depends upon the accuracy of computation of the stator-flux magnetizing current and the accuracy of rotor position information. These methods, which make use of field-oriented control, require mathematical computations involving coordinate transformation and parameter estimation.

An alternative approach may be considered where, instead of rotor current, the rotor flux is directly to regulate the active and reactive power flow in the machine. Direct self-control (DSC) of an induction motor has been proposed by Depenbrock [16], wherein the stator flux is controlled to track a hexagonal trajectory. The switching scheme controls the torque within a defined band. Direct torque control (DTC) schemes have also been proposed [17, 18]. The primary difference from the earlier method is the circular trajectory of the stator flux. Two hysteresis controllers, namely a torque controller and a flux controller, are used to determine the switching states for the inverter. The method of control is computationally simple and does not require the rotor position information. However, the problem associated with low-frequency sensorless operation exists.

Until recently, the application of direct torque control has been primarily restricted to cage rotor-induction motors and permanent magnet synchronous motors. Very recently, an algorithm has been proposed by Datta and Ranganathan [19] that extends the switching concepts of DTC to rotor-side control of the DFIM. Here, the active and reactive powers are directly controlled. Hence, the algorithm is referred to as *direct stator power control.* The sector in which the rotor flux is presently residing is identified, and the switching vectors are selected to control its trajectory with respect to the stator flux. The sector information is updated based on the direction of change of the reactive power resulting from the application of a switching vector. This method is inherently sensorless in regards to position and does not use any machine parameters in the computation.

The concept of direct stator power used by Datta and Ranganathan [18] was demonstrated for a balanced system. Also, their method was prone to higher THD because the sector update method is not flawless, and for some operating points the sector may not be updated over a span of 120°. In this report, the sector identification method is modified, and a more reliable control algorithm is found. We also observed that the proposed direct stator power control algorithm functions well even if the windings of the three phases of the machine are not identical (i.e., if the system is unbalanced). In the system reported here, a two-phase three-wire rotary transformer is connected in cascade with the rotor of a DFIM, which introduces an unbalanced condition into the system. The proposed control algorithm has been found to track the rotor flux in a controlled manner, so as to obtain smooth torque and balanced stator and rotor currents from the machine in spite of the unbalancing nature of the system.

### *7.4.1 Concept of Control using Direct Stator Power*

The basic concept of direct control of active and reactive power can be appreciated from phasor diagrams based on the equivalent circuit of the DFIM (Figure 7.3). From the phasor diagram in Figure 7.4, it is noted that the component *isq* of the stator current has to be controlled in order to control the stator active power *Ps,* and *isd* has to be controlled to control the stator reactive power *Qs.* This is achieved in turn by controlling the rotor currents *irq* and *ird,* respectively, as discussed in the previous chapters.

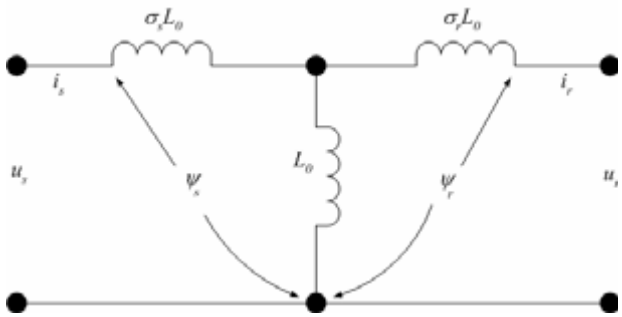


**Figure 7.3. Equivalent circuit of a DFIM**

The effect of injection of these rotor currents on the air-gap and on the rotor-fluxes can be derived by subtracting and adding the respective leakage fluxes. The variation of the rotor flux with variations in the active and reactive power demand is shown in figures 7.5a and 7.5b. In Figure 7.5a, *ird* = 0, (i.e., the reactive power is fed completely from the stator side). Under this condition, if *irq* is varied from 0 to full load, the locus of $\underline{\psi}_r$ varies along A-B, which indicates a predominant change in angle $\delta_P$ between $\underline{\psi}_s$ and $\underline{\psi}_r$, whereas the magnitude of $\underline{\psi}_r$ does not change appreciably. In other words, a change in the angle $\delta_P$ would definitely result in a predictable change in the active power handled by the stator. For example, in Figure 7.5a, which is the motoring mode of operation, decelerating the rotor flux in relation to the stator flux can increase the active power. Conversely, accelerating the rotor flux can reduce the active power. In Fig. 7.5b, the stator active power demand is maintained constant, so that *irq* is constant, and *ird* is varied from 0 to the rated value of *ims*. Here the locus of $\underline{\psi}_r$ varies along C-D, resulting in a predominant change in magnitude of $\psi_r$, whereas the variation in $\delta_P$ is small. Therefore, increasing the magnitude of the rotor flux and vice-versa can reduce the reactive power drawn from the grid by the stator.

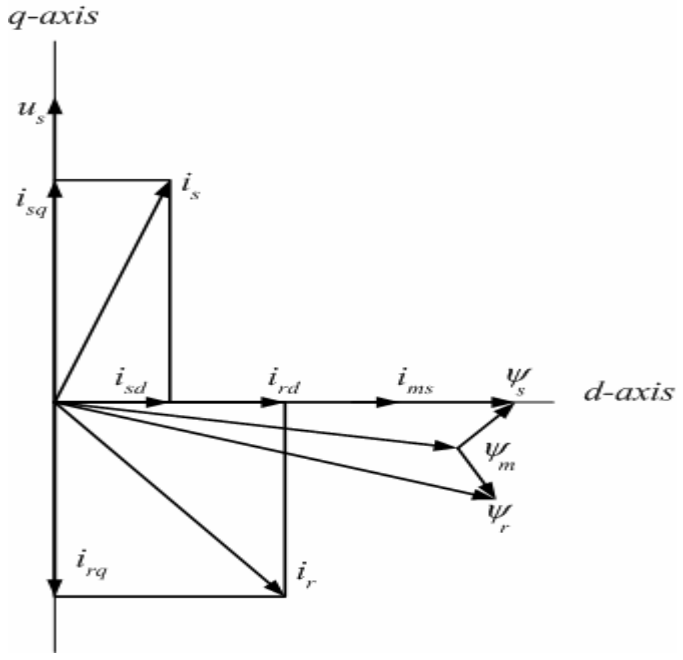


**Figure 7.4. Phasor Diagram of a doubly-fed induction machine**

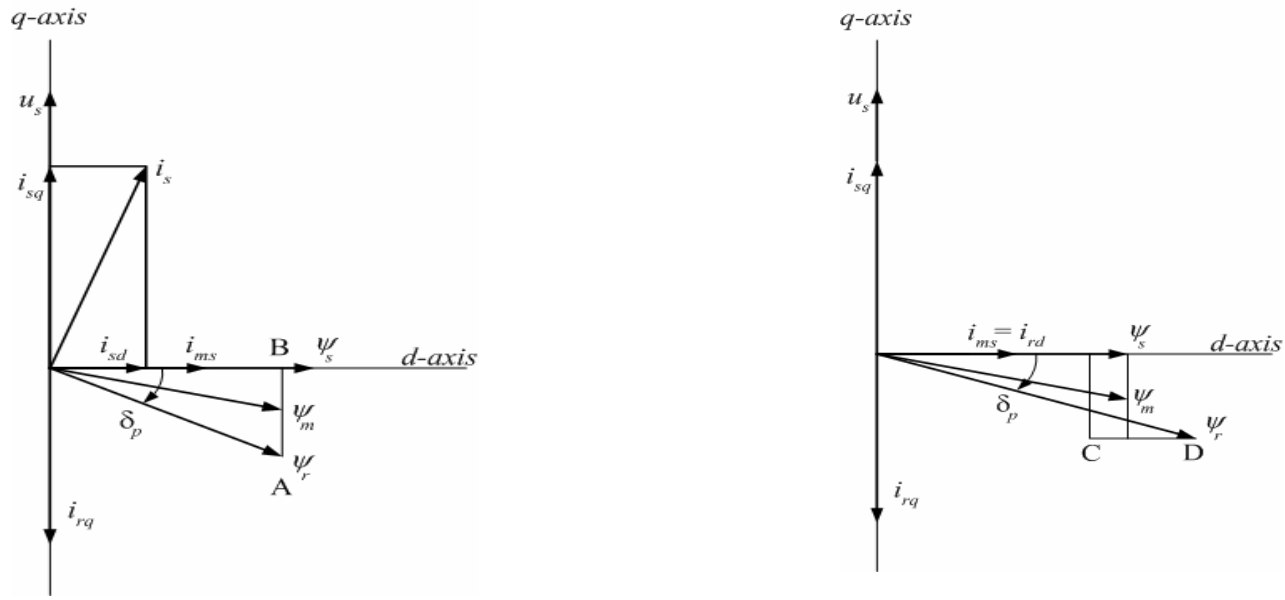


**Figure 7.5a (left hand side) and Figure 5b (right hand side)**

The phasor diagrams (figures 7.5a and 7.5b) remain the same irrespective of the reference frame. The frequency of the phasors merely changes from one reference frame to the other. Therefore, we can conclude the following:

- **(i)** The stator active power can be controlled by controlling the angular position of the rotor flux vector
- **(ii)** Controlling the magnitude of the rotor flux vector can control the stator reactive power.

These two basic derivations are used to determine the instantaneous switching state of the rotor side converter to control the active and reactive power.

Figure 7.6 shows the possible six active switching states (S1, S2, S3, S4, S5, S6). The six active switching states would correspond to the voltage space vectors U1, U2...U6. In order to make an appropriate selection of the voltage vector, the space phasor plane is first subdivided into six 60° sectors 1, 2…6. The instantaneous magnitude and angular position of the rotor flux space phasor can now be controlled by selecting a particular voltage vector from the appropriate location. The effect of the different vectors, as reflected on the stator-side active and reactive powers when the rotor flux is positioned in sector 1, is illustrated in the following sub sections.

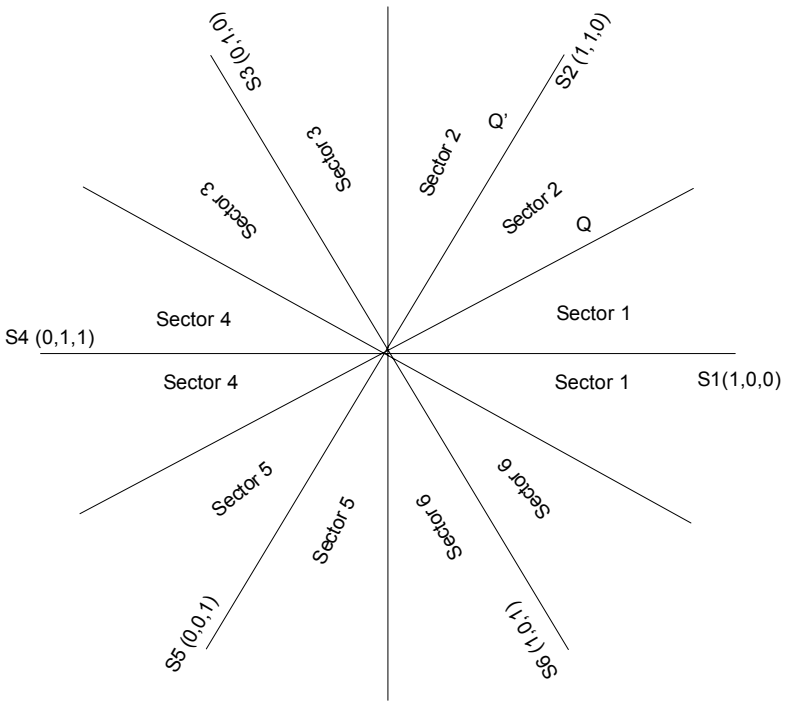


**Figure 7.6. Switching vectors and designated sectors for the direct-power control algorithm for a balanced three-phase DFIM**

### *7.4.2 Effect of Active Vectors on Active power*

Considering the anticlockwise direction of rotation of the flux vectors in the rotor reference frame to be positive, we note that $\psi_s$ is ahead of $\underline{\psi_r}$ in motoring mode of operation and $\psi_s$ is behind $\psi_r$ in generating mode. In the rotor reference frame, the flux vectors rotate in the positive direction at sub-synchronous speeds, remain stationary at synchronous speed, and begin rotating in the negative direction at super-synchronous speeds.

In the motoring mode of operation in sector 1, the application of voltage vectors U2 and U3 accelerates $\underline{\psi_r}$ in the positive direction. This reduces the angular separation between the two fluxes, resulting in a reduction of active power drawn by the stator. At sub-synchronous speeds, U2 and U3 cause $\underline{\psi_r}$ to move in the same anticlockwise direction as $\underline{\psi_s}$; hence, the effect on $P_s$ depends on the difference between the angular velocities of the two fluxes. The factors effecting the angular velocities of the fluxes $\underline{\psi_s}$ and $\underline{\psi_r}$ are the slip speed and the DC bus voltage, respectively. In the rotor reference frame, $\underline{\psi_s}$ rotates at slip speed, and the rate of change of $\underline{\psi_r}$ depends on the DC bus voltage and the applied inverter state. Therefore, for a given bus voltage, the higher the slip, the lower the relative angular velocity between the two flux vectors, thereby effecting a slower change in $P_s$ and *vice versa*. At super-synchronous speeds, the relative velocity is additive, and the change in $P_s$ is faster.

In the generating mode of operation, application of vectors U2 and U3 result in an increase in angular separation between the two and, therefore, an increase in the active power generated by the stator. (With Ps being negative for generation, U2 and U3 still result in a reduction of positive active power.) The relative speeds of the vectors in sub-synchronous and super-synchronous generation are the same as in motoring operation. Hence, the same conclusions can be drawn. Similarly, it can be seen that the effect of U5 and U6 on the active power would be exactly opposite to that of U2 and U3 in both motoring and generating modes.

Power drawn by the stator is considered to be positive and power generated is considered to be negative. Therefore, it may be concluded that, if the rotor flux is in k-th sector, application of vectors U(k+1) and U(k+2) would result in a reduction in the stator active power, and application of vectors U(k-1) and U(k-2) would result in an increase in the stator active power.

### *7.4.3 Effect of Active Vectors on Reactive Power*

From the phasor diagrams (figures 7.5a and 7.5b), it can be seen that the reactive power drawn by the stator depends upon the component of $\underline{\psi}_r$ along $\underline{\psi}_s$ (i.e. $\psi_{rd}$). Therefore, when the rotor flux vector is located in sector 1, voltage vectors U1, U2 and U6 increase its magnitude, whereas vectors U3, U4 and U5 reduce its magnitude. This holds well irrespective of whether the machine is operating in motoring or generating mode. An increase in magnitude of $\psi_r$ indicates an increased amount of reactive power being fed from the rotor side and therefore, a reduction in the reactive power drawn by the stator. This results in an improved stator power factor. A decrease in magnitude of $\underline{\psi}_r$ amounts to lowering of the stator side power factor.

As a generalization, it can be therefore said that if the rotor flux resides in the kth sector, where k=1, 2, 3...6, switching vectors U(k), U(k + 1), and U(k - 1) reduce the reactive power drawn from the stator side. U(k + 2) , U(k - 2), and U(k + 3) increase the reactive power drawn from the stator side.

### *7.4.4 Effect of Zero Vectors on Active Power*

The effect of the zero vectors is to stall (stop rotating) the rotor flux without affecting its magnitude. This results in an opposite effect on the stator active power in sub-synchronous and super-synchronous modes of operation.

In sub-synchronous motoring, application of a zero vector increases $\delta_P$ as $\underline{\psi}_s$ continues to rotate in the positive direction at slip speed. Above synchronous speed, $\underline{\psi}_s$ rotates in the counterclockwise direction, thereby reducing $\delta_P$. Hence, active power drawn by the stator increases for sub-synchronous operation and decreases for super-synchronous operation. Active power generated being negative, the same conclusion holds true for the generating mode as well. The rate of change of Ps depends on the slip speed alone because $\underline{\psi}_r$ remains stationary in the rotor reference frame.

### *7.4.5 Effect of Zero Vectors on Reactive Power*

Because a zero vector does not change the magnitude of the rotor flux, its effect on the reactive power is rather small. Nevertheless, there is some small change in Qs; its effect being dependent on whether the angle between the stator and rotor fluxes increases or decreases due to the application of a zero vector. An increase in angular separation between the two fluxes reduces $\psi_{rd}$ resulting in an increment of Qs being drawn from the stator side. The converse is true when $\delta_P$ reduces.

## 7.5 Control Algorithm

With the inferences drawn in the previous section, it is possible to switch an appropriate voltage vector on the rotor side at any given instant of time to increase or decrease the active or reactive power in the stator side. Therefore, any given references for stator active and reactive powers can be tracked within a narrow band by selecting proper switching vectors for the rotor-side converter. This is the basis of the stator-power-based control strategy.

It should be noted that in a VSCF system, the outer loop will decide the reference for the overall active power P generated or absorbed by the machine. This includes both the stator and rotor powers (Ps and Pr). From this set value and the present speed, the reference torque $m_d^*$ can be computed. The reference for the stator power can, therefore, be calculated as Ps* = $md^*$. ωs. The quantity Qs* is set according to the desired power factor at the stator terminals.

### *7.5.1 Measurement of Stator Active and Reactive Power*

The active and reactive power on the stator side can be directly computed from the stator currents and voltages. The stator active and reactive powers can be expressed in the following manner:

$$Ps = \frac{2}{3}\left(u_{s\alpha} i_{s\alpha} + u_{s\beta} i_{s\beta}\right) \tag{7.1}$$

$$Qs = \frac{2}{3}\left(u_{s\beta} i_{s\alpha} - u_{s\alpha} . i_{s\beta}\right) \tag{7.2}$$

where, $$u_{s\alpha} = \frac{3}{2} u_{s1}, u_{s\beta} = \frac{\sqrt{3}}{2}\left(u_{s2} - u_{s3}\right) \tag{7.3}$$

$$i_{s\alpha} = \frac{3}{2} i_{s1}, i_{s\beta} = \frac{\sqrt{3}}{2}\left(i_{s2} - i_{s3}\right) \tag{7.4}$$

### *7.5.2 Sector Identification of Rotor Flux*

To implement the switching algorithm, the current sector of the rotor flux has to be identified. The exact position of the rotor-flux space phasor is not of importance when selecting which switching vector to apply. The concept is illustrated by the following example. Let one assume that the present position of the rotor flux is in sector 1 and it is moving in the counterclockwise direction (corresponding to sub-synchronous operation). Therefore, application of switching vector states S2 and S6 results in a reduction of Qs, and application of S3 and S5 results in an increment of Qs. As soon as the rotor flux vector crosses over to sector 2, the effect of states S3 and S6 on Qs would reverse. Vector U3 would now act to reduce Qs instead of increasing it. Similarly, the effect of vector U6 on Qs would also be opposite. These reversals in the direction of change in Qs, when a particular vector is applied, can be detected, and a decision of sector change may be made on this basis. Similarly, if the flux vector is rotating in the clockwise direction (super-synchronous operation), the effect of states S2 and S5 on Qs would change in direction when $\psi_r$ changes over from sector 1 to sector 6. Thus, in any particular direction of rotation there are two vectors that can provide the information for a sector change. Because the rotor flux vector cannot jump through sectors, the change will be always by one sector, either preceding or succeeding. In this method, even though the exact position of the flux is unknown, the sector identification can be updated just by observing the changes in Qs caused by the applied vectors. It may be noted that the effect of the vectors on Ps would not provide a conclusive inference about the change in sector.

However, during a particular sector, not all vectors will be applied. For example, in sector k, vectors U(k) and U(k + 3) will never be applied. These vectors would have predominant effect on the reactive power, but their effect on the active power would depend on the actual position of the rotor flux vector in the sector. In the switching logic, therefore, only those vectors are selected that have uniform effects on Ps and Qs in terms of their direction of change, irrespective of the position of the rotor flux in a particular sector.

For any given vector applied in a particular sector, the expected direction of change in Qs can be read from a pre-stored table. The actual direction of change can be computed from the present value of Qs and its previous value. If they are in contradiction, then a decision on change of sector is taken. Whether the sector change has to be effected in the clockwise or counterclockwise direction depends on the applied vector and the observed change in Qs. This information is stored in another reference table.

## 7.6 Modified Stator Power Control Algorithm

The control algorithm for direct stator power discussed in the previous chapter suffers from a few shortcomings. At any sector, only two active vectors can be used for sector updating, whereas the remaining two active vectors cannot make any decision on a sector change. For example, when the rotor flux is in sector 1 and the flux is rotating in the counterclockwise direction, application of vectors S3 and S6 can determine sector updating, whereas vector S2 and S5 cannot. Application of S2 vector should ideally decrease both Ps and Qs, while application of S5 should increase both of them. An arbitrary selection of the hysteresis bands for Ps and Qs may force the application of S2 and S5 vectors repeatedly at every alternative sampling instants. If such process goes on for a long time, then sector update may not take place even though the rotor flux has passed to sector 2 from sector 1.

In such case, the controller still functions stably until the rotor flux vector remains within the first half of sector 2 (up to 30°) without sector updating. After that, the application of vector S2 will increase This work has been authored by Midwest Research Institute under Contract No. DE-AC36-99GO10337 with the U.S. Department of Energy. The United States Government retains and the publisher, by accepting the article for publication, acknowledges that the United States Government retains a non- exclusive, paid-up, irrevocable, worldwide license to publish or reproduce the published form of this work, or allow others to do so, for United States Government purposes.Ps instead of decreasing the same, whereas it still decreases Qs. Similarly, application of vector S5 will decrease Ps instead of increasing the same and still increases Qs. Because the sector identification takes place only when there is a change in direction of Qs, the sector cannot be updated if S2 and S5 are applied repeatedly. In such a situation, the system could become unstable. As a remedy to this problem, the hysteresis band needs to be chosen carefully, so that both Ps and Qs do not change direction in unison for two consecutive sampling instants. In the present system, the band for Ps is chosen to be almost half that of Qs.

The above direct power control algorithm is explained with reference to a balanced three-phase system; so far nothing has been discussed about the validity of the same for an unbalanced condition. Our analysis has shown that the same control algorithm can be used for an unbalanced system. The proposed controller functions well without any stability problem if the system encounters a phase unbalance up to 30°. On the other hand, the controller functions become unreliable when the unbalancing of the phases exceeds more than 30°.

In the present system, the tow-phase three-wire rotary transformer introduces an unbalanced condition into the rotor circuit. The rotary transformer is designed so that its secondary winding is stationary and its primary winding rotates with the rotor. Instead of using three primary windings connected to the corresponding phase of the wound rotor, and three secondary windings connected to the converter, only two windings on each side will be used by means of a three-phase to two-phase transformation. The basic principle of the transformation is to phase shift the MMF of the two windings by 60° with the same amplitude. The angle of 60° is desirable because the MMF in the vertical middle section of the transformer core is proportional to the difference of the MMFs of the two windings. If it is assumed that these MMFs are sinusoidal with the same amplitude, then their difference would have the same amplitude. As a result, the width of the middle section of the core can be the same as the width of the outer ones. In this way, the flux through all the core sections is maintained, and volume of the transformer can be reduced. On the other hand, this arrangement inherently introduces unbalancing into the system. With such a two-phase transformer, when one side is excited with a balanced supply, the other side has unbalanced voltage. The degree of unbalancing is a function of load. The maximum unbalancing can be observed when operating at full load or, in other words, when the transformer is handling its rated power. If the primary winding of the rotary transformer is excited through a balanced three-phase supply voltage while the secondary side is shorted, the maximum unbalanced current can be expected at both the primary and secondary side of the same. Similarly, when the secondary side is connected to infinite impedances or kept open-circuited, the transformer behaves like a fully balanced system.

To detect the maximum possible unbalancing introduced into the system, the transformer alone is simulated with its secondary side in a short-circuited conditions. The simulation results (Figure 7.7) show that the Phase C current is leading Phase A currents by only 60° instead of 120°, whereas the

Phase B current is lagging the Phase A current by 150°, instead of 120°. Besides, the phase B current is almost √3 times that of the phase A and phase C currents. Thus, it may be concluded that in the worst-case condition, even though the unbalancing is almost 73% in magnitude, the unbalancing in phase is only 50%. However, because the secondary winding of the rotary transformer will always experience the rotor impedance of the motor (which is higher than a short-circuited condition), in practice the unbalancing will be less than that of the short circuit condition, both in magnitude and phase. It may be concluded that, in practice, the phase unbalance will never exceed 50% (60°) for this particular application. The simulation results with open-circuited conditions are given in the previous chapter (figures 6.15 to 6.19). The results show that the system behaves like a balanced system during no-load operation.

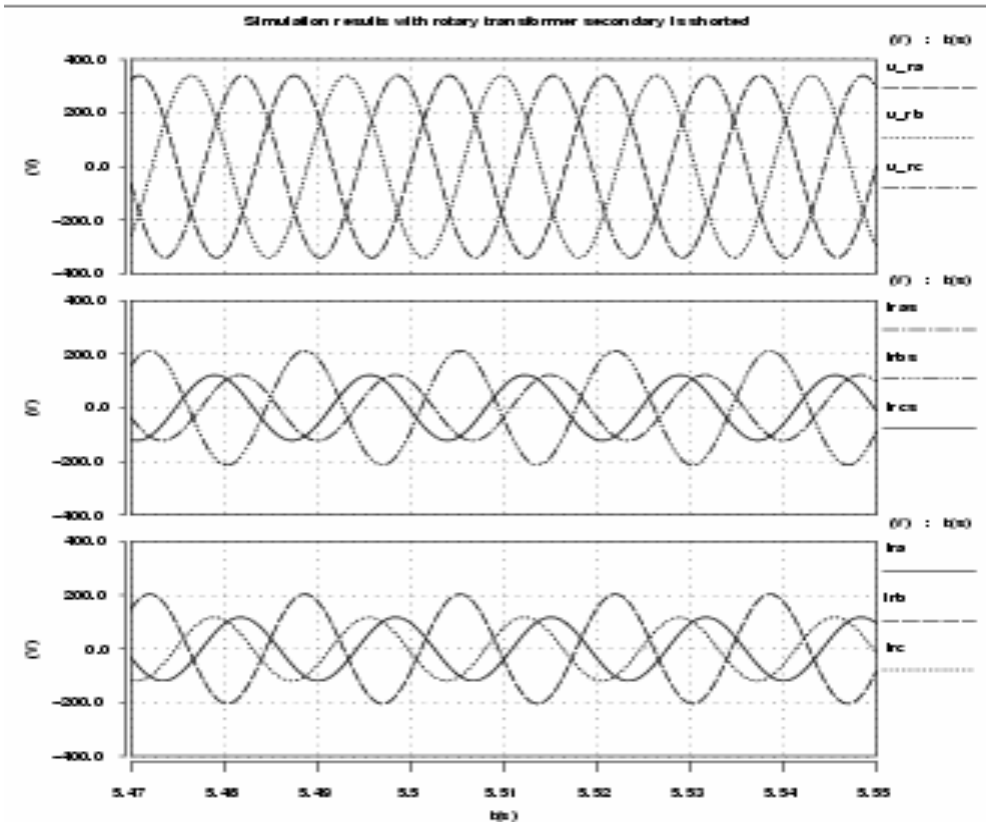


**Figure 7.7. The primary and secondary currents of the two-phase three-wire rotary transformer when the primary side is excited with a balanced supply voltage and the secondary side is short circuited**

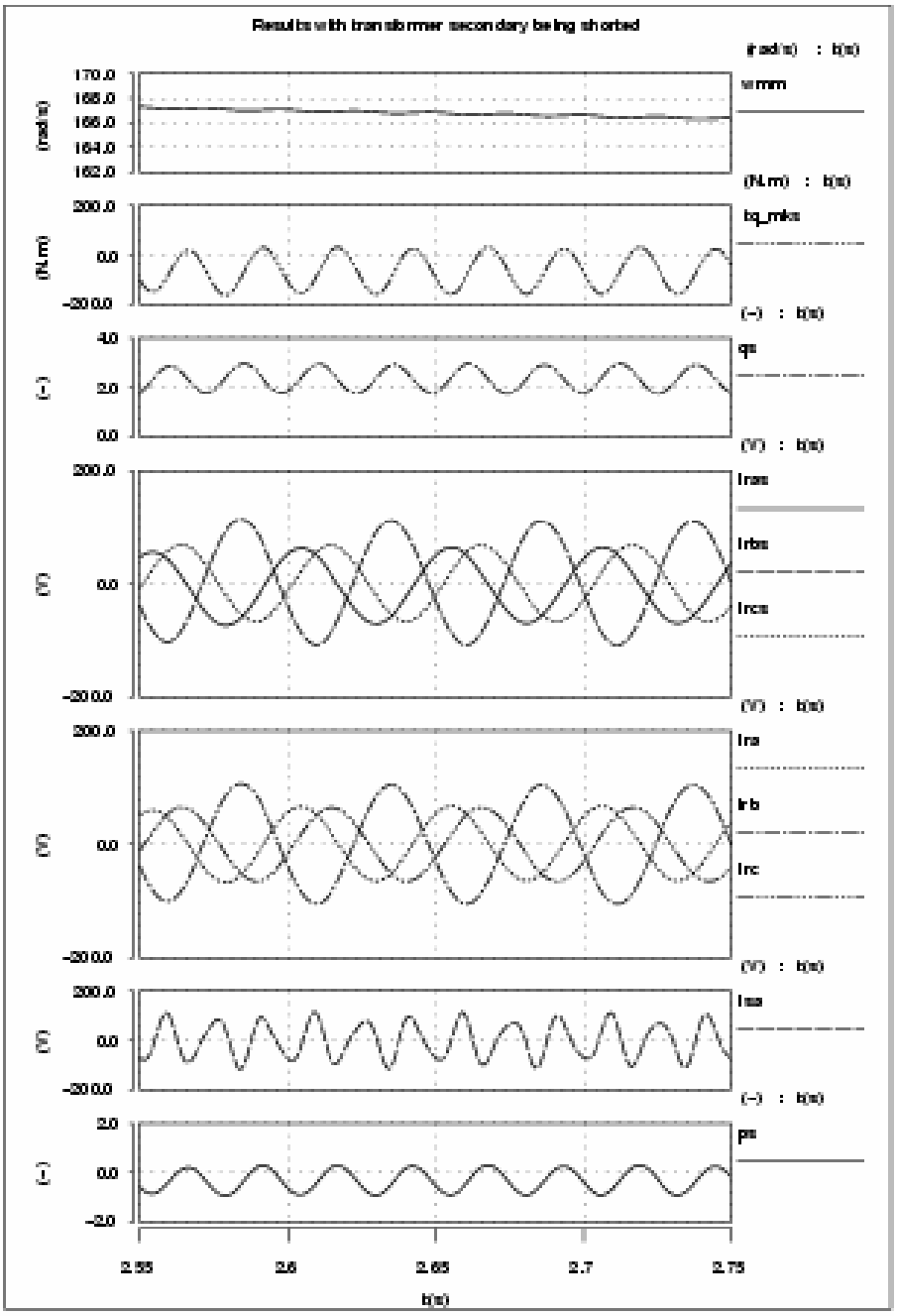


**Figure 7.8. The primary and secondary currents of the two-phase three-wire rotary transformer along with the different machine waveforms when the primary side is connected to the rotor winding of the DFIM and the secondary side is short circuited**

The simulation results of the system (combining DFIM and rotary transformer) when the secondary winding of the rotary transformer is short-circuited are given in Figure 7.8. Both the stator and rotor currents of the induction machine are highly distorted and unbalanced in nature. In this proposed control algorithm, the unbalancing in phase is more important than the unbalancing in magnitude because the control algorithm is more dependent on the relative displacement of the phase voltages or the effective switching vectors, rather than their magnitudes. The nature of unbalancing for different load can be explained with the help of phasor diagrams in figures 7.9 to 7.13.

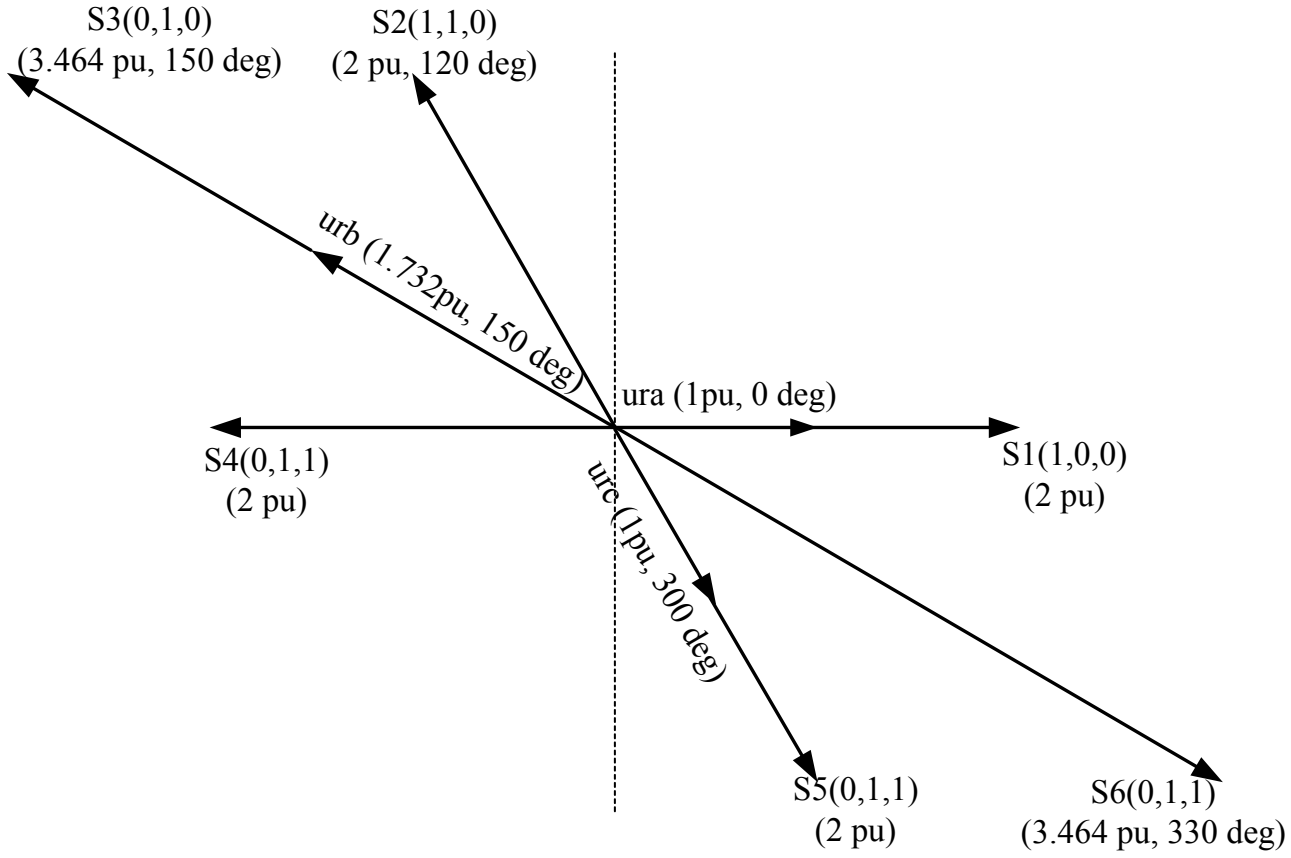


**Figure 7.9. The unbalanced phase voltages (at maximum unbalanced condition of 50%) at the machine rotor terminals and corresponding switching vectors for the proposed unbalanced direct power control algorithm of a DFIM**

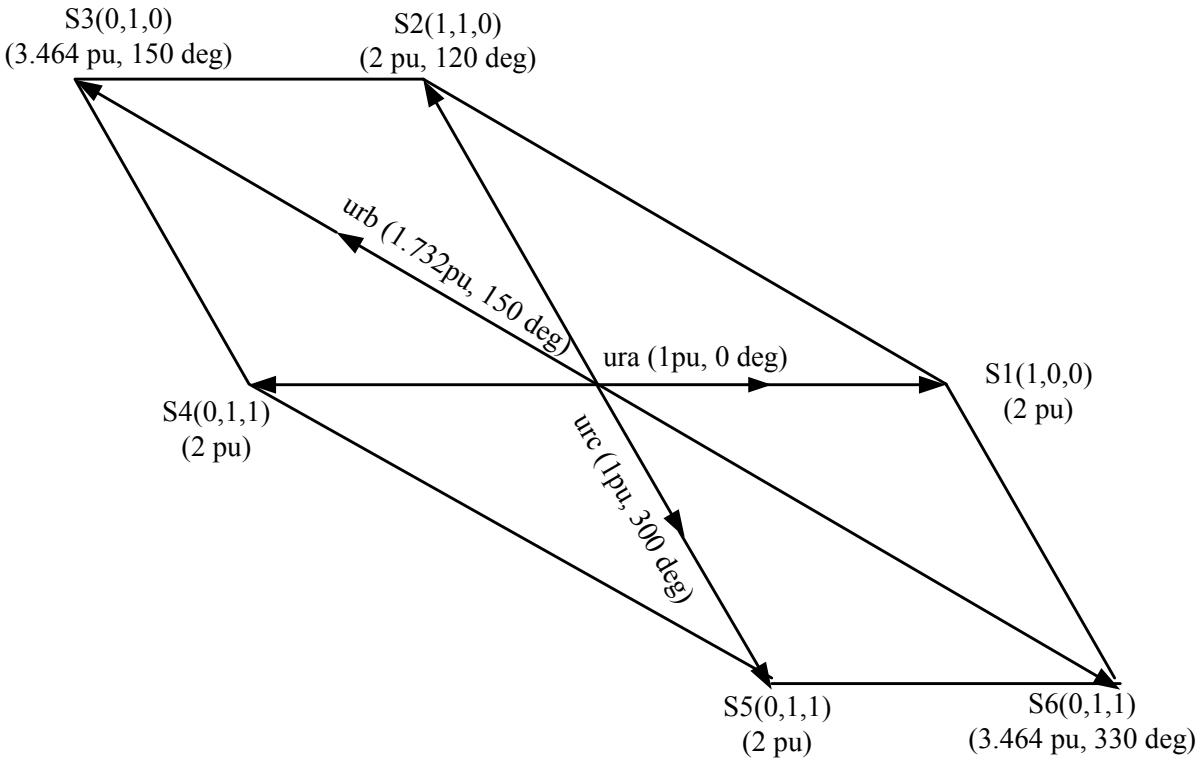


**Figure 7.10. An irregular hexagon incorporating the switching vectors for a DFIM at maximum (50%) unbalanced condition (short circuit condition)**

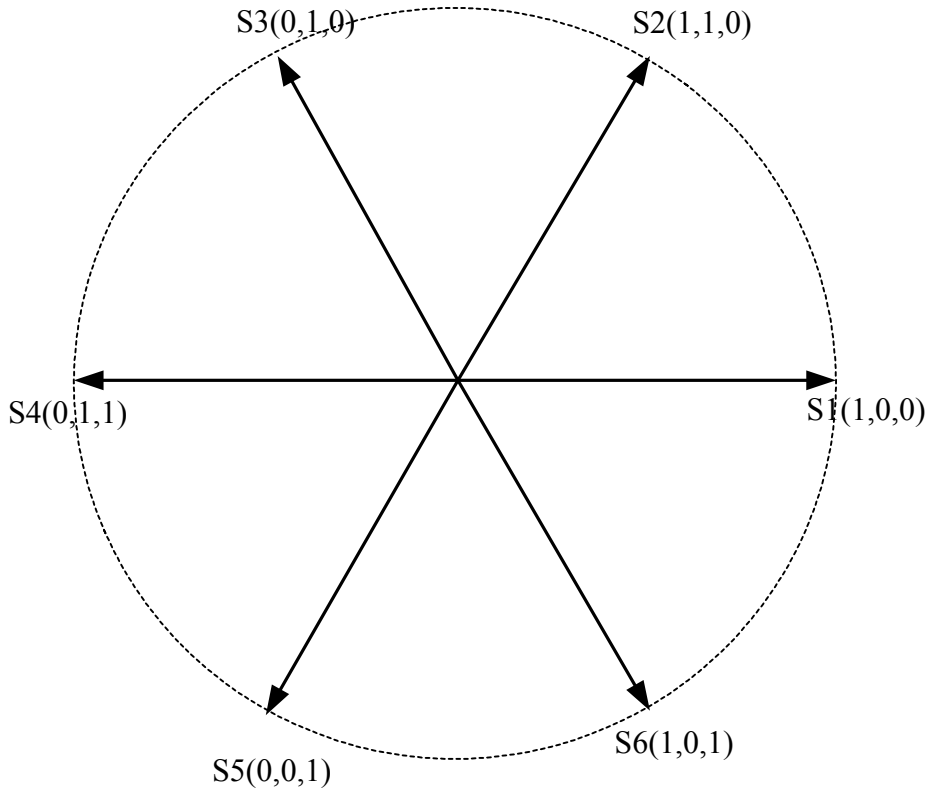


**Figure 7.11. A regular circle showing the switching vectors for a DFIM at maximum balanced condition (open circuit condition)**

Assuming the maximum unbalanced condition as given in figures 7.7 and 7.8, the phasor diagram of the currents through the rotor winding of the motor (when the stationary winding of the transformer is excited with balanced voltages) is given in Figure. 7.9. If one assumes that the three phases of the motor windings are identical (assuming the impedances of the rotor windings are same), then the voltages across the windings of the machine will also have similar phasor diagram (Figure7.9). Ura, Urb, Urc are the three phase voltages at the primary (rotating winding side) of the rotary transformer when the secondary side (stationary winding side) is excited with a balanced three-phase voltages.

It may be inferred from this relative displacement between the different phases that the voltage vectors applied by the power converter will be reflected to the motor side as given by S1, S2…S6 in Figure 7.9. The magnitude of all the effective vectors at the motor terminal are not the same and also they are not placed at regular interval. The relative magnitudes (1.732 pu to 3.464 pu) and angles between any two consecutive vectors are different (varying from 30° to 120°). A hexagon is drawn connecting the tips of the different voltage vectors (Figure 7.10). For a balanced system, the tip of the switching vectors would have been on a circle and their magnitude would have been the same. The phase difference between two consecutive switching vectors would have been the constant (60°) as shown in Figure 7.11.

Thus, it may be concluded that if the converter excites the secondary (stationary winding) of the transformer with a balanced three-phase voltage then the voltages at the motor terminal and flux in the rotor will follow a similar hexagon (Figure 7.10). To obtain a circular flux trajectory in the rotor, the excitation voltages by the converter need to be asymmetric. To accomplish that task the direct power control algorithm can be used. Assuming the unbalancing nature of the reflected voltage vectors at the rotor terminal, the sectors of the rotor flux are redefined and redrawn in Figure 7.12 for a typical 30° phase unbalanced condition.

The direct power control algorithm still works with such unbalanced condition. For example, let's say that the rotor flux vector is in sector 1 (Figure 7.12). In such a case, by applying S5 and S6, the rotor flux can be dragged behind and the relative angle between the stator and the rotor will increase. Thus the active power Ps can be increased. The application of S6 decreases Qs, whereas S5 increases it. Similarly, by applying S2 and S3, the active power will be decreased, whereas S2 decreases Qs and S3 increases Qs. When the rotor flux is rotating in the counterclockwise direction and when it reaches from sector 1 to sector 2, then by applying either S3 or S6, the direction of change of Qs will be detected and the sector can be updated accordingly. On the other hand, when the rotor flux is rotating in the clockwise direction, the sector can be updated by applying either S2 or S6. Similarly, it can be shown that the proposed controller functions well for all the other sectors (Figure 7.12).

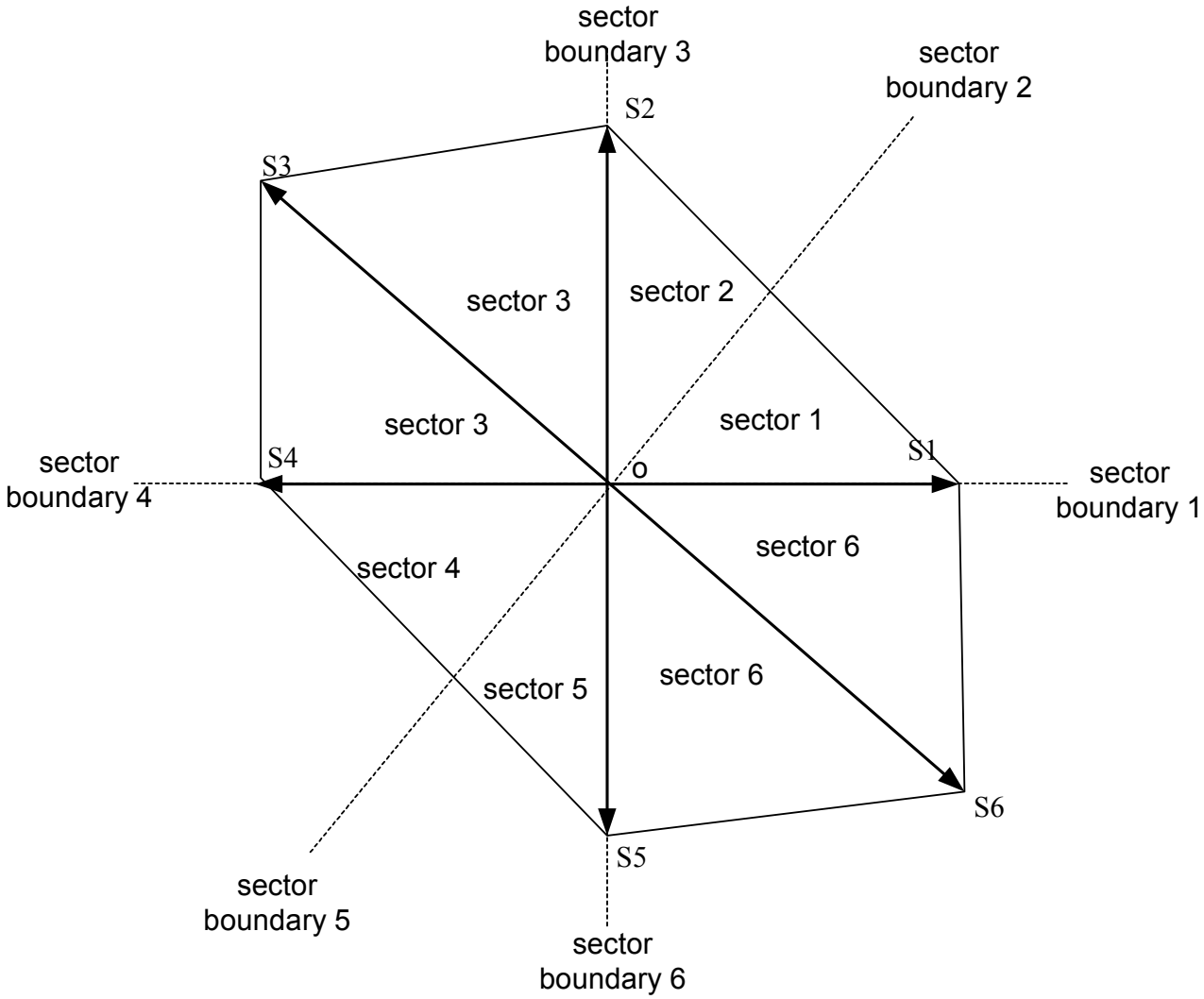


**Figure 7.12. Switching vectors and designated sectors for a modified direct-power control algorithm for a maximum 30° phase unbalanced condition of the system incorporating a two-phase three-wire rotary transformer and a DFIM**

The successful operation of the proposed controller depends on the relative displacement of the successive switching vectors and the sector boundaries. For successful operation of the controller, the following conditions need to be fulfilled:

(i) Each switching vector must lie exactly at 90º phase apart from two sector boundaries

(ii) Between two consecutive sector boundaries, at least one switching vector should be present

(iii) None of the sectors should be wider than 90º.

In both Figure 7.6 (balanced operating condition) and Figure 7.12 (30º phase unbalanced condition) it can be seen that all the above three conditions are satisfied. For example, in Figure 7.12 the sector boundary 1 lies exactly at a 90º phase displacement from S2 and S5. The same result can be verified for all other sector boundaries. Similarly, it can be seen between two sector boundaries there is at least one switching vector (figures 7.6 and 7.12). For example, in Figure 7.12 for sector 1 and sector 4, the vectors S1 and S4 lie just on the boundary of the sectors, which may be the limiting case, but still a valid case. Similarly, it is seen that none of the sectors in figures 7.6 and 7.12 are wider than 90º. In Figure 7.12, sector 3 and sector 6 are just 90º wide. So, again, it may be inferred that this is the limiting case, but still is a valid operating condition.

The switching vectors, sector boundaries and the sector width for the worst-case scenario (i.e., at maximum unbalanced operating condition [short circuit condition] are given in Figure 7.13. For this case only, the first condition is satisfied. On the other hand the second and third conditions are violated. For example, in sector 1, sector 2, sector 4, and sector 5 there is no switching vector. Similarly, the widths of sector 3 and sector 6 are 120º, which is in violation of the third condition. Thus, it may be concluded that this operating condition is not a valid stable condition.

Following a similar process, if the system is investigated for other unbalanced operating conditions, it can be found that for any phase unbalance more than 30º between the three phases of the rotary transformer, the proposed control algorithm will be unstable. Similarly for any phase unbalance less than or equal to 30º the system will be controlled satisfactorily. The locus of the switching vector S2 and S5 for different degrees of unbalanced conditions and their stable and unstable operating zones are plotted in Figure 7.14. It may be noted that S1, S2, … S6 represent the vector location during 100% balanced condition. For the present system, they represent the case for no-load operation. Similarly, the location of S1', S2', … S6' represents the worst-case unbalanced condition, which is the short circuit condition for the present system. However, in reality the switching vectors will neither operate in short circuit condition nor purely at no load condition. Therefore, the location of the vectors will depend on the operating load, and they will be somewhere in between the above two extreme positions. Over the entire operating region, the system will be divided in two halves depending on their operating condition (i.e., operating loads). If the switching vectors are located within a 30º region from their balanced operating point, then they are well within the stable operating region. Any vector lying beyond 30º region from the balanced operation position is called an unstable operating point. In Figure 7.14, the stable and unstable operating regions are distinctly divided by shaded and dotted area.

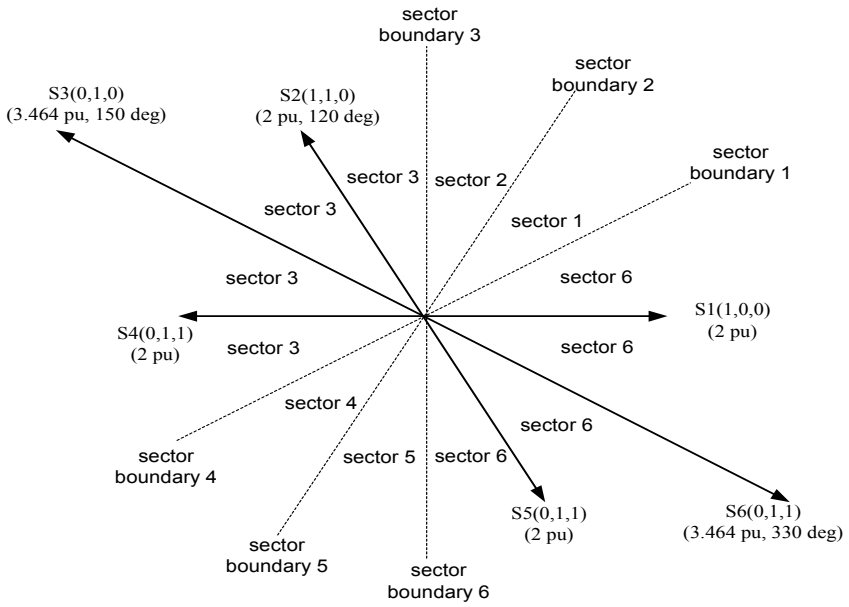


**Figure 7.13. Switching vectors and designated sectors for a maximum phase unbalanced condition (60º unbalanced system found with short circuit condition) of the system composed of a two-phase three-wire rotary transformer and a DFIM**

vectors are located within a 30º region from their balanced operating point, then they are well within the stable operating region. Any vector lying beyond 30º region from the balanced operation position is called an unstable operating point. In Figure 7.14, the stable and unstable operating regions are distinctly divided by shaded and dotted area.

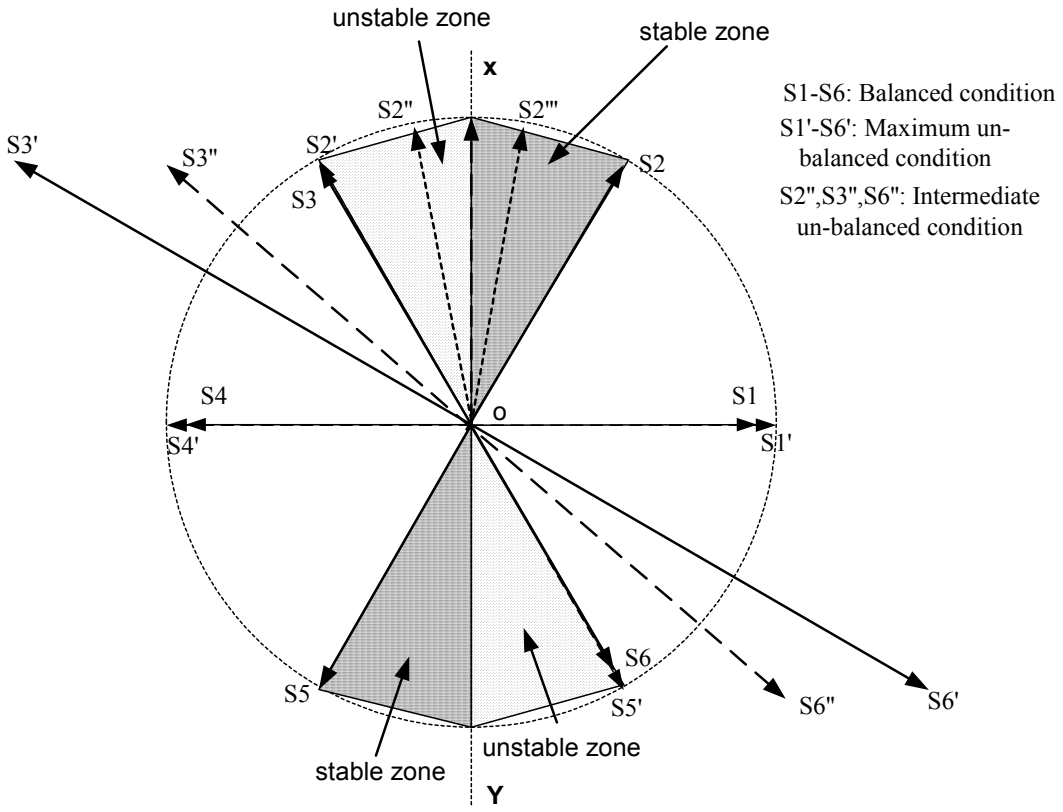


**Figure 7.14. Locus of the switching vectors from maximum unbalanced condition (short circuit condition) to a fully balanced condition (open circuit condition) and the corresponding stable and unstable operating zones**

The controller works up to a 30º phase unbalanced condition for the present rotary transformer application. It may be concluded that the system works well for any phase unbalance less than or equal to 30º. However, we now need to investigate if the system works well for unbalanced conditions more than 30º. The simulation results show that the degree of unbalancing for the present system with rotary transformer is directly a function of load, and it is necessary to verify the validity of the proposed controller throughout the operating regime.

The locus of the switching vectors for different load conditions and their relative displacements are given in Figure 7.13. The phasors S1, S2… S6 represent the balanced operating condition, which is the case for the open-circuit or no-load operating conditions (Figure 7.13) for the present system. Similarly S1', S2', … S6' represents the location of the switching vector for the short-circuit condition or the maximum unbalanced condition. The magnitude of the switching vectors and their relative phase displacement for this condition are not uniform. However, the location and magnitude of phasors S1 and S4 remain the same for all the time. Only the switching vectors S2, S3, S5, and S6 alter their magnitude and location depending on the degree of unbalancing. The switching vectors S2', S3', S5', S6' represent some intermediate locations of these vectors for some other unbalanced conditions.

From the above diagram, it is clear that the phase angles between S2 and S2' and between S5 and S5' varies by 60º depending on the operating load. Similarly, the phase angles between S3 and S3'; S6 and S6' varies by 30º. Given the nature of the controller, the switching vectors S1, S3, S4, and S6 do not pose any problem for the system operation. However, the position or swinging of vectors S2 and S5 is a concern. Their positions vary by almost 60º, which makes the relative displacement between consecutive switching vectors more than 90º. Operation during those sectors becomes unstable.

The system works well for a 30º phase unbalance. However, for the system having more than 30º unbalance, it does not work. The system tends to become inherently unstable. Because the degree of phase unbalancing of the present system is directly a function of the load, it may be inferred that the system will work up to a certain load (approximately up to 75% load). Up to that stable operating load, the machine torque as well as the current waveforms can be controlled smoothly with the proposed controller. However, beyond 75% load, the system behaves unpredictably with the proposed controller and sometimes, the system is rendered instable. The proposed control algorithm, even though is capable of handling a great deal of unbalancing in a system, it is not quite adequate for controlling the present two-phase rotary transformer over its full operating load regime. Therefore, either an alternative control algorithm needs to be found or the topology of the rotary transformer has to be changed to fit with the proposed controller for successful operation of the system with a rotary transformer. However, it may be concluded that for a three-phase balanced rotary transformer, the proposed controller will be an excellent choice.

This is because the controller can work up to a 30º phase unbalanced condition. For the present system with rotary transformer This appears to be located in the middle of the operating region. Therefore, it may be concluded that the system works well for any phase unbalance less than or equal to 30º. However, it may be inferred from the phasor diagram that any phase unbalance more than 30º may cause system instability. With the latter case, the relative displacement between two consecutive switching vectors may exceed 90º and two consecutive sectors may overlap each other, and the system will loose uniform controllability. Thus, it can be concluded that, with less than 30º phase unbalance, the proposed direct power control algorithm works satisfactorily and beyond that it does not work. Selection of active and zero switching vectors at different conditions for the stable operating region are given in tables 7.1, 7.2, and 7.3.

**Table 7.1. Selection of Active Switching States When $P_{err} \leq 0$**

| Switching State | Sector 1 | Sector 2 | Sector 3 | Sector 4 | Sector 5 | Sector 6 |
|---|---|---|---|---|---|---|
| $Q_{err} > 0$ | S3 | S4 | S5 | S6 | S1 | S2 |
| $Q_{err} \leq 0$ | S2 | S3 | S4 | S5 | S6 | S1 |

**Table 7.2. Selection of Active Switching States When $P_{err} > 0$**

| Switching State | Sector 1 | Sector 2 | Sector 3 | Sector 4 | Sector 5 | Sector 6 |
|---|---|---|---|---|---|---|
| $Q_{err} > 0$ | S5 | S6 | S1 | S2 | S3 | S4 |
| $Q_{err} \leq 0$ | S6 | S1 | S2 | S3 | S4 | S5 |

**Table 7.3. Condition for Selection of Zero Vector**

| Speed | Motoring | Generating |
|---|---|---|
| Sub-synchronous | $Q_{err} \geq 0$ and $P_{err} \geq 0$ | $Q_{err} < 0$ and $P_{err} \geq 0$ |
| Super-synchronous | $Q_{err} < 0$ and $P_{err} < 0$ | $Q_{err} \geq 0$ and $P_{err} < 0$ |

## 7.7 Simulation Results with and without Rotary Transformer

Utilizing the modified control algorithm, the complete system including the unbalanced rotary transformer, the DFIM, and the power converter was simulated in SABER (figures7.12 to 7.18). The results showed that the proposed control algorithm works well with a rotary transformer up to a certain load (approximately up to 75% load). The plots show that both the stator active and reactive powers are controlled in desired fashion within the stable operating regime. In figures 7.12 to 7.15, the different waveforms of the system are plotted when the system is simulated with a two-phase unbalanced rotary transformer, along with the wound-rotor induction machine. Both the primary- and secondary-side currents through the rotary transformers are plotted along with stator currents, stator active power (Ps), stator reactive power (Qs), speed, and torque of the system. In these plots, the secondary side (stationary) of the transformer is connected to the converter, and the primary side (rotating) is connected to the rotor winding. The currents on the converter side (iras, irbs, ircs) are visibly unbalanced in nature (from the top, trace 1 in Figure 7.12, trace 2 in Figure 7.14, trace 3 in Figure 7.16). The rotor-side currents (ira, irb, irc) in all the plots are almost balanced. The three-phase stator currents (ias, ibs, ics) are also plotted. It may be seen that they also are closely balanced and that they maintain almost unity power factor over the entire stable operating range. Thus, it can be concluded that, applying our proposed control algorithm, satisfactory control is possible in an unbalanced system up to 30º.

Also, the proposed control algorithm works well for both sub- and super-synchronous operating ranges (figures 7.12 to 7.16). Figure 7.16 displays conditions for the machine operating at approximately 1.25 pu speed while the load torque is varied monotonically from 50 Nm (20%) to 180 Nm (75% load). Note that the system works well within that operating condition.

However, when the machine operates near synchronous speed, the rotor currents and voltages become almost DC quantity, and the transformer starts saturating. The simulation results of the system when it approaches synchronous speed are given in Figure 7.17. The system works smoothly down to 6% operating slip, and below that the transformer starts saturating.

To verify the system performance over its entire operating region, the machine is made to operate at 0.8 pu speed, and the load torque of the machine is varied from 20% to 100%. At about 200 Nm load torque, the machine operation becomes unstable (Figure 7.18). At about 200 Nm load, the machine loses stability; none of the machine variables - for example, stator and rotor currents, torque, speed, Ps, and Qs- give the desire values after it looses stability. Thus, it may be inferred that beyond 75% load, the system does not behave stably with the proposed controller.

The system was simulated with the control algorithm for direct stator power when the rotary transformer was not connected to the machine. In this case, the system works well over its torque and speed operating regimes without any stability problem. The simulation results of the wound-rotor induction machine along with a regular IGBT inverter and this control algorithm are given in figures 7.19 to 7.22 for both sub- and super-synchronous operation. Both steady state and transient results are provided for the entire operating region.

Once again, the system was simulated with a rotary transformer and diode bridge chopper combination with the assumption that the direct measurement of rotor currents is possible. With such measured values (Fig. 7.23). The resulting torque ripple in this plot is less compared to the results without rotor current measurement (Figure 7.24). However, this was a fictitious case. In reality the rotor current cannot be measured directly because the rotor winding is rotating with the shaft. It is difficult to mount the measuring devices.

The regular field-orientation control algorithm with a regular IGBT inverter and rotary transformer was also verified in a simulation assuming that the direct rotor current is available for control purposes (Figure 7.25). The system performance was improved greatly with such controller if rotor current measurement was possible. The torque ripple produced by the machine is much smaller.

## 7.8 Conclusions

In this chapter, a variety of rotor side control algorithms for a DFIM with or without rotary transformer were examined. First, the characteristics of a two-phase rotary transformer was illustrated through simulation, and it was shown that the rotary transformer behaves from a balanced system to a maximum 60º phase unbalancing as the operating point varies from conditions of no-load to short-circuit load. In addition, the controller design for such system becomes critical because direct rotor winding current measurement is no longer possible. The rotor windings rotating with the rotary transformer are not accessible from outside the machine. Many rotor-side controllers including the field-orientated controller, ideally require measurement of the rotor winding currents. However, their inaccessibility in this system complicates the situation.

The performance of a diode bridge and chopper controller with such an unbalanced system was verified. The system produces excessive torque ripple. Thus, an alternative control algorithm is needed.

Finally, a control algorithm for direct stator power was devised, and its operating principle was explained in relation to the present unbalanced system. Through analysis and simulation, we found that such a controller works well with the above unbalanced system up to 75% load. Control performance within this operating zone was excellent. However, for loads beyond 75%, the system behaves unpredictably, and the system looses its stability. Therefore, it can be concluded that even though the proposed controller is inadequate for controlling the system over its entire operating regime, the applicability of such controller up to a certain unbalancing can be established. However, for a system with a three-phase balanced rotary transformer, the proposed controller can be considered an excellent choice.

The behavior of the controller and rotary transformer around synchronous speed was demonstrated. The system operates well for a slip more than or equal to 6%. However, for slips less than 6%, the rotary transformer tends to saturate, and the system looses its stability. This instability may be considered another shortcoming for a rotor-side control of a system based on a rotary transformer. This instability can be observed irrespective of the three-phase or two-phase configuration. For a system with rotary transformer, the double-side control algorithm (as explained in Chapter 5) would be an ideal solution because the rotor frequency can be varied at will.

Finally, a fictitious condition was simulated assuming that direct rotor current measurement is possible. With this assumption, the system was simulated with a diode bridge chopper combination. The system performance was improved partially. Similarly, we verified a field-orientation control algorithm and the performance of the system improved greatly. However, because rotor current measurement was difficult to obtain, the last two control schemes cannot be implemented in a real-world case.

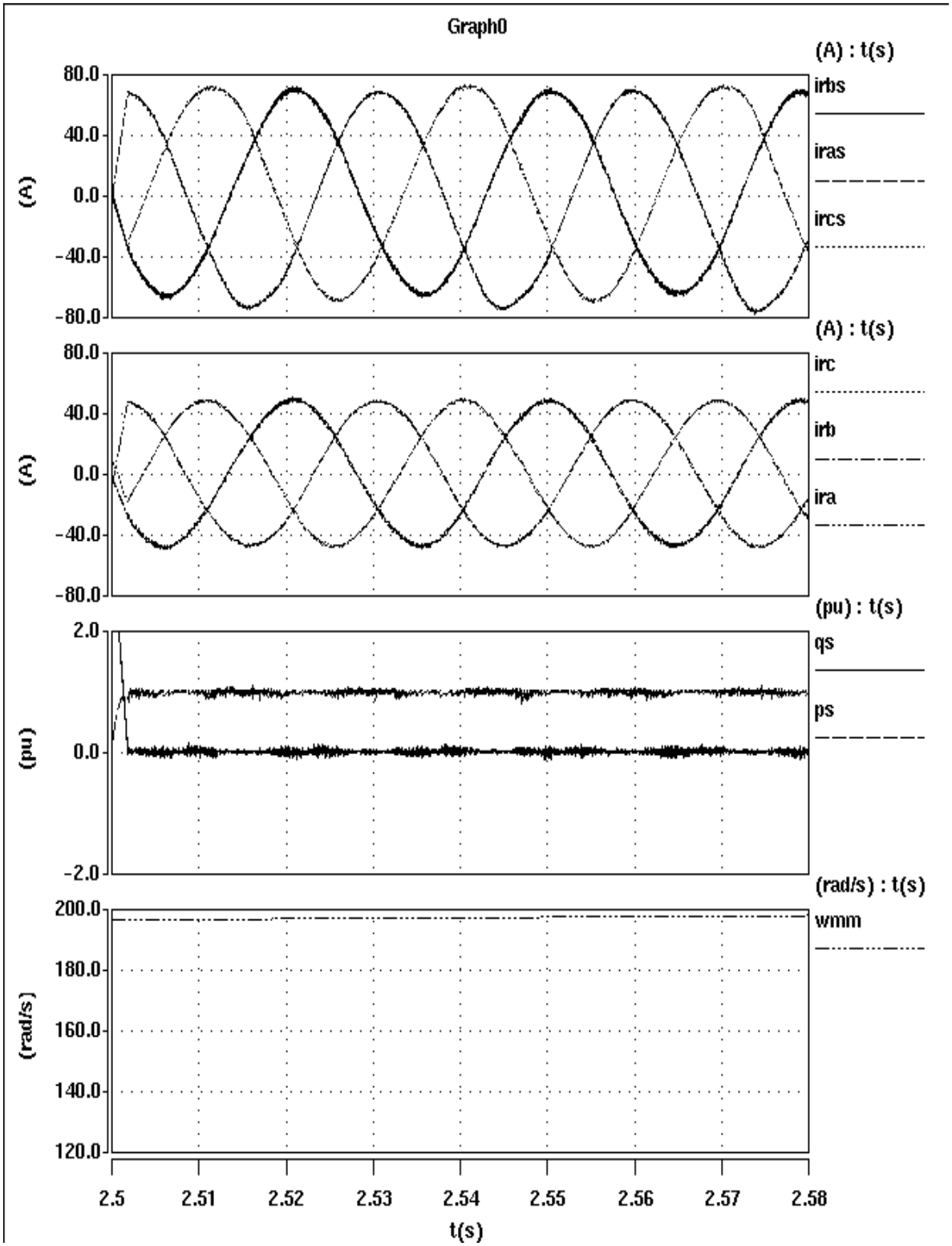


**Figure 7.12. Simulation results of the complete system with the proposed modified control algorithm for direct power with an unbalanced condition in the super-synchronous region**

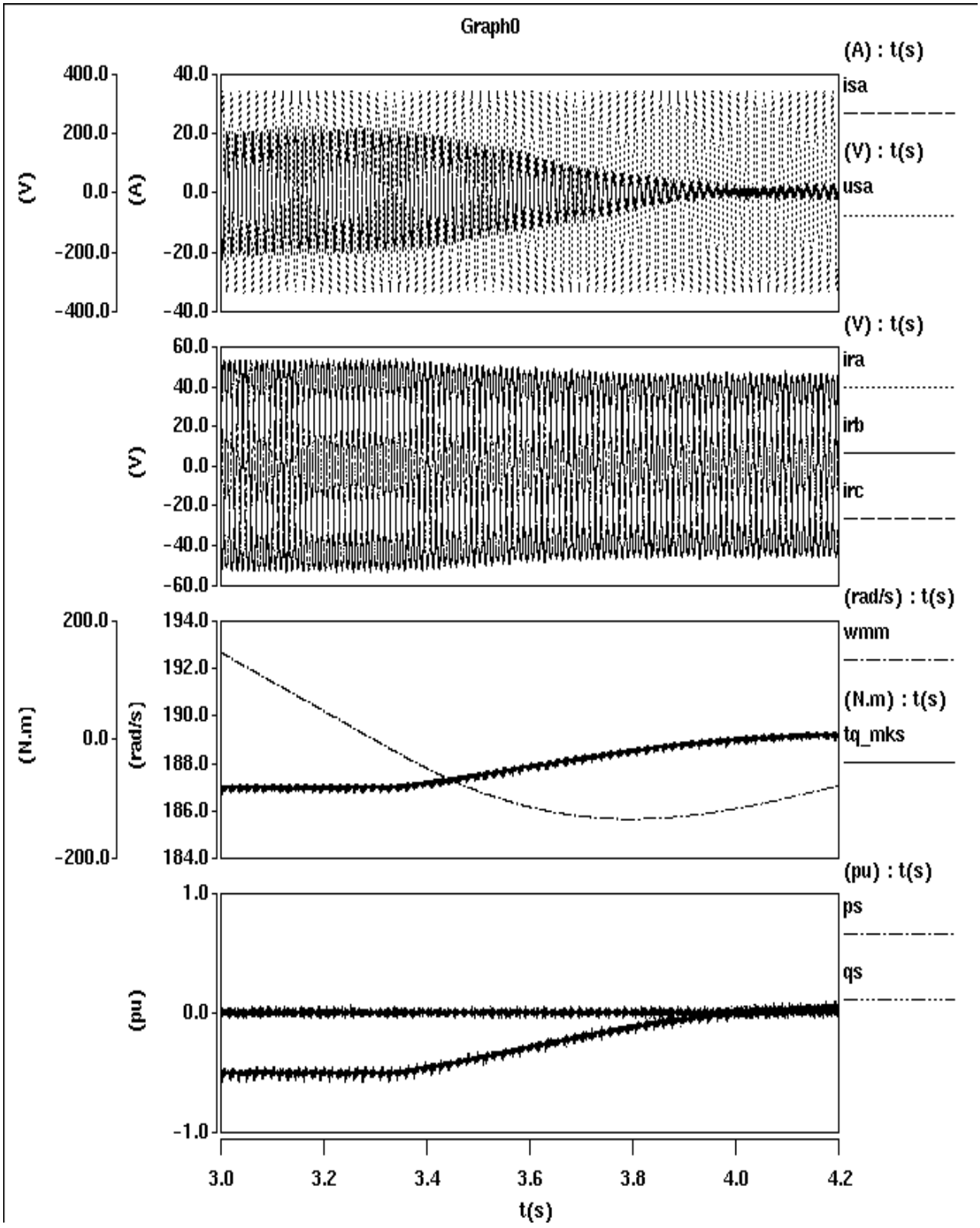


**Figure 7.13. Simulation results of the complete system with the proposed modified control algorithm for direct power with an unbalanced condition (super-synchronous speed, transient condition)**

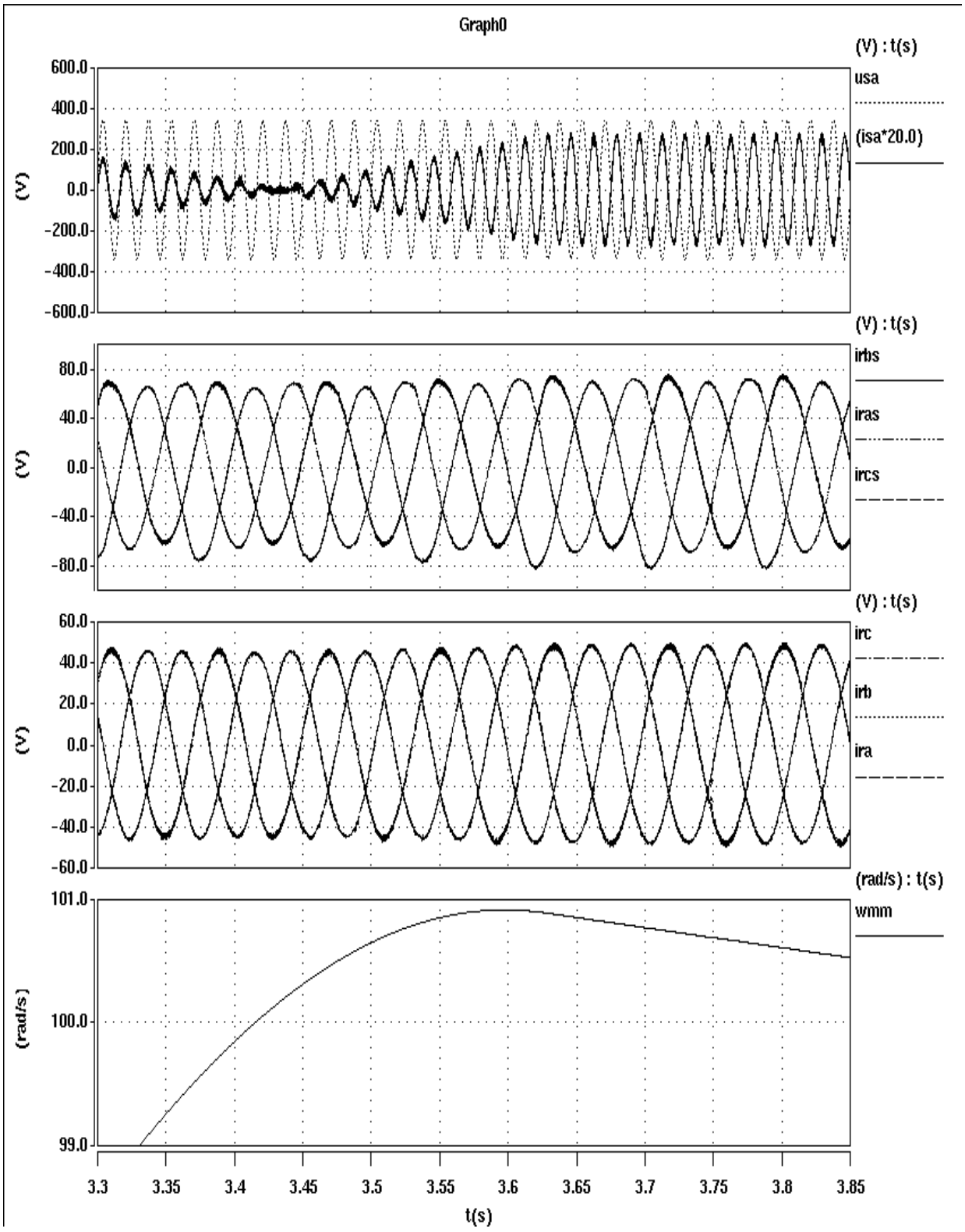


**Figure 7.14. Simulation results of the complete system with the proposed modified control algorithm for direct power with an unbalanced condition at sub-synchronous speed range (40% load)**

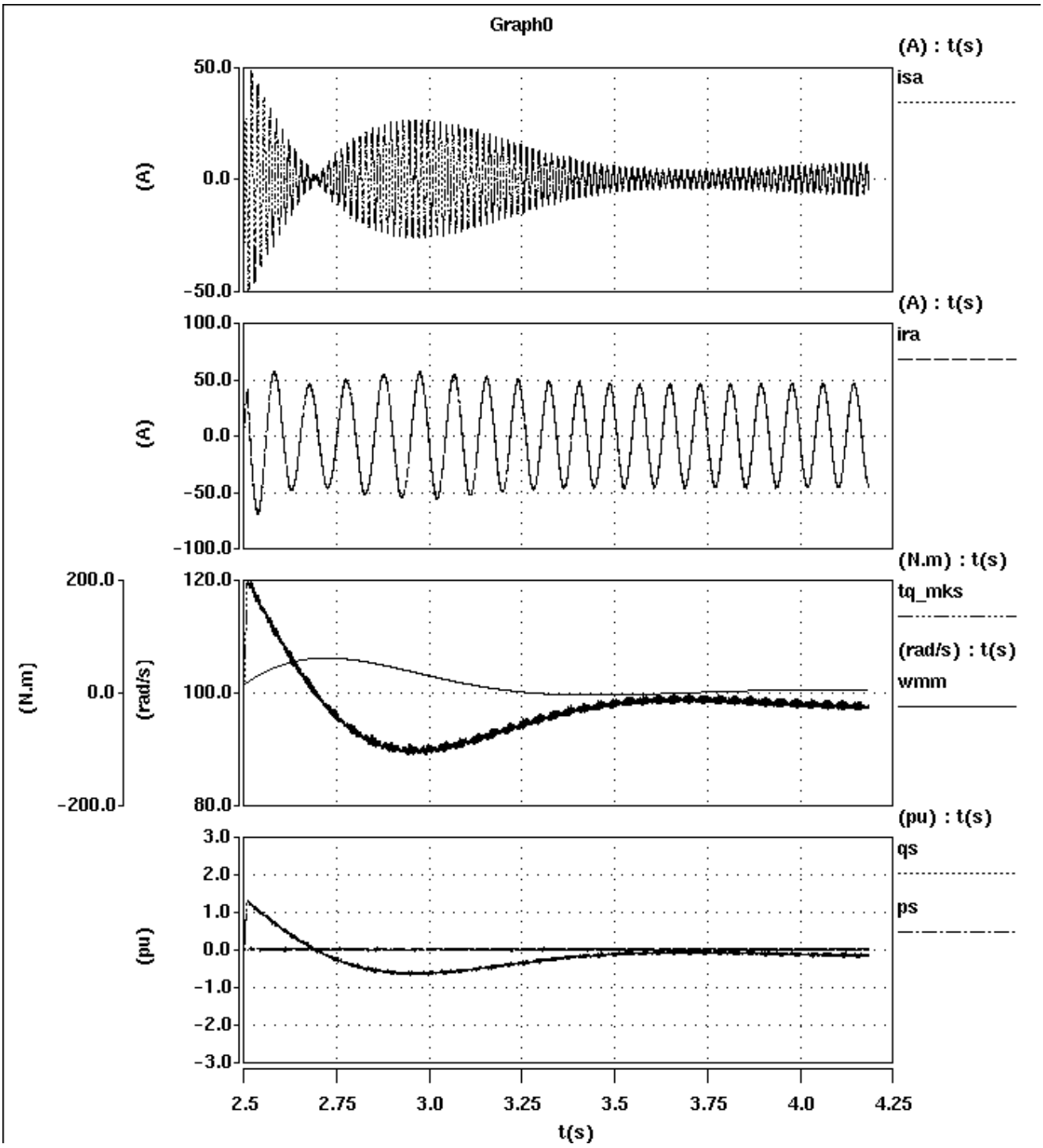


**Figure 7.15. Simulation results of the complete system with the proposed modified control algorithm for direct power with an unbalanced condition at sub-synchronous speed range (20% load)**

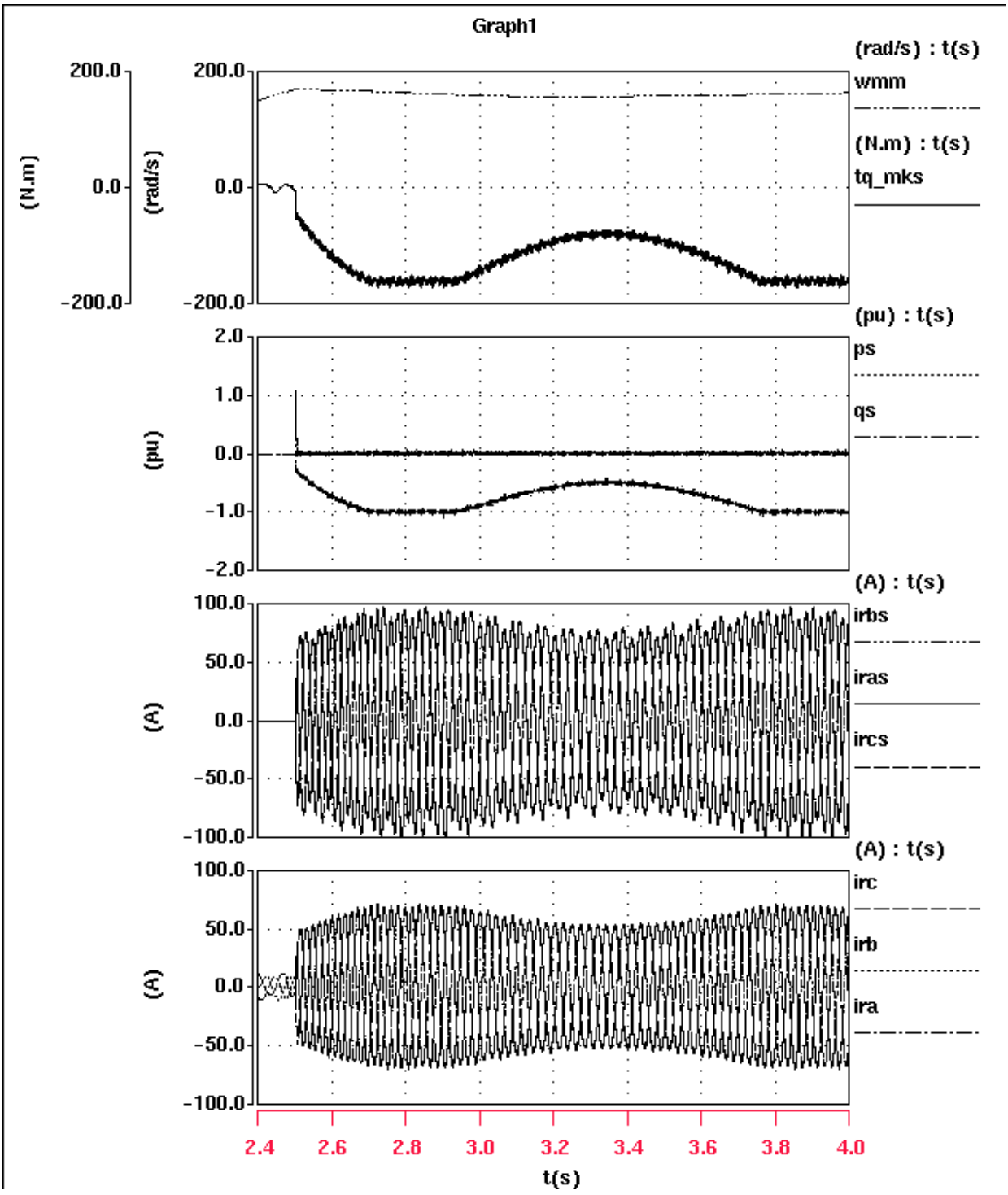


**Figure 7.16. Simulation results of the complete system with the proposed modified control algorithm for direct power with an unbalanced condition at 1.25 pu speed (super-synchronous speed range) when load torque varies from 20% to 75%**

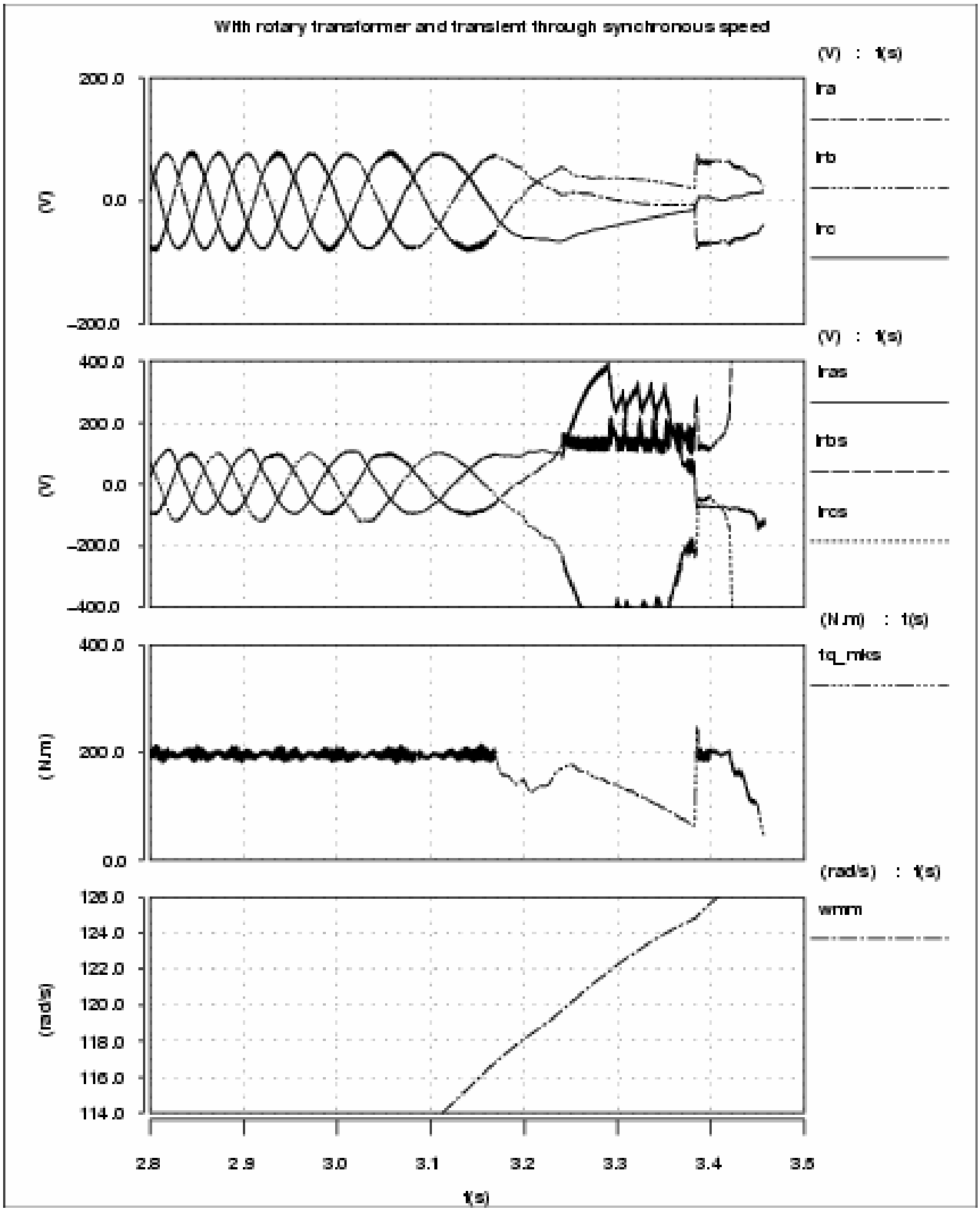


**Figure 7.17. Simulation results of the complete system with the proposed modified control algorithm for direct power near synchronous speed**

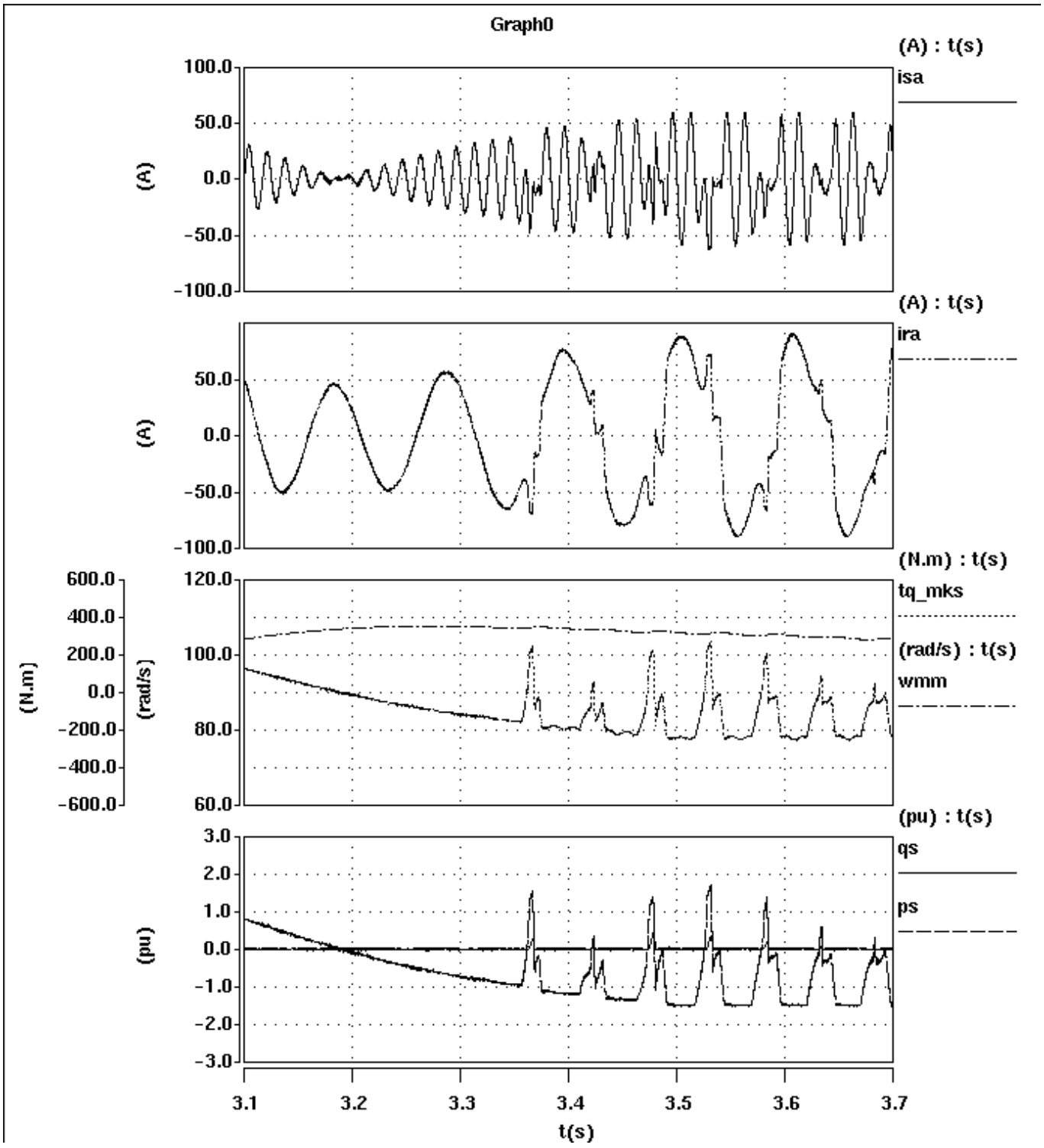


**Figure 7.18. Simulation results of the complete system with the proposed modified control algorithm for direct power with an unbalanced condition at 0.8 pu speed (sub-synchronous speed range) when load torque varies from 20% to 100%**

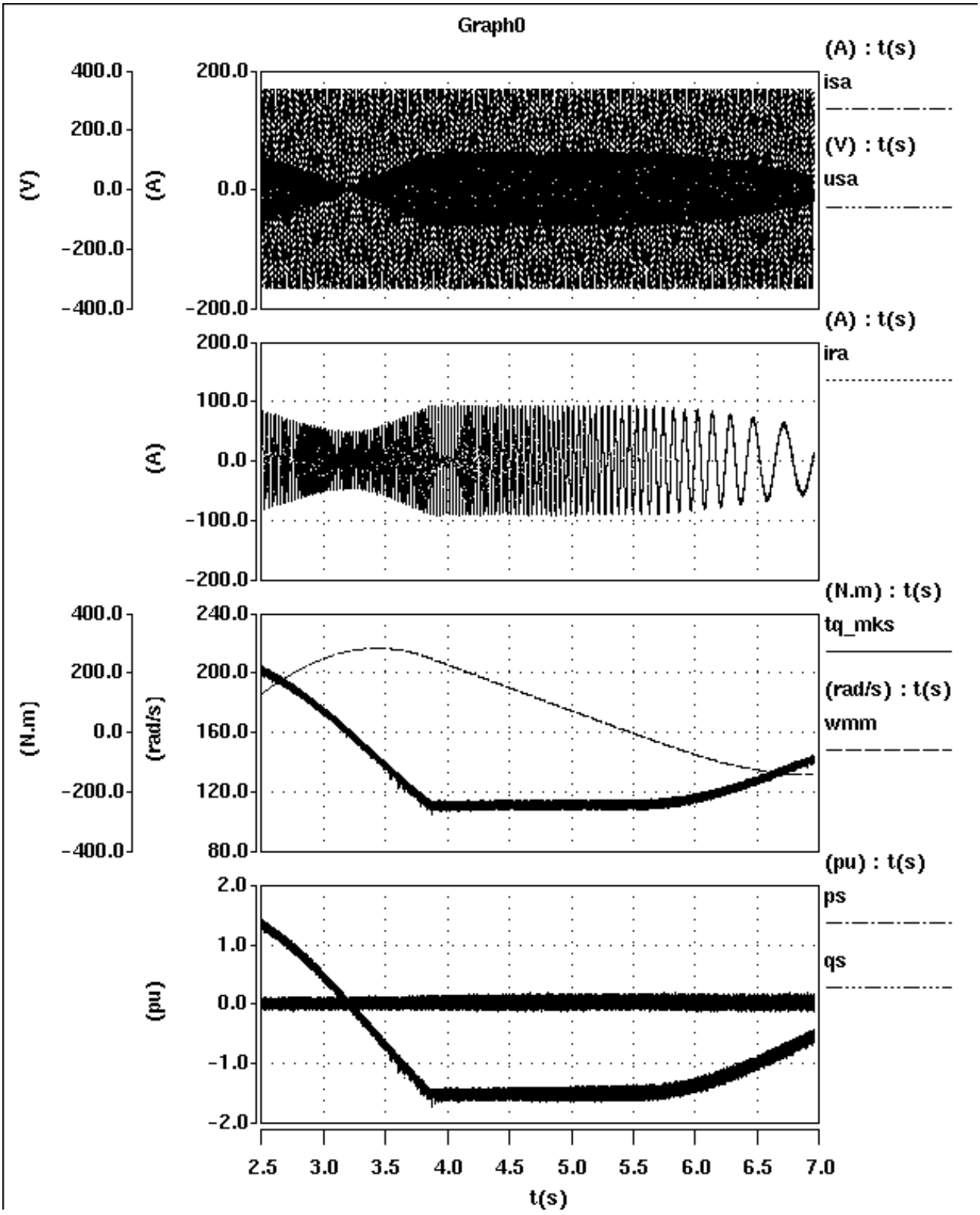


**Figure 7.19. Simulation results for super-synchronous operation of a DFIM control with a control algorithm for direct power and without rotary transformer (100% balanced condition)**

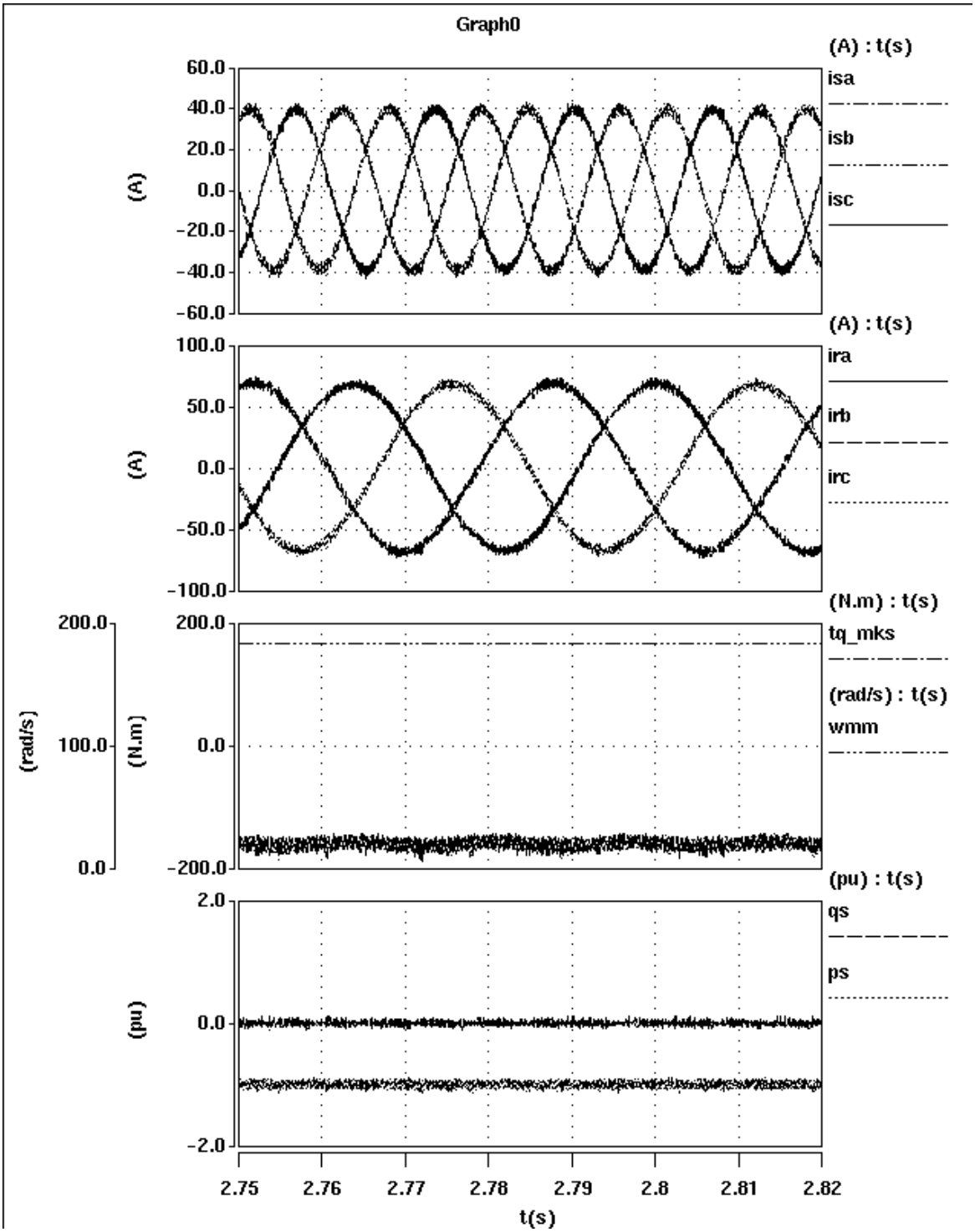


**Figure 7.20. Simulation results at super-synchronous operation of a DFIM control with a control algorithm for direct power and without rotary transformer (100% balanced condition)**

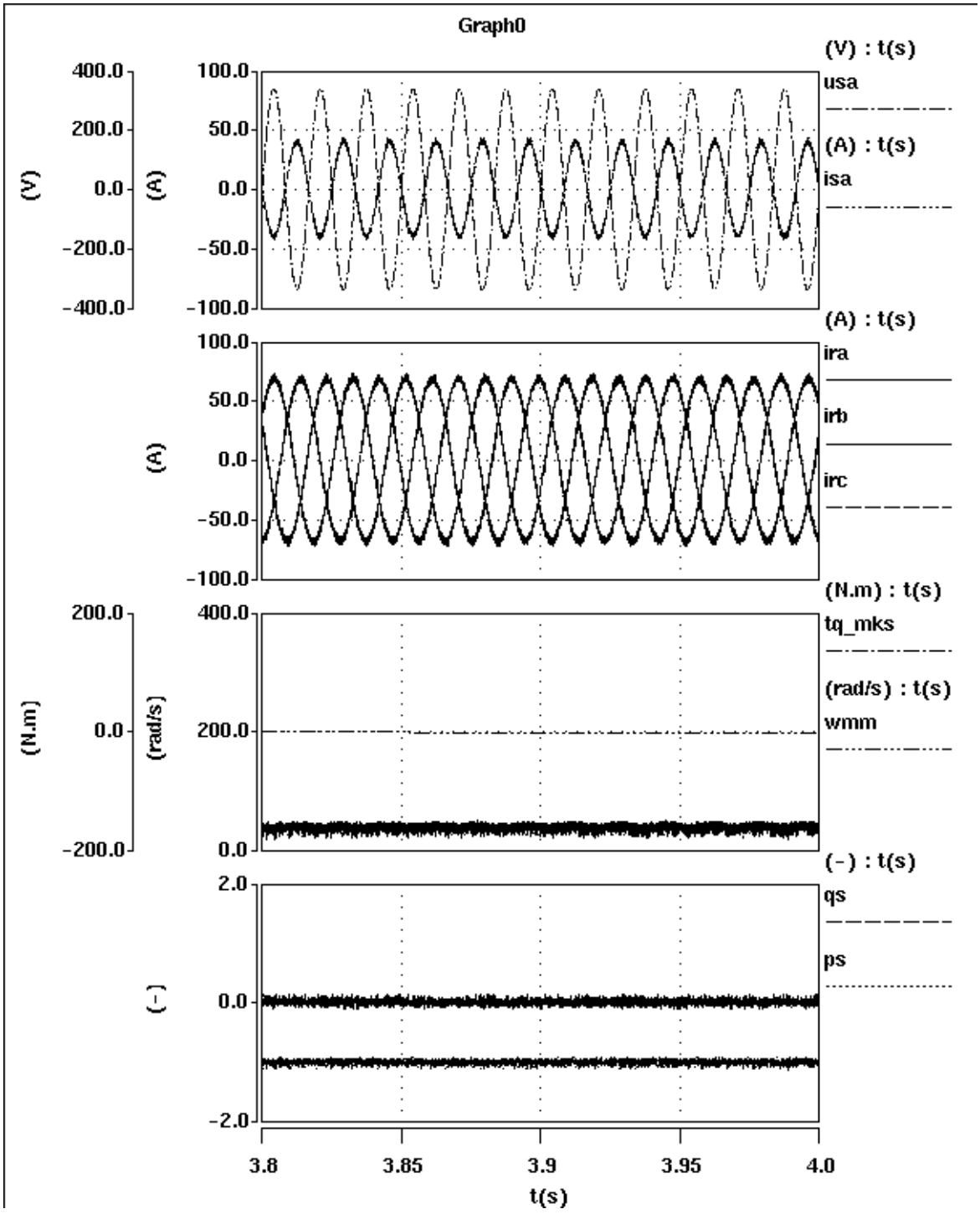


**Figure 7.21. Simulation results of a DFIM control with a control algorithm for direct power and without rotary transformer (100% balanced condition)**

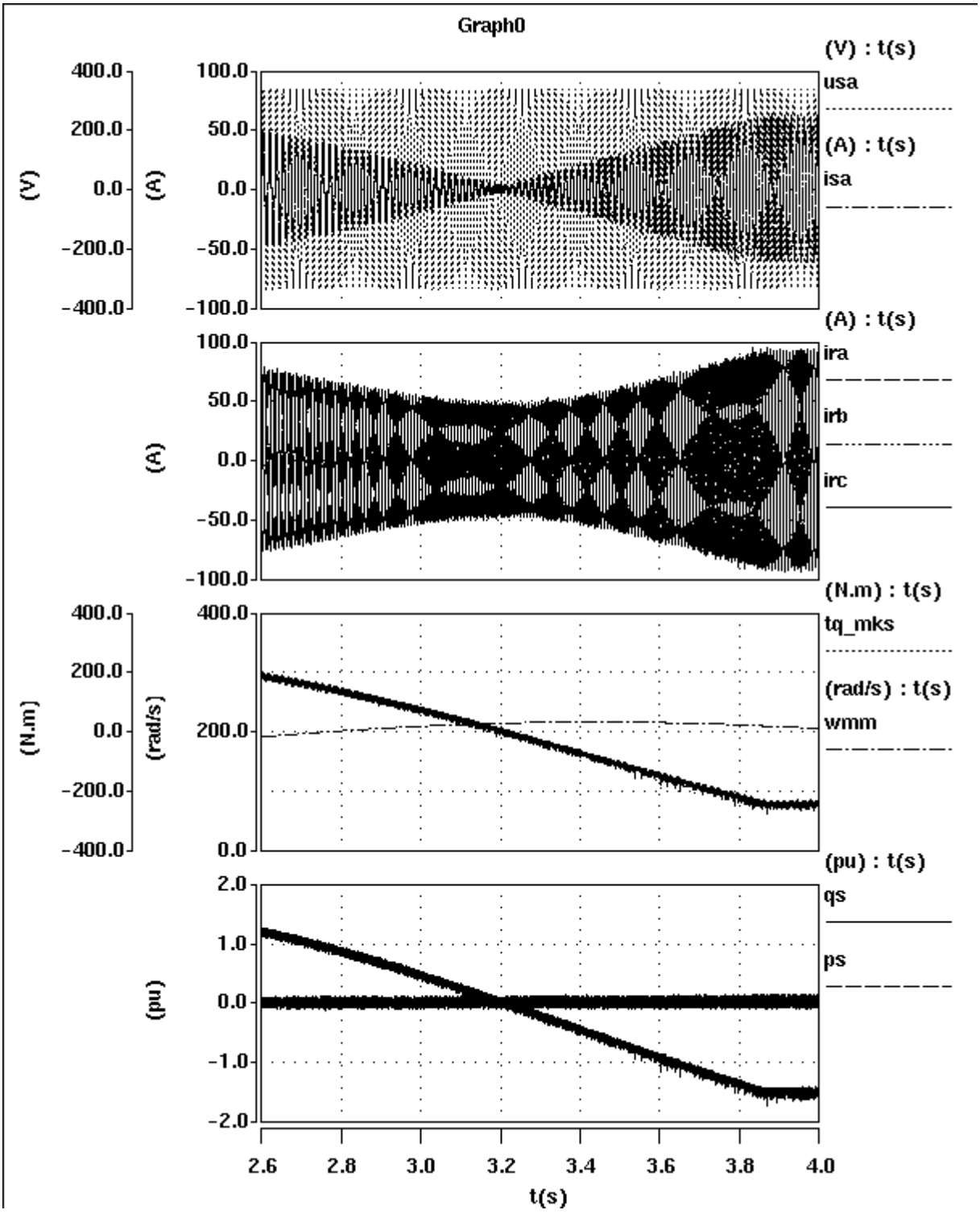


**Figure 7.22. Simulation results of a DFIM control with a control algorithm for direct power and without rotary transformer (100% balanced condition) during a super-synchronous motoring to generating mode transient**

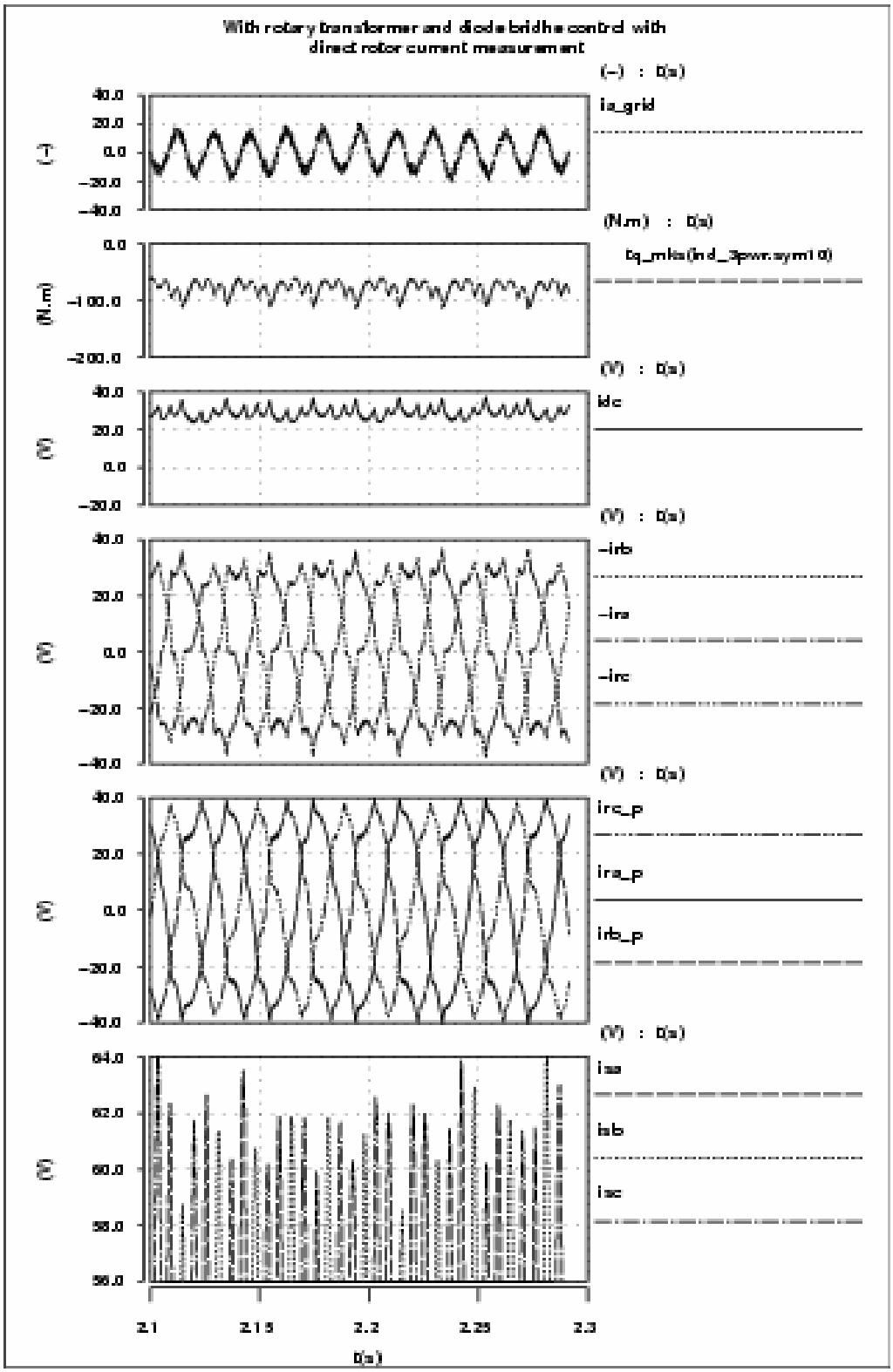


**Figure 7.23. Simulation results of a DFIM control with diode bridge and boost chopper combination, along with a rotary transformer when the rotor current is measured directly**

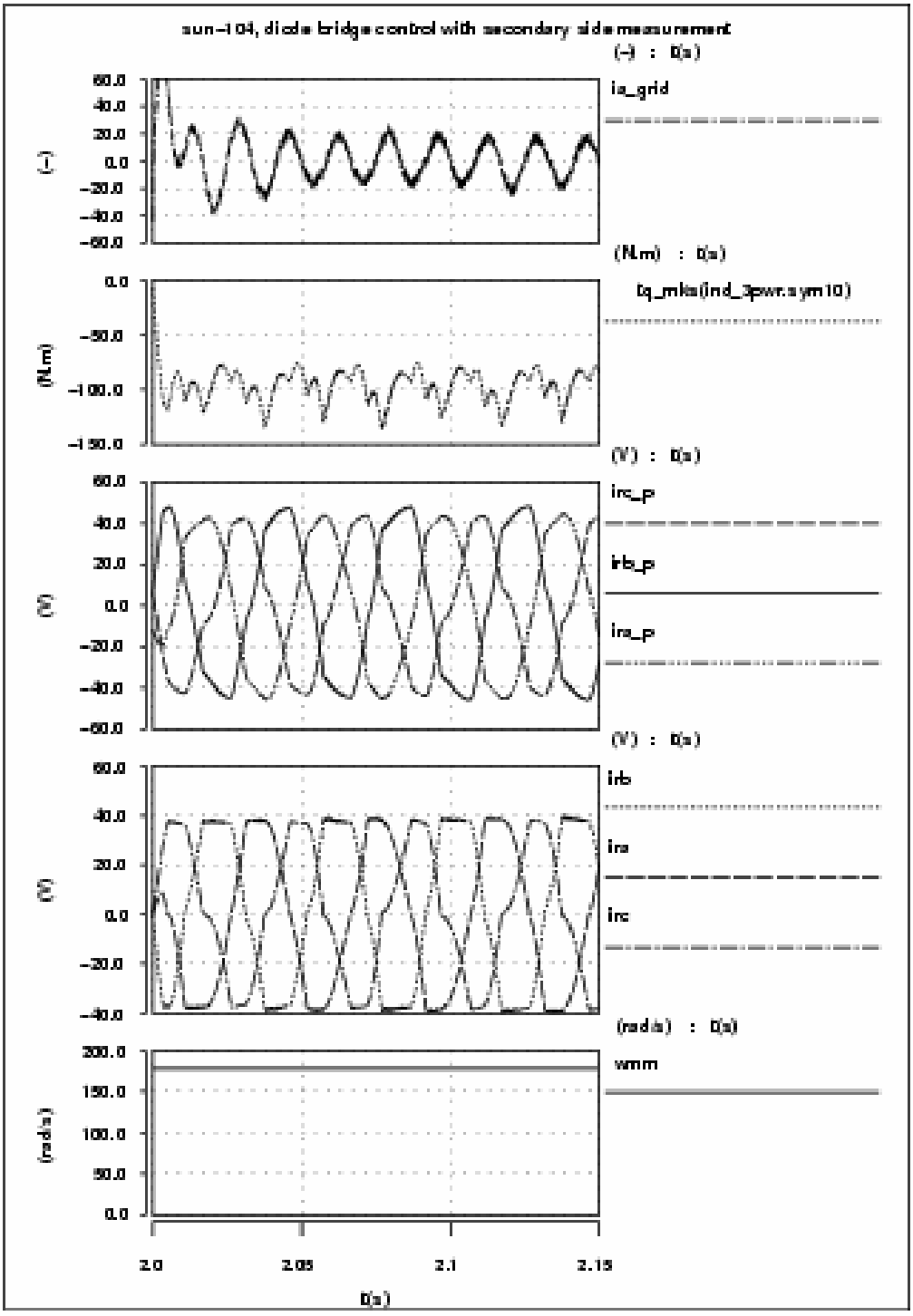


**Figure 7.24. Simulation results of a DFIM control with diode bridge and boost chopper combination, along with a rotary transformer when the rotor current is not measured directly**

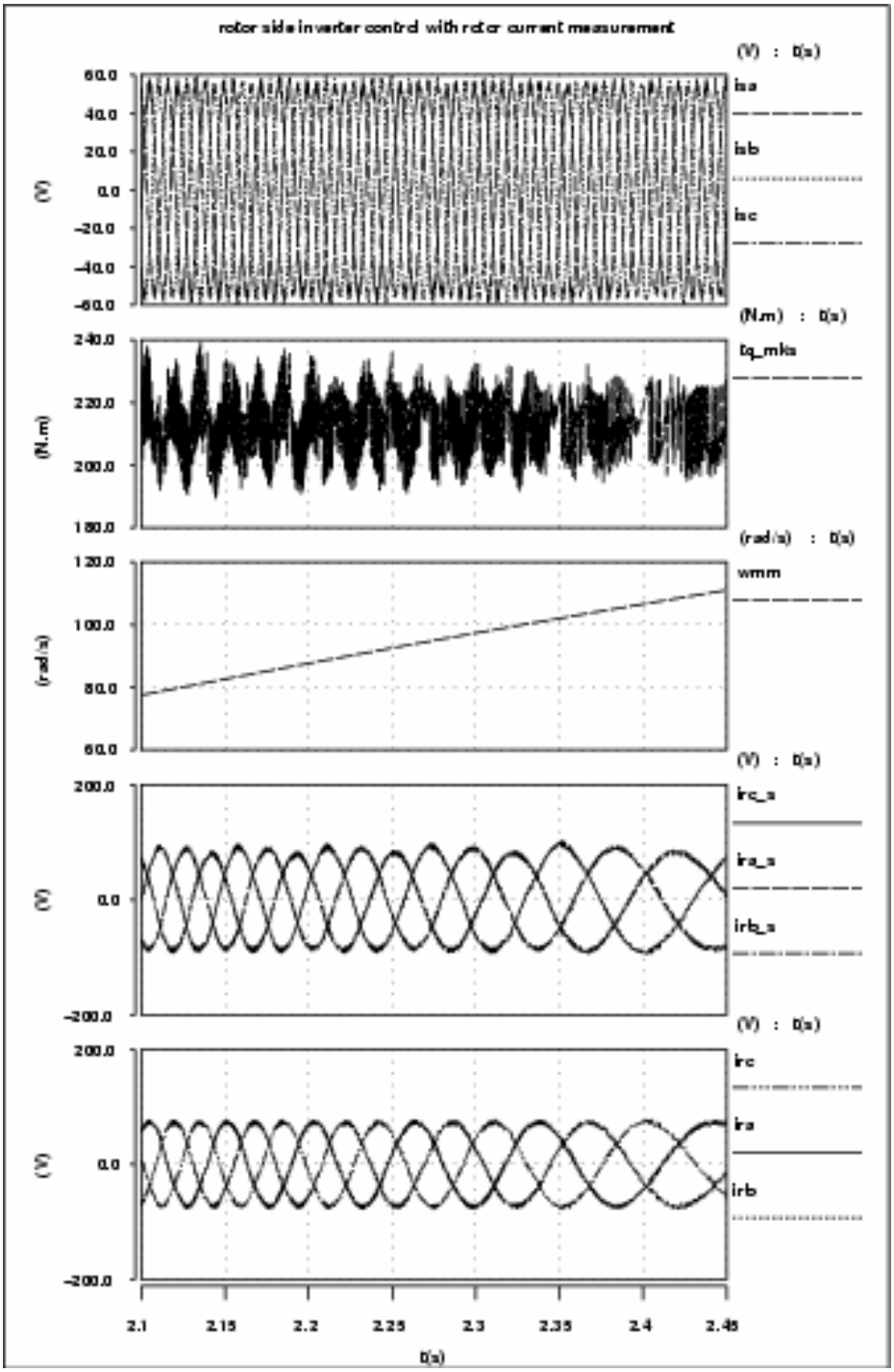


**Figure 7.25. Simulation results of a DFIM control with field-orientation control by a regular IGBT inverter, along with a rotary transformer when the rotor current is measured directly for controlling the drive**

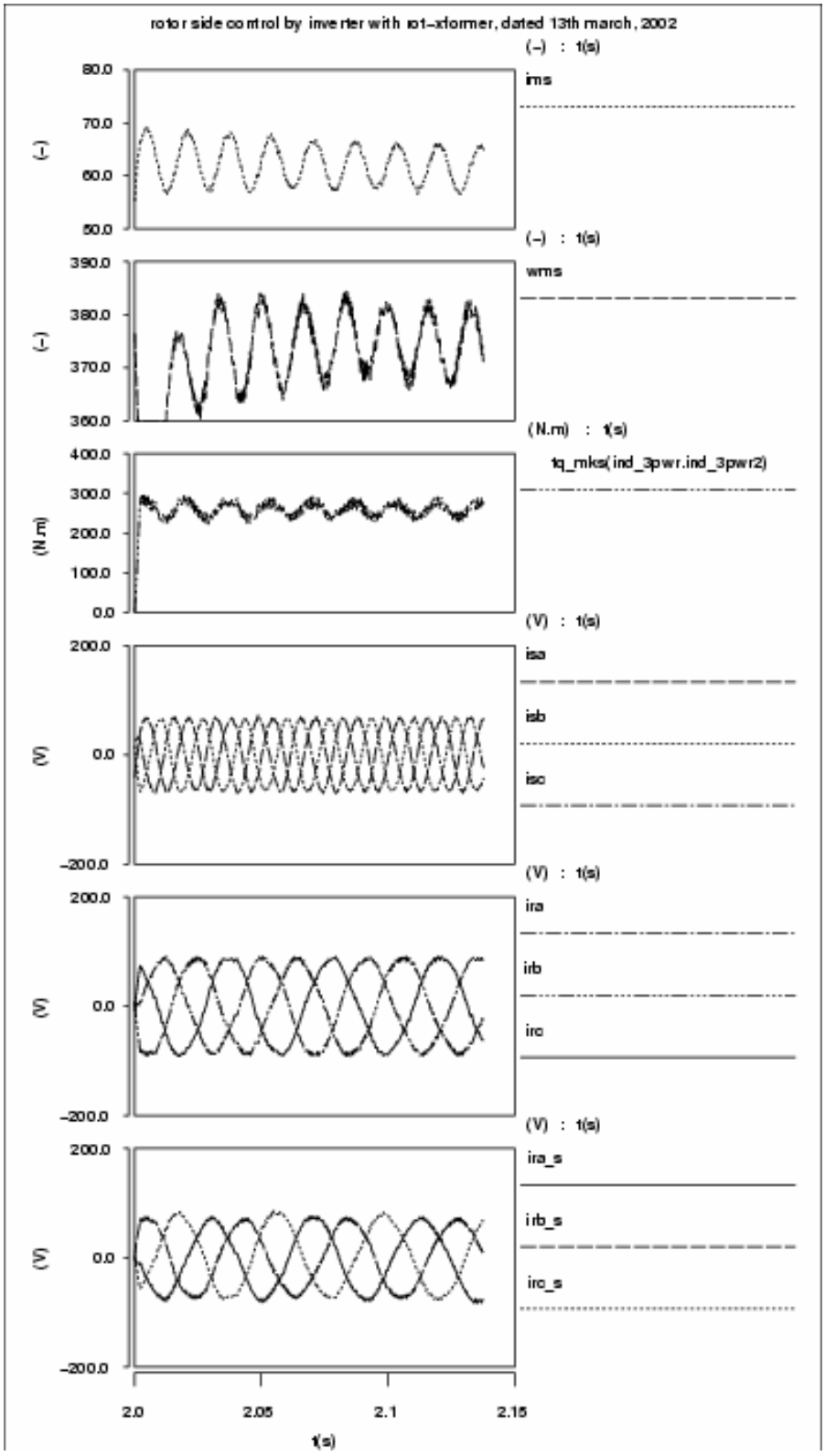


**Figure 7.26. Simulation results of a DFIM control with field-orientation control by a regular IGBT inverter, along with a rotary transformer when the rotor current is not measured directly for controlling the drive**

# Chapter 8: Development of a Power Converter and DSP Control Platform and Experimental Test Results

## 8.1 Overview

The converter topologies and detailed simulation results of the complete system, including the controller for various proposed power converters, have been discussed in the previous chapters. In this section, we focus on hardware development for the experimental setup. Based on SABER simulation of the complete system, we obtained the design values of the semiconductor devices and the passive elements like inductors and DC-link capacitors. The detailed parts list and photographs of important hardware components are presented in this chapter. Two DSP-based control boards (TMS320F240, Texas Instrument) with required digital and analog interfacing were developed for controlling the FEC and the machine-side converter. Two integrated inverter modules with six IGBTs, necessary gate drivers, and heat sink were packaged as one unit (SKIIP module) purchased from SEMIKRON. The other important components such as DC-link capacitors, inductors (line-side), contactors, sensors (for voltage and current sensing), fuses, and suitable connectors were obtained from different vendors. A DC-link braking resistor along with an IGBT switch was designed for over-voltage protection of the DC bus. For testing the setup, a 40-hp Danfoss drive and a Baldor motor were used and these items were installed employed in the present setup. A two-phase rotary transformer along with a DFIM has been fabricated by WEG Motors of Jaragua do Sul, in Brazil, and currently this company is testing different loads. A representative set of test results is included in this report. While awaiting the delivery of the special DFIM with rotating transformer, the hardware setup for testing this drive was completed and tested with a 7.5-kW V/F induction motor drive. We present typical experimental result with the above induction motor control with the designed experimental setup as a testimony of the functionality of the hardware. We will begin testing the DFIM as soon as it arrives from the manufacturer. Photographs of the prototype experimental setup are also included in this chapter.

## 8.2 Introduction

Because our research was intended to test a two-phase unbalanced rotary transformer, it was desirable to have a back-to-back configuration composed of two-full bridge inverters for the experimental setup. The full-bridge inverters can be used as a half-controlled configuration if needed, so that the setup can also be used for testing the topology discussed in Chapter 5 for both stator- and rotor-side control of a wound-rotor induction machine using two half-controlled configurations. For the latter case, the generated power from both the stator and the rotor will be dumped into a DC bus, and this DC bus will be actively controlled for an R-L load for controlling the DC bus voltage.

The hardware design can be divided into two sections: design of the power module and design of the DSP-based control platform. The power module consisted of inverter, rectifier, and DC link. A braking resistor was incorporated across the DC bus, so that the DC bus voltage never exceeded a set value. For the control platform, a state-of-the-art DSP (TMS320F240) was selected for controlling the system. In the following sections we present the design of both the power module and DSP based controller.

## 8.3 Design of Power Module

Figure 8.1 shows the complete power electronics of the system, which was composed of a front-end active rectifier and machine-side inverter along with a doubly fed induction generator and rotary transformer. The major design objective for this system was to choose the power rating of the semiconductor devices (diodes and IGBTs) and to design passive elements like line-side inductors and DC-link capacitors. In addition, a three-phase inductor (not shown in Figure 8.1) was incorporated into the line-side for filtering the line side harmonics.

The design of the heat sink was also important because if the heat lost by the semiconductor device was not removed, the temperature at the device junction would exceed the specified value, and the device might cease to function. Hence, suitable cooling arrangements were necessary so that junction temperature never exceeded the specified value (in our case 125º C). Suitable cooling system design ensured proper functioning of the semiconductor devices.

### *8.3.1 Power Rating of Semiconductor Devices*

The intended power rating of the power electronics system is 30kW. The device selection is made based on a 50% overload condition. Because, the line-to-line voltage was 480 V, the DC bus voltage was designed for 700 V. Therefore, 1200-V devices were suitable for our system. Through SABER simulation, the full-load current rating of each individual phase was found to be 52 A. At a 50% overload condition, this value goes up to 76 A. As a consequence, the continuous current rating of each individual devices had to be more than 76 A. The final selection of devices was made based on availability of the components and lead-time of the vendors. The parts details for different semiconductor devices are given in Table 8.1. For the inverter, an intelligent power module (SkiiP342GD120-314CTVU) was used. The intelligent module consists of six IGBT; with anti-parallel diodes; six isolated gate drivers, incorporating over-current protection; and a suitable heat sink on which the devices were mounted. Such compact packaging reduces the volume. Besides, these modules are less affected by parasitics and were therefore less prone to noises. Three dual-diode modules (Table 8.1) were used for the rectifier. Two single-module IGBTs were used for the chopper and braking arrangement.

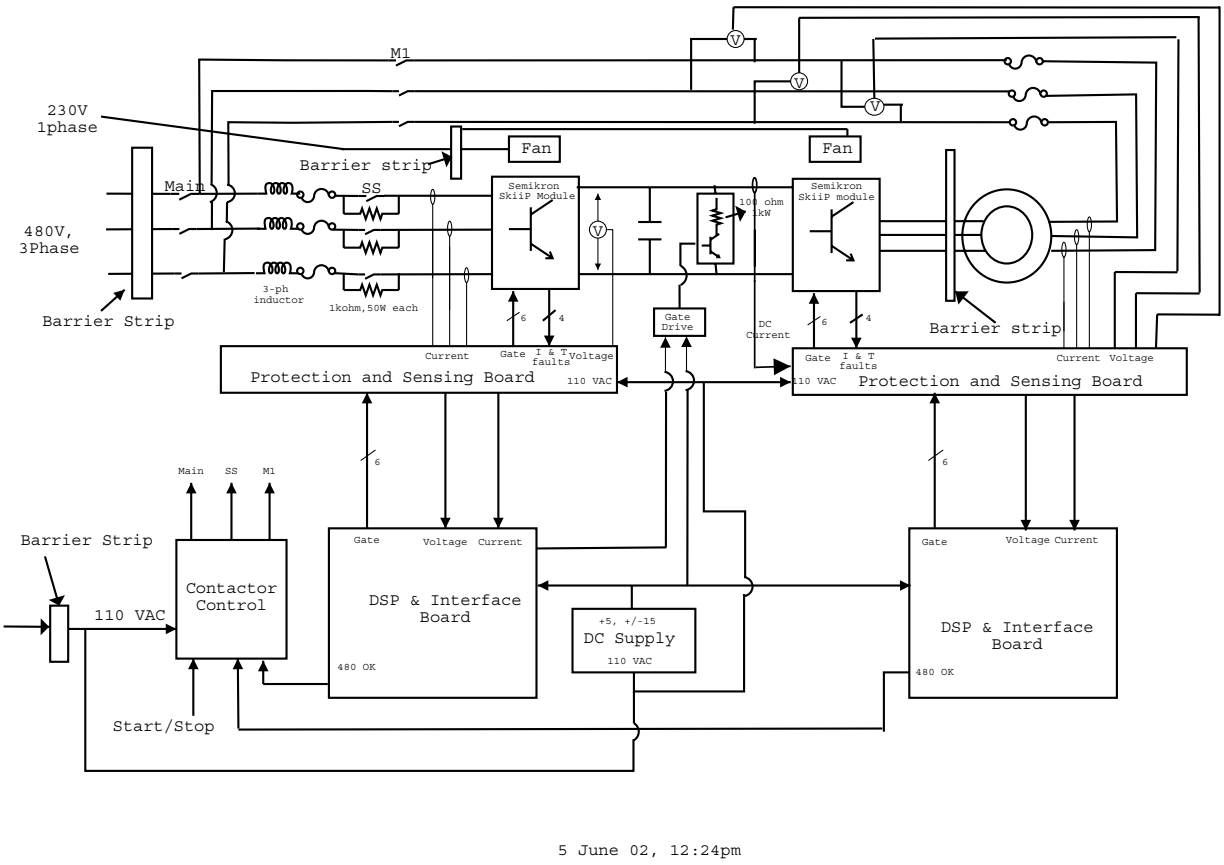


**Figure 8.1. Detailed schematic of the designed hardware**

**Table 8.1. Semiconductor Parts List**

| Part Name | Part No. | Current Rating | Voltage Rating | Module Type |
|---|---|---|---|---|
| Rectifier | SkiiP342GD120-314CTVU | 300 A (max) | 1200 V | IGBT six-pack, drivers, heat sink suitable for 30 kW |
| Inverter | SkiiP342GD120-314CTVU | 300 A (max) | 1200 V (max) | IGBT six-pack, drivers, heat sink suitable for 30 kW |
| Braking IGBT | SKM300GA123D | 300 A | 1200 V | Single Module |
| Gate Driver | SKHI10/12 | — | Up to 1200 V device | Single gate drivers for the braking IGBT |

### *8.3.2 DC-Link Design*

DC link design consisted of designing the DC-link capacitor, bus bar design and DC-link braking circuit. The DC capacitor was designed based on the ripple current passing through it at 50% overload condition and the specific requirement of ride-through capability. From the load characteristics and switching strategy (through pulse-width modulation [PWM]), the ripple current through the DC bus capacitor was formulated, and the ripple current was found through a MATLAB program. The specifications for our selected device are listed in Table 8.1. The parts list of the DC-link capacitor and the DC-link braking resistor is listed in Table 8.2. The braking resistors were selected to handle five times the rated power for 10 seconds.

**Table 8.2. DC Link Parts List**

| Item | Rating | Parts No. | Specification | Quantity |
|---|---|---|---|---|
| DC link capacitor | 4700 uF 450 V | UTOR450L6472M76x168CT | Ripple current 60.3 A rms each | 9 |
| Braking Resistor | 100 ohms 1000 W | L1000J100, Ohmite | 270 series enamel power resistor | 1 |

A line-side inverter was used for unity power factor interfacing with the grid. Because a conventional PWM inverter will generate a high-frequency switching ripple, a three-phase inductor was used between the grid and the inverter so that these high-frequency harmonics were attenuated. The current waveform was then maintained sinusoidal, and the overall THD of the current waveform was maintained within acceptable limits. Thus, the major factors contributing to the design of line-side inductors were namely the power rating of the system, the switching frequency of the inverter, and the DC bus voltage.

For our 30-kW system, a 500-uH, 60-A three-phase inductor was selected; our selection was verified through SABER simulations. The part number and other details of the inductor are given in Table 8.3.

**Table 8.3. Line-side Inductor**

| Item | Rating | Parts No. | Power loss | Quantity |
|---|---|---|---|---|
| Three-phase line side inductor | 500 uH, 82 A (max) | RL05502, MTE corporation make | 67 W | 1 |

### *8.3.3 Thermal Design*

Thermal design is an important aspect of the power converter. For proper functioning of the semiconductor and for reliable performance, thermal design plays an important role. The losses incurred in different semiconductor modules and power electronics components need to be dissipated efficiently, so that junction temperature of the device is not excessive. For proper thermal design, we used detail loss modeling of the semiconductor devices. The manufacturer supplied the device loss characteristics for different operating conditions, such as during turn-on, turn-off, and during conduction. The characteristics were complex in nature and depended on various parameters, such as junction temperature, operating DC bus voltage, and current through the device. The characteristics were fitted to a suitable curve using MATLAB, and the fitted curves were used to obtain a complete loss model for the inverter. The loss model was simulated at rated load condition, while a sine-triangle PWM switching strategy was adopted for controlling the inverter. Based on PWM waveforms and given phase currents, the current through the different components of the inverter was found. The instantaneous losses in different components were found through the fit curve and summed up to obtain the total losses within one fundamental cycle.

The above losses, multiplied by fundamental frequency, gave the total loss of the inverter. For one phase leg of the inverter, the control PWM signal, the phase current, and the currents through the different components of the same phase leg are shown in Figure 8.2. The losses in diodes and IGBT during conduction and during switching were calculated separately as a function of current through it and the DC bus voltage. Summation of these individual losses gave the total losses of the inverter. The calculated losses from the above simulation for the inverter are shown in Figure 8.3. Similarly, the losses in the rectifier and DC link were calculated and listed in the tables. Based on these loss figures, suitable heat sinks were chosen from the manufacturer data sheet, and we verified that the selected heat sinks were capable of cooling the system. In this way, safe operation of the devices was ensured. The designed heat sinks and their specifications are listed in Table 8.5.

**Table 8.4. Losses in the DC link**

| Item | Conduction Loss | Turn-on loss | Turn-off loss | Total Loss |
|---|---|---|---|---|
| Braking IGBT (1 khz) | 102.5 W | 8 W | W | 118.5 W |

**Table 8.5. Heat Sink for the Rectifier and Inverter Units**

| Item | Part No. | Dimension | Thermal resistance | Description |
|---|---|---|---|---|
| Rectifier and Inverter heat sink | SEMIKRON make P16/280 | | $R_{thjctr} = 0.09^{o}$ C/W<br>$R_{thchtr} = 0^{o}$ C/W<br>$R_{thjcd} = 0.25^{o}$ C/W<br>$R_{thha} = 0.036^{o}$ C/W | Forced cool heat sink with 5 $m^3$/h air flow rate |

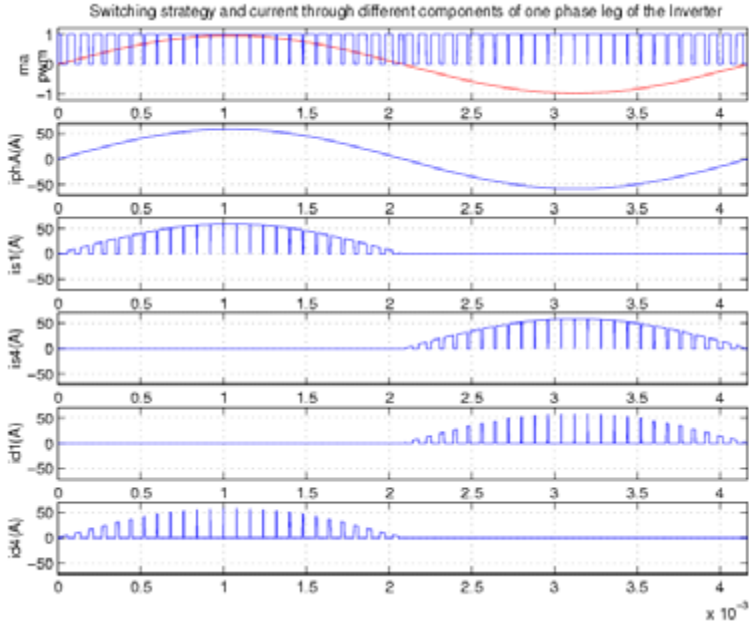


**Figure 8.2. Simulation results for PWM waveforms and current through different components (IGBTs and diodes) of one leg of the Inverter (ma = modulating signal, PWM = pulse-width modulation waveform, iphA = phase current at rated load, is1 = current through upper-half IGBT of phase 1, is4 = current through lower-half IGBT of phase 1, id1 = current though upper-half diode of phase 1, id4 = current through the lower-half diode of phase 1)**

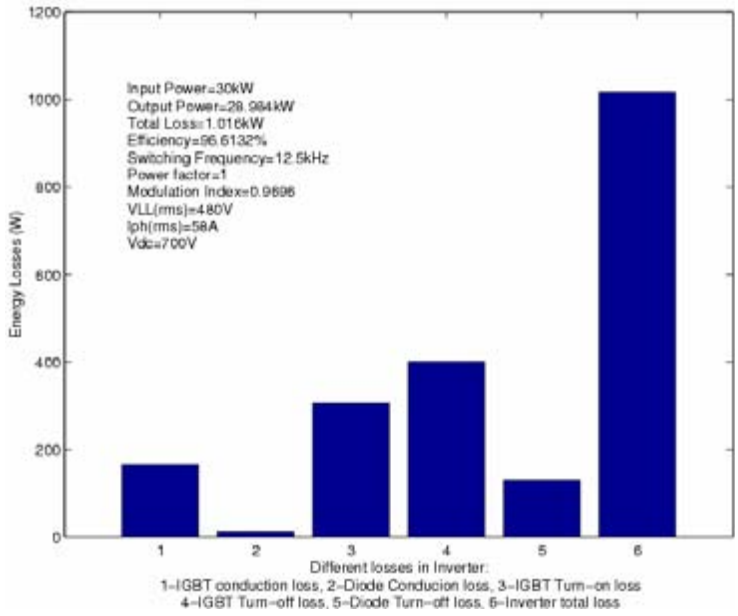


**Figure 8.3. Simulation results for losses in different components of the inverter**

### *8.3.4 Sensors*

Sensing of machine and line-side currents as well as DC bus voltage and line voltages is essential for controlling the DFIM. Suitable sensors are needed that will give high signal-to-noise ratios, have built-in isolation, and have output signals compatible with the control signals. LEM voltage and current sensors were selected for sensing the voltages currents of the system.

**Table 8.6. Current and Voltage Sensor**

| Item | Part No. | Rating | Description | Quantity |
|---|---|---|---|---|
| LEM Voltage sensor | LV 100-1200/SP3<br><br>Swiss made | Primary side voltage 1200 V, secondary voltage ± 12 V to ± 18 V | Three input line voltages and one<br><br>DC link voltage sensing | 4 |
| LEM current sensor | LA 205-S | 200A LEM current sensor | Three stator currents, three rotor currents, three FEC currents and one DC link current measurement | 10 |
| Shaft sensor | Will be supplied by manufacturer of the machine | | | 1 |

### *8.3.5 Other Components*

The other essential components for the power converters were contactors, fuses and charging resistors as shown in Table 8.7.

**Table 8.7. Auxiliary Parts List**

| Item | Part No. | Rating | Description | Quantity |
|---|---|---|---|---|
| Contactor | LC1 D8011B7, Telemecanique make | Coil voltage 110 V 60 Hz, Power rating 480 V, 37 kW | Stator and rotor circuits are connected to the line through contactors | 2 |
| Fuses | 100L09CB | 600 V, 100 A | Cooper-Bussman make | 3 |
| Fuse Block | H60100-3CR | Fuse block 600 V, 100 A | Cooper-Bussman make | 1 |
| Charging resistor | B20J200 | 200 ohm, 20 W | Ohmite make | 3 |

## 8.4 DSP Based Controller Design

DSP-based control has emerged as a popular choice for most of the motion-control applications. For control in our DFIM for wind energy application, we chose a Texas Instruments TMS320F240 DSP chip, which had been specifically optimized for motor/motion-control applications, running from a 20-MHz clock oscillator. Our DSP-based control platform was made of two parts: (i) mother board (containing a DSP chip and essential components for running the DSP) and (ii) daughter board (signal conditioning for analog and digital I/Os). A schematic diagram of the DSP board is given in Figure 8.4. The major components of each board and their functions are discussed in the following sections.

### *8.4.1 Mother Board*

The motherboard consisted of the Texas Instruments DSP chip, a 128-k x 16-bit on-card memory, analog inputs, PWM outputs, Digital I/O, and peripheral interfaces. The card accepted 16 analog signals with an input voltage range of ±10 V. These signals were put through a signal conditioning circuit that translated them to a 0 – 5 V reference. Two analog-to-digital converters with 10-bit resolution and a conversion time of 6.6 μs then processed the signals. There were eight PWM output signals. Digital input/output (I/O) consists of two banks of 8-bit signals. Communications interfaces included a RS-232 serial interface, a clocked serial port, an 8-bit MINI bus interface, and a JTAG port for software development. The board was powered by ±18 V current, which was converted to a ±15 V analog supply, a + 5 V analog reference, and a + 5 V regulated digital supply. A functional diagram of the board is shown in Figure 8.4.

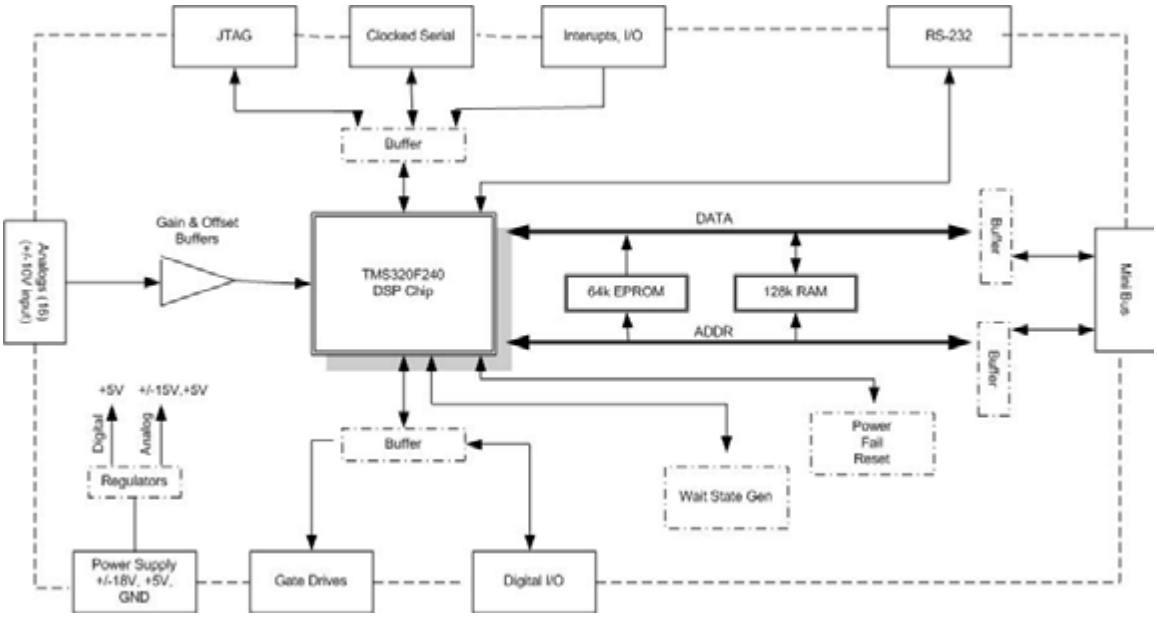


**Figure 8.4. Functional diagram of DSP controller board**

### *8.4.2 Daughter Board*

The logic the controlling daughter board was in a Xilinx chip that operated at 125 MHz with a maximum internal delay time of 10 ns. The board accepted 12 analog input signals, 24 digital input signals (16 miscellaneous inputs and 8 designated for PWM signals), 4 DAC outputs, and 18 digital output signals. A user had the option of using the digital outputs for PWM signals. Analog inputs were sent through conditioning circuits, where they are translated to a 0 – 5 V reference. These values were then fed into the digital inputs of the Xilinx board. A digital-to-analog converter accepted 8 digital inputs, with 4 analog outputs at 12-bit resolution. There was on-board, over-current, and over-voltage protection for all of the analog inputs. All gate drive control signals were conditioned through opto-isolators for surge protection. There were two comparators that were used as zero-crossing detectors. The gate drive signals were selected as an electrical or fiber-optic output. Serial interfaces included a RS-232 port and an encoder interface, both of which had optical isolation for surge protection. The board was powered by a ±15 V source along with a + 5 V reference.

## 8.5 Status of the Test Set-Up

The test setup was fabricated according to this design and with these selected parts. The complete system included the FEC, machine-side inverter, DC-link capacitors, braking IGBT, and braking resistors and was mounted on a vertical panel. The DC bus bar was designed so that the parasitics in the DC bus design were minimized. A total of nine capacitors were mounted on the panel to form the DC link. The capacitors were distributed into three parallel branches, each having three capacitors in series. The bus bars were sandwiched and mounted directly on the SKIIP modules and capacitors without any bending or extra connections or extra wiring. Suitable insulating materials were used between the bus bars, so that they did not become shorted because of insulation failure. An

aluminum plate was mounted at the top of the bus bar and on the aluminum plate with suitable spacers; the DSP control board, along with the signal conditioning and protection circuit PCB were mounted for both MSC and FEC.

Contactors, fuses, line-side inductors, and machine-side inductors were placed on or near the panel so as to minimize the wiring length. A start-stop push-button was used for energizing the power circuit. Two emergency stop buttons were placed in suitable position, so as to switch off the circuit in an emergency. The total schematic for the setup has already been given in Figure 8.1. The photographs of the different hardware components and the test setup are presented in figures 8.5 to 8.13.

A *Danfoss* drive, together with a *Baldor,* motor was installed, and their combination served as the dynamometer for testing our setup. The designed experimental setup was thoroughly debugged and tested at the component level and as a complete system. With the experimental setup and DSP-based V/F control software, a 7.5-kW induction motor was run in speed-control mode. A typical experimental result for the line-to-line voltage and one-phase current of the test motor is given in Figure 8.14.

## 8.6 Status of the Wound-Rotor Induction Machine and Rotary Transformer

A 30-kW DFIM along with a 20-KVA two-phase rotary transformer was fabricated by the WEG Motor Company in Brazil. The motor and the rotary transformer were tested in blocked rotor condition with the secondary winding of the transformer at open circuit. The circuit diagram is shown in Figure 8.15 and measured results follow on the next page. The test results include the currents through the stator winding, currents through the primary winding of the rotary transformer, stator voltage, and rotor voltages. The test was repeated with the secondary winding of the rotary transformer connected to a resistive load. Those results are given in Figure 8.16 with numerical data immediately following. The phase shift in stator and rotor quantities for the test condition given in Figure 8.15 are presented in figures 8.17 and 8.18, respectively. It can be seen that both the stator and the rotor quantities were unbalanced in phase. This is a direct effect of using the two-phase unbalanced rotary transformer. Figures 8.19 and 8.20 are photos of the end portion of the machine that show the rotating transformer.

## 8.7 Conclusions

In this chapter, we explained the detailed hardware setup for testing the control algorithm of Chapter 7 for a 30-kW DFIM along with a two-phase rotary transformer. The schematic in Figure 8.1 shows the complete hardware system and the hardware set-up. Each individual module was explained and each component was illustrated. Photographs show important components for the setup and different views of the complete power electronics system. Using the designed hardware setup, a 7.5-kW induction motor drive was tested with a V/F control software using the DSP equipment. A sample test result for the induction motor drive was given in support of the functionality of the designed hardware.

The WEG Motor Company of Brazil has fabricated a 30-kW wound rotor induction motor with an integral 20-KVA rotary transformer in one frame. They are performing preliminary no-load and load tests on the motor and rotary transformer unit. Examples of their test results are given.

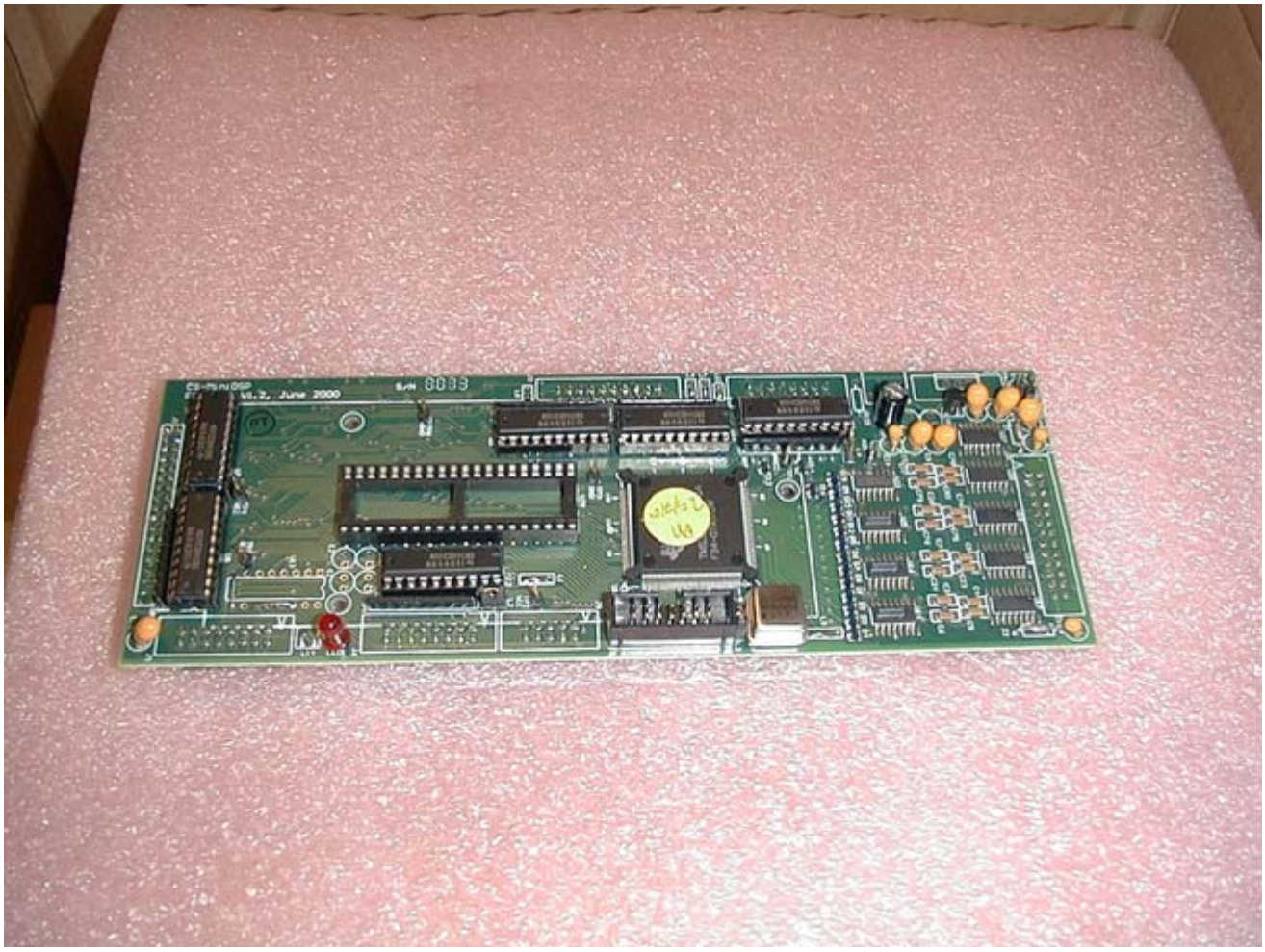

**Figure 8.5. DSP motherboard**

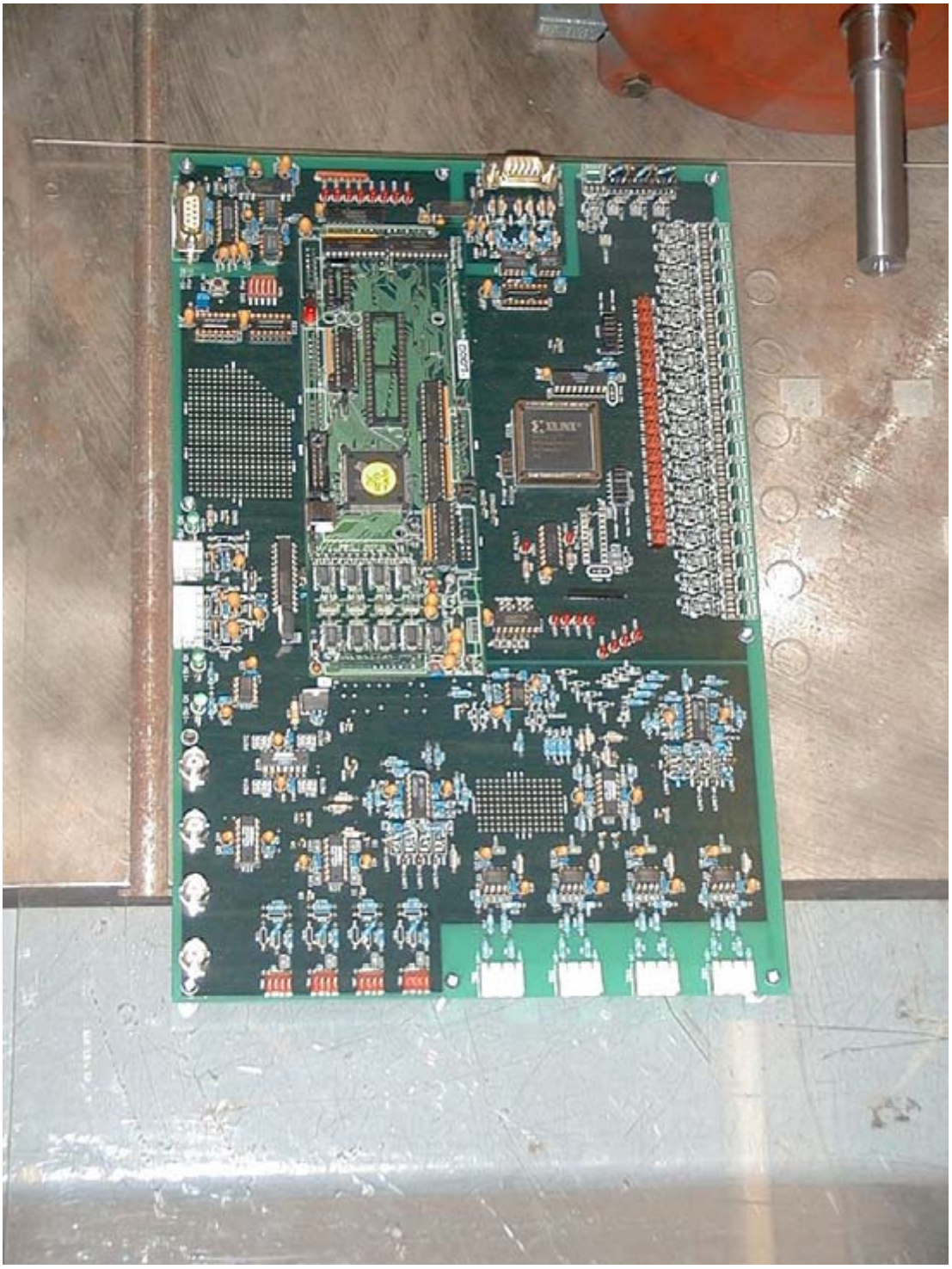

**Figure 8.6. DSP daughter board**

**Figure 8.7. SKIIP module**

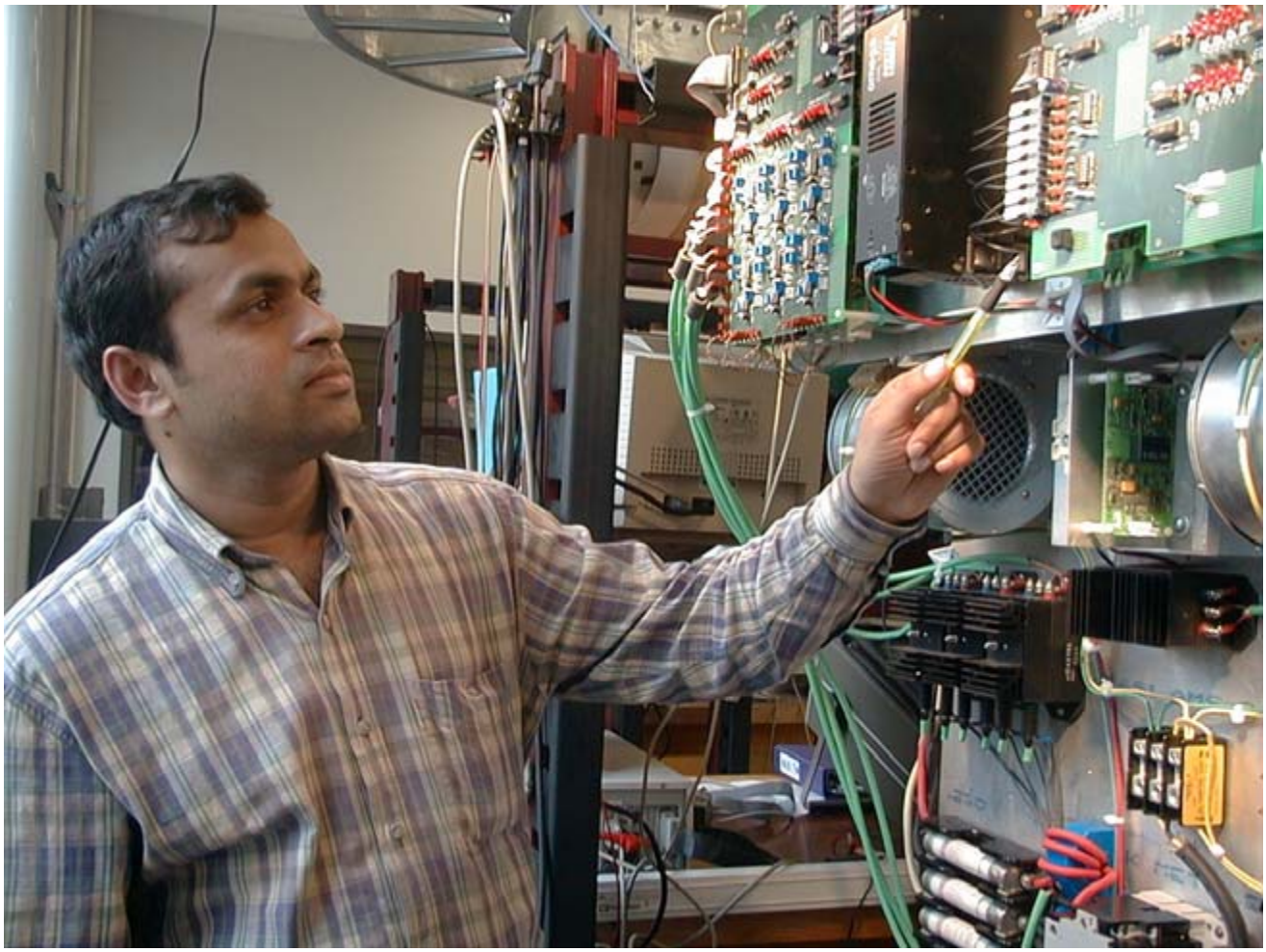

**Figure 8.8. Front view of the middle part of the experimental set-up**

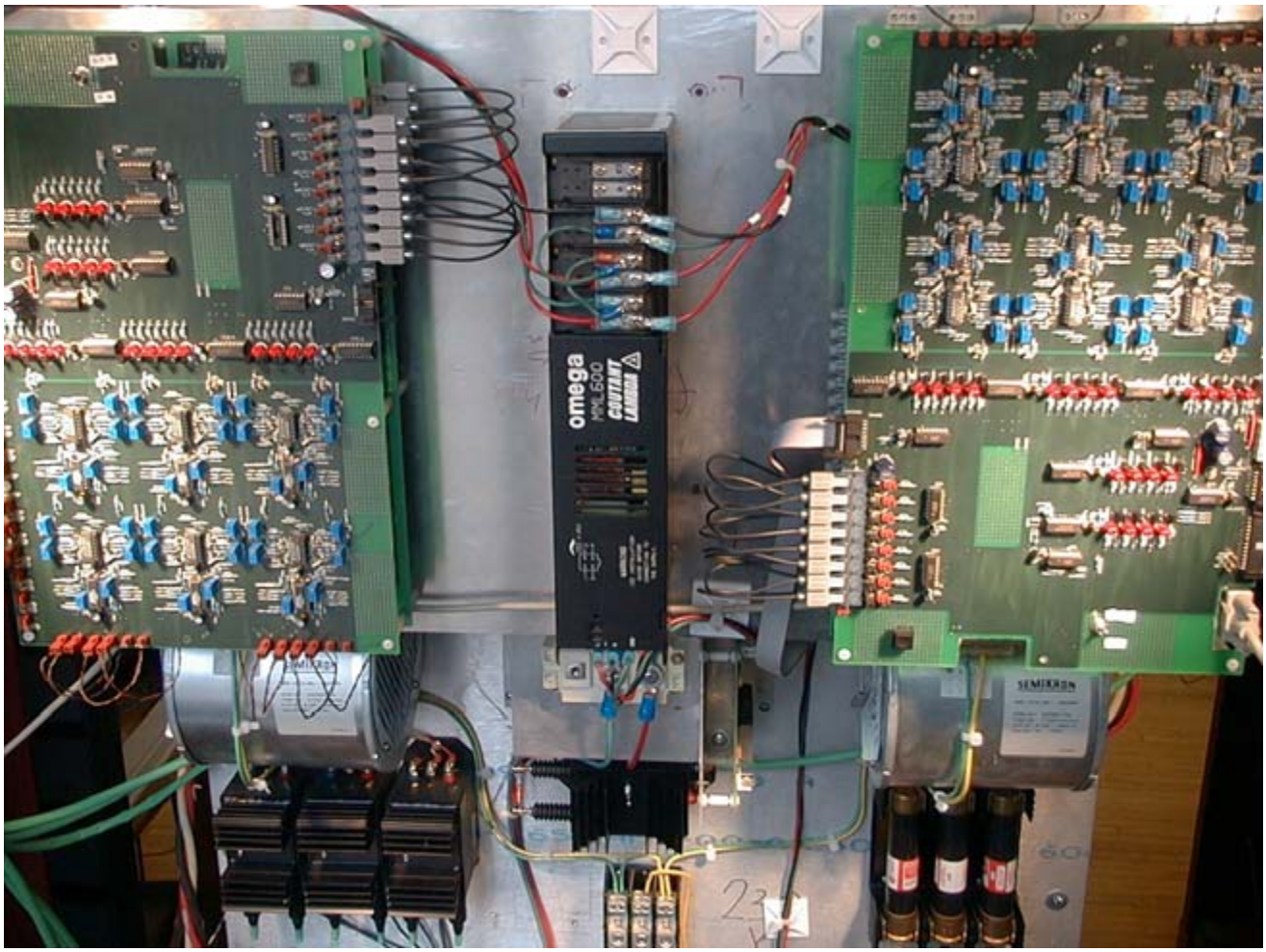


**Figure 8.9. Front view of the upper part of the experimental set-up**

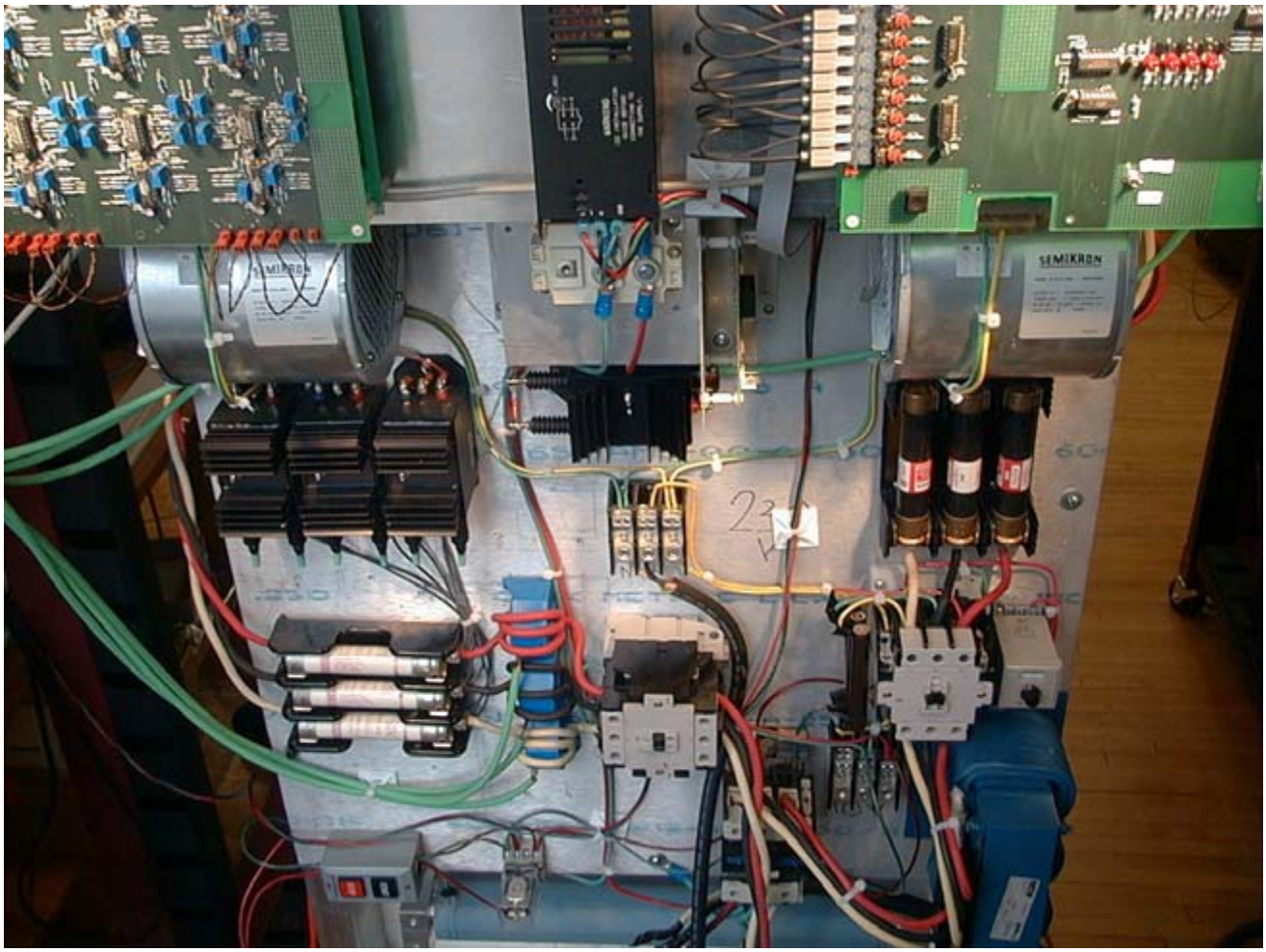


**Figure 8.10. Front view of lower part of the experimental set-up**

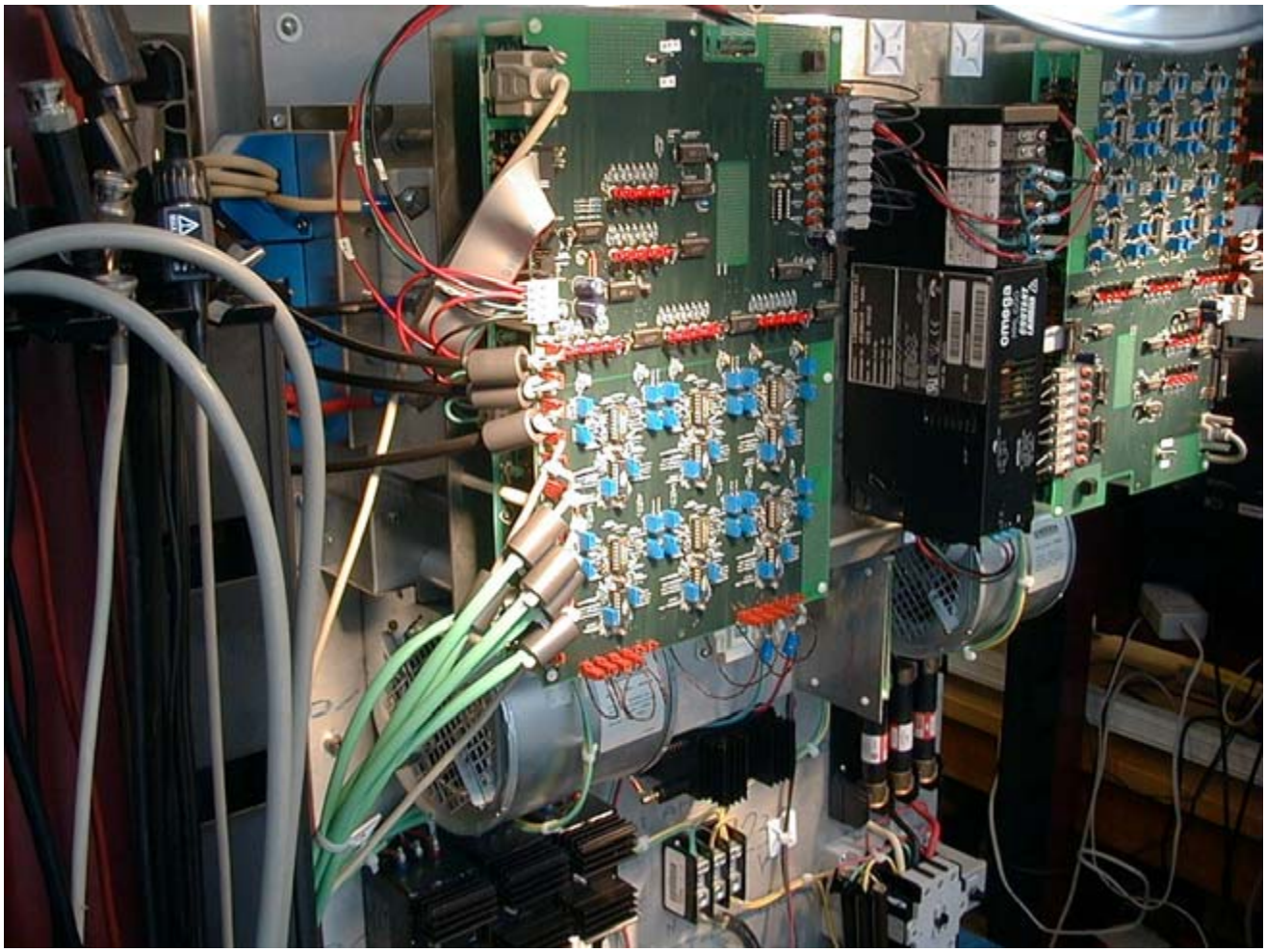


**Figure 8.11. LHS view of part of the experimental set-up**

**Figure 8.12. RHS view of part of the experimental set-up**

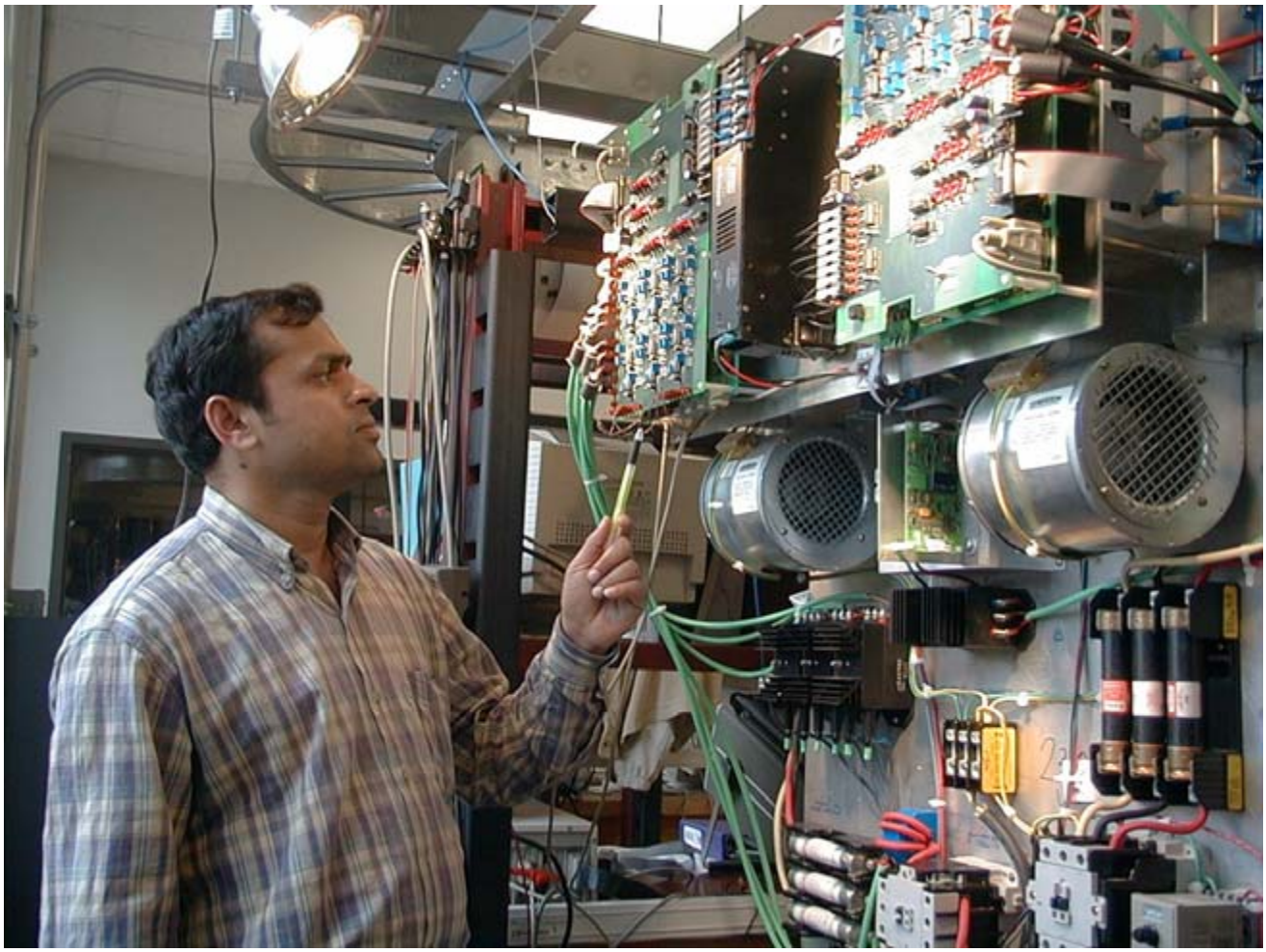

**Figure 8.13. Front view of part of the experimental set-up**

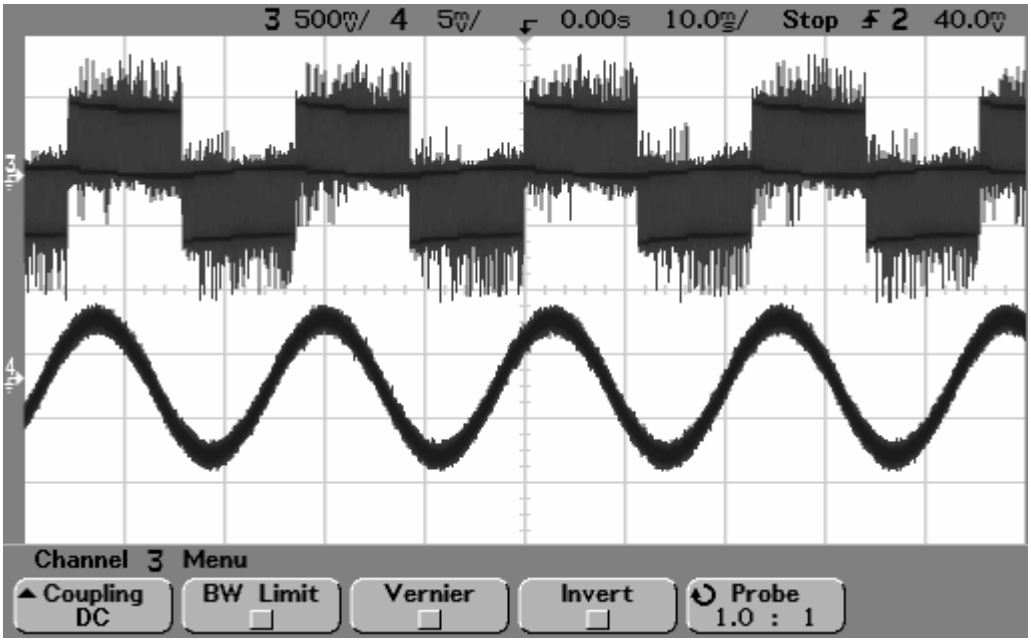


**Figure 8.14. Experimental waveforms for line-to-line voltage and phase current when a 7.5-kW induction motor was run from the present test setup**

**WEG MÁQUINAS Ltda.**
**Project Section**

April, 01 2003.

**Subject: Rotary transformer no-load test.**

**Test condition 1: Locked rotor condition, slip s = 1 and secondary open**

**Test Diagram:**

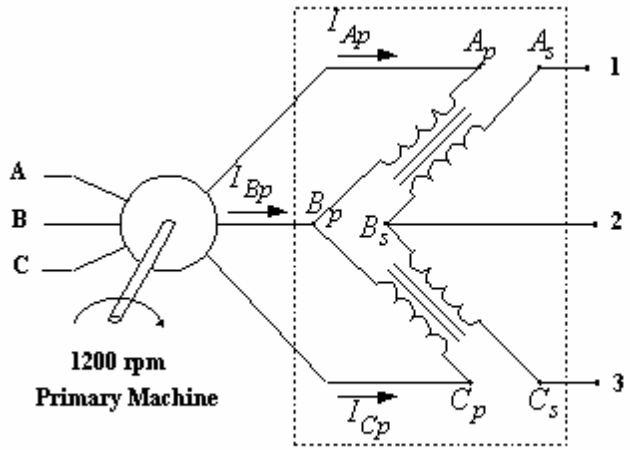


**Figure 8.15. Circuit schematic of a DFIM with a two-phase rotary transformer for test condition 1**

## Stator Measured Values

| Source applied voltage (A-B, B-C, A-C) in volts | between (A-B) [volts] | between (A-C) [volts] | between (B-C) [volts] |
|---|---|---|---|
| 105.8 | 105.8 | 105.8 | 100 |
| 220 | 220 | 221.7 | 209 |

Obs: The source voltage measured values were equal

| Source measured voltage (A-B, B-C, A-C) in volts | Current (A) [A] | Current (B) [A] | Current (C) [A] |
|---|---|---|---|
| 105.8 | 15.3 | 14.0 | 25.6 |
| 220 | 31.0 | 31.9 | 55.0 |

## Rotor Measured Values

| Source applied voltage (A-B, B-C, A-C) in volts | between (Ap-Bp) [volts] | between (Ap-Cp) [volts] | between (Bp-Cp) [volts] |
|---|---|---|---|
| 105.8 | 55 | 71.5 | 49.7 |
| 220 | 115 | 152 | 104 |

| Source applied voltage (A-B, B-C, A-C) in volts | between (As-Bs) [volts] | between (As-Cs) [volts] | between (Bs-Cs) [volts] |
|---|---|---|---|
| 105.8 | 55.4 | 75.8 | 52 |
| 220 | 116 | 158 | 109 |

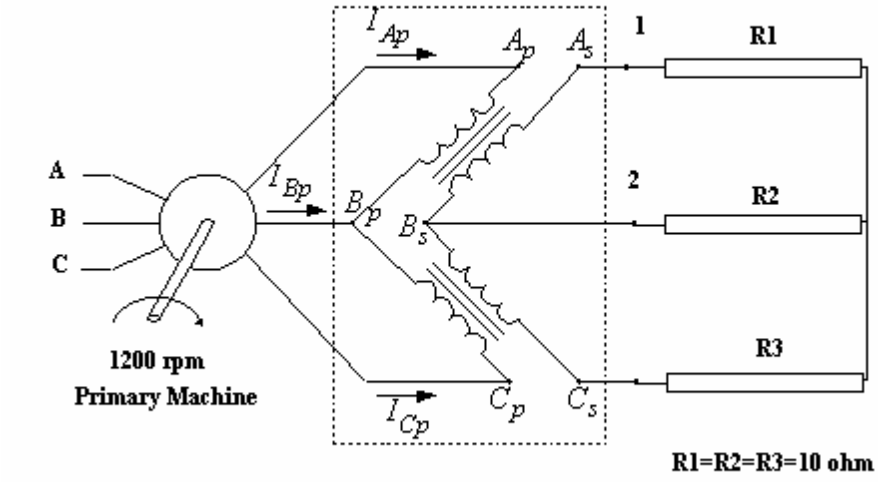


**Figure 8.16. Circuit schematic of a DFIM with a two-phase rotary transformer for test condition 2- Locked rotor condition, slip s = 1 and secondary winding connected to a wye balanced connected load.**

## Stator Measured Values

| Source applied voltage (A-B, B-C, A-C) in volts | between (A-B) [volts] | between (A-C) [volts] | between (B-C) [volts] |
|---|---|---|---|
| 103.5 | 103.5 | 103.8 | 98.6 |

Obs: The source voltage measured values are equal

| Source measured voltage (A-B, B-C, A-C) in volts | Current (A) [A] | Current (B) [A] | Current (C) [A] |
|---|---|---|---|
| 103.5 | 14.8 | 15.2 | 25.8 |

## Rotor Measured Values

| Source applied voltage (A-B, B-C, A-C) in volts | between (As-Bs) [volts] | Between (As-Cs) [volts] | between (Bs-Cs) [volts] |
|---|---|---|---|
| 103.5 | 48.5 | 66.6 | 51.3 |

| Source measured voltage (A-B, B-C, A-C) in volts | Current (1)[A] | Current (2)[A] | Current (3)A] |
|---|---|---|---|
| 103.5 | 3.3 | 2.3 | 3.4 |

## Stator Measured Values

| Source applied voltage (A-B, B-C, A-C) in volts | between (A-B) | between (A-C) |
|---|---|---|
| 103.5 | 126.19° | 245.14° |


**Figure 8.17. Phase shift measurement of the stator quantity for test condition 3- Locked rotor condition, slip s = 1 and secondary open, for phase shift measurement.**

## *Rotor Measured Values*

| *Source applied voltage (A-B, B-C, A-C) in volts* | *between (1-2)* | *between (1-3)* |
|---|---|---|
| ***103.5*** | 136.37° | 257.24° |


**Figure 8.18. Phase shift measurement for rotary transformer primary quantities with test condition 3**

**Figure 8.19. Photo of overall view of 30-kW DFIM with two-phase rotating transformer; the end shield on the transformer end was removed to show transformer details**

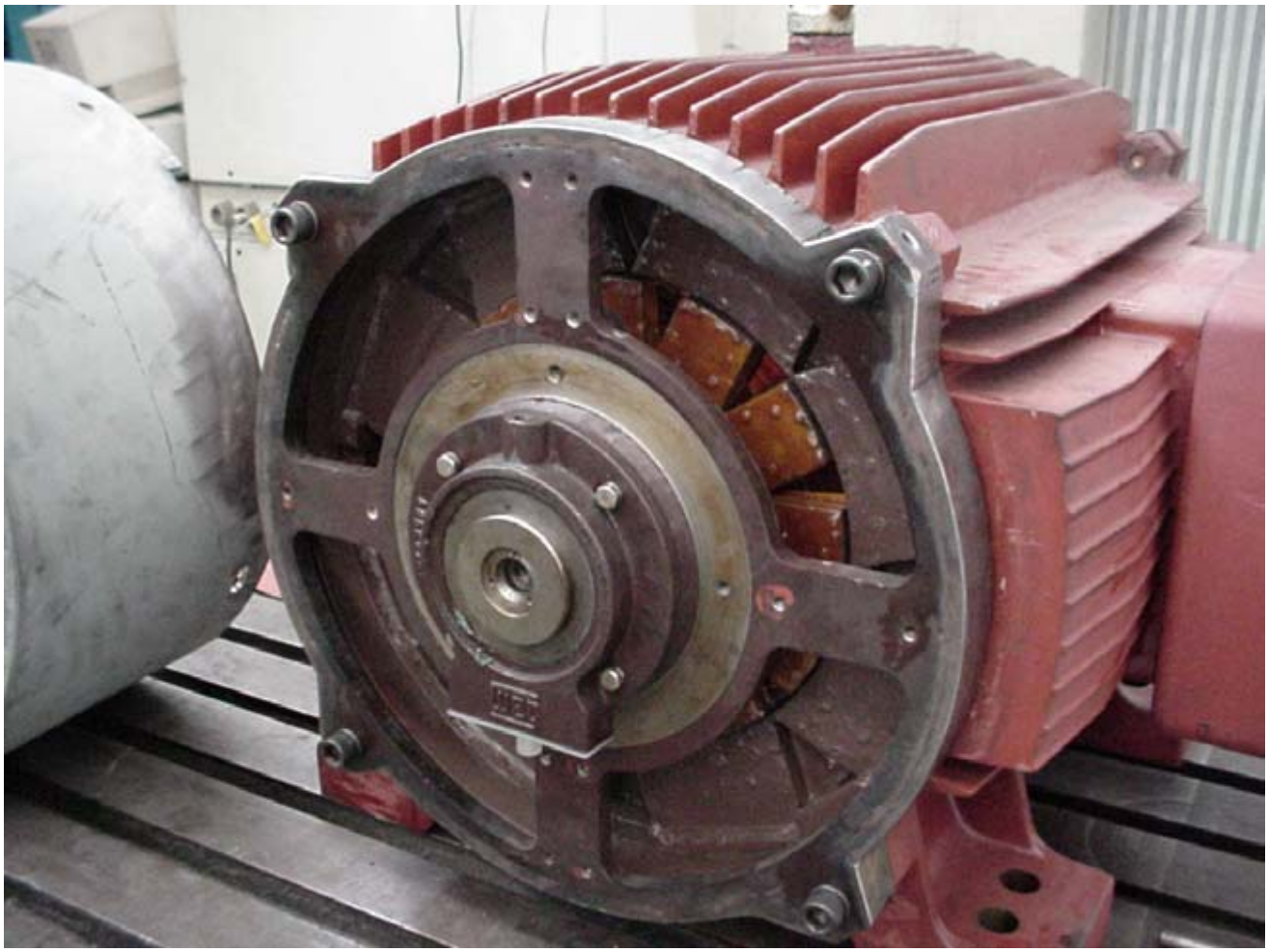

**Figure 8.20. Close up of 30-kW DFIM with two-phase rotating transformer; the end shield on transformer end was removed to show transformer details**

# Chapter 9: Conclusions

The objective of our project was three-fold: reducing system cost by seeking low-cost power converter options, maximizing wind power utilization by operating the drive for a wide range of speeds, and improving reliability by eliminating the carbon brush and slip ring and utilizing a rotary transformer. We were satisfied with the results for the first two objectives. The third objective was only partly fulfilled.

We proposed four low-cost alternative-power converters for processing the power developed by a doubly fed wound-rotor induction generator. All of these power converters were capable of operating the machine as a generator for both sub- and super-synchronous speed zone, and they also supported bi-directional power flow. The quality of the generated power was maintained to a high standard by interfacing the wind generator with the grid at almost unity power factor for all four proposed converters. Thus, without sacrificing performance, the cost of the system was reduced by choosing specified converters. Most of the components for all these power converters were either diodes or thyristors, which are relatively much cheaper than an equivalent power rating IGBTs.

The schematics, operating principle, control features, and comparative merits and demerits of each of the power converters were explained in detail and, finally, the performance of each of them was verified through SABER simulations. Relevant simulation results for all four power converters were presented. Thus, we illustrated the satisfactory performance of the proposed converters. Critical points or remarks for each converter relative to its operation and controls and special control efforts were discussed in detail.

After successful illustration of the variable-speed operation and performance of the four proposed power converters, we can conclude that the first objective of this project--reduction of the system cost by finding appropriate power converter--was accomplished quite satisfactorily.

The second objective for this project was to maximize the operating speed range of the variable-speed drive to optimize wind utilization. In conventional rotor-side control of a DFIM, the operating speed range of the drive was limited to twice the rated speed of the machine. This occurred because with the stator being directly connected to the grid, typical field weakening of the drive was no longer possible. However, we proposed a new control algorithm project wherein both the stator and the rotor side can be controlled by individual three-phase half-controlled power converters. Compared to the conventional schemes, the proposed control algorithm is advantageous in many respects.

First, the operating speed range of the drive was extended beyond twice the rated speed because field weakening is possible by employing power converters in both the stator and rotor of the machine. With such a control scheme, the speed can be theoretically increased for beyond twice the rated speed. Operating speeds of such drives may be limited only because of mechanical constraints.

Second, the proposed control scheme improved the efficiency of the drive (the machine, as well as power converters) by splitting the excitation current equally between the stator and the rotor windings. In a conventional rotor-side control scheme, the rotor winding as well as the machine-side power converter have to handle the rated reactive as well as the rated active component of the currents of the machine. This increases the current ratings for the rotor windings, as well as the machine-side power

converter, by 41%. Thus, the KVA rating of the rotor-side power converter has to be 41% higher than the rated operating slip power. Also, the losses in the rotor windings and the power converter will be high given the 41% increase in current rating through the rotor. Because of the construction features of an electrical machine, the cooling of the rotor is always difficult compared to its stator winding. Any extra loss in the rotor winding is disadvantageous with respect to thermal rating of the machine. However, with the proposed double-sided converter control scheme, the excitation current is equally split between the stator and the rotor winding. The losses in the rotor windings, as well as in the rotor-side power converter, are reduced. The combined KVA rating of both machine stator and rotor-side power converters was 30% less than that of a single power converter employed for conventional rotor side control. In addition, the combined stator and rotor copper loss was reduced by 17% with the proposed double-sided control scheme.

More importantly, in the proposed control scheme, the machine was always operated in super-synchronous generating mode. In this mode, power is always generated from both the stator and the rotor windings of the machine. Thus, the possibilities of circulating power flowing between the stator and the rotor side of the machine are completely eliminated. This latest feature will certainly improve the efficiency of the drive further. The added advantage of using the half-controlled configuration is that the machine-side converters become shoot-through safe, and they do not require any isolated power supply for their gate drives. Thus, it can be concluded that with the proposed double-sided control scheme, the second objective of this project- operation of the drive over a wide speed range- was achieved. We also showed that the losses in the drive were reduced and the system became much more rugged.

The third objective of the project was to eliminate the carbon brush and slip ring, and replace them with a rotary transformer. Normally, the rotary transformer is restricted to low-power, high-frequency applications. However, in this project, we explored the concept of the brushless operation of a DFIM for wind generator applications. Initially, a three-phase rotary transformer was investigated. We found that in the conventional configuration, the volume of the rotary transformer is too large to accommodate a three-phase transformer in the shaft of the machine. Rotary transformers have an air gap between the rotating primary winding and the stationary secondary winding, which increases the leakage inductance of the transformer. This, in turn, increases its volume. Power density is an important criterion for any electro-mechanical energy conversion system; therefore, a regular three-phase rotary transformer will obviously be a disadvantage for that reason. To improve the power density of the system, a two-phase transformer was explored in this project. By a thorough analysis we show that with the latter the volume of the rotary transformer can be reduced by 35% compared to a similar power-rated three-phase rotary transformer.

Unfortunately, the two-phase rotary transformer combined with a regular three-phase DFIM introduces unbalancing into the system. Such a scheme may introduce as much as a 60° phase unbalance into the machine. Such an unbalanced system calls for more complex control algorithm and a converter with full control flexibility. When the rotor winding is combined with a rotary transformer, the rotor current of the machine is no longer measurable. The latter introduces even more complexity into the system, and the control of the combined system becomes a challenging task.

In this project, several control schemes for connection with the diode bridge-chopper combination, as well as a full-bridge IGBT-based inverter, was explored. We found that with a simple diode bridge and

boost chopper, the performance of the drive was far from satisfactory. Hence, a converter with more control flexibility was desired. Finally, a regular IGBT-based three-phase full bridge inverter was chosen for driving the system. A regular field-orientation control scheme did not function satisfactorily with such a system because the field-orientation control was only valid for a linear and balanced system. The rotor current measurement was essential for the field-orientation controller. Because many of these conditions were not satisfied with the present system, the performance of the field-orientation controller could not be satisfactory. We simulated the system with such a field orientation scheme and found that the system generated excessive torque ripple with the conventional control scheme.

Finally, we devised a direct-stator power-based control algorithm for the present system. With the latest control scheme, no rotor current or rotor voltage measurement of the machine was required. One only needs to measure stator voltage and stator current, which are readily available for measurement in the given system. From the measured stator quantities, the stator active and reactive powers were calculated and used for indirectly controlling the machine torque and speed. Essentially, the active and reactive power generated by the system was directly controlled with such a control scheme. Control of these quantities was a desirable requirement for any generator application.

The direct-stator power-based control scheme was first applied for a regular three-phase balanced wound-rotor induction machine, and the performance of the system with such controller was quite satisfactory. Subsequently, the same control scheme was explored for an unbalanced system composed of a wound-rotor induction machine and a two-phase rotary transformer. Through analysis and simulation, we evaluated the unbalanced nature of the combined system. A detailed analysis of the proposed direct-stator power-based control scheme for an unbalanced system was carried out. We found that the proposed controller can support satisfactory performance of the system for a maximum 30° phase unbalancing. However, the proposed brushless generator system may introduce as high as 60 degree phase unbalancing when the secondary winding of the transformer is shorted. In the actual system, the unbalancing may be much less than 60°, but still it can be higher than 30° for some operating load. We showed through simulation that the proposed control scheme operated satisfactorily up to 75% system load. Within this load range, the torque and speed of the machine are controlled quite smoothly with this controller. However, beyond 75% load, the system was found to be unstable. A detailed SABER simulation combining the system and the controller was carried out.

Another drawback for a rotary transformer was that it became prone to saturation when the machine reached near-synchronous speed. We demonstrated through simulation that the rotary transformer showed saturation for any slip less than the ± 6% range. This condition could be a typical case for any rotary transformer, irrespective of two-phase or three-phase structure. However, with the control scheme proposed in Chapter 5, employing a double-sided converter, the operation of a balanced three-phase rotary transformer can be fulfilled without any saturation problem because near-zero frequency operation of the rotor can be avoided with this scheme. A three-phase rotary transformer increases the volume of the system and, thus, is not an attractive solution for this application.

We concluded that for successful elimination of carbon brush and slip ring either a more sophisticated control scheme needs to be found or a more elegant rotary transformer structure has to be designed. This issue will be considered for future work.

To test the system, a 30-kW prototype was built using a state-of-the-art DSP and SKIIP power module. The hardware was tested with a 7.5-kW squirrel-cage induction motor with a DSP-based V/F control scheme. A sample experimental result was presented in this report. A 30-kW motor, along with a 20-KVA rotary transformer was fabricated by WEG motor of Brazil. Preliminary tests were conducted on the factory premises, and the nature of unbalancing in both stator and rotor quantities were illustrated through test results.

A total of four new low-cost power converters have been proposed for driving a doubly fed wound-rotor induction generator. Also, a new control scheme incorporating both stator- and rotor-side control has been proposed, through which the performance of the system is improved. We investigated a rotary transformer based system thoroughly and proposed a new control scheme for controlling an unbalanced system. Even though our proposed controller is inadequate for controlling the system over its entire operating range, such a scheme can handle a considerable amount of unbalancing in the system. This information is useful for future investigation on any unbalanced rotary transformer and wound- rotor induction machine combination.

## 9.1 Scope of Future Work

A series of future research projects could be proposed as the outcome of this present work. First, a more elegant rotary transformer-based system could be investigated so as to improve the power density of the system. Also, a more sophisticated control scheme may be investigated to achieve satisfactory performance of the rotary transformer.

There is also room for improvement in the performance of all four power converters proposed in this report. For example, in Chapter 1 we proposed a converter topology composed of a diode bridge, boost chopper, inverter, and reversible contactors. However, the line-side harmonics for sub-synchronous operation could not be eliminated completely in this project. A more elegant method could be investigated for reducing the line-side harmonics further.

Similarly, for topology 2 in Chapter 3, the operation of near-synchronous speed is not well controlled. A better control scheme may be found to improve the performance of the drive at or near synchronous speed.

For topology 4 in Chapter 5, the harmonics caused by half-controlled converter configuration was a point of concern. New control schemes may be designed for reducing the stator- and rotor-side harmonics. Also, for this converter topology, the line-side converter has to handle the full power produced by both the stator and the rotor windings. Hence, the KVA rating is higher. Efforts may be given to find an alternative converter scheme, so as to reduce the cost of the line-side converter.

# Nomenclature

| | |
|---|---|
| μs | microsecond, page 193 |
| δp | Angle between Stator and Rotor magnetic flux, page 140 |
| ρ | Mass density, page 120 |
| λ | Magnetic flux, page 119 |
| φ | Magnetic flux linkages, page 115 |
| $\mu$ | Angular position of stator magnetizing flux |
| $\varepsilon$ | Angular position of the shaft |
| $\sigma_s$ | Stator leakage factor |
| $\sigma_s \mathrm{L_o}$ | Rotor leakage inductance |
| $\sigma_r$ | Rotor leakage factor |
| $\psi_s$ | Stator flux |
| $\psi_r$ | Rotor flux |
| $\psi_m$ | Air gap flux |
| $\omega_s$ | Stator angular frequency |
| μH | Microhenries of induction, page 67 |
| A | Ampere, page 185 |
| AC | Alternating current |
| b | (Can't find) page 126 |
| B | Dimensionless frictional coefficient (table 5.1) |
| bjt_14.bjt_14_2_ | Lower-leg IGBT (page 73) |
| Cs1, Cs2, Cs3, etc | Capacitors |
| CSCF | Constant-speed, constant-frequency operation |
| d-axis | Direct axis component of flux within generator, page 91, 99 |

| | |
|---|---|
| D1, D2, D3, etc | Diodes (page 44 and 66) |
| DAC | Digital to analogue converter, page 194 |
| DC | Direct current |
| DFIM | Doubly fed induction machine |
| DSC | Direct self-control, page 138 |
| DSP | Digital signal processor, page 10 |
| DTC | Direct torque control, page 138 |
| D_st | Label for starting circuit diode, page 96 |
| $e_s$ | Stator induced voltage |
| $e_r$ | Rotor induced voltage |
| *f* | Frequency page 119 |
| FEC | Front-end converter, page 47 |
| FFT | Fast Fourier transform, page 74 |
| fs | Synchronous frequency (table 5.1) |
| h | Various iron core dimensions in millimeters, page 123 |
| i(1.sym24) | Phase current through front-end rectifier |
| i(sw1_14.sw1_14_1) | Current through lower MOSFET (Sw4) |
| ia | Total phase-A grid current |
| ia_fec | Front-end converter phase a current |
| iar | Rotor-phase current |
| ias | Stator-phase current |
| ic(bjt_14.bjt_14_2) | Current through lower half IGBT (Sw2) |
| idc | DC link current (page 55) |
| idi(d.sym56) | Current through the anti-parallel diode of the lower-half MOSFET (Sw4) |
| igaa | Front-end converter phase-A current |
| I/O | Input/out page 193 |

| | |
|---|---|
| IGBT | Insulated gate bipolar transistor |
| i_scr(scr1.sym31) | Current through lower-half thyristor (T1) of phase A |
| i_scr(scr1.sym34) | Current through lower-half thyristor (T4) of phase A |
| I(short_d_rot_a) | Current through the diode rectifier |
| i(short.in_rot_a) | Current through the IGBT inverter |
| isd | Direct axis stator current, page 139 |
| isq | Quadrature axis stator current, page 16 |
| $i_s = i_{sd} + ji_{sq}$ | Stator current |
| $i_r = i_{rd} + ji_{rq}$ | Rotor current |
| $i_{ms}$ | Stator magnetizing current |
| $i_{rd}$ | Direct axis rotor current, page 99, 139 |
| $i_{rq}$ | Quadrature axis rotor current, page 98, 139 |
| $i_s^r$ | Stator current in rotor reference frame |
| $i_{sd}$ | Direct axis page 98 |
| $i_r^s$ | Rotor current in stator reference frame |
| J | Moment of inertia (table 5.1) |
| JTAG | Page 193 |
| KVA | Kilovolt-amperes, page 132 |
| LHS | Rotor-side control page 89 |
| Lm | magnetizing inductance (table 5.1) |
| Lp | Primary winding inductance (page 67) |
| Ln | Secondary winding inductance (page 67) |
| $L_0$ | Magnetizing inductance |

| | |
|---|---|
| $m_d$ | Reference torque, page 145 |
| MATLAB | Engineering computer program, page 186 |
| MMF | Magnitomotive force page 113 |
| MOSFET | Metal oxide semiconductor field effect transistor |
| MSC | Machine-side converter |
| MWh | Megawatt-hour |
| _n2556 | Contactor changeover logic |
| $n_s/n_r$ | Turns ratio |
| N, $N_1$, $N_2$, $N_3$, etc | Number of turns in a coil, page 115 |
| nc | Normally closed |
| no | Normally open |
| ns | Nanosecond |
| P | Pole count (table 5.1) also defined as Power generated on page 145 |
| pitch_cntrl_en | Rotor pitch control (+1) / converter control (0) logic signal |
| PM | Mechanical power |
| pu | Per unit (EE usage meaning normalized by rated value), page 29 |
| Pr | Rotor power |
| Ps | Stator power |
| PWM | Pulse-width modulation |
| q-axis | Quadrature axis within an electric machine. |
| Q1, Q2 | Labels for electronic switches, page 44 |
| Qs | Quantity of reactive power in volt-ampere units, page 139 |
| $R_1$, $R_2$, $R_3$, etc | Algebraic symbols for resistance or resistors, page 115 |
| rect_inv_lgc | Rectifier mode (+1) / inverter mode (-1) logic signal |
| RMS | Root mean square value of variable, page 73 |
| Rr | Rotor resistance (table 5.1) |

| | |
|---|---|
| Rs | Stator resistance (table 5.1) |
| Rs1, Rs2, Rs3, etc | Resistors |
| S1, S2, S3, etc | Active switching state, page 141 |
| SABER | Electric circuit simulation computer program |
| scr_lgc | Two valued logic signal, page 51 |
| SCR | Silicon controlled rectifier, page 56 |
| $T_q$ | Electromagnetic torque |
| T1, T2, T3, etc | Thyristors, page 66 |
| T* | Generator torque command signal, page 47 |
| $t_q$ | Turn-off time for a thyristor, page 70 |
| tq_mks | Torque developed by the machine |
| THD | Total harmonic distortion, page 32 |
| U1, U2, U3 | Voltage space vectors, page 141 |
| u_ra | Rotor-phase voltage |
| $V_1$, $V_2$, $V_3$, etc | Voltage symbols, page 115 |
| vas | Stator-phase voltage |
| vdc | DC bus voltage |
| V/F | Voltage to frequency ratio (to be held constant during variable speed operation), page 10 |
| $V_r$ | Rotor terminal voltage, page 44 and page 85 |
| $V_s$ | Stator terminal voltage |
| VSCF | Variable-speed constant-frequency |
| WECS | Wind energy conversion system |
| wmm | Mechanical speed of the machine |

# References


[1] Miller, A.; Muljadi, E.; and Zinger, D.S. "A Variable-Speed Wind Turbine Product Power Control." *IEEE Transaction Energy Conversion*, Vol. 12(2), 1997, pp 181-187.

[2] Barun, D.H.; Gilmore, T.P.; and Maslowski, W.A. "Regenerative Converter for PMW AC Drives." IAS' 91, Conference record of the 1991 *IEEE Industry Applications Conference Twenty-sixth Industrial Application Society Annual Meeting*, pp. 862-868.

[3] Sen, P.C.; and Ma, K.H.J. "Rotor Chopper Control for Induction Motor Drive: TRC Strategy." *IEEE Transactions on Industry Applications*, Vol. IA-11, Jan/Feb 1975, pp. 43-49.

[4] Bhattacharya, S.; Divan, D.M.; and Banerjee, B. "Synchronous Frame Harmonic Isolator Using Active Series Filter." *EPE '91 4th European Conference on Power Electronics and Applications,* Vol. 3, 1991, pp. 030-035.

[5] Oriti, G.; and Julian, A.L. "Hybrid Rectifier Using Thyristors and IGBTs for Low-Cost Regenerative Drives." *Proceedings of 15th IEEE APEC Conference*," Vol. 2, 2000, pp. 951-956

[6] Pena, R.; Clare, J.C.; and Asher, G.M. "Doubly Fed Induction Generator Using Back-to-Back PWM Converters and its Application to Variable-Speed Wind-Energy Generation." *IEEE Proc.,* Vol. 143 (3), Pt. B, May 1996, pp. 231-241.

[7] Tang, Y.; and Xu, L. "A Flexible Active and Reactive Power Control Strategy for a Variable-Speed Constant-Frequency Generating System." *Proceedings of the IEEE IAS Annual Meeting*, 1993, pp. 568-573.

[8] Panda, D.; Benedict, E.; Venkataramanan, G.; and Lipo, T.A. "A Novel Control Strategy for the Rotor-Side Control of a Doubly Fed Induction Machine." *Proceedings of IEEE IAS Annual Meeting*, Vol. 3, 2001, pp. 1695-1702.

[9] Datta, R.; and Ranganathan, V.T. "Direct Power Control of Grid-Connected Wound-Rotor Induction Machine Without Rotor Position Sensors." *IEEE Transactions on Power Electronics*, Vol. 16 (3), May 2001, pp 390-399.

[10] Kawabata, Y; Ejiogu, E. C.; and Kawabata, T. "Vector-Controlled Double-Inverter-Fed Wound-Rotor Induction Motor Suitable for High-Power Drives." *IEEE Transactions on Industry Applications,* Vol. 35 (5), Sept/Oct 1999, pp. 1058-1066.

[11] Kikuchi, J.; Manjrekar, M.D.; and Lipo, T.A. "Performance Improvement of Half Controlled Three-Phase PWM Boost Rectifier." *Proceedings of IEEE Power Electronic Specialists Conference, 1999*, Vol. 1, January 1999, pp. 319-324.

[12] Karttunen, S.; Arkkio, A.; Tellinen, J.; Mantere, J.; Varis, J.; and Westerlund, J. "Rotary Transformer for the Excitation of Synchronous Motors." *Proceedings of International Conference on Electrical Machines, ICEM 98*, Vol. 2, 1998, pp. 1066-1070.

[13] Van Vlerken, J.J.L.M.; and Blanken, P.G. "Lumped Modeling of Rotary Transformers, Heads and Electronics for Helical-Scan Recording." *IEEE Transactions on Magnetics*, Vol. 31 (2), March 1995, pp. 1050-1055.

[14] Stuart, T.A.; King, R.J.; and Shamseddin, H. "Rotary Transformer Design with Fixed Magnetizing and/or Leakage Inductances*." IEEE Transactions on Aerospace and Electronic Systems*, Vol. AES-22, No. 5, September 1986, pp. 565-572.

[15] McLyman, W. T. *Split Coil Forms for Rotary Transformers.* NASA Tech Briefs (ISSN 0145-319X) / vol. 6; no. 4; P. 465

[16] Depenbrock, M. “Direct Self Control (DSC) of Inverter-fed Induction Machine.” *IEEE Trans. Power Electronics*, Vol. 3 (4), October 1988, pp. 420-429.

[17] Takashi, I; and Ohmori, Y. “High Performance Direct Torque Control of an Induction Motor.” *IEEE Transactions Ind. Application*, Vol. 25 (2), March/April 1989, pp. 257-264.

[18] Nash, J.N. “Direct Torque Control of Induction Motor without an Encoder.” *IEEE Trans. Industry Applications*, Vol. 33 (2), March/April 1997, pp. 333-341.

[19] Datta, R.; and Ranganathan, V.T. “Decoupled Control of Active and Reactive Power for a Grid-Connected Doubly Fed Wound-Rotor Induction Machine Without Position Sensors.” *Proceedings Conference Record, 1999 IEEE IAS Annual Meeting*, Vol. 4, October 1999, pp. 2623-2630.

# REPORT DOCUMENTATION PAGE

*Form Approved*
*OMB No. 0704-0188*

The public reporting burden for this collection of information is estimated to average 1 hour per response, including the time for reviewing instructions, searching existing data sources, gathering and maintaining the data needed, and completing and reviewing the collection of information. Send comments regarding this burden estimate or any other aspect of this collection of information, including suggestions for reducing the burden, to Department of Defense, Executive Services and Communications Directorate (0704-0188). Respondents should be aware that notwithstanding any other provision of law, no person shall be subject to any penalty for failing to comply with a collection of information if it does not display a currently valid OMB control number.

**PLEASE DO NOT RETURN YOUR FORM TO THE ABOVE ORGANIZATION.**

| 1. REPORT DATE *(DD-MM-YYYY)* | 2. REPORT TYPE | 3. DATES COVERED *(From - To)* |
|---|---|---|
| November 2005 | Subcontract Report | August 1999 - May 2003 |

**4. TITLE AND SUBTITLE**
Design and Test of DC Voltage Link Conversion System and Brushless Doubly-Fed Induction Generator for Variable-Speed Wind Energy Applications

**5a. CONTRACT NUMBER**
DE-AC36-99-GO10337

**5b. GRANT NUMBER**

**5c. PROGRAM ELEMENT NUMBER**

**6. AUTHOR(S)**
T.A. Lipo, D. Panda, and D. Zarko

**5d. PROJECT NUMBER**
NREL/SR-500-34583

**5e. TASK NUMBER**
WER5.3203

**5f. WORK UNIT NUMBER**

**7. PERFORMING ORGANIZATION NAME(S) AND ADDRESS(ES)**
Department of Electrical and Computer Engineering
University of Wisconsin - Madison
Madison, Wisconsin

**8. PERFORMING ORGANIZATION REPORT NUMBER**
XCX-9-29204-02

**9. SPONSORING/MONITORING AGENCY NAME(S) AND ADDRESS(ES)**
National Renewable Energy Laboratory
1617 Cole Blvd.
Golden, CO 80401-3393

**10. SPONSOR/MONITOR'S ACRONYM(S)**
NREL

**11. SPONSORING/MONITORING AGENCY REPORT NUMBER**
NREL/SR-500-34583

**12. DISTRIBUTION AVAILABILITY STATEMENT**
National Technical Information Service
U.S. Department of Commerce
5285 Port Royal Road
Springfield, VA 22161

**13. SUPPLEMENTARY NOTES**
NREL Technical Monitor: Alan Laxson

**14. ABSTRACT** *(Maximum 200 Words)*
This report describes four low-cost alternative power converters for processing the power developed by a doubly fed wound-rotor induction generator for wind energy conversion systems.

**15. SUBJECT TERMS**
wind turbine; alternative power converters; induction generator; wind energy

| 16. SECURITY CLASSIFICATION OF: | | | 17. LIMITATION OF ABSTRACT | 18. NUMBER OF PAGES | 19a. NAME OF RESPONSIBLE PERSON |
|---|---|---|---|---|---|
| a. REPORT | b. ABSTRACT | c. THIS PAGE | | | 19b. TELEPHONE NUMBER (*Include area code*) |
| Unclassified | Unclassified | Unclassified | UL | | |

**Standard Form 298** (Rev. 8/98)
Prescribed by ANSI Std. Z39.18